NASA

**National Aeronautics and
Space Administration**

AERODYNAMIC STABILITY ANALYSIS
OF NASA J85-13/PLANAR PRESSURE
PULSE GENERATOR INSTALLATION

by

K. Chung
W.M. Hosny
W.G. Steenken

GENERAL ELECTRIC COMPANY

Prepared For

National Aeronautics and Space Administration

1. Report No. NASA CR-165141	2. Government Accession No.	3. Recipient's Catalog No.
4. Title and Subtitle Aerodynamic Stability Analysis of NASA J85-13/Planar Pressure Pulse Generator Installation		5. Report Date November, 1980
		6. Performing Organization Code

7. Author(s)   K. Chung
    W. M. Hosny
    W. G. Steenken
		8. Performing Organization Report No
		R80AEG429

		10. Work Unit No.
9. Performing Organization Name and Address General Electric Company Aircraft Engine Group Cincinnati, Ohio 45215		11. Contract or Grant No. NAS3-21259
		13. Type of Report and Period Covered Contract Report
12. Sponsoring Agency Name and Address National Aeronautics and Space Administration		14. Sponsoring Agency Code

15. Supplementary Notes
Project Monitor· P. G. Batterton
NASA Lewis Research Center
Cleveland, Ohio 44135

16. Abstract

The primary objective of the program described in this report was to develop a digital computer simulation model for the NASA-developed J85-13/P^{3}G test installation. This objective was accomplished by modifying an existing General Electric compression system model. This modification included the incorporation of a novel method for describing the unsteady blade lift force. This new approach significantly enhanced the capability of the model to handle unsteady flows. In addition, the frequency response characteristics of the J85-13/P^{3}G test installation were analyzed in support of selecting instrumentation locations to avoid standing wave nodes within the test apparatus and thus, low signal levels. The feasibility of employing explicit analytical expressions for surge prediction was also studied as a part of this program effort.

17. Key Words (Suggested by Author(s)) Compressor Stability Aerodynamic Stability Analytical Simulation Technique Planar Wave Simulation Frequency Response Analysis Analytical Surge Criteria		18. Distribution Statement		
19. Security Classif. (of this report) Unclassified	20. Security Classif. (of this page) Unclassified		21. No. of Pages 151	22. Price*

NASA-C-168 (Rev. 10-75)

FOREWORD

The program described in this report was conducted by the Aircraft Engine Group of the General Electric Company, Cincinnati, Ohio for the NASA Lewis Research Center, National Aeronautics and Space Administration under contract NAS3-21259.

The program was carried out under the technical cognizance of Mr. P. G. Batterton of the NASA-Lewis Research Center, Turbine Engine Branch.

The contract effort was conducted at the Evendale Plant of the General Electric Aircraft Engine Group, Cincinnati, Ohio under the technical direction of Dr. W. G. Steenken with this writer being the primary technical contributor.

Technical consultation was provided by Mr. G. G. Reynolds throughout this program. Support was provided by Dr. W. M. Hosny in the initial derivation of the explicit analytical surge criteria and by Mr. R. H. Moszee in running computer programs.

Support was provided also by Mrs. J. Brooke in preparing this manuscript, by Mrs. L. G. Radcliffe in preparing figures, and by Ms. M. J. Millikin in running computer programs.

<div align="center">

Kiyoung Chung, Engineer
Engine Operability Technology
Aircraft Engine Group
General Electric Company

</div>

TABLE OF CONTENTS

LIST OF ILLUSTRATIONS

LIST OF ILLUSTRATIONS (Continued)

LIST OF ILLUSTRATIONS (Continued)

LIST OF ILLUSTRATIONS (Continued)

LIST OF TABLES

NOMENCLATURE

A	-	Area and Complex Function Defined by Equation 37
a	-	Acoustic Velocity
B	-	Complex Function Defined by Equation 38
C	-	Absolute Velocity and Theodorsen Function
C	-	Axial Velocity
F	-	Complex Function Defined by Equation 32
F_D	-	Drag Force
F_L	-	Lift Force
F_T	-	Tangential Blade Force
F	-	Axial Blade Force
G	-	Complex Function Defined by Equation 32
g_c	-	Dimensional Constant
g_o	-	Gravitational Constant
H	-	Hankel Function
I	-	Incidence Angle Vector
i	-	Incidence Angle
J_n	-	Bessel Function of First Kind
j	-	Imaginary Number
K	-	Complex Argument Defined by Equations 34 and 35
K_1, K_2	-	Lift Force Correction Factors
L	-	Volume Length
M	-	Mach Number
N	-	Revolutions Per Minute
P	-	Static Pressure
P	-	Mean Static Pressure on Control Volume
P_t	-	Total Pressure
r	-	Radius
S	-	Entropy

NOMENCLATURE (Concluded)

S_F	-	Internal Entropy Production Term
S	-	LaPlace Transform Variable
T	-	Temperature
t	-	Time
U	-	Velocity
U_n	-	Forcing Function
V	-	Volume
W	-	Mass Flow Rate
Y_n	-	Bessel Function of Second Kind
α	-	Angle of Attack, Absolute Air Angle
β	-	Relative Air Angle
β^*	-	Blade Metal Angle
β_c	-	Lift Direction Correction Angle
γ	-	Isentropic Exponent
δ	-	Deviation Angle
θ	-	Phase Angle
λ	-	Roots of Matrix Characteristic Equation
μ	-	Damping Coefficient
ρ	-	Density
ω	-	Frequency
ω	-	Blade Loss Coefficient

Subscripts

1	-	Volume Inlet
2	-	Volume Exit
z	-	Axial Direction

1. SUMMARY

A one-dimensional compression system model that simulates the unsteady aerodynamics in the NASA J85-13/P^{3}G (Planar Pressure Pulse Generator) test installation has been developed. In addition, the frequency response characteristics of the test apparatus were evaluated using a linearized frequency analysis technique. This analysis was performed in support of selecting instrumentation 'ocations to avoid standing wave nodes of the installation and thus, low signal levels. The feasibility of employing a set of explicit analytical surge criteria in evaluating the stability of an axial compressor was also investigated.

The J85-13/P^{3}G simulation program was developed by modifying an existing program known as the Dynamic Digital Blade Row Compressor System Stability Model (also called AEROSTAP). The capability of the model to handle unsteady flows was enhanced by introducing an analytical expression for the unsteady-blade-lift force to compute the blade force acting upon the fluid. The validity of the modified model was verified by comparing the simulation results with the test data for the F101 Fan/P^{3}G – a test installation similar to the J85-13/P^{3}G.

Subsequent to the program validation, the model was run at 100% compressor design speed over the P^{3}G frequency range of 100 to 850 Hz to simulate the stationary operations of the J85-13/P^{3}G. Pressure waveforms at various locations of the test installation were obtained to provide a direct comparison with future test data. Then, the model was throttled to surge at five different frequencies, i.e. 100, 150, 200, 250, and 300 Hz. and the inlet planar wave distortion sensitivity of the J85-13 turbojet engine was determined as a function of the P^{3}G frequency.

The frequency response analysis of the J85-13/P^{3}G was performed for the frequencies ranging from 10 to 1000 Hz using a General Electric developed linearized frequency analysis program. This analysis yielded the nodes and anti-nodes of the test installation as a function of frequency. The resonance frequencies of the test apparatus were also identified from the analysis.

The explicit analytical surge criteria were derived from the linearized conservation equations (mass and momentum) based upon the Lyapunov first theorem of stability. The criteria were applied to two different configurations, "Moss" and "Mehalic", of the J85-13 engine. They were found effective at 100% design speed, but were ineffective at lower speeds. This is believed mainly due to the boundary conditions whose validity is weakened as the speed is lowered. Recommendations to improve the capability of the criteria are listed in the last section of this report.

2.0 INTRODUCTION

NASA Lewis Research Center is developing a test installation known as the J85-13/P^{3}G, Figure 1, for the purpose of investigating unsteady aerodynamics in gas turbine engines. The apparatus includes a General Electric J85-13 turbojet engine and a device known as the Planar Pressure Pulse Generator (P^{3}G). The P^{3}G, which was modelled after a similar device used earlier by General Electric (Reference 1), was designed and fabricated by Battelle Columbus Laboratories.

The function of the P^{3}G is to generate sinusoidally oscillating flow over a wide range of frequencies and amplitudes. This is accomplished by modulating the flow area with a rotating disc and a stationary disc with mating holes in each. The frequency of the planar wave is varied by changing the rotor speed. The amplitude of the oscillation is varied by changing the rotor-to-stator spacing. When the J85-13 engine is operated coupled with the P^{3}G, the engine can be subjected to oscillating inlet flows in which both the frequency and amplitude are independently variable over wide ranges.

The J85-13/P^{3}G test is the first of a series of experimental efforts planned at NASA Lewis Research Center. The objective of this test is to evaluate the unsteady aerodynamic responses of a multi-stage compressor, e.g. unsteady-operating-point excursion, compressor instability, etc., with oscillating inlet flow conditions. The J85-13 engine was selected for this test because of the extensive operational and analytical experience that NASA has obtained with the compressor. A large amount of data has been accumulated for both the performance and distortion sensitivity of the J85-13 compressor (References 2 and 3). In addition, several computer models have been developed to simulate the unsteady as well as the steady operations of the compressor (References 2, 3, and 4).

The main objective of the effort discussed in this report was to develop a digital computer simulation code that is capable of modelling the unsteady behavior of a compressor subjected to the oscillating inlet flow generated by the P^{3}G. This program will be utilized for the pretest predictions as well as for posttest analyses to aid in obtaining an understanding of the unsteady responses of the compressor. In addition, the frequency response characteristics of the J85-13/P^{3}G test facility were studied in support of selecting instrument locations to avoid the standing wave nodes within the apparatus and thus low signal levels. The feasibility of employing explicit analytical expressions for surge prediction was also investigated as part of this effort. A set of explicit surge criteria was developed as a result of this study. These criteria are applicable only to an isolated rotor although the inlet and exit rotor boundary conditions are obtained from the simulation of a complete compression system including stators and free volumes.

2
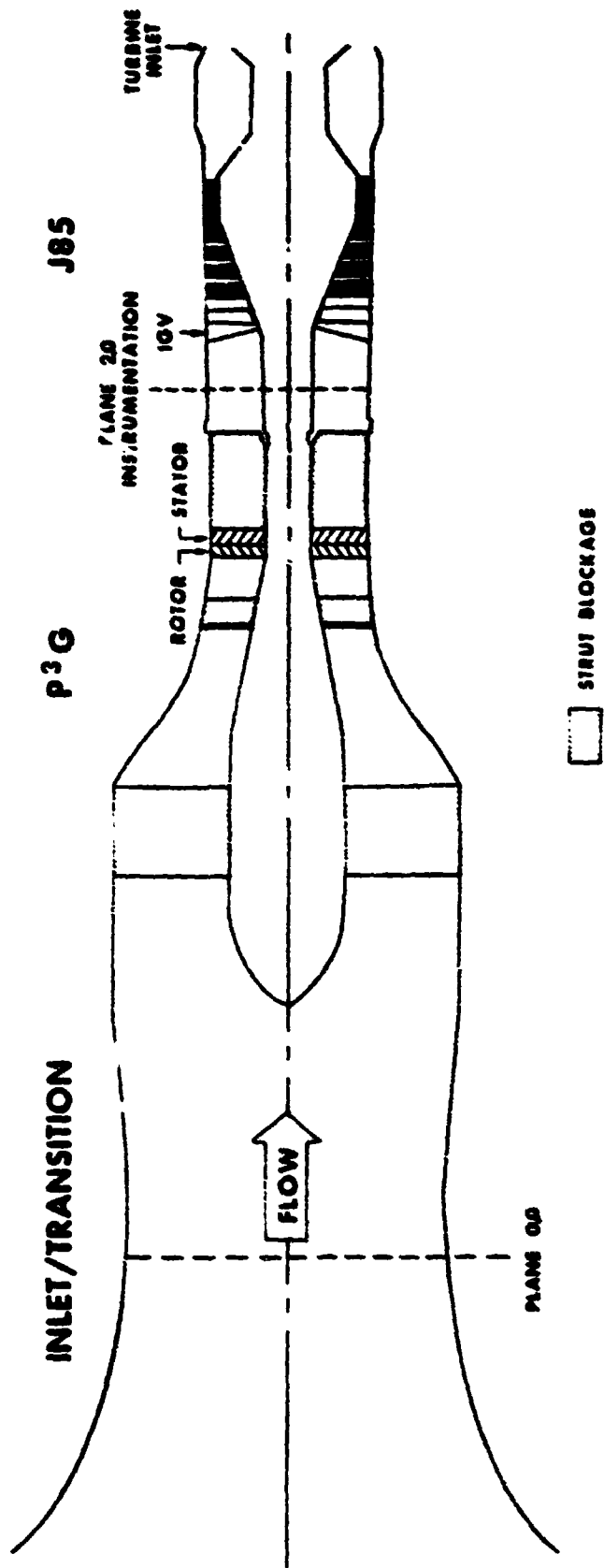
Figure 2. Sketch of J85-13/P³G Model Flowpath.

3

The J85-13/P^{3}G simulation program was developed by modifying the Dynamic Digital Blade Row Compression System Stability Model (called AEROSTAP, Reference 5) developed by the General Electric Company. This program employs a one-dimensional, pitch line, blade row-by-blade row model to solve the three conservation equations with the proper thermodynamic relationships. These three governing equations (mass, momentum, and energy) are written in a volume-average form and the dynamic solution is obtained through a time-marching scheme. Derivation of the three governing equations and the solution method employed in the AEROSTAP Program is outlined in Subsection 3.1. The essence of the modifications to this program is the incorporation of an expression for the unsteady-blade lift force that is induced by the oscillating inlet flow produced by the P^{3}G. The expression employed to describe the unsteady-lift force of a cascade was derived from the unsteady-lift force that is applicable to an isolated thin airfoil subjected to gust loading (Reference 6). The derivation of this expression is presented in Subsection 3.3.

The validity of employing the resultant expression for the unsteady-blade-lift force for a cascade was verified by comparing the simulation results with experimental data obtained during a test similar to that proposed for the J85-13/P^{3}G (Reference 7). This verification procedure and the results are discussed in Subsection 4.1. The modified AEROSTAP Program was then utilized to simulate the operations of the J85-13/P^{3}G at various operating conditions. The results of the simulation are presented also in Subsection 4.1.

The frequency analysis of the J85-13/P^{3}G test facility was performed using a digital frequency analysis program known as the DSP (Digital Surge Prediction) program (Reference 4). In this program, the frequency response characteristics are evaluated by linearizing the three conservation equations and then determining the transfer function of the linearized system by means of Laplace transforms. These techniques which are discussed in detail in Reference 4 are outlined in Subsection 3.4.

The analysis of the frequency response characteristics of the J85-13/P^{3}G was conducted by dividing the geometry into two regions; i.e., the region forward of the P^{3}G and the region aft of the P^{3}G including the J85-13 engine. This analysis yielded the resonance frequencies of the two sections and their higher-order harmonics as well as the nodal points at various frequencies. These results are presented in Subsection 4.2.

The explicit analytical stability criteria were derived based upon the Lyapunov's first theorem; the theorem states that a system of nonlinear equations is stable if the eigenvalues of the linearized version of the system have negative real parts. In this derivation, the eigenvalues of the linearized

4

conservation equations are examined by the Routh-Hurwitz criterion. At this point of development and for the ease of analysis, only the mass and momentum conservation equations are employed; i.e. the flow through a compression system is assumed homentropic. The explicit stability criteria are derived in Subsection 3.5. A more detailed derivation of the equations is given in Appendix A. Application of these criteria and a critique of the technique are found in Subsection 4.3.

3.0 ANALYTICAL TECHNIQUES

This section presents the analytical techniques used to develop the digital computer program that simulates the operation of the J85-13/P^{3}G test installation. A brief description of the techniques employed to investigate the frequency response characteristics of the J85-13/P^{3}G apparatus is also presented. In addition, derivation of explicit analytical stability criteria for axial compressors is discussed.

The J85-13/P^{3}G simulation program was developed by modifying a version of the Dynamic Digital Blade Row Compression System Stability Model (called AEROSTAP, Reference 5) developed by the General Electric Company to simulate a test facility, known as the F101 Fan/P^{3}G, similar to that of the J85-13/P^{3}G. Reference 2 indicated that while this program adequately simulates most aspects of F101 Fan/P^{3}G operations, the phase angles of the pressure waveforms computed at various locations in the test facility did not compare well with the test data. It was believed that this mismatch in phase angles is due to inadequate description of the unsteady behavior of the compressor blades under the oscillating inlet flow generated by the Planar Pressure Pulse Generator. Thus, a novel method of describing the unsteady behavior of the compressor cascade has been added to the AEROSTAP to enhance the accuracy of the simulation.

Previously, the axial force acting on the fluid due to the compressor blades was computed via the tangential blade force which was obtained from the generalized Euler Turbine Equation. This approach has been utilized successfully for the simulation of steady as well as transient operations of various compressors. However, the expression for the tangential force does not permit accounting for the phase difference between the oscillating flow incident on the blade and the similarily oscillating blade force. Therefore, in the new approach, the axial blade force is computed through the blade-lift force within which the phase difference can be easily included.

The governing equations of motion that are in the form used in the AEROSTAP are derived in Subsection 3.1. The ancillary relations required to solve the governing equations and the solution technique are also presented in the subsection. Modelling of the P^{3}G which generates sinusoidally oscillating flow over a wide range of frequencies and amplitude is discussed in Subsection 3.2.

The expression for the unsteady-blade-lift force is derived in Subsection 3.3. This expression was derived from the unsteady-lift force that is applicable to an isolated thin airfoil subjected to gust loading. It was assumed that by introducing correction constants, the resultant relationship is valid also for a cascade.

6

The frequency analysis of the J85-13/P^{3}G test facility was conducted with the use of a frequency analysis program known as the Digital Surge Prediction (DSP) program. The frequency response characteristics are evaluated by linearizing the three conservation equations and subsequently determining the transfer function of the linearized system by means of Laplace transforms. This program is also capable of determining the stability of an equilibrium solution of the three conservation equations by examining the eigenvalues of the linearized system. NASA developed subroutines are used in the DSP program for the evaluation of Laplace transform and for the inspection of the eigenvalues. This program which is discussed in detail in Reference 4 is briefly described in Subsection 3.4.

In Subsection 3.5, the explicit analytical criteria are derived based upon the Poincaré - Lyapunov stability theory. These criteria check the stability of an equilibrium solution of the three governing equations by examining the eigenvalues of the linearized conservation equations by the Routh-Hurwitz criteria. These stability criteria are applied to each rotor volume of a compressor. It is assumed that the operation of the compressor is unstable if the sign of the real part of the eigenvalues associated with one or more of the rotor volumes changed from negative to positive.

3.1 ANALYTICAL TECHNIQUE FOR THE SIMULATION OF COMPRESSION SYSTEM

In this subsection, the equations of change which describe the motion of the compressible fluid flowing through a compression system are derived. They are written in volume-averaged form in terms of the nomenclature given in Pages xiii through xiv. In addition, the auxillary relationships used in the conservation equations are also derived.

The three conservation equations, mass, momentum, and energy, are solved by a technique known as the time-marching scheme. This technique which is discussed in detail in Reference 3 is outlined in Subsection 3.1.2.

3.1.1 Governing Equations

The equations of motion are derived for an arbitrary volume, V_k, with the inlet area, A_i, the exit area, A_{i+1}, and the volume length, L_k, as shown in Figure 2. The macroscopic balances of mass, momentum, and energy for this volume for quasi one-dimensional flow yield the following equations:

Continuity:

$$\frac{\partial \bar{\rho}_k}{\partial t} = \frac{1}{V_k} \left[W_i - W_{i+1} \right] \tag{1}$$

Momentum:

$$\frac{\partial \bar{W}_k}{\partial t} = \frac{g_c}{L_k} \left[\frac{W_i^2}{g_c \rho_i A_i} - \frac{W_{i+1}^2}{g_c \rho_{i+1} A_{i+1}} + P_i A_i - P_{i+1} A_{i+1} + \Sigma F_K \right] \tag{2}$$

Energy:

$$\frac{\partial \bar{\rho S}}{\partial t} = \frac{1}{V_k} \left[W_i S_i - W_{i+1} S_{i+1} + S_F \right] \tag{3}$$
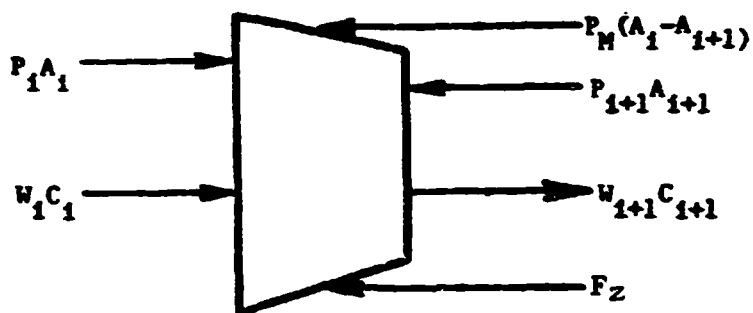

Figure 2. Quasi One-Dimensional Volume.

where the quantities with the bar " - " are defined by the following relationship.

$$\bar{F}_k = \frac{1}{V_k} \int_{V_k} F_k \, dV \tag{4}$$

8

This set of the conservation equations provides an exact description of the quasi one-dimensional flow through an arbitrary volume. Note that the only assumption applied in the derivation of these equations is that the flow is one-dimensional. All the boundary effects such as the wall friction loss and heat transfer can be included in the right-hand side of the momentum and energy equation through ΣF_k and S_F. However, it should be noted that these boundary effects are not included in the solution since their orders of magnitude are much smaller than other terms in the conservation equations.

In order to obtain a solution of the three conservation equations, it is necessary to supply the ideal gas equation of state, the caloric equations of state and expre. ns for ΣF_k and S_F.

The force ....ms, ΣF_k, in Equation 2 represents the force exerted on the fluid by all the solid surfaces such as the end walls and blades. As stated previously, the wall friction is neglected in this analysis. Then, the force term can be expressed as

$$\Sigma F_k = \int_{\substack{\text{lateral} \\ \text{area}}} Pd\underline{A} + F_z \tag{5}$$

where $d\underline{A}$ is the differential area vector and F_z is the axial-direction force acting on the fluid due to the compressor blades.

The lateral surface pressure integral can be evaluated by

$$\int_{\substack{\text{lateral} \\ \text{area}}} Pd\underline{A} = \int_1^2 PdA \tag{6}$$

Introduction of the definition of a mean pressure

$$P_M = \int_1^2 PdA \bigg/ \int_1^2 dA \tag{7}$$

enables one to rewrite Equation 6 as

$$\int_{\substack{\text{lateral} \\ \text{area}}} Pd\underline{A} = - P_M(A_1 - A_2) \tag{8}$$

Three different expressions for P_M are given in References 1 and 4: 1) a polynomial representation developed from the isentropic relations for blade-free volumes

$$P_M = \frac{(P_{t1} - P_{t2})}{2 (M_2 - M_1)} \left[0.99998104 \, (M_2 - M_1) + 0.000908125 \, (M_2^2 - M_1^2) \right.$$

$$- 0.24098565 \, (M_2^3 - M_1^3) + 0.02419741 \, (M_2^4 - M_1^4)$$

$$\left. + 0.03442452 \, (M_2^5 - M_1^5) \right] \tag{9}$$

2) an empirical relationship for blade-free volumes

$$P_M = (P_1 + CP_2)/(1 + C) \tag{10}$$

where $\quad C = C_1 (A_2 - A_1)/A_1 + C_2 \tag{11}$

$$C_1, \; C_2 = \text{empirical constants}$$

and 3) an empirical correlation for bladed volumes

$$P_M = \frac{2P_H + P_L}{3} \tag{12}$$

where P_H is the higher of the values of the inlet or exit static pressure and P_L is the lower of the two. The empirical correlation for blade-free volumes was developed by examining the behavior of the mean pressure in the blade-free volumes of the J85-13 engine. The correlation for bladed volumes was derived from the observation of P_M in bladed volumes of various General Electric compressors where there were no losses. This empirical relationship is assumed to be equally valid when blade losses are present.

The other term in the sum of the surface forces is the axial force, F_z, exerted by the blade. This force can be determined from the various force components depicted in the following sketch.
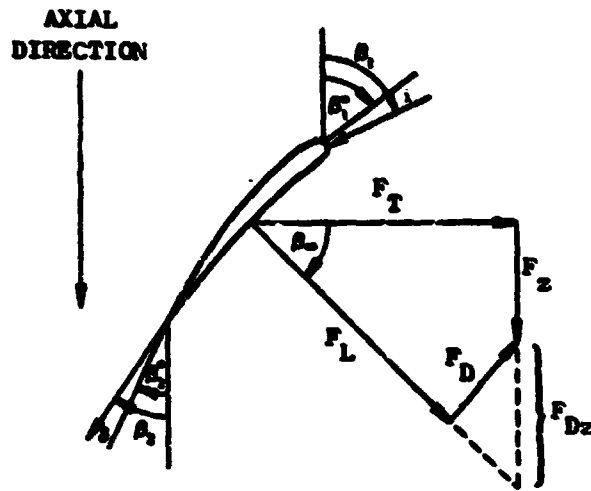
10

Figure 3. Components of Blade Forces.

Examination of the force vectors in the sketch shows that

$$F_z = F_T \tan\beta_\infty \quad - F_{Dz} \tag{13}$$

where F_T is the tangential force at the pitch line and F_{Dz} is the axial component of the blade drag force acting upon the fluid. The lift direction angle, β_∞, in the expression of F_z is given by the following equation.

$$\beta_\infty = (\beta_1 + \beta_2)/2 + \beta_c \tag{14}$$

$$\text{where } \beta_1 = \beta_1^* + i \tag{15}$$

$$\beta_2 = \beta_2^* + \delta \tag{16}$$

β_c : lift correction angle

β_1^*, β_2^* : metal angles at the inlet and exit respectively

The tangential force, F_T, can be obtained from the generalized Euler Turbine Equation and is written as

$$F_T = \frac{1}{g_c} \left[\frac{r_2 W_2 C_{u2} - r_1 W_1 C_{u1}}{r_1 + r_2} \right] + V \frac{\partial(\overline{\rho C_u})}{\partial t} \tag{17}$$

11

where r_1 and r_2 are the pitch line radii at the inlet and exit of the blade row, respectively. The second term in Equation 17 represents the tangential force due to the storage of angular momentum within a blade row volume.

The drag force acts perpendicular to the lift force at an angle of β_∞ from the axial direction. Thus, the axial component of the drag force, F_{Dz}, can be written as

$$F_{Dz} = F_D / \cos \beta_\infty \tag{18}$$

where

$$F_D = \omega' \frac{P_1}{P'_{t1}} \frac{P'_d}{q'_1} A_{1\beta} q'_1 \tag{19}$$

The prime (') symbol indicates that the quantities are evaluated with respect to the relative velocity frame of reference. The area, $A_{1\beta}$, is the flow area perpendicular to the direction of the inlet relative air angle, β_1. The relative total-pressure loss coefficient, ω', is defined by the equation.

$$\omega' = \frac{P'_{t2})_{Ideal} - P'_{t2})_{Actual}}{P'_{t1} - P_1} \tag{20}$$

The values of ω' are evaluated from the experimental data that are correlated as a polynomial function of tan i.

The term S_F in Equation 3 is known as the internal entropy generation term in the absence of the heat transfer at the boundaries. This term can be expressed as

$$S_F = WR \ln \left[\frac{P'_{t2}/P_{t1}) \, Ideal}{P'_{t2}/P'_{t1}) \, Actual} \right] \tag{21}$$

The ideal total-pressure ratio can be written (Reference 8) as

$$\frac{P'_{t2}}{P'_{t1}} \right)_{Ideal} = \left\{ 1 + \frac{\gamma-1}{2} M_t^2 \left[1 - (\frac{r_1}{r_2})^2 \right] \right\}^{\frac{\gamma}{\gamma-1}} \tag{22}$$

12

where $M_t = 2\pi N r_2 / a'_{t1}$ (23)

and a'_{t1} is the inlet speed of sound evaluated with the relative total temperature. The expression for the actual total-pressure ratio can be obtained by rearrangement of Equation 20 and substitution of the isentropic relation for total pressure and static pressure as

$$\left.\frac{P'_{t2}}{P'_{t1}}\right)_{\text{Actual}} = \left.\frac{P'_{t2}}{P'_{t1}}\right)_{\text{Ideal}} - \omega'\left\{1 - \left[\frac{1}{1 + \frac{\gamma - 1}{2}(M'_1)^2}\right]^{\frac{\gamma}{\gamma - 1}}\right\}$$ (24)

For more detailed derivation of the governing equations and their ancillary relationships, readers sh ld consult Reference 3.

3.2.2 Solution Technique

The technique employed in solving the governing equations, Equations 1 through 3, is known as the time marching scheme. This technique is based upon a Taylor series expansion of the volume-averaged flow properties at time, t, to predict the flow properties at time, t + Δt. The time derivatives of volume-averaged properties that are used in the Taylor series are obtained from the properties at the inlet or exit station of a volume. A suitable interpolation scheme should be selected to assure the numerical stability of the solution technique. Reference 3 gives a detailed account and a critique of various interpolation schemes; thus, they are not discussed here.

Once the volume-averaged properties and their time derivatives are o' tained, a Taylor expansion of the variables, $\bar{\rho}$, $\bar{W}$, and $\bar{\rho S}$ is straight f rward. This expansion is illustrated for one variable, namely, the volume-averaged density. The Taylor series for $\bar{\rho}$ correct to second order can be written as

$$\bar{\rho}(t + \Delta t) = \bar{\rho}(t) + \frac{\partial \bar{\rho}(t)}{\partial t}\Delta t + \frac{\partial^2 \bar{\rho}(t)}{\partial t^2}\frac{\Delta t^2}{2}$$ (25)

where $\bar{\rho}(t)$ is established by the initial conditions or a vious time step and

$$\frac{\partial \bar{\rho}(t)}{\partial t} = \frac{1}{V}\left[W_1 - W_2\right]$$ (26)

13

$$\frac{\partial^2 \bar{\rho}(t)}{\partial t^2} = \frac{1}{V} \left[\frac{\partial W_1}{\partial t} - \frac{\partial W_2}{\partial t} \right] \tag{27}$$

Examination of Equation 27 reveals that the right-hand side is composed of derivatives of station properties, W_1 and W_2. These derivatives are evaluated from the momentum equation through an interpolation scheme since Equation 2 provides only the volume-averaged derivative. Substitution of Equations 26 and 27 into Equation 25 permits one to evaluate the volume-averaged density correct to second order at the next time increment. Similarily, this technique can be used for the remaining two variables, $\overline{W}$ and $\overline{\rho S}$, and can be continued from one time step to the next for the desired number of time steps.
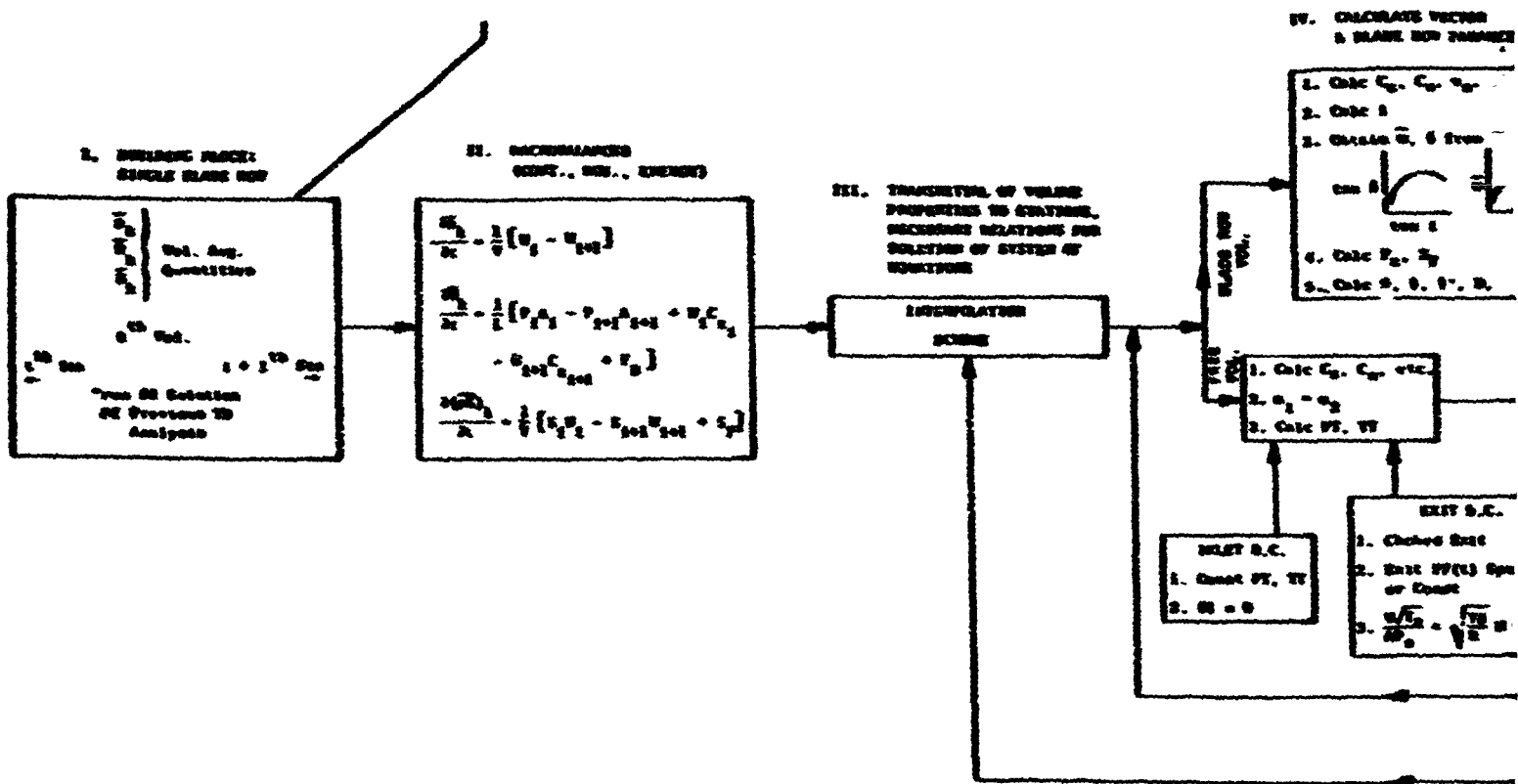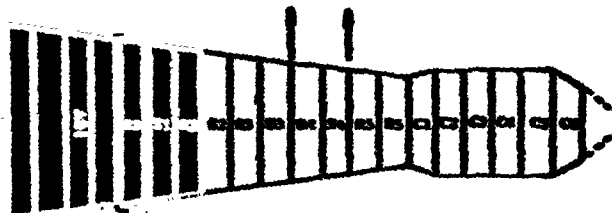
This computational technique is illustrated in Figure 4 in block diagram format. For more detailed discussion of the solution technique, readers should consult Reference 3.

3.2 Modelling of Planar Pressure Pulse Generator

The function of the Planar Pressure Pulse Generator (P^3G) is to generate a sinusoidally oscillating flow over a wide range of frequencies and amplitudes. This is accomplished by modulating the flow area with a rotating disc and a stationary disc with mating holes in each. The air flow is induced by the compressor downstream of the P^3G. The frequency of the planar wave is varied by changing the rotor speed while the amplitude of the oscillation is varied by changing the rotor-to-stator spacing. The change in the rotor-to-stator spacing alters the effective flow area and, thus, varies the amplitude of the oscillation.

The P^3G area is essentially choked at all times and the total pressure loss results mainly from shock losses as the supersonic stream immediately after the P^3G adjusts to higher pressure further downstream. Some viscous losses are present due to mixing of the air streams from adjacent holes in the stator. However, for the flow rates and planar wave amplitude of interest, the shock losses are predominent; therefore, the viscous losses are neglected in this model.

The P^3G model approximates the aerodynamics of the actual operation as follows: A steady-state condition satisfying the mean conditions of the P^3G operation is established using the mean steady-state total-pressure recovery across the P^3G as measured during the test. This enables one to compute an effective choked area at the P^3G from the flow function

14

Figure 4.   Dynamic Model Blo

IV. CALCULATE VECTOR DIAGRAMS
& BLADE ROW PARAMETERS

1. Calc C_x, C_u, a_u, etc.
2. Calc i
3. Obtain $\bar{a}$, δ from Char.

4. Calc F_x, S_p
5. Calc θ, η, θ', D, etc.

BLADE ROW VOL.

INLET VOL.

1. Calc C_x, C_u, etc.
2. $a_1 = a_2$
3. Calc PT, TT

V. CALCULATE 1st DERIVATIVES
OF VOLUME AVERAGE PROPER-
TIES FOR BACKBALANCES

SEE BLOCK IX

VI. CALCULATE 2nd DERIVATIVES
OF V.A. PROPERTIES
(DIFFERENTIATE II)

$$\frac{\partial}{\partial t}\frac{\partial v}{\partial t} = \frac{1}{V}\frac{\partial}{\partial t}\left[v_1 - v_{i+1}\right]$$

VIII. PREDICT NEW VALUES OF
V.A. PROPERTIES THROUGH
TAYLOR'S SERIES EXP.

$$\bar{v}(t+\Delta t) = \bar{v}(t) + \frac{\partial \bar{v}}{\partial t}\bigg|_t \Delta t + \frac{\partial^2 \bar{v}}{\partial t^2}\bigg|_t \frac{\Delta t^2}{2}$$

INLET B.C.
1. Const PT, TT
2. $\Omega = 0$

EXIT B.C.
1. Choked Exit
2. Exit PT(t) Specified
or Const
3. $\frac{w\sqrt{T_s}}{A P_s} = \sqrt{\frac{\gamma g}{R}}$ $S = PT$

VII
CALCULATIONS CARRIED OUT
FOR ALL VOLUMES

IX
REPEAT COMPUTATIONAL PROCEDURE
AS MANY TIME STEPS AS DESIRED

4. Dynamic Model Block Diagram.

$$FF = \frac{w\sqrt{T_t}}{A^* P_t} \tag{28}$$

where A is the choked area. The flow function and the total temperature across the P^3G remains constant. This mean area becomes the base for the amplitude of the area fluctuation. The amplitude is controlled by the parameter "amp" as illustrated in the following equation.

$$A^*_{P^3G} = A^*_{P^3G \, base} \left[1 + amp \, sin \, (2\pi Nt/60) \right] \tag{29}$$

This choked area can be related to the upstream duct A^*/A_{duct} and provides the exit boundary condition to the P^3G.

As much of the existing General Electric Dynamic Digital Blade Row Compression Component Stability Model logic was utilized as possible, and the P^3G model was constructed as a subroutine to the main program. For further information concerning the modelling and operation of the P^3G the readers should consult References 1 and 7.

3.3 Blade Lift Force

In Subsection 3.1, the axial-direction blade force, F_z, was expressed in terms of the tangential forces, F_T, and the axial component of the drag force, F_{Dz}. As stated previously, this approach of computing F_z was highly successful in simulating transient as well as steady-state operations of axial compressors under various operating conditions. However, when a large amplitude oscillation such as the planar pressure wave generated by the P^3G is present at the inlet, this method cannot satisfactorily describe the frequency response, namely the phase angle, of the compressor (Reference 7). Therefore, a new method of computing F_z has been added to the AEROSTAP program to improve the frequency response of the simulation. This new technique calculates the axial-direction blade force through the blade lift force, F_L, instead of the tangential force, F_T; the drag force, F_D, is evaluated in the same manner as described before. From the force component diagram depicted in Figure 3, the new relationship can be derived as

$$F_z = F_L \, sin\beta_\infty - F_D \, cos\beta_\infty \tag{30}$$

The expression for the unsteady-blade-lift force, F_L, was derived from the lift force applicable to a thin airfoil subjected to sinusoidal vertical gust. That is: First, the unsteady lift force for the thin airfoil is obtained by considering the lift force due only to the gust loading. It is assumed that

17

the airfoil is placed initially in a uniform incompressible velocity field of U without any angle of attack. Next, the uniform velocity field is tilted slightly to give a steady-state lift force to the airfoil. This is intended to approxi-mate the flow over a compressor blade. The total lift force acting on the fluid by the airfoil is then obtained by superposing the unsteady lift force determined previously on the steady lift force. Subsequently, this expression for the total lift force is applied to a cascade by introducing two correction factors. These factors account for the cascade effect, profile shape and camber, profile drag and compressibility.

For a thin airfoil, Figure 5, encountering a sinusoidally oscillating vertical gust of $W_G = \overline{W}_G e^{j\omega t}$ in an otherwise uniform stream of U, Reference 6 expresses the unsteady lift force due only to the gust loading as

$$F_{L, dyn} = \pi \rho U b \overline{W}_G \left\{ C(K) \left| Jo(K) - jJ_1(K) \right| + jJ_1(K) \right\} e^{j\omega t} \qquad (31)$$
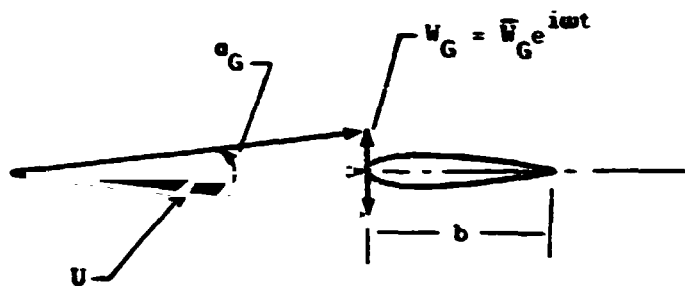
Figure 5. Thin Airfoil Under Sinusoidal Vertical Gust, Initial Angle of Attack is Zero.

where the Theodorsen function, C(K), is defined by

$$C(K) = F(K) + jG(K)$$

$$= \frac{H_1^{(2)}(K)}{H_1^{(2)}(K) + j H_0^{(2)}(K)} \qquad (32)$$

18

$H_n^{(2)}$ (n = 0, 1) in the right-hand side cf Equation 32 is the Hankel function of the second kind which is a combination of Bessel functions of the first and second kinds:

$$H_n^{(2)}(K) = J_n(K) + jY_n(K) \tag{33}$$

The complex argument, K, is given as

$$K = \frac{\omega b}{2U} - j\frac{\mu b}{2U} \tag{34}$$

For constant amplitude oscillations, however, μ is zero and K is expressed simply as

$$K = \frac{\omega b}{2U} \tag{35}$$

Substitution of the Theodorsen function into Equation 31 and rearrangement gives

$$F_{L, \ dyn} = \pi\rho U b\overline{W}_G (A + jB) \, e^{j\omega t} \tag{36}$$

where

$$A = F(K)J_0(K) + G(K)J_1(K) \tag{37}$$

$$B = J_1(K) + G(K)J_0(K) - F(K)J_1(K) \tag{38}$$

This expression for the unsteady lift force can be rewritten with the aid of a trigometric relation as

$$F_{L, \ DYN} = \pi\rho U b\overline{W}_G \sqrt{A^2 + B^2} \, e^{j\omega t} \, e^{j\theta}, \quad \theta = \tan^{-1}(B/A) \tag{39}$$

Examination of Figure 5 reveals that if $\overline{W}_G \ll U$, the time-dependent angle of attack, α_G, can be expressed as

$$\alpha_G = \frac{\overline{W}_G}{U} \, e^{j\omega t} \tag{40}$$

Substitution of this angular relationship into Equation 39 yields

$$F_{L, \text{dyn}} = (\pi \rho U^2 b \alpha_G) \sqrt{A^2 + B^2} \; e^{j\theta} \tag{41}$$

Note that the bracketed term in the right-hand side of the above expression is equivalent to the steady-state lift force except that the angle of attack, α_G, varies sinusoidally with time. The term, $A^2 + B^2$ accounts for the change in the amplitude of the lift force due to the transient effect. The phase difference between the gust velocity fluctuation and the lift force oscillation is represented by the unit vector, $e^{j\theta}$.

A similar derivation can be applied to the case where a steady-state lift force exists prior to the introduction of gust loading. The steady-state lift force is induced by giving the airfoil an initial angle of attack, α_{ss}, Figure 6.
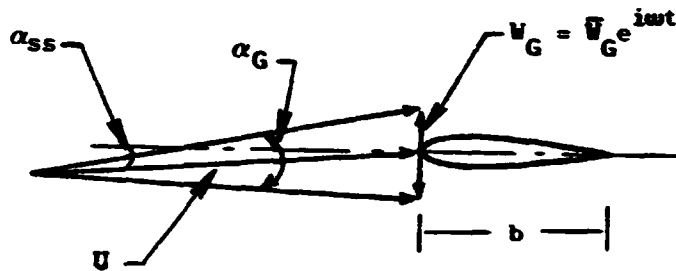
Figure 6.   Thin Airfoil Under Sinusoidal Vertical
Gust, Initial Angle of Attack is α_{ss}.

Under the flow conditions illustrated in the above sketch, the total lift force can be obtained by superposing the unsteady lift force due to a gust on the steady-state lift force, Reference 6, i.e.

$$F_L = F_{L, ss} + F_{L, \text{dyn}} \tag{42}$$

where

$$F_{L, ss} = \pi \rho U^2 b \alpha_{ss} \tag{43}$$

It is assumed that α_{ss} is small. Since α_G is also assumed to be small, the dynamic lift force represented by Equation 41 is equally valid for this case. Thus, the total lift force, F_L, becomes

$$F_L = \pi\rho U^2 b \alpha_{ss} \left[1 + \frac{\alpha_G}{\alpha_{ss}} \sqrt{A^2 + B^2} \, e^{j\theta} \right] \qquad (44)$$

Now, this expression is applied to a compressor blade by introducing two correction factors, K_1 and K_2, and replacing α_G by the incidence angle fluctuation, $I = \overline{\Delta i} \, e^{j\omega t}$. That is

$$F_L = \pi\rho U^2 b K_2 \alpha_{ss} \left[1 + \frac{I}{K_2 \alpha_{ss}} \sqrt{A^2 + B^2} \, e^{j\theta} \right] \qquad (45)$$

where $\quad \theta = \tan^{-1} \left(\dfrac{K_1 B}{A} \right)$

As stated previously, K_1 and K_2 provide corrections for the cascade effect, profile shape and camber, profile drag and compressibility.

The steady-state lift forces

$$F_{L, ss} = \pi\rho U^2 b K_2 \alpha_{ss} \qquad (46)$$

for the compressor blades are computed in the AEROSTAP program with the proper K_2 for each blade. The steady-state-lift force for each blade at a given corrected speed was computed and represented as a polynomial function of tan i where i is the incidence angle. In order to utilize these polynomials, Equation 45 is rearranged as

$$F_L = F_{L, ss} \left[1 + \frac{\pi\rho U^2 b}{F_{L, ss}} \sqrt{A^2 + B^2} \, \overline{\Delta i} e^{j(\omega t + \theta)} \right] \qquad 47)$$

This expression can be rewritten by substituting the relationship

$$e^{j\phi} = \cos\phi + j \sin\phi \qquad \text{where } \phi = \omega t + \theta \qquad (48)$$

as

$$F_L = F_{L, ss} \left| 1 + \frac{\pi\rho U^2 b}{F_{L, ss}} \sqrt{A^2 + B^2} \, \overline{\Delta i} [\cos(\omega t + \theta) + j \sin(\omega t + \theta)] \right| (49)$$

Equation 49 represents the final expression for the unsteady-blade-lift force. Note that the dynamic portion of the lift force is composed of real and imaginary parts. Use of the real or imaginary part in the actual computation depends upon the oscillatory mode of $I = \overline{\Delta i} e^{j\omega t}$. If the incidence angle fluctuates as a sine wave, the imaginary term is used without j; while real part is utilized if I changes as a cosine wave.

Evaluation of A and B in Equation 49 with a digital computer is difficult since Hankel and Bessel functions are not readily available as a library functions. Consequently, the functions, F(K) and G(K), Figures 7 and 8, as well as the first and second order Bessel functions of the first kind are curve-fitted by polynomials and included in AEROSTAP as a subroutine. The amplitude of the incidence angle fluctuation, $\overline{\Delta i}$, is computed from that of the mass flow oscillation produced by the P^3G.

Finally, it should be noted that the correction factor, K_1 was evaluated by comparing the simulation results with the test data of the F101 Fan/P^3G installation. As will be shown later, K_1 was found to be very close to unity.

3.4 FREQUENCY RESPONSE ANALYSIS TECHNIQUE

The frequency analysis technique employed in the Digital Surge Prediction (DSP) program is essentially a Laplace transfer analysis of a set of linear equations.

$$\frac{dx_i}{dt} = A_{ij} x_i + B_{in} U_n \tag{50}$$

$$R_m = C_{mi} x_i \tag{51}$$

where $i = 1, 2, 3, ----- , 3K$

$j = 1, 2, 3, ----- , 3K$

$n = 1, 2, 3, ----- , L$

$m = 1, 2, 3, ----- , P$

K: Number of model volumes

L: Number of forcing function variables

P: Number of output variables

22
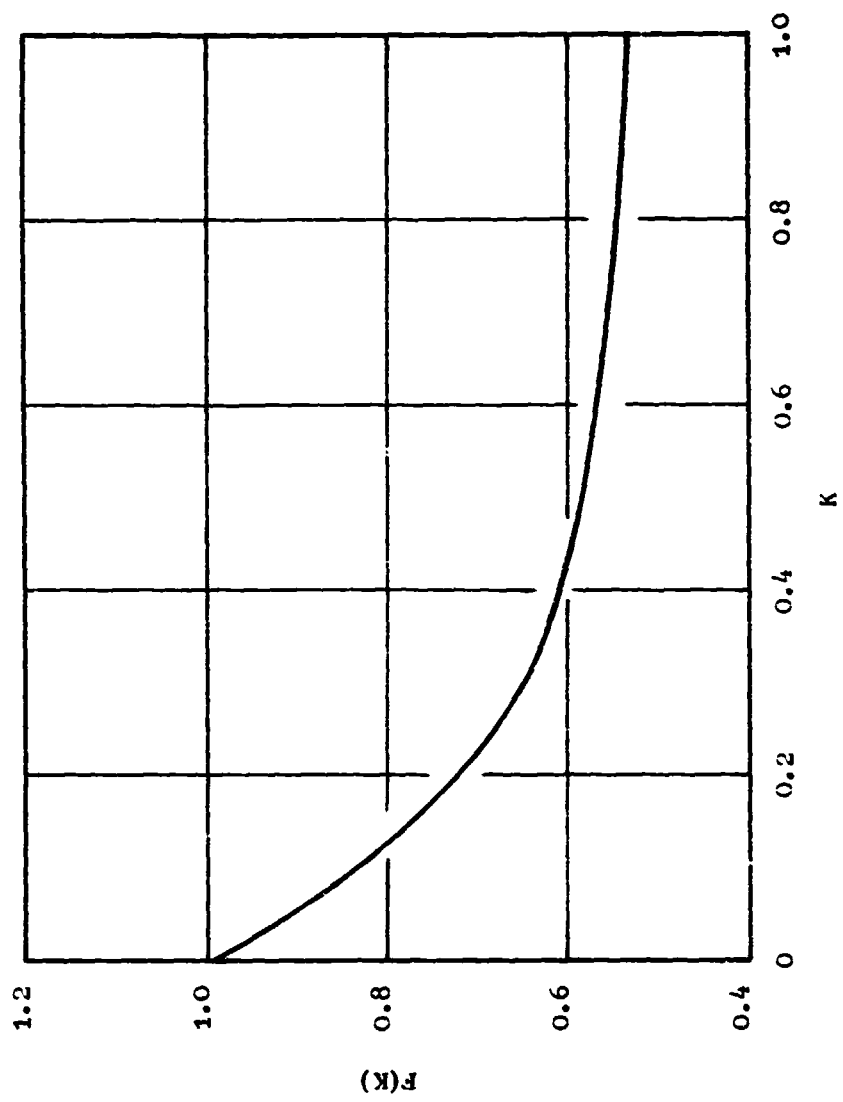
Figure 7.   Complex Function F.

23
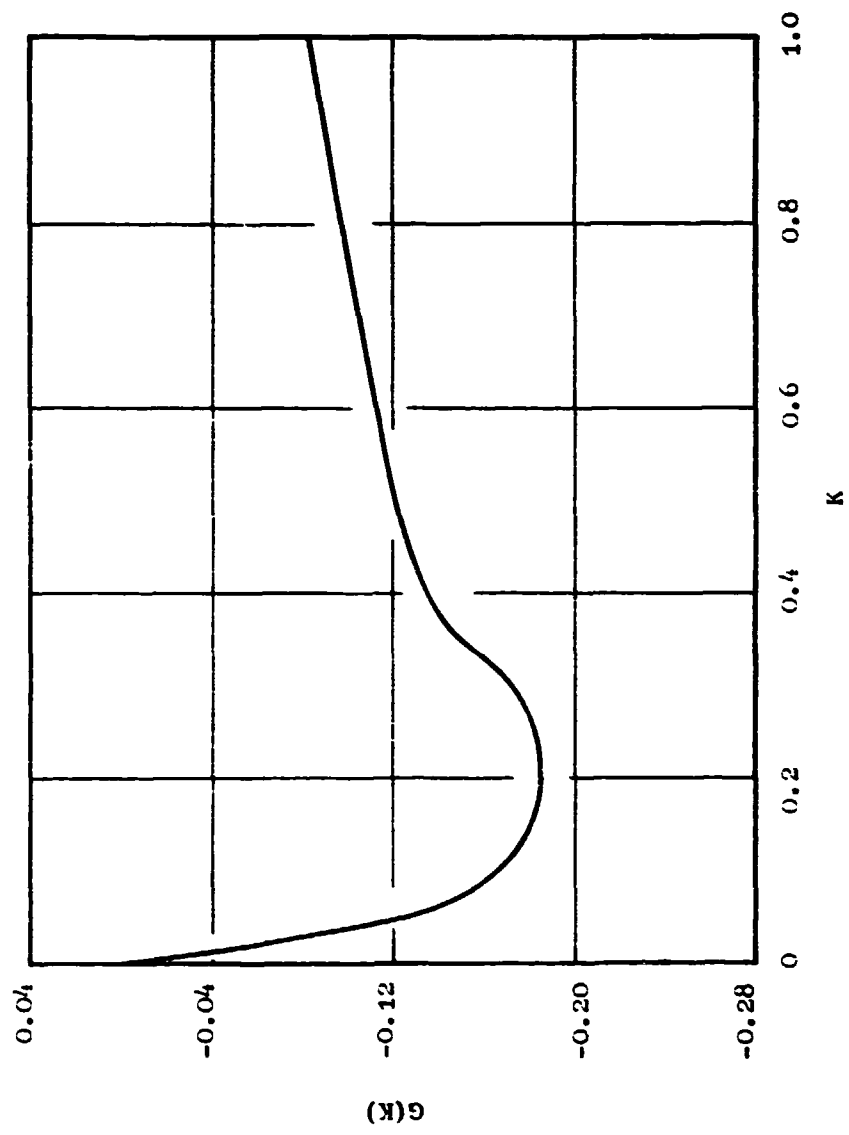
Figure 8. Complex Function G.

24

Equation 50 describes the sensitivity of the perturbations, x_i, of the independent variables about an equilibrium solution to the forcing function, $B_{in} U_n$. This equation is obtained by linearizing the three conservation equations written in vector form as

$$\frac{dy_i}{dt} = f(y_i) \tag{52}$$

and adding the forcing function, $B_{in} U_n$. Note that the conservation equations are applied to all the volumes and the volume-averaged density, mass flow rate and entropy for all the volumes are taken as independent variables. Therefore, there are 3K equations for 3K independent variables. Linearization of Equation 52 about an equilibrium solution, y_{ei}, yields

$$\frac{dy_i}{dt} = \sum \frac{\partial f_i}{\partial y_j} (y_i - Y_{ei}) \tag{53}$$

Introduction of a matrix

$$A_{ij} = \frac{\partial f_i}{\partial y_k} \tag{54}$$

and the definition of the perturbation about y_{ei}

$$x_i = y_i - y_{ei} \tag{55}$$

into Equation 53 gives

$$\frac{dx_i}{dt} = A_{ij} x_i \tag{56}$$

Now, addition of the forcing function, $B_{in} U_n$, to this relationship yields Equation 50. The forcing function is formulated from the inlet and exit boundary conditions or any other conditions imposed within the model.

Equation 51 represents the output response in terms of a linear combination of the perturbations. The vector, R_m is the output variables such as the pressures, mass flow rates, etc. at various locations in the model. The matrix, C_{mi} expresses the linear relationship between the output variables and the perturbation variables.

The Laplace transform equivalents of the system represented by Equations 50 and 51 are

$$sx_i(s) = A_{ij} x_i(s) + B_{in} U_n(s) \tag{57}$$

$$R_m(s) = C_{mi} x_i(s) \tag{58}$$

where s is the Laplace variable. These two equations can be combined and rearranged in transfer function form as

$$\frac{R_m(s)}{U_n(s)} = C_{mi} (sI_{ij} - A_{ij})^{-1} B_{in} \tag{59}$$

where I_{ij} is the unity matrix.

Equation 59 forms the basis for the frequency response analysis. Evaluation of this relationship with a digital computer is, however, not desirable since it involves the inversion of a matrix that contains a free parameter. Therefore, each element of the transfer function is evaluated separately in the DSP program. That is, the transfer function between the K-th element of R_m and 1-th element of U_n

$$\frac{L\{R_k\}}{L\{U_l\}} = \frac{\det (W_{ij})}{\det (sI_{ij} - A_{ij})} \tag{60}$$

for the desired combination of m and n are computed individually. The matrix, W_{ij} is a Wronskian Matrix whose derivation is explained in detail in Reference 4.

The determinants in the transfer function represented by Equation 60 are each polynomials in s. Therefore, the frequency response is numerically evaluated by substitution $s = j\omega$ into these polynomials where ω is a given frequency and j is the imaginary number, $\sqrt{-1}$.

3.5 EXPLICIT ANALYTICAL SURGE CRITERIA

One of the important parameters in the design and operation of gas turbine engines is surge margin. If a gas turbine engine is operated in the compressor stall region, not only is the engine performance adversely affected, but also the engine life deteriorates due to high mechanical stresses and high temperatures. Thus, the normal operating line is selected

26

below the surge line with proper allowances for the external as well as the internal destabilizing effects such as inlet distortion, power transients, thermal acceleration transient, manufacturing tolerances, etc. However, lowering of the operating point from the surge limit usually results in decreasing the pressure ratio and efficiency of the engine. Therefore, the necessity of determining the exact stall line and subsequently, the proper surge margin that assures efficient and successful steady or transient engine operation is evident.

Stall lines for compressors have been determined usually through engine tests. However, this process is costly and time consuming. Consequently, there is a need to obtain stall lines analytically. In recognition of this need, the General Electric Company has developed two independent techniques for estimating compressor stability limits. These two analytical methods are discussed briefly below.

The first method utilizes the time-dependent solution of the General Electric developed Aerodynamic Stability Analysis Program (AEROSTAP, see Subsection 3.2). This method determines the stability limits by examining two time-dependent parameters (Reference 3), i.e., 1) The amplification factor, $(d\overline{W}/dt)_{rotor}/(d\overline{W}/dt)_{exit}$ and 2) The mass flow ratio, $(W_2/W_1)_{rotor}$.

The first parameter represents the ratio between the time-rate change of mass flow rate of a rotor and that of the exit volume of the model. It was observed that the amplification factor becomes greater than two in all the rotor volumes at the experimentally determined stability limit. The second parameter is the ratio of the exit mass flow rate to the inlet mass flow rate of a rotor volume. At the experimental surge limits, this ratio for one or more rotors deviates from unity by more than 0.00004. This means that a compressor system becomes unstable if more than 0.004% of the inlet flow is stored or depleted from any of the rotor volumes.

These two stability criteria based on the time-dependent solution of the AEROSTAP simultaneously indicate instability at the experimental surge limits. Therefore, they are used in support of each other.

The second method of predicting stall line utilizes the steady-state solution or a quasi-steady-state equilibrium solution of the AEROSTAP. This technique is based on the Poincaré - Lyapunov theory of stability. This theory states that an equilibrium solution of any nonlinear system of the form.

$$\frac{dy_i}{dt} = f_i (y_1, y_2, \ldots\ldots, y_n) \qquad (i = 1, 2, \ldots\ldots, n) \qquad (61)$$

27

is asymptotically stable whenever the linearized system

$$\frac{dy_i}{dt} = \frac{\partial f_i}{\partial y_k} (y_k - y_{lk}) \qquad (i = 1, 2, \ldots, n) \qquad (62)$$

is completely stable. The partial derivatives in Equation 62 are evaluated with the equilibrium solution, y_{lk}, (K = 1, 2, ..., n). The linear system represented by Equation 61 is completely stable if and only if all the roots, λ, of the characteristic equation

$$\det \left[\frac{\partial f_i}{\partial y_k} - \lambda \delta_{ik} \right] = 0 \qquad (63)$$

where $\delta_{ik} = 1$ if $i = K$

ik = 0 if $i \neq K$

have negative real parts.

Based on this principle, the three conservation equations express in volume-averaged form (see Subsection 3.2) are linearized to obtain the square matrix, $\partial f_i / \partial y_k$, (i, K = 1, 2, ..., n), where n is equal to 3 x number of volumes. Then the eigenvalues of this matrix are examined by the Routh-Hurwitz criterion to determine the stability of the solution of the conservation equations. One or more of the eigenvalues will have a positive real part at the stability limit.

The two methods described thus far have been utilized successfully in computing the stability limits of various General Electric manufactured gas turbine engines (References 3, 4, and 7). The results show an excellent agreement between the computed stability limits and the experimentally determined surge lines.

At the present time, these two methods provide adequate estimates of the surge limits. However, these techniques are tedious and costly; the first method requires a slow quasi-steady-state throttling along a speed line and the latter technique requires evaluation of a large size matrix and its characteristic equation. Therefore, there is a need to develop a new technique that is simple and less expensive. Further, it is desirable to possess a technique that can readily show the relationships between the occurrence of the instability and the aerodynamic and geometric characteristics of a compressor. In recognition of these needs, explicit analytical stability criteria for the evaluation of the surge limits were derived.

28

This new technique, described hereinafter, is also derived from the Poincaré - Lyapunov theory of stability. However, this method differs significantly from the previously described method in the fact that the stability is accessed for individual rotors; whereas the previous method evaluates the stability of a compressor as a whole. Further, for the ease of analysis, the flow through the compression system is assumed homentropic.

For the homentropic flow of a compressible fluid in a rotor volume, Figure 9, the governing equations can be written, in volume-averaged form, as

$$\frac{\partial \bar{\rho}}{\partial t} = f_1 (\rho_1, W_2) = \frac{1}{V} \left[W_1 - W_2 \right] \tag{64}$$

$$\frac{\partial \bar{W}}{\partial t} = f_2 (\rho_1, W_2) = \frac{g_c}{L} \left[\frac{W_1^2}{g_c \rho_1 A_1} - \frac{W_2^2}{g_c \rho_2 A_2} + P_1 A_1 - P_2 A_2 \right.$$

$$\left. - P_M (A_1 - A_2) + F_B \right] \tag{65}$$

where $P_M = \frac{1}{3} P_1 + \frac{2}{3} P_2$ \tag{66}

The boundary conditions are

$$P_{t1}, \ T_{t1} = const. \ (at \ inlet) \tag{67}$$

$$\frac{W_2 \sqrt{T}_2}{P_2} = const. \ (at \ exit) \tag{68}$$

These boundary conditions are based on the assumption that any small perturbations in the rotor volume under consideration cannot propagate into the adjacent rotor volumes due to an abrupt change in acoustic impedence between rotors. This assumption is quite valid at high speeds; however, its validity is weakened as the operating speed is lowered.

Page 30 Missing from Original Document

$$\frac{\partial f_2}{\partial W_2} = \frac{g_c}{L}\left[\ -\frac{2\gamma}{\gamma+1}\ \frac{W_2}{c A_2 \rho_2} - \frac{2\gamma}{\gamma+1}\ A_e \frac{P_2}{W_2} + \frac{\partial F_B}{\partial W_2}\right] \tag{73}$$

Derivation of the partial derivatives, Equations 70 through 73, $\partial F_B/\partial \rho_1$ and $\partial F_B/\partial W_2$, is given in Appendix A.

According to the Poincaré - Lyapunov stability theory, the solution for the simultaneous differential equations, Equations 64 and 65, are stable if all the eigenvalues of the matrix, Equation 69, have negative real parts. The characteristic equation of this matrix is

$$\lambda^2 + \left(-\frac{\partial f_1}{\partial \rho_1} - \frac{\partial f_2}{\partial W_2}\right)\lambda + \left(\frac{\partial f_1}{\partial \rho_1}\ \frac{\partial f_2}{\partial W_2} - \frac{\partial f_1}{\partial W_2}\ \frac{\partial f_2}{\partial \rho_1}\right) = 0 \tag{74}$$

The Routh-Hurwitz criterion states that the roots, λ, of this equation have negative real parts if all the coefficients of this polynomial are positive. Therefore, the stability criteria are expressed as

$$\frac{\partial f_1}{\partial \rho_1} + \frac{\partial f_2}{\partial W_2}\ < \ 0 \tag{75}$$

$$\frac{\partial f_1}{\partial \rho_1}\ \frac{\partial f_2}{\partial W_2}\ > \ \frac{\partial f_1}{\partial W_2}\ \frac{\partial f_2}{\partial \rho_1} \tag{76}$$

These two inequalities are the final expressions for the stability criteria and can be evaluated with the substitution of partial derivatives given in Appendix A. Application of these criteria to a stability evaluation of the J85-13 "Mehalic" and "Moss" engines and the results are discussed in Subsection 4.3. A critique of the method is also presented.

4.0 PRESENTATION OF RESULTS

This section presents the results of the analysis performed using the analytical techniques outlined in the previous section. First, the results of the J85-13/P^{3}G simulations are discussed in Subsection 4.1. This subsection includes a description of the digital model of the J85-13/P^{3}G test apparatus, validation of the simulation program, time-dependent analysis of the test installation and an estimate of the stability limit of the J85 compressor with inlet planar wave distortion. Second, the frequency analysis of the test apparatus is described in Subsection 4.2. Items discussed in this subsection are the amplitude transmission and the nodal analysis of the system model. Finally, the results obtained by applying the explicit analytical stability criteria to two different configurations of the J85 compressor are presented in Subsection 4.3 along with a critique of the criteria.

4.1 J85-13/P^{3}G SIMULATION

The model geometry, the procedure for operating the model, and verification of the model capabilities are discussed in the following paragraphs as are the results of time-dependent simulation of the J85-13/P^{3}G operation and surge line estimations.

4.1.1 Geometry and Operating Procedures of the J85-13/P^{3}G Model

The geometry of the J85-13/P^{3}G test installation simulated by the digital model was shown previously in Figure 1. The entire setup from the bellmouth entrance to the combustor exit is modelled by 79 volumes. Table 1 defines the individual characteristics of these 79 volumes. The area distribution of the test apparatus as used in this simulation is shown in Figures 10 and 11. Note that the volume representing the plenum (Volume 1) and the first five volumes of the bellmouth (Volumes 2 through 6) were replaced by smaller constant area volumes, denoted by the dotted line in Figure 10. This was necessary since the large areas as well as the large area gradients in this region caused numerical instability in the AEROSTAP program.

The physical characteristics of the compressor geometry, i.e., metal angles, pitch-line radii, areas and solidities, are defined in Table 1 for each blade row.

The locations of the instrumentation are shown in Table 1. Instrumentation locations that will be used during the J85-13/P^{3}G test are duplicated in the model to provide a direct comparison between the model results and the future test data. The parameters chosen for this comparison are defined in Table 2.

32

Table 1. System Geometry

Volume Description	Station Number	Instrumentation	Physical	Area (In.^{2}) Blockage	Effecti
Plenum	1		16286.00	1.0	16286.
Bellmouth Lip	2		2827.43	1.0	2827.
	3		2135.50	1.0	2135..
	4		1851.42	1.0	1851.
	5		1659.74	1.0	1659.
	6		1397.08	1.0	1397.
Bellmouth	7		1219.22	1.0	1219.
	8		1090.73	1.0	1090.
	9		995.72	1.0	995.
	10		925.52	1.0	925.
	11		874.90	1.0	874.
	12	PTBME, PSBME	840.64	1.0	840.
	13		820.82	1.0	820.
Bellmouth Exit, Plane 0.0	14		814.33	1.0	814.
	15		814.33	1.0	814.
	16	PSFPI	814.33	1.0	814
	17		814.33	1.0	814

Physical	Area (In.^{2}) Blockage	Effective	RR (In.)	Volume Number	β_1^* (Deg.)	β_2^* (Deg.)	Length (In.)	Solidity
16286.00	1.0	16286.00	--	1	--	--	4.3	--
2827.43	1.0	2827.43	--	2	--	--	1.7	--
2135.50	1.0	2135.50	--	3	--	--	2.0	--
1851.42	1.0	1851.42	--	4	--	--	2.0	--
1659.74	1.0	1659.74	--	5	--	--	4.0	--
1397.08	1.0	1397.08	--	6	--	--	4.0	--
1219.22	1.0	1219.22	--	7	--	--	4.0	--
1090.73	1.0	1090.73	--	8	--	--	4.0	--
995.72	1.0	995.72	--	9	--	--	4.0	--
925.52	1.0	925.52	--	10	--	--	4.0	--
874.90	1.0	874.90	--	11	--	--	4.0	--
840.64	1.0	840.64	--	12	--	--	4.0	--
820.82	1.0	820.82	--	13	--	--	4.0	--
814.33	1.0	814.33	--	14	--	--	4.24	--
814.33	1.0	814.33	--	15	--	--	4.0	--
814.33	1.0	814.33	--	16	--	--	4.0	--
814.33	1.0	814.33	--	17	--	--	2.56	--

33

FOLDOUT FRAME

Volume Description	Station Number	Instrumentation	Physical	Area (In.^{2}) Blockage	Effectiv
	18		839.82	1.0	839.8
	19		897.27	1.0	897.2
		PSFP2			
Duct Ahead of P^{3}G	20		951.15	1.0	951.1
	21		1006.60	1.0	1006.6
	22		1063.62	1.0	1063.6
	23		1086.86	1.0	1086.8
		PSFP3			
	24		1052.65	1.0	1052.6
	25		1001.92	1.0	1001.
	26		991.83	1.0	991.
	27		991.83	1.0	991.
		PSFP4			
	28		991.83	1.0	991.
	29		966.27	1.0	966.2
		PSFP5			
	30		856.11	1.0	856.
Duct Ahead of P^{3}G	31		689.23	1.0	689.
	32		506.68	1.0	506.
	33		404.51	1.0	404.
	34		315.09	1.0	315.
	35		263.15	1.0	263.

Physical	Area (In.^{2}) Blockage	Effective	RR (In.)	Volume Number	β_1^* (Deg.)	β_2^* (Deg.)	Length (In.)	Solidity
839.82	1.0	839.82	--		--	--		--
				18			4.0	
897.27	1.0	897.27	--		--	--		--
				19			4.0	
951.15	1.0	951.15	--		--	--		--
				20			4.0	
1006.60	1.0	1006.60	--		--	--		--
				21			4.0	
1063.62	1.0	1063.62	--		--	--		--
				22			2.55	
1086.86	1.0	1086.86	--		--	--		--
				23			4.0	
1052.65	1.0	1052.65	--		--	--		--
				24			4.0	
1001.92	1.0	1001.92	--		--	--		--
				25			4.0	
991.83	1.0	991.83	--		--	--		--
				26			4.0	
991.83	1.0	991.83	--		--	--		--
				27			4.0	
991.83	1.0	991.83	--		--	--		--
				28			4.4	
966.27	1.0	966.27	--		--	--		--
				29			2.0	
856.11	1.0	856.11	--		--	. --		--
				30			2.0	
689.23	1.0	689.23	--		--	--		--
				31			2.0	
506.68	1.0	506.68	--		--	--		--
				32			2.0	
404.51	1.0	404.51	--		--	--		--
				33			2.0	
315.09	1.0	315.09	--		--	--		--
				34			2.0	
263.15	1.0	263.15	--		--	--		--
				35			2.0	

Volume Description	Station Number	Instrumentation	Physical	Area (In.^{2}) Blockage	Effec
Duct Ahead of P^{3}G	36		229.30	1.0	22
	37		210.20	1.0	21
	38		209.51	1.0	20
	39		204.92	1.0	20
P^{3}G Rotor Inlet Plane	40		203.83	1.0	2
	41	PSFP6, PTFP6	198.67	1.0	1
P^{3}G Discharge Plane	42		192.54	1.0	1
	43	PSAPI, PTAPI	192.54	1.0	1
	44		192.54	1.0	1
	45		192.54	1.0	1
	46		192.54	1.0	1
Duct Ahead of J85 Compressor	47		192.54	1.0	1
	48		206.46	1.0	
	49		187.96	1.0	
Plane 2.0	50	PSAP2	187.96	1.0	
	51		187.96	1.0	
	52		187.96	1.0	
Engine Inlet IGV	53	PTIGV, WIIGV	187.11	1.0	

Physical	Area (In.^{2}) Blockage	Effective	RR (In.)	Volume Number	β_1^* (Deg.)	β_2^* (Deg.)	Length (In.)	Solidity
229.30	1.0	229.30	--		--	--		--
				36			2.0	
210.20	1.0	210.20	--		--	--		--
				37			2.0	
209.51	1.0	209.51	--		--	--		--
				38			2.0	
204.92	1.0	204.92	--		--	--		--
				39			2.0	
203.83	1.0	203.83	--		--	--		--
				40			2.0	
198.67	1.0	198.67	--		--	--		--
				41			2.75	
192.54	1.0	192.54	--		--	--		--
				42			1.0	
192.54	1.0	192.54	--		--	--		--
				43			2.0	
192.54	1.0	192.54	--		--	--		--
				44			2.0	
192.54	1.0	192.54	--		--	--		--
				45			2.0	
192.54	1.0	192.54	--		--	--		--
				46			2.0	
192.54	1.0	192.54	--		--	--		--
				47			2.0	
206.46	1.0	206.46	--		--	--		--
				48			2.0	
187.96	1.0	187.96	--		--	--		--
				49			1.0	
187.96	1.0	187.96	--		--	--		--
				50			1.0	
187.96	1.0	187.96	--		--	--		--
				51			2.0	
187.96	1.0	187.96	--		--	--		--
				52			2.25	
187.11	1.0	187.11	5.918		0.0	--		
				53			2.51	3.000
				37				

Volume Description	Station Number	Instrumentation	Area (In.^{2}) Physical	Blockage	Effe
	54		165.53	0.97	16
Free Volume					
	55		153.48	0.97	1
R1					
	56		136.38	0.97	13
S1					
	57		120.89	0.97	11
R2					
	58		108.48	0.97	1
S2					
	59		98.23	0.97	
R3					
	60		90.42	0.97	
S3					
	61		81.07	0.97	
R4					
	62		75.07	0.97	
S4					
	63		67.54	0.97	
R5					
	64		63.45	0.97	
S5					
	65		58.40	0.97	
R6					
	66		56.04	0.97	
S6					
	67		53.25	0.97	
R7					
	68		52.47	0.97	
S7					
	69		51.55	0.97	
R8					
	70		51.01	0.97	
S8					
	71		51.01	0.97	
OGV					

Physical	Area (In.²) Blockage	Effective	RR (In.)	Volume Number	β_1^* (Deg.)	β_2^* (Deg.)	Length (In.)	Solidity
165.53	0.97	160.56	6.195			0.0		
				54	--		0.92	--
153.48	0.97	148.88	6.272		48.39	37.5		
				55			1.186	1.143
136.38	0.97	132.29	6.400		34.84	5.4		
				56			1.041	1.057
120.89	0.97	117.26	6.504		50.20	30.20		
				57			0.789	1.204
108.48	0.97	105.23	6.600		40.58	12.10		
				58			0.848	1.208
98.23	0.97	95.28	6.712		51.05	26.49		
				59			0.599	1.326
90.42	0.97	87.71	6.792		45.68	14.80		
				60			0.740	1.350
81.07	0.97	78.64	6.896		50.81	26.69		
				61			0.517	1.384
75.07	0.97	72.82	6.960		46.40	19.40		
				62			0.655	1.390
67.54	0.97	65.51	7.032		55.95	28.35		
				63			0.430	1.432
63.45	0.97	61.55	7.080		46.03	23.20		
				64			0.617	1.436
58.40	0.97	56.65	7.128		54.80	34.10		
				65			0.363	1.306
56.04	0.97	54.36	7.152		44.90	22.20		
				66			0.584	1.311
53.25	0.97	51.65	7.184		55.11	40.37		
				67			0.333	1.318
52.47	0.97	50.90	7.192		43.79	21.10		
				68			0.597	1.322
51.55	0.97	50.01	7.200		52.94	44.82		
				69			0.303	1.326
51.01	0.97	49.48	7.208		42.10	9.58		
				70			0.466	1.209
51.01	0.97	49.48	7.205		9.58	0.00		
				71			0.417	1.209

FOLDOUT FRAME 2

Volume Description	Station Number	Instrumentation	Physical	Area (In.^{2}) Blockage	Effecti
Compressor Discharge	72	PSAC1	51.01	0.97	49.
	73		65.19	1.0	65.
Combustor Inlet	74		124.66	1.0	124.
	75		182.53	1.0	182.
	76		189.10	1.0	189.
Combustor Volume	77		189.10	1.0	189.
	78		184.83	1.0	184.
	79		94.87	1.0	94.
Turbine Nozzle Inlet	80		97.95	1.0	97.

FOLDOUT FRAME

Physical	Area (In.^{2}) Blockage	Effective	RR (In.)	Volume Number	β_1^* (Deg.)	β_2^* (Deg.)	Length (In.)	Solidity
51.01	0.97	49.48	7.205		--	--		
				72			1.0	--
65.19	1.0	65.19	--		--	--		
				73			2.0	--
124.66	1.0	124.66	--		--	--		
				74			2.0	--
182.53	1.0	182.53	--		--	--		
				75			2.0	--
189.10	1.0	189.10	--		--	--		
				76			2.0	--
189.10	1.0	189.10	--		--	--		
				77			2.0	--
184.83	1.0	184.83	--		--	--		
				78			1.5	--
94.87	1.0	94.87	--		--	--		
				79			1.0	--
97.95	1.0	97.95	--		--	--		

41
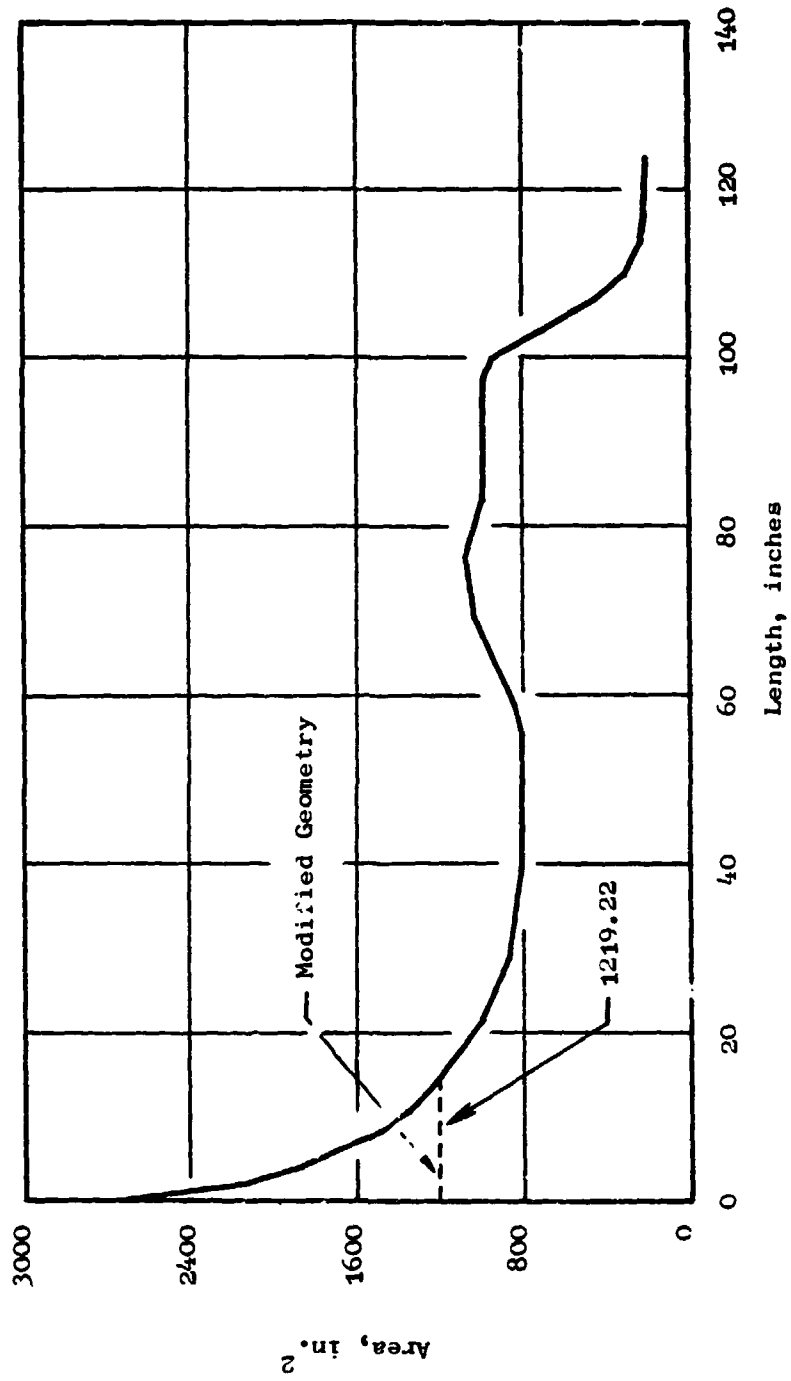
Figure 10. Area Distribution from Bellmouth to P^3G.
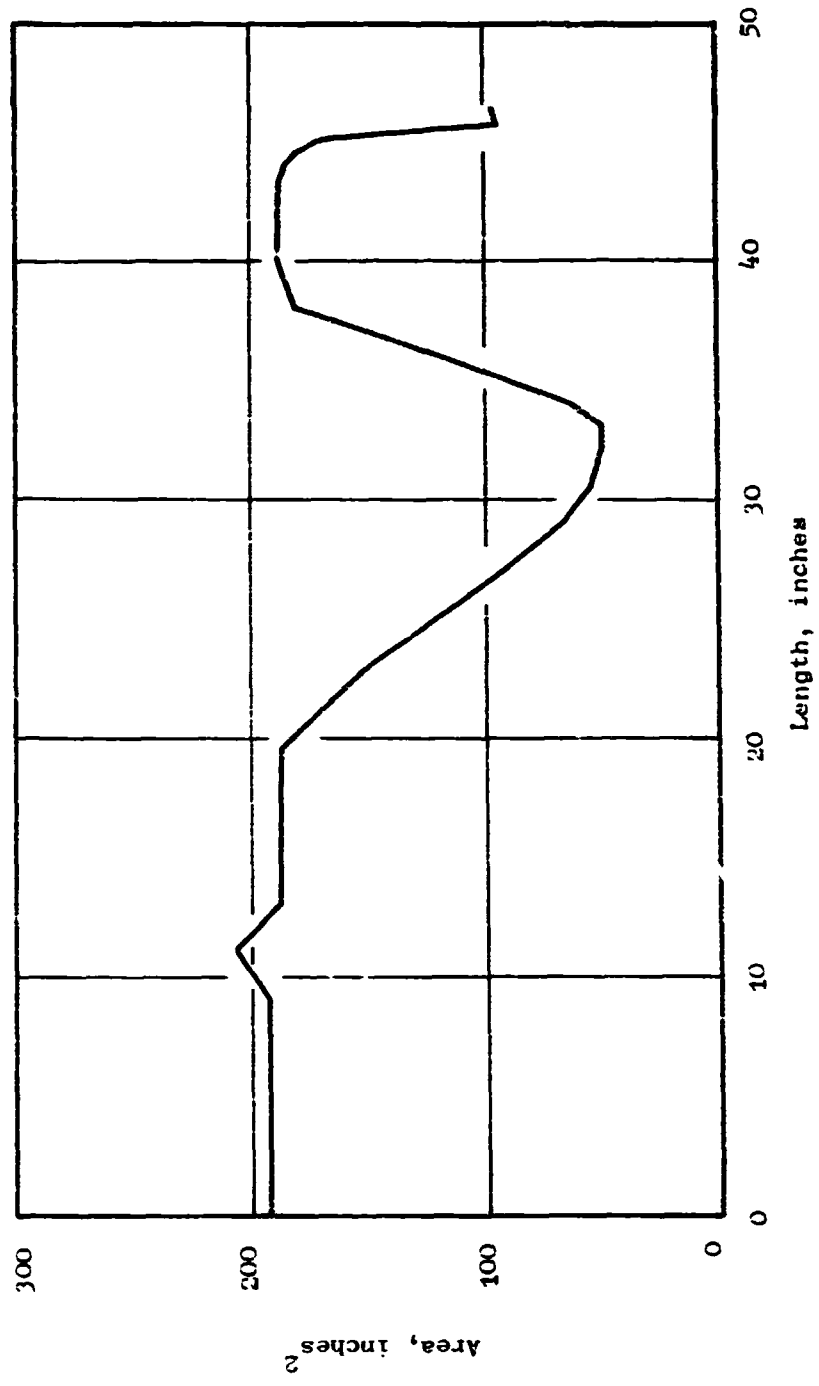
Figure 11. Area Distribution from P^3G to Combuster Exit.

Table 2. J85-13/P^{3}G Instrumentation Location

Name	Location	Reference Plane
PTBME	– 7.0"	Plane 0.0
PS3ME	– 7.0"	Plane 0.0
PSFP1	+12.1"	Plane 0.0
PSFP2	+21.6"	Plane 0.0
PSFP3	+35.5"	Plane 0.0
PSFP4	+51.7"	Plane 0.0
PSFP5	+59.5"	Plane 0.0
PSFP6	+82.8"	Plane 0.0
PTFP6	+82.8"	Plane 0.0
PSAP1	– 14.0"	Plane 2.0
PTAP1	– 14.0"	Plane 2.0
PSAP2	0.0"	Plane 2.0
PTIGV	+ 5.3"	Plane 2.0
WIIGV	+ 5.3"	Plane 2.0
PSAC1	+19.2"	Plane 2.0
PR-OA	Over-all Pressure Ratio	

a) First two characters PT, PS and WI stand for total pressure, static pressure and physical mass flow rate, respectively.

b) – and + denote upstream and downstream from the reference plane, respectively.

Table 3. F101 Fan/P^{3}G Instrumentation Location

Name	Description
P^{3}GPS	Static pressure at the P^{3}G strut
AXP53	Static pressure at the fan inlet
PTIGV	Total pressure at the inlet guide vane
PS14	Static pressure at the fan exit
FDPSC	Static pressure at the splitter

The performance characteristics of the eight stage compressor are represented in the form of blade row relative total-pressure loss coefficients, ω', and deviation angles, δ, as a function of incidence angle, tan i. In these representations, all losses are assigned to the rotor and it is assumed that only lossless turning of flow occurs in the stators. The loss coefficients and deviation angles of the J85 compressor are discussed in detail in Reference 3.

The blade characteristics, ω' and δ, represent blade-row performance up to the steady-state surge line. However, due to the large amplitude planar waves that are to be imposed on the compression system, the incidence angles encountered during model operation may instantaneously exceed the steady-state surge line. Therefore, an extrapolation technique is employed to extend the blade characteristics into the post steady-state surge regime. A detailed discussion of this extrapolation is also given in Reference 3.

The system model is subject to two boundary conditions; i.e., constant total-pressure and total-temperature condition at the bellmouth inlet and constant flow function at the combustor exit. In an actual engine test, the entire test setup or the bellmouth is placed in a large plenum. Usually, the total pressure and total temperature of the plenum are not affected by the operation of the engine. Therefore, in the digital model, a plenum volume is added in front of the bellmouth and the constant total-pressure and total-temperature condition is employed as the boundary condition. During the actual operation of a gas turbine engine, the turbine diaphragm is choked due to high pressure and high temperature of the combustor gas. This choked condition is simulated by assigning the constant flow function boundary condition to the combustor exit plane.

The method of simulating the dynamic events of the J85-13/P^{3}G with the model is very similar to the actual test procedure used for F101-Fan/P^{3}G test, Reference 7. The test procedure was as follows: First, the compression component was brought to steady-state operation at a low operating point on a chosen speed line. Then, the P^{3}G was actuated with the rotor-to-stator (RTS) spacing at its maximum. This was done to maintain the minimum amplitude of the planar wave while the P^{3}G accelerates to a desired rotational speed (frequency). After the P^{3}G had attained the desired frequency, the RTS spacing was decreased to increase the planar wave amplitude to a desired value. Similarily, the model enters the computation at the chosen operating point on a speed line and simulates the steady operation at this point for a period of time. This process is called "settling". Then, a frequency is assigned to the P^{3}G and the amplitude of the planar wave is increased gradually by increasing the amplitude of the choked area fluctuation (see Subsection 3.2). This process is called "ramping". After the ramping, the model can be run with the chosen frequency and amplitude of the planar wave in a stationary manner and subsequently, throttled to an instability point.

46

After the $J85\text{-}13/P^3G$ model geometry and the model operation scheme were established, the newly modified AEROSTAP was run with the F101 Fan/ P^3G geometry as well as with the $J85\text{-}13/P^3G$ geometry for the purpose of validating the computer program. These validation runs and the results are discussed in the following subsection.

4.1.2 Program Verification

Verification of the program capabilities was accomplished in a threefold manner: 1) Evaluation of one of the correction factors used in the expression for the unsteady-blade-lift force, 2) Verification of the validity of employing the lift force in describing the aerodynamic behavior of compressor blades, and 3) Assessment of the numerical stability of the AEROSTAP program when it is run with the $J85\text{-}13/P^3G$ geometry.

As shown in Subsection 3.3, the expression for the unsteady-blade-lift force contains two correction factors, K_1 and K_2. These factors correct the expression for the cascade effect, compressibility, profile shape and camber, profile drag, etc. The first correction factor, K_1, provides an adjustment to the phase angle of the dynamic portion of the lift force while K_2 provides corrections to the steady-state lift force as well as to the amplitude of the dynamic lift force.

As stated in Subsection 3.3, K_2 is accounted for when the steady-state lift force is computed within the AEROSTAP program. This is accomplished through the lift direction correction angle, β_c, Reference 3. The values of β_c are determined experimentally from compressor performance data. Therefore, only K_1 is evaluated in this study.

The phase difference between the oscillating incidence angle and blade lift force was defined in Subsection 3.3.

$$\theta = \tan^{-1}(K_1 \, A/B) \tag{77}$$

A and B in the above relationship are given in terms of the zeroth and first order Bessel functions of the first and second kinds and are plotted as a function of $K = \omega b/2U$ in Figures 12 and 13, respectively. The values of θ for $K_1 = 1$ are plotted in Figure 14 also as a function of K.

In order to determine the correction factor, K_1 experimentally, it is necessary to obtain the phase angle, θ, from test data. However, evaluation of θ is extremely difficult, if not impossible, at this point since there is no reliable means of deducing the lift force from the F101 Fan/P^3G test data; however, the incidence angle can be computed readily from the experimental

47
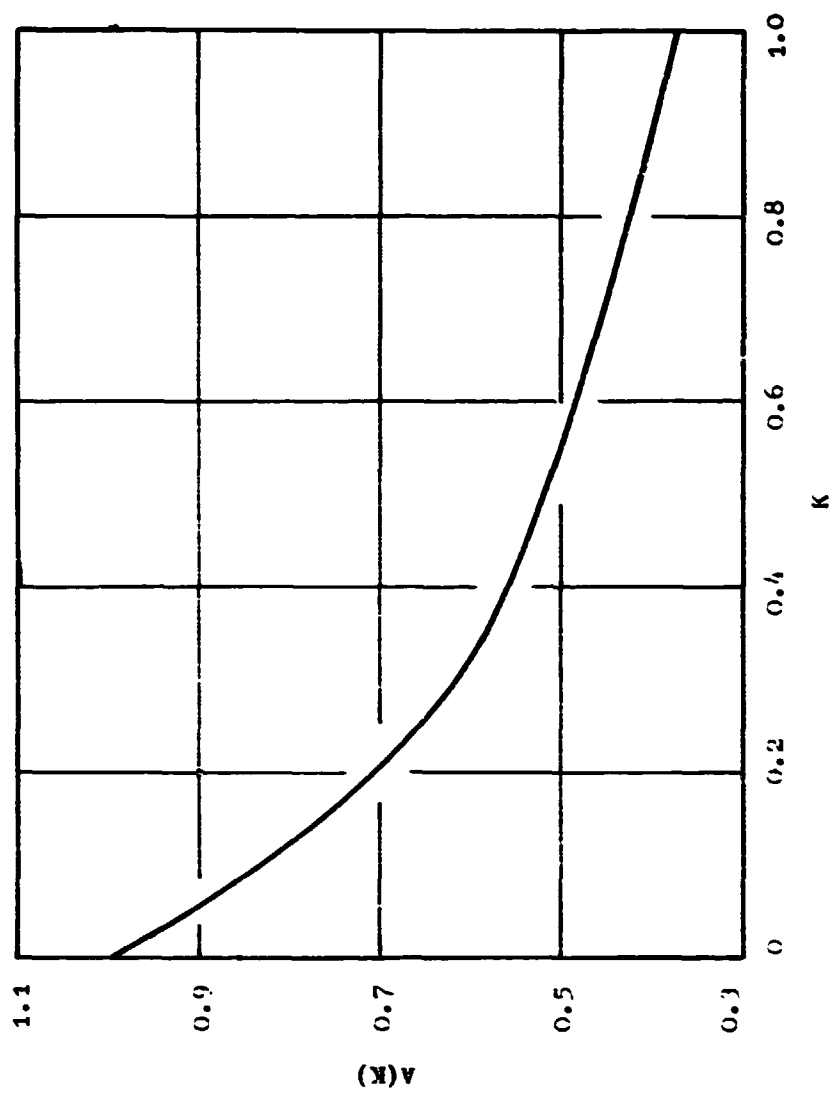
Figure 12. A as a Function of K.

48
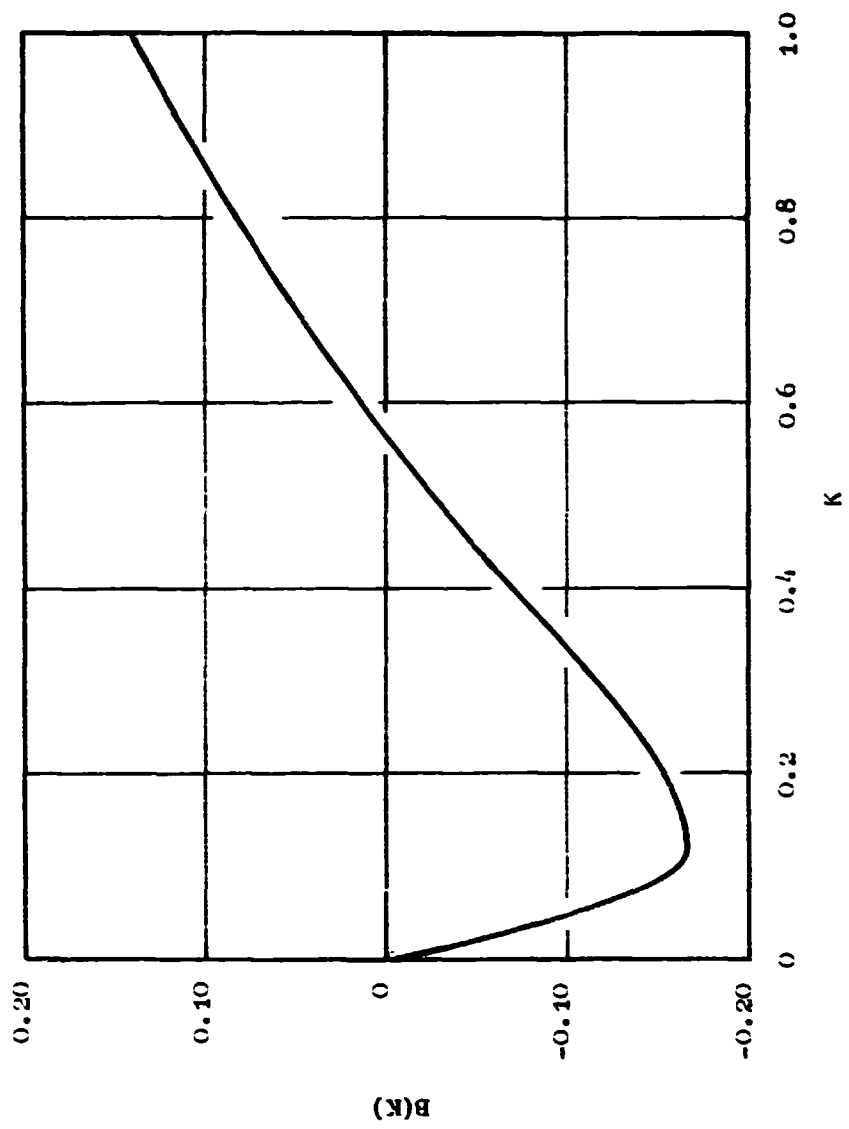
Figure 13. B as a Function of K.
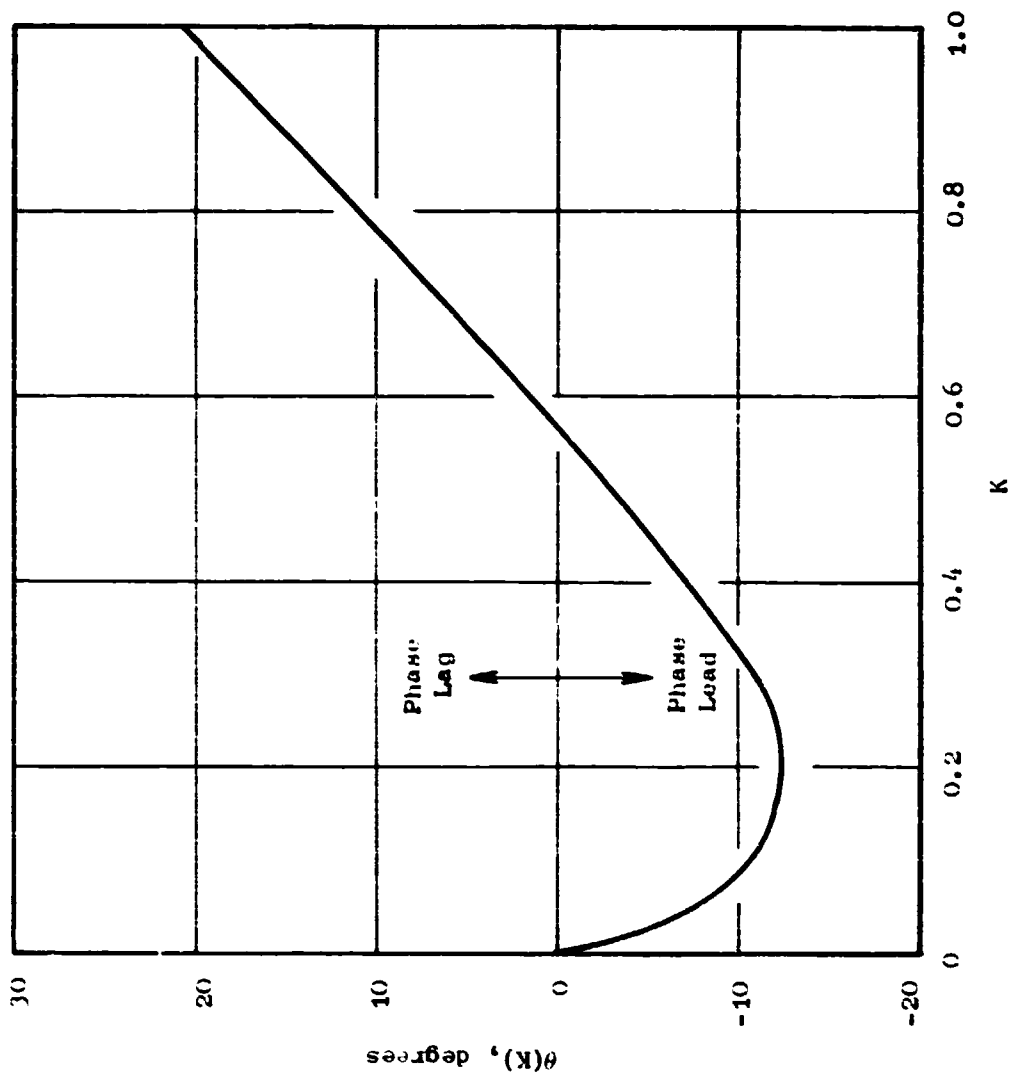
Figure 14. Phase Angle as a Function of K.

50

data. Therefore, evaluation of K_1 was attempted through a comparison of the pressure waveforms obtained during the F101 Fan/P^3G test with those simulated with K_1 as an independent variable. The experimental as well as the theoretical waveforms were obtained at five different locations in the F101 Fan/P^3G test installation (Figure 15). These locations are defined in Table 3.

Operation of the F101 Fan/P^3G with a P^3G frequency of 118 Hz and an IGV total-pressure oscillation of 15% peak-to-peak about the mean pressure were simulated for the K_1 values ranging from 0.5 to 1.5 in increments of 0.1. The average corrected mass flow rate and total-pressure ration across the fan were 151.8 Kg/sec (334.6 lb_m/sec) and 2.243, respectively. The pressure waveforms computed at the five different locations were compared with the corresponding experimental waveforms. The result indicated that the best agreement between the two sets of data was achieved when K_1 was between 0.9 and 1.1. These K_1 values yielded little differences in the simulation results.

A similar comparison was performed at a P^3G frequency of 350 Hz to determine the effect of frequency on K_1. Other operating conditions were similar to those for the 118 Hz case. The result of this comparison also showed that the best agreement between the test data and simulation results was obtained when K_1 is close to unity.

In addition, the relationship of K_1 to the amplitude of the IGV total-pressure variation was investigated. The amplitudes of the IGV total-pressure oscillation for both the 118 Hz and 350 Hz runs were increased to 22.8% and 25.6% peak-to-peak about the mean pressure, respectively. The result of this investigation indicated that K_1 is also independent of the amplitude of the inlet 'otal-pressure fluctuation.

Therefore, it was concluded that the correction factor, K_1 is a constant and is independent of the frequency and the amplitude of the planar inlet distortion. The constant value of K_1 was chosen to be unity since a small variation of K_1 about unity resulted in little difference in the simulation results.

After the correction factor, K_1 was chosen, operation of the F101 Fan/ P^3G was simulated at five different frequencies, i.e., 42, 80, 118, 220, and 350 Hz, for the purpose of verifying the validity of employing the lift force in describing the aerodynamic behavior of compressor blades. Previously, the AEROSTAP program computed the blade force acting on the fluid from the blade tangential force and the drag force. The newly modified AEROSTAP utilizes the blade lift force and the drag force in computing the blade force.
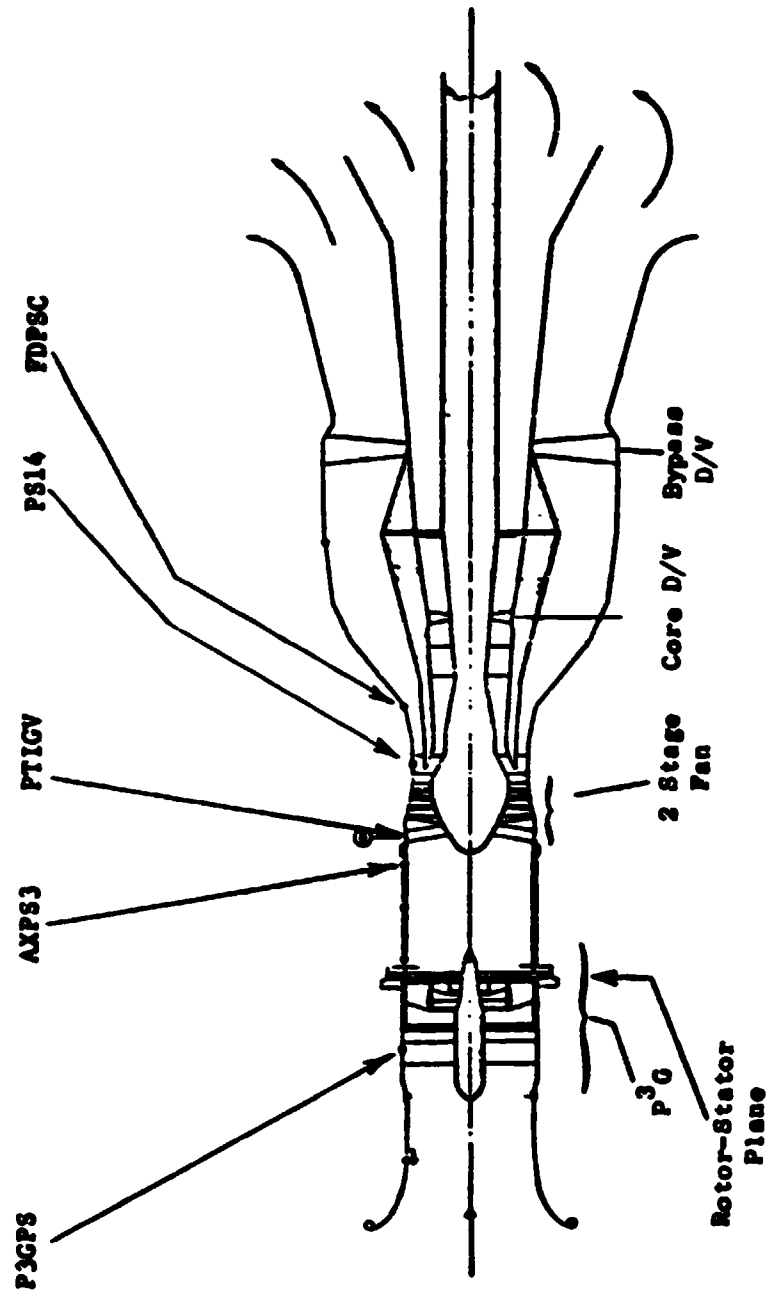
Figure 15. F101 Fan/P³G Installation Layout and Instrumentation Locations.

52

The validity of employing the new approach cannot be demonstrated easily through any theoretical deductions. Therefore, the validation was attempted through a comparative study of the experimental data with simulation results at the five frequencies previously listed.

In Figures 16 through 20, the results of the simulation are superposed on the experimental pressure waveforms at various locations in the test apparatus. The solid line represents the experimental data while the dotted line represents the simulation results. Examination of these figures indicates that the two sets of data are generally in a good agreement with each other within computational and experimental errors. Therefore, it was concluded that the use of the unsteady-blade-lift force in evaluating the blade force is a valid means of describing the aerodynamic behavior of a compressor blade.

The remaining discrepancy between the experimental and theoretical waveforms may be attributable to the following computational factors.

1) Model does not include the higher order harmonics of the P^3G that are present in the test data (amplitude and phase angle).

2) One-dimensional volume averaged model with a finite volume length (amplitude and phase angle).

3) Model does not provide any dissipatory mechanisms such as viscous dissipation and heat transfer for the pressure waves (amplitude).

Further, the polarity of the last two channels for 220 Hz run, Figure 19, might have been inverted during the recording or play back of the test data. The recording and play back were conducted with two different setups on different run days.

Some of the results of the F101 Fan/P^3G simulations are presented graphically in Appendix B.

Subsequent to the verification runs with the F101 Fan/P^3G geometry, the AEROSTAP program was run with the J85-13/P^3G geometry to assess the numerical stability of the program with the new geometry.

At the beginning of this study, the model encountered a numerical instability that originated from reverse flow in the bellmouth region. Initially, the axial velocity in the bellmouth inlet region is very small, and the static
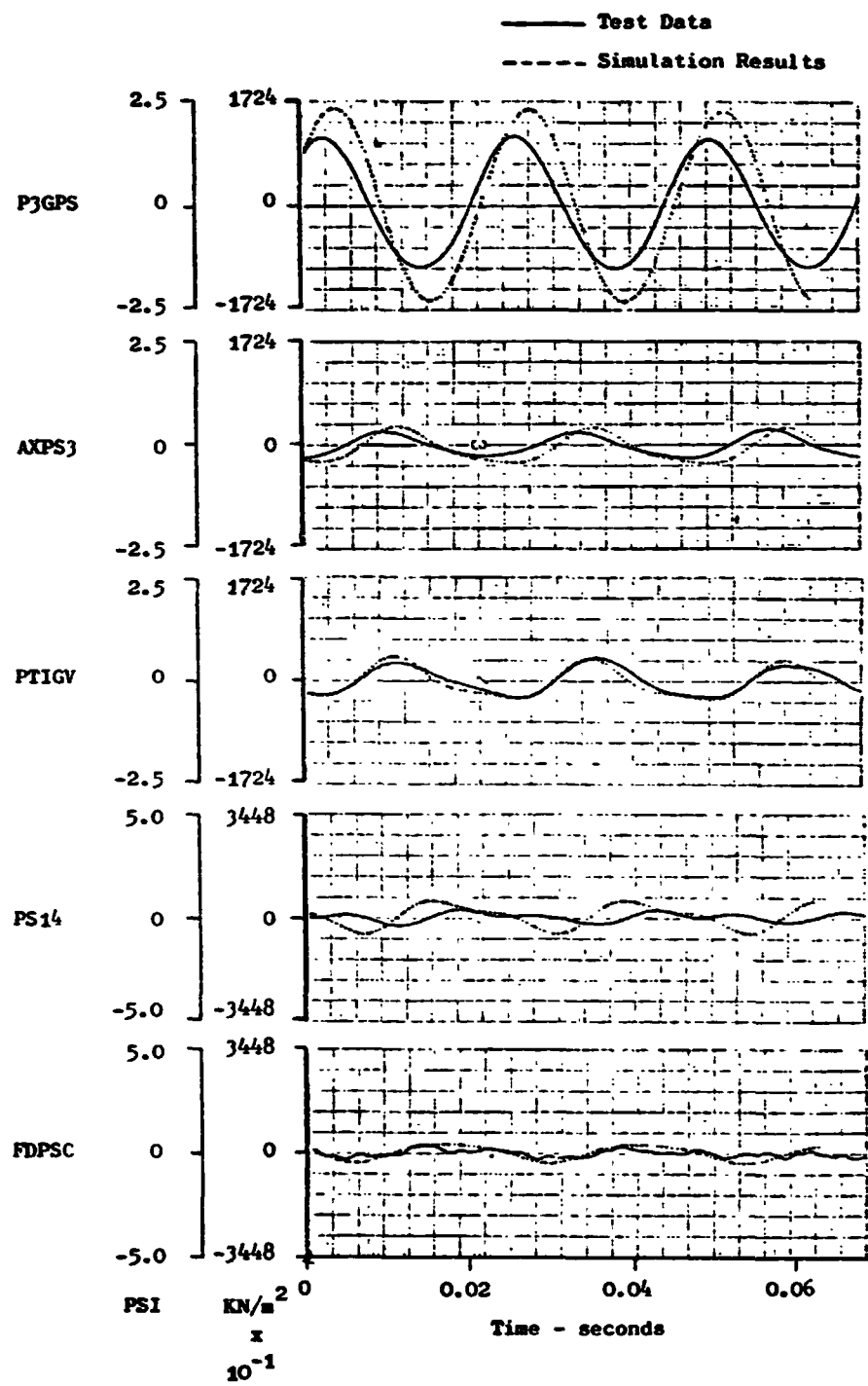
Figure 16. F101 Fan/P³G Simulation, 100% N/√θ, 42Hz.

54
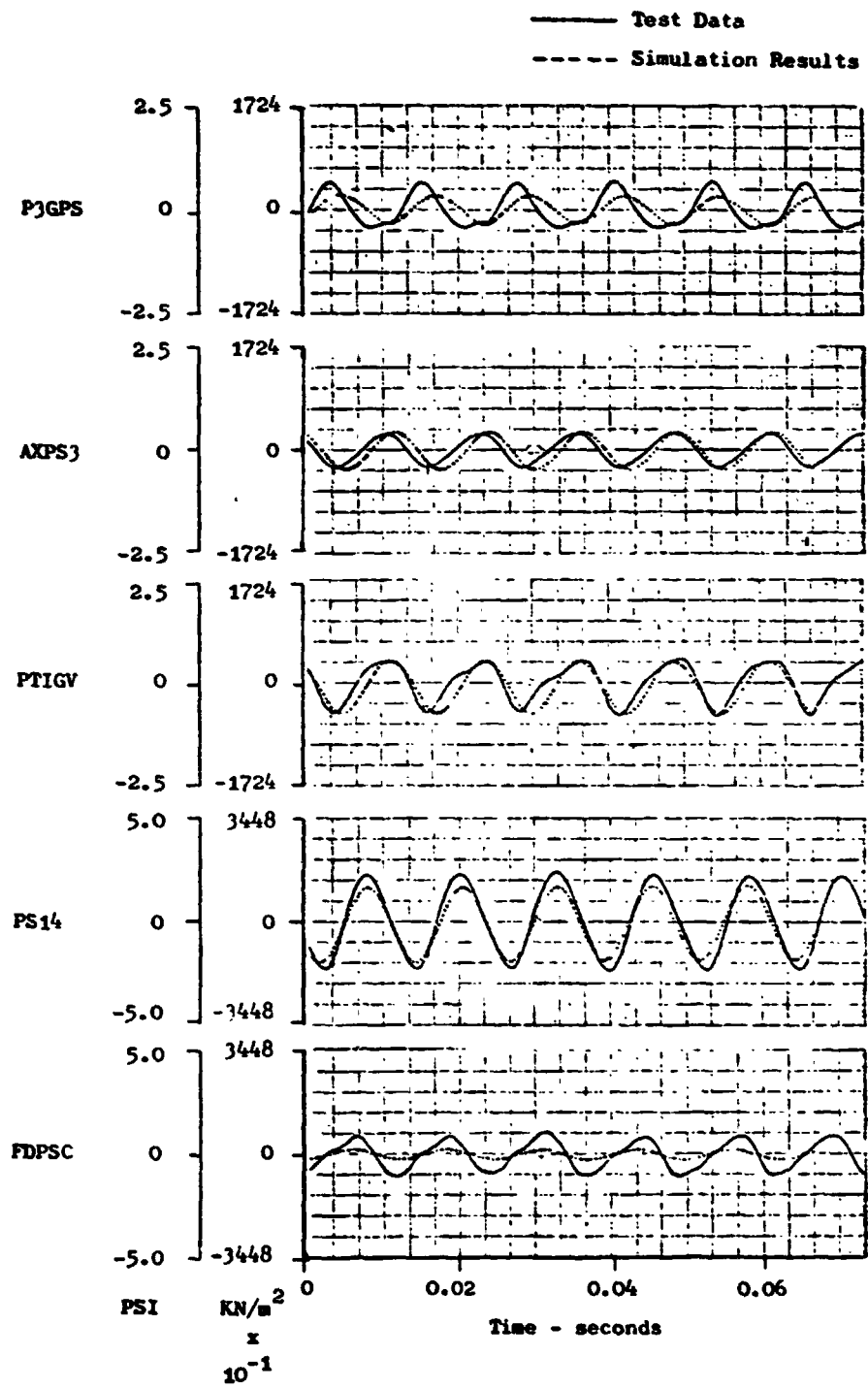
Figure 17. F101 Fan/P^{3}G Simulation, 100% N/$\sqrt{\theta}$, 80Hz.

55
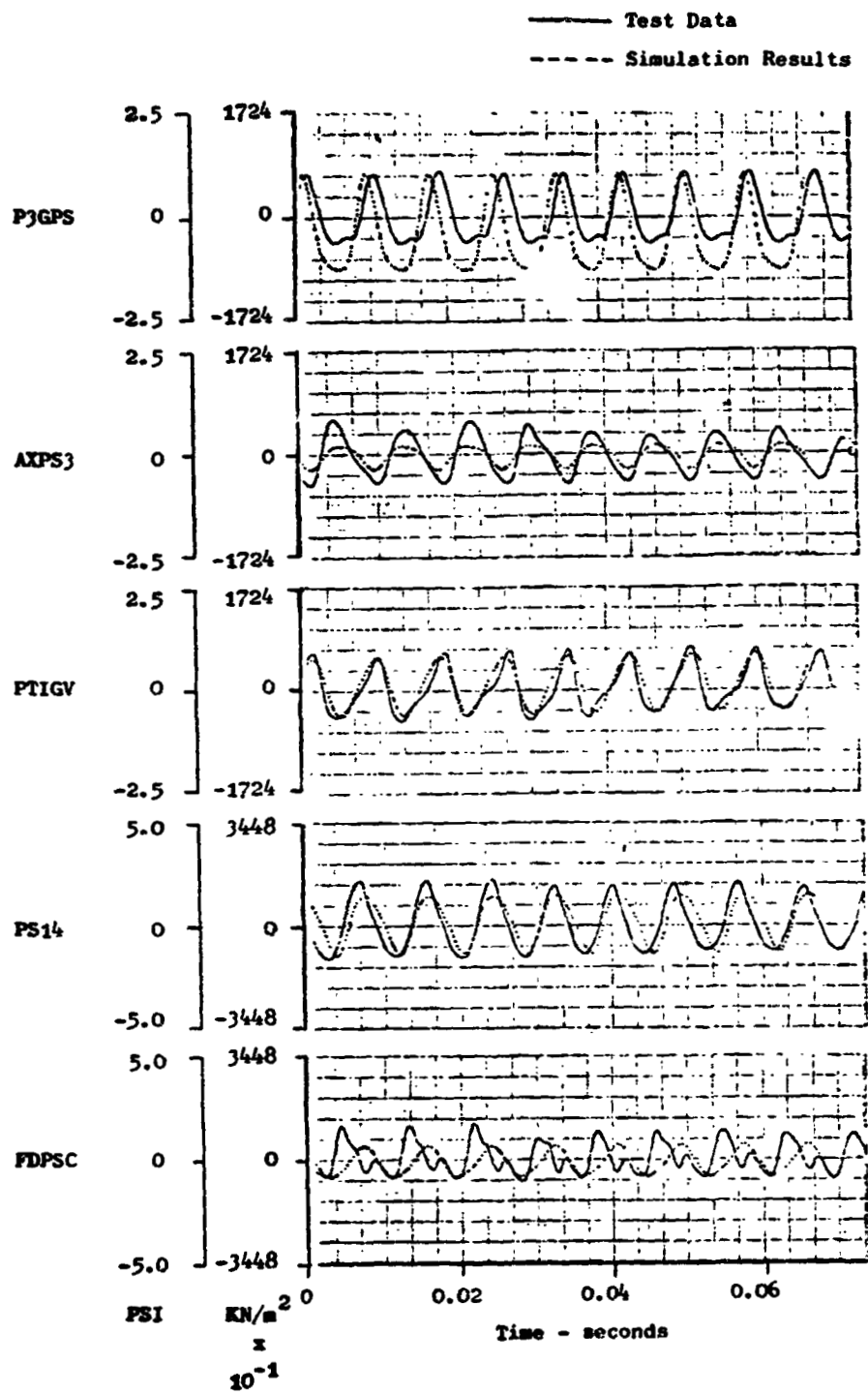
Figure _ᴿ_. F101 Fan/P³G Simulation, 100% N/√θ̄, 118Hz.
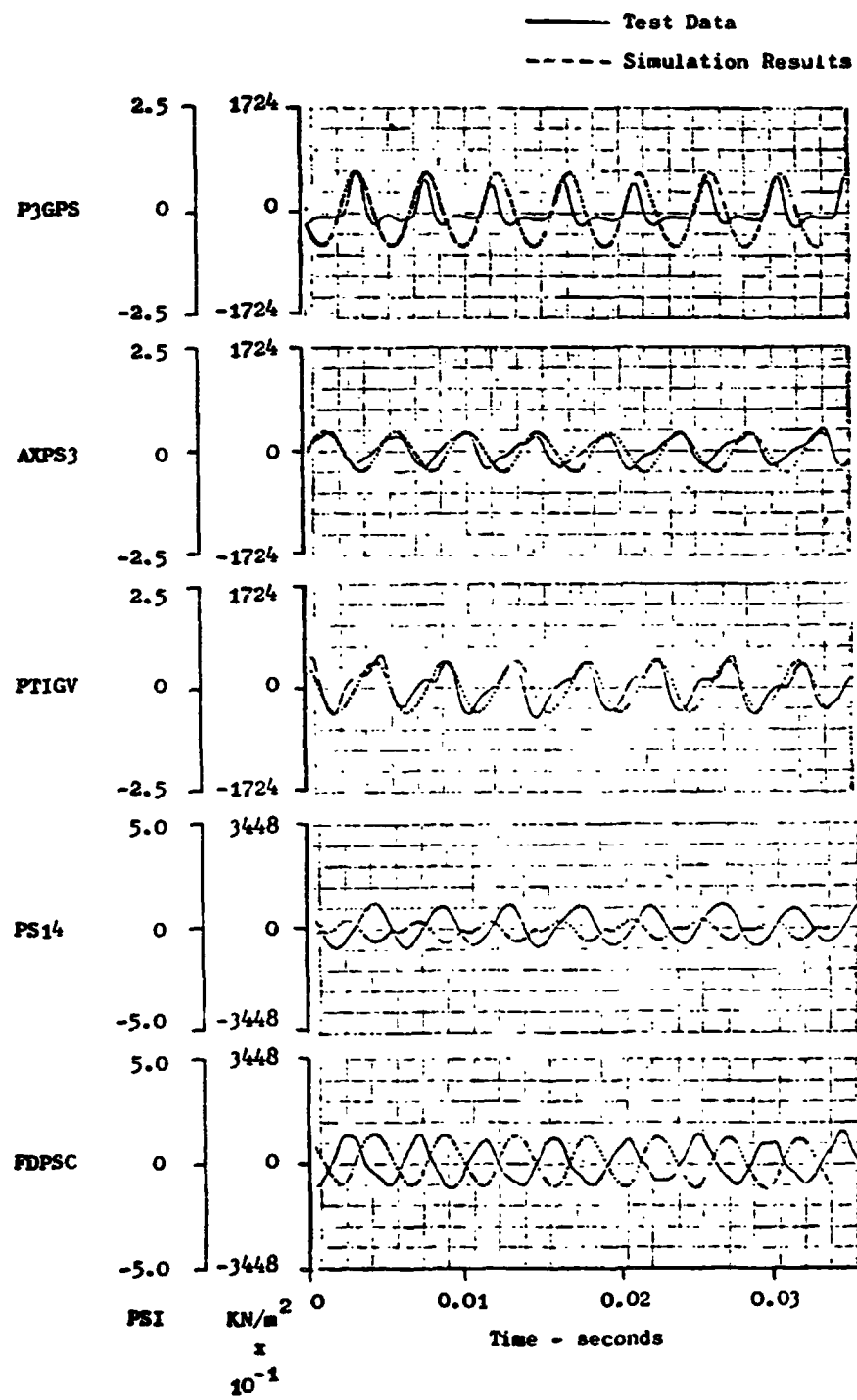
Figure 19. F101 Fan/P^{3}G Simulation, 100% N/$\sqrt{\theta}$, 220Hz.
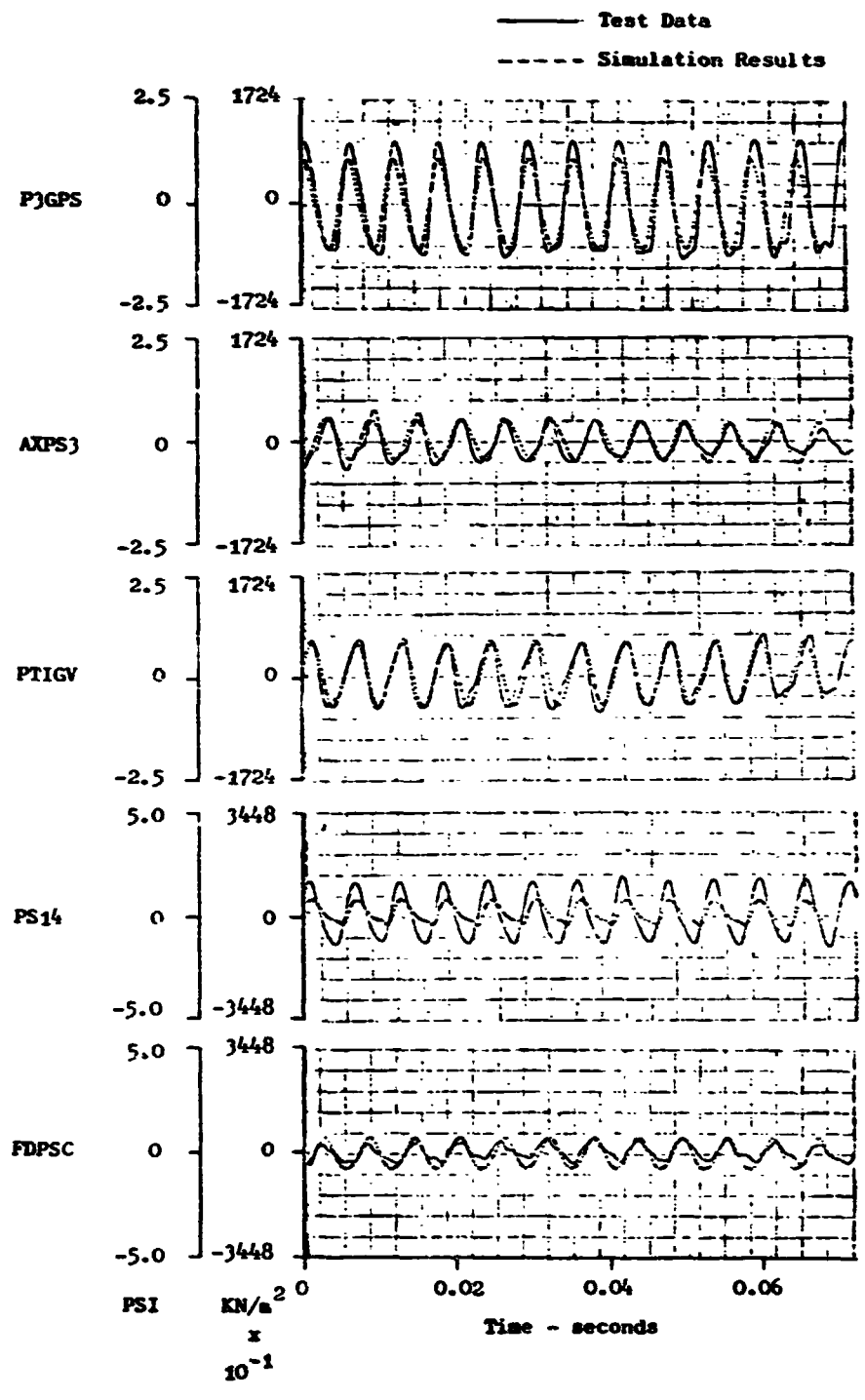
Figure 20. F101 Fan/P^{3}G Simulation, 100% N/$\sqrt{\theta}$, 350Hz.

pressure is very close to the inlet total pressure, due to the extremely large flow area of this region. When the planar wave generated by the P^3G reaches this region, the flow reverses since the small kinetic head of the flow cannot overcome the pressure hill of the wave. Once the inlet velocity of a volume reverses, the density and the pressure of the volume decreases rapidly to satisfy the continuity relationship. This drop in pressure forces the velocity to the inlet of the adjacent downstream volume to reverse and subsequently, a similar process continues to the downstream volumes. Eventually, the reverse flow propagates down to the compressor and as a result, the compressor is "starved" and is thrown into an unstable operation that leads to the solution failure of the model.

This type of instability, however, may not occur in actual test unless the amplitude of the planar wave propagated upstream to the bellmouth is unusually high. If the area is too large for a given mass flow rate, the flow does not necessarily follow the contour of the bellmouth. Instead, an annular stagnation region exists near the solid wall and the air flows only through the core region of the bellmouth. Thus, the kinetic head of the flow can be high enough to counter the pressure rise due to the P^3G oscillation.

In order to approximate the actual flow at the bellmouth, the plenum volume and the first five volumes of the bellmouth were replaced by smaller constant area volumes as described in the previous subsection. After this modification to the geometry, the digital model was free of the instability due to reverse flow.

With the modified geometry of the J85-13/P^3G test apparatus, the AEROSTAP program was run according to the model operation scheme established in the previous subsection. The model entered computation at the steady-state operating point at W_c = 19.73 Kg/sec (43.5 lb_m/sec), see Figure 21. The total-pressure ratio at this point is 7.61. After "settling" for 1000 time steps, the P^3G frequency of 100 Hz was assigned to the model and then the amplitude of the P^3G area oscillation was "ramped" until the IGV total-pressure variation reached approximately 10% peak-to-peak about the mean total pressure. This ramping procedure is denoted by the dotted line in Figure 21. When the ramping was completed, the model was allowed to run steadily with a constant amplitude of the P^3G area fluctuation for 10,000 time steps which are equivalent to 10 cycles of the 100 Hz oscillation. It was observed that the operating points of the J85 compressor formed a repetitive orbit of an ellipse, Figure 21, after three cycles. This clearly demonstrated that the model can be brought to a stable operation according to the operating procedure given in Subsection 4.1.1.
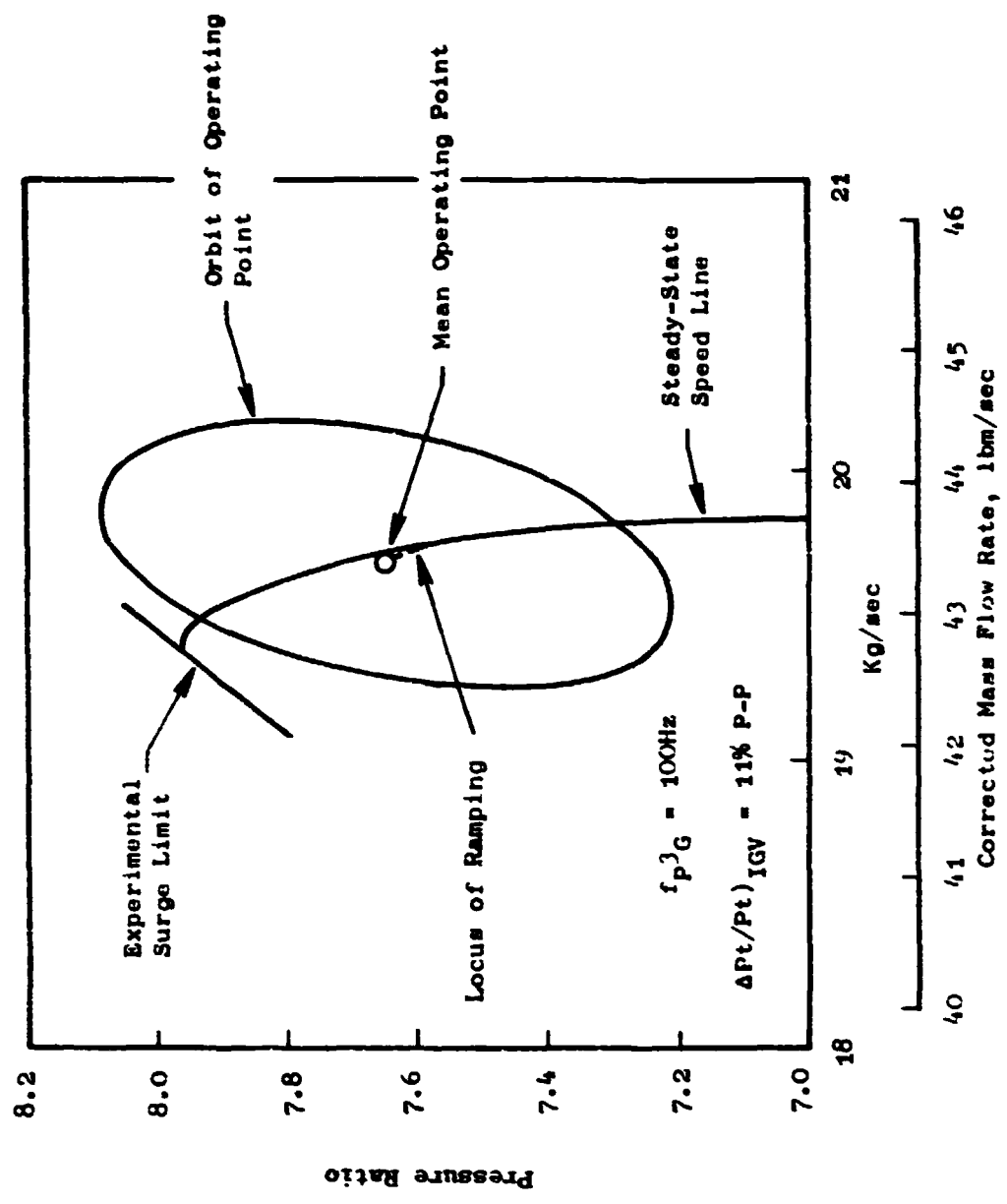
Figure 21. J85-13/P³G Operating Point Excursion.

60

Subsequent to the program verification, the AEROSTAP program was run at eight different P^3G frequencies to investigate the time-dependent operation of the J85-13/P^3G test installation and then, throttled at four different frequencies to determine the instability points of the J85 compressor under the inlet planar distortions of various frequencies. The results of this series of investigations are presented in the following two subsections.

4.1.3 Time-Dependent Analysis

The time-dependent analysis of the J85-13/P^3G test installation was performed at 100% compressor design speed at eight different frequencies, i.e., 100, 150, 200, 250, 300, 400, 600, and 850 Hz. The IGV total-pressure variation was greater than 10% peak-to-peak about the mean total pressure for all the frequencies. All the simulation runs were initiated from the steady-state operating point on the 100% speed line defined by the corrected mass flow rate of 19.75 Kg/sec (43.5 lb_m/sec.). The settling, ramping of P^3G amplitude, and steady operation of the model were performed according to the model operation procedure outlined in Subsection 4.1.1.

The results of the analysis for the P^3G frequencies of 100, 250, and 600 Hz are summarized in Figures 22 through 30. Figures 22 through 27 show pressure waveforms at various locations of the J85-13/P^3G test installation. The locations are defined in Table 2. These figures also contain the plots of the physical mass flow rate at the IGV and the overall pressure ratio across the compressor as a function of time. Figures 28 through 30 show the blade lift force as a function of time. Similar plots for other frequencies, namely 150, 200, 300, 400, and 850 Hz, are presented in Appendix C.

An interesting observation is that the model operation is relatively unstable for the frequencies ranging from 200 to 300 Hz. These frequencies are close to the resonance frequency, approximately 230 Hz, of the duct between the P^3G and the first rotor of the compressor. Therefore, it is believed, any small perturbations due to numerical inaccuracy amplify and cause a slightly nonstationary operation of the model. When this type of nonstationary behavior occurs, the operating points of the compressor cannot attain a constant orbit such as the one depicted in Figure 21. Instead, the orbit shifts slightly as the average operating point fluctuates sinusoidally about a mean value. The frequency of this fluctuation could not be determined due to the insufficient amount of computed data. However, this type of oscillatory behavior is not severe enough to prohibit operation of the model. The simulation can be continued and run indefinitely without encountering a major shift of the orbit or drifting into compressor instability.

61
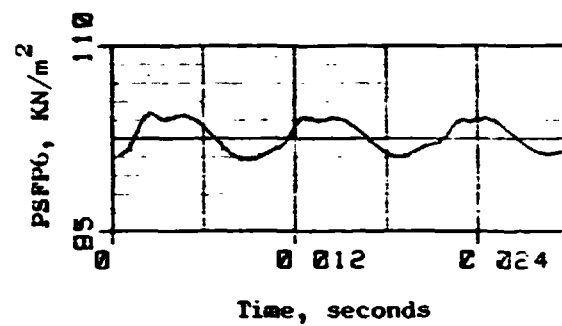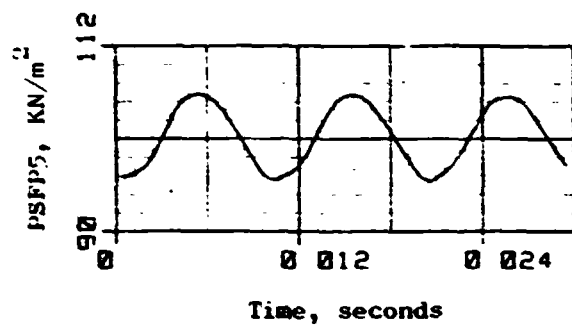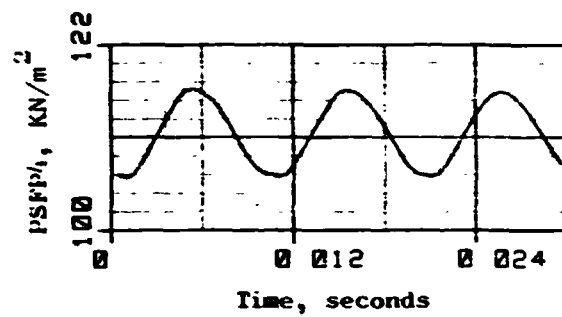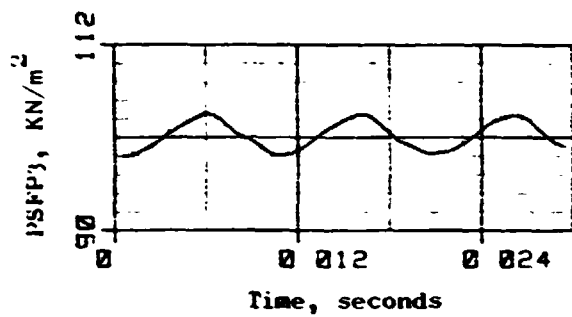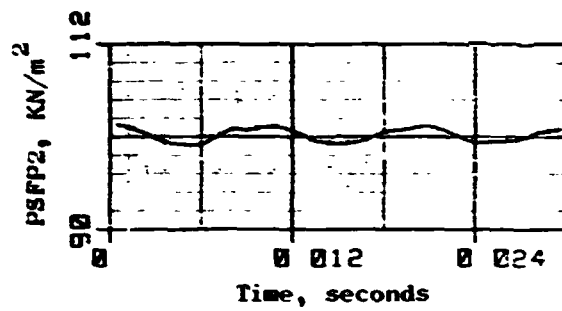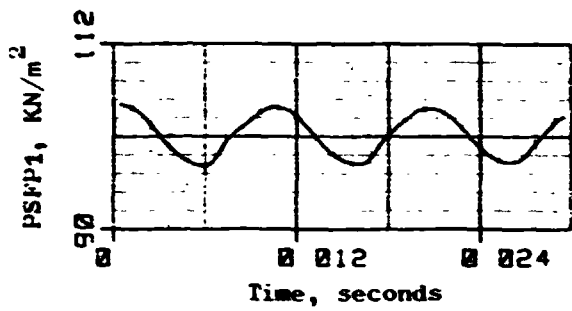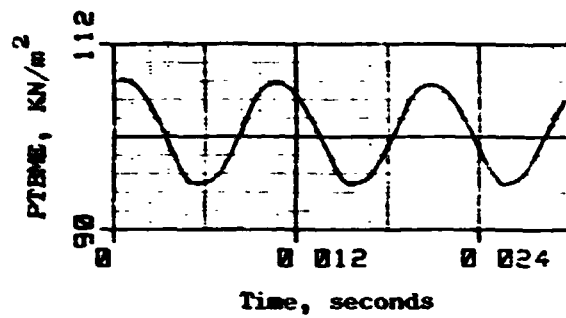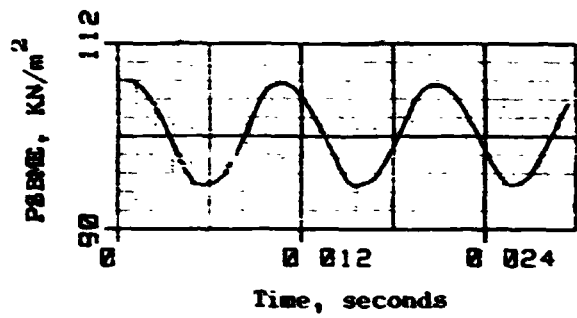
Figure 22. J85-13/P^{3}G Simulation Results, f_{P^3G} = 100Hz.

62
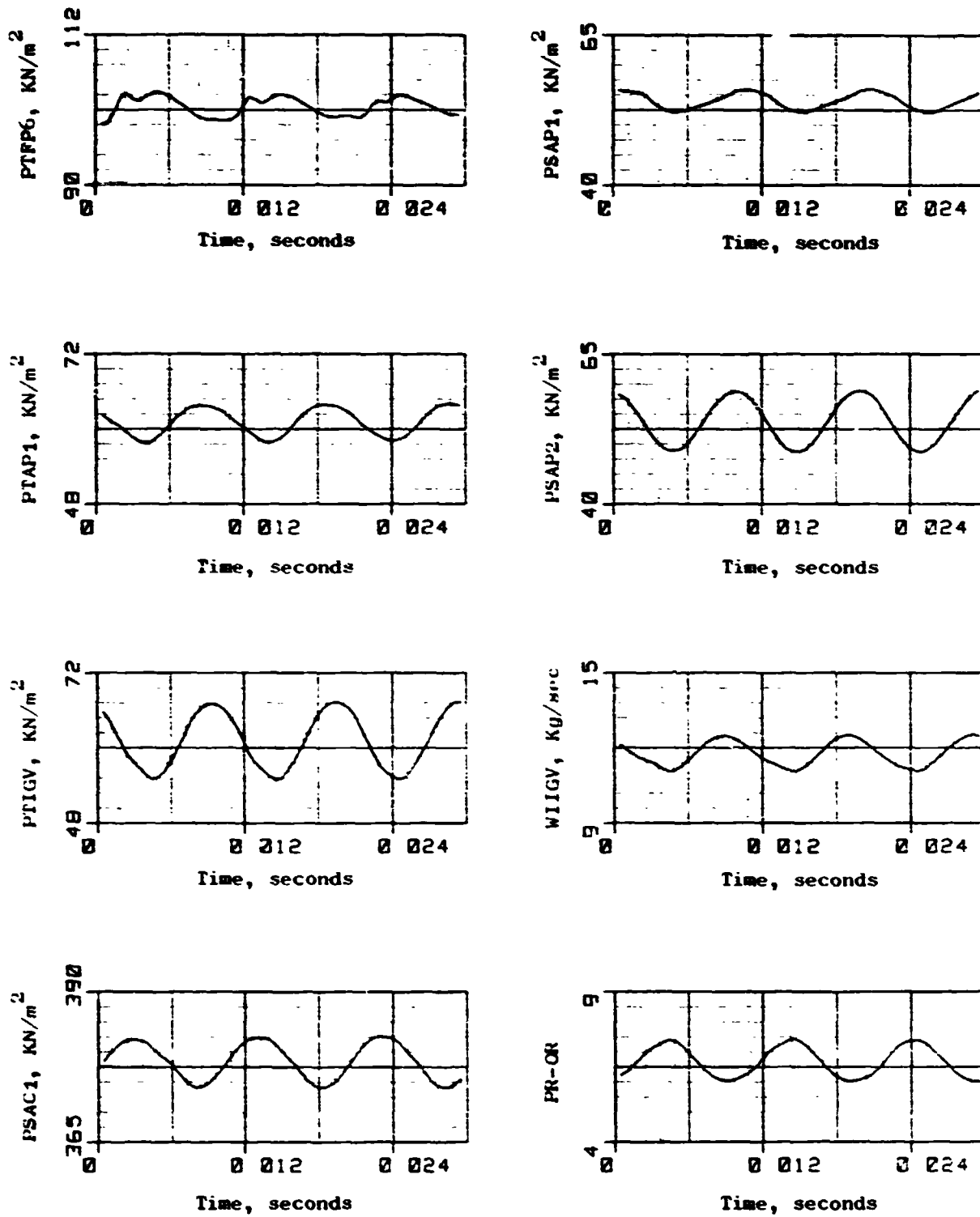
Figure 23. J85-13/P^{3}G Simulation Results, f_{P^3G} = 100Hz (Concluded).
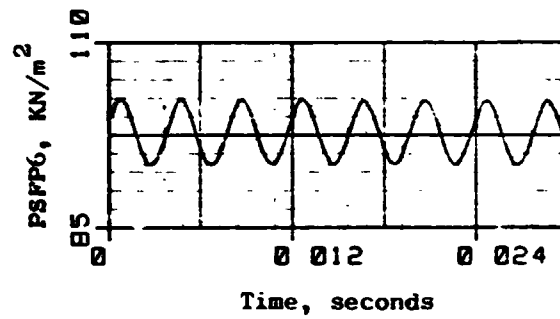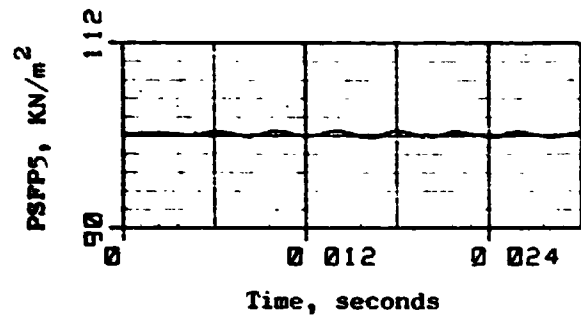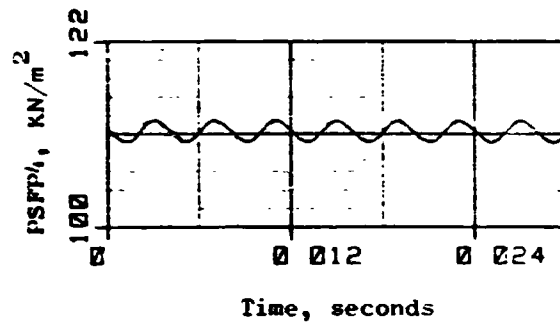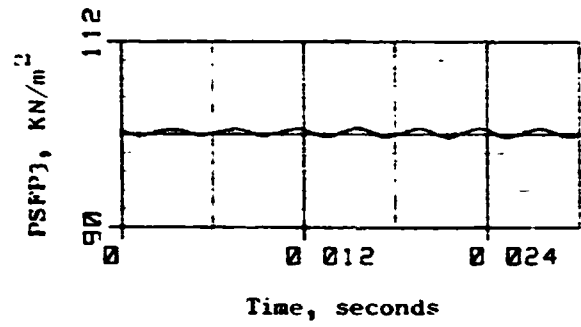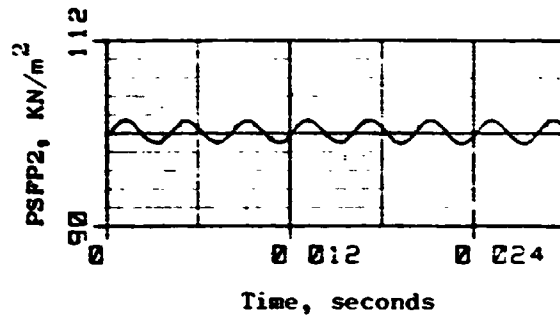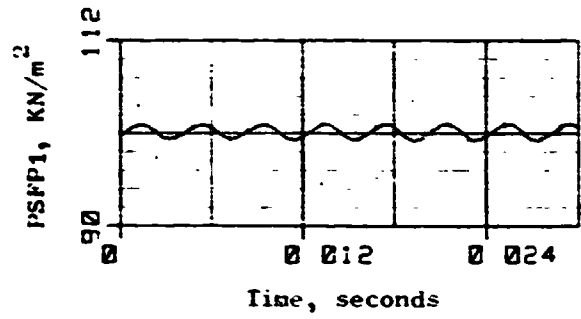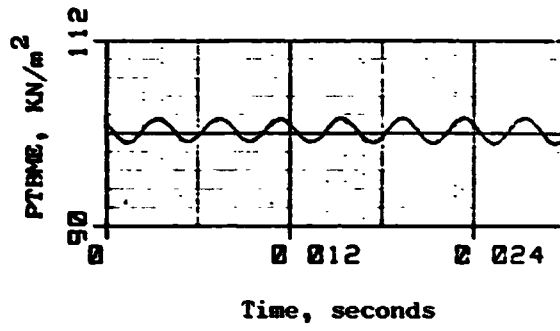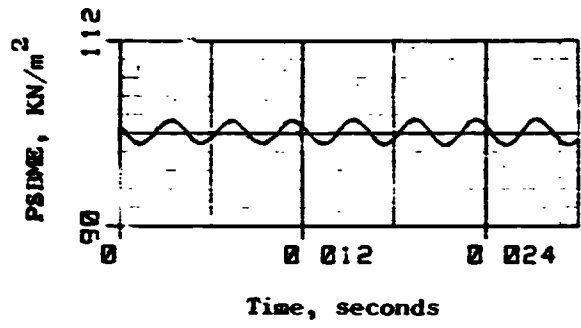
Figure 24. J85-13/P^{3}G Simulation Results, f_{P^3G} = 250Hz.

64
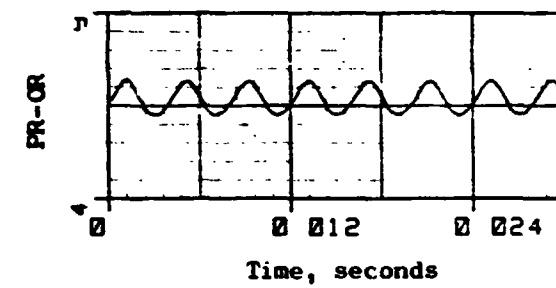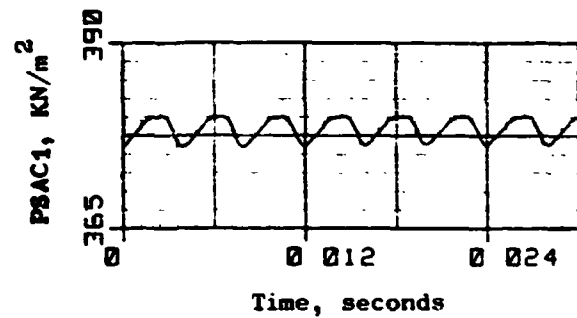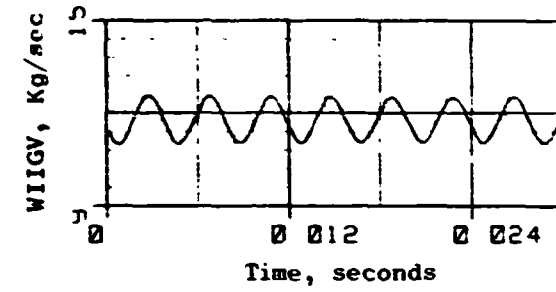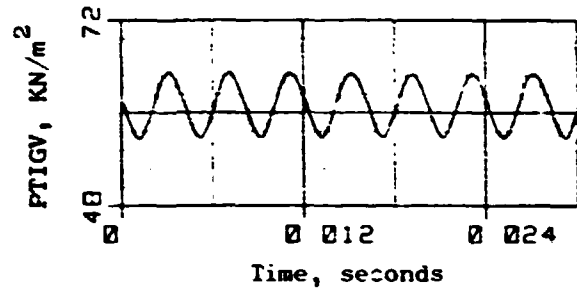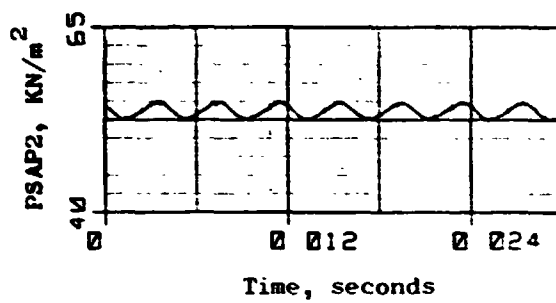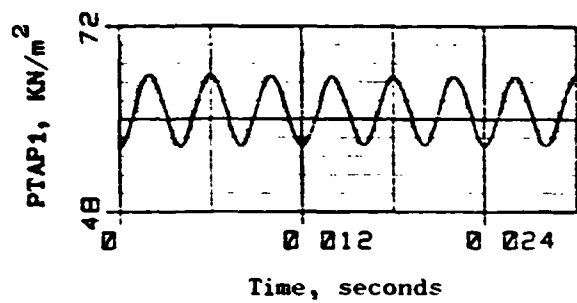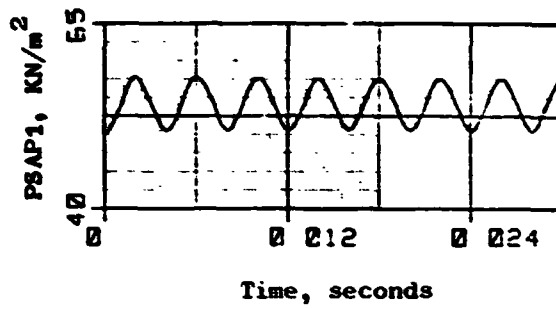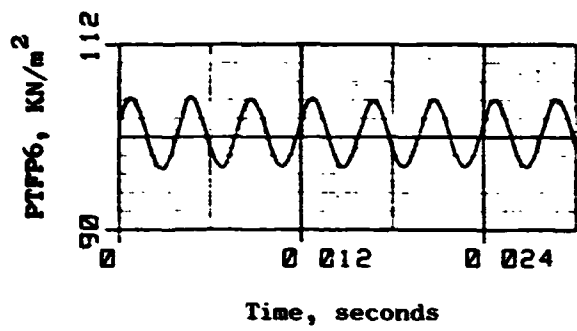
Figure 25. J85-13 Simulation Results, $f_p{}^3{}_G$ = 250Hz (Concluded).

65
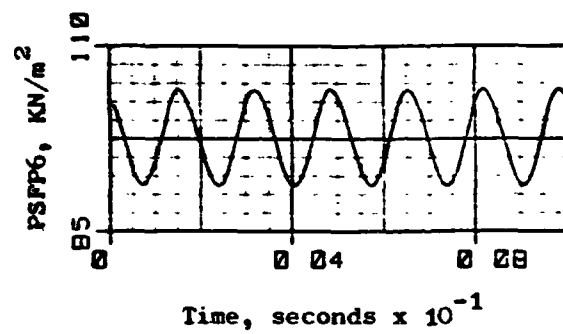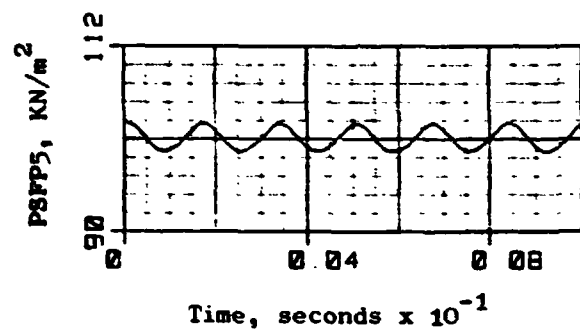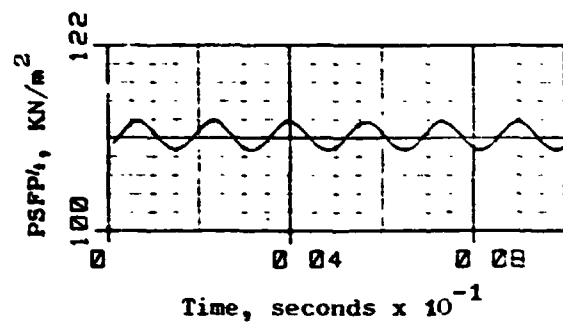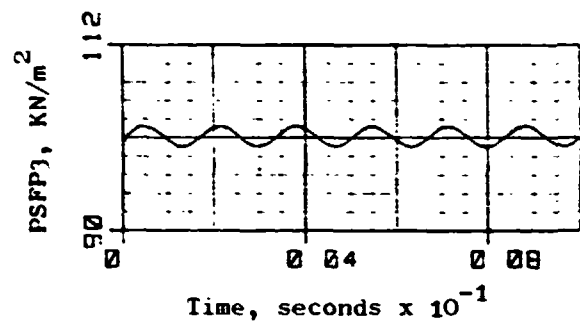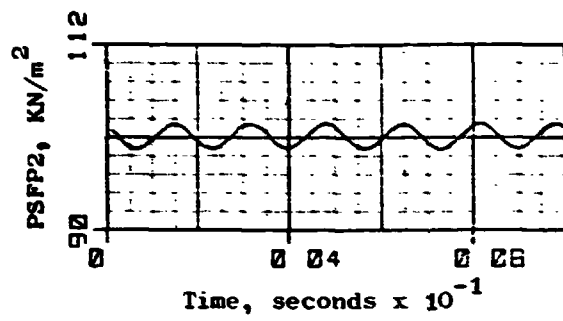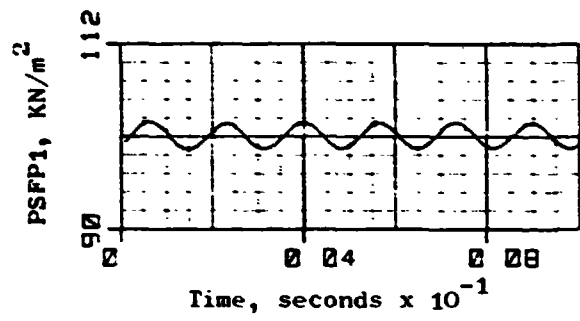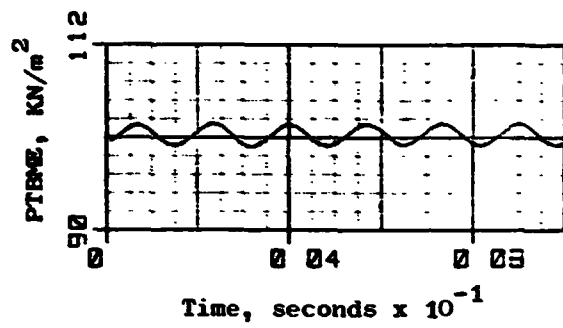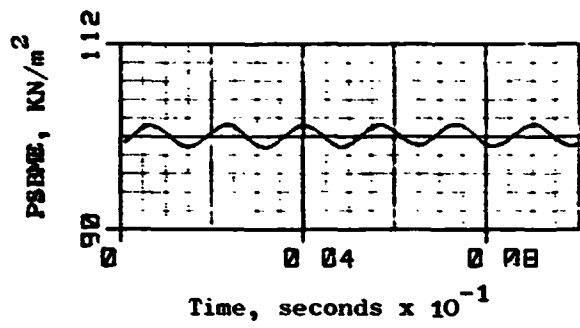
Figure 26. J85-13/P³G Simulation Results, f_{P^3G} = 600Hz.
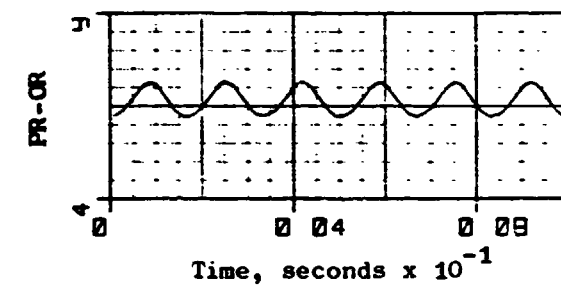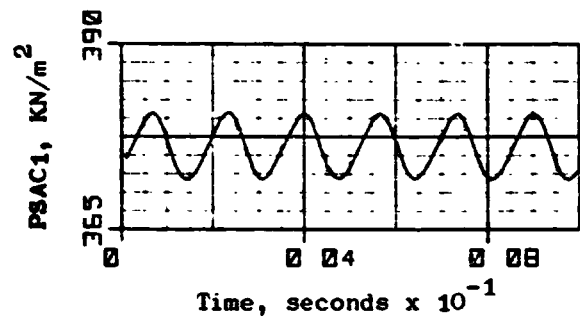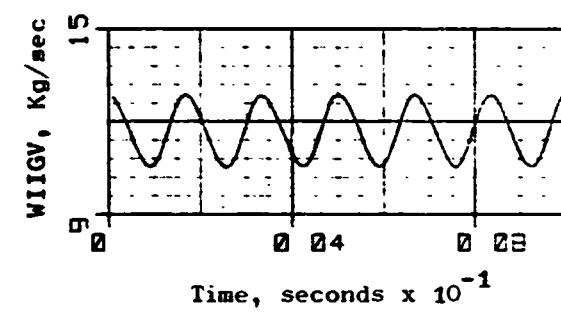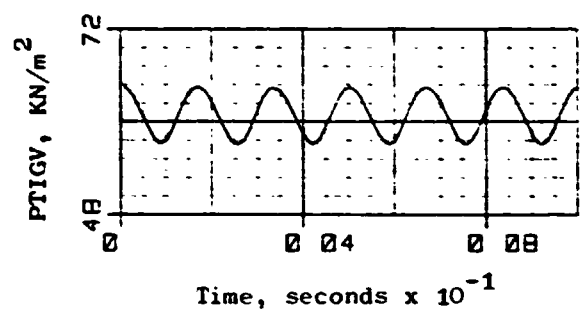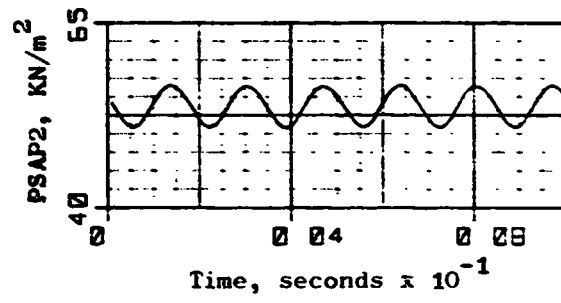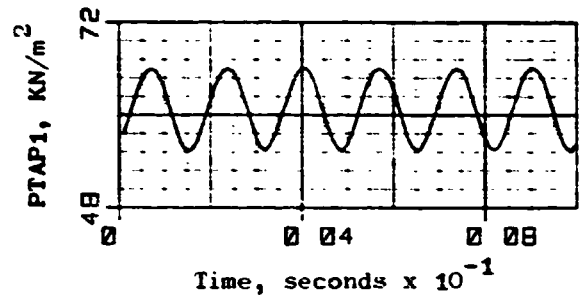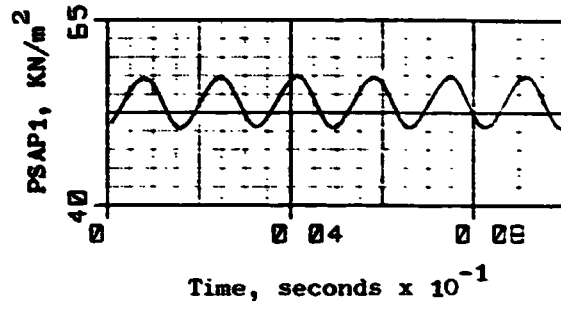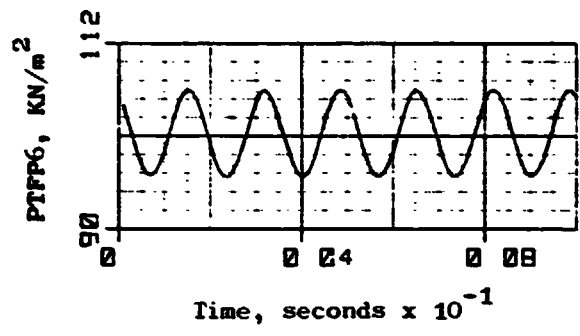
Figure 27. J85-13/P^{3}G Simulation Results, f_{P^3G} = 600Hz (Concluded). 67
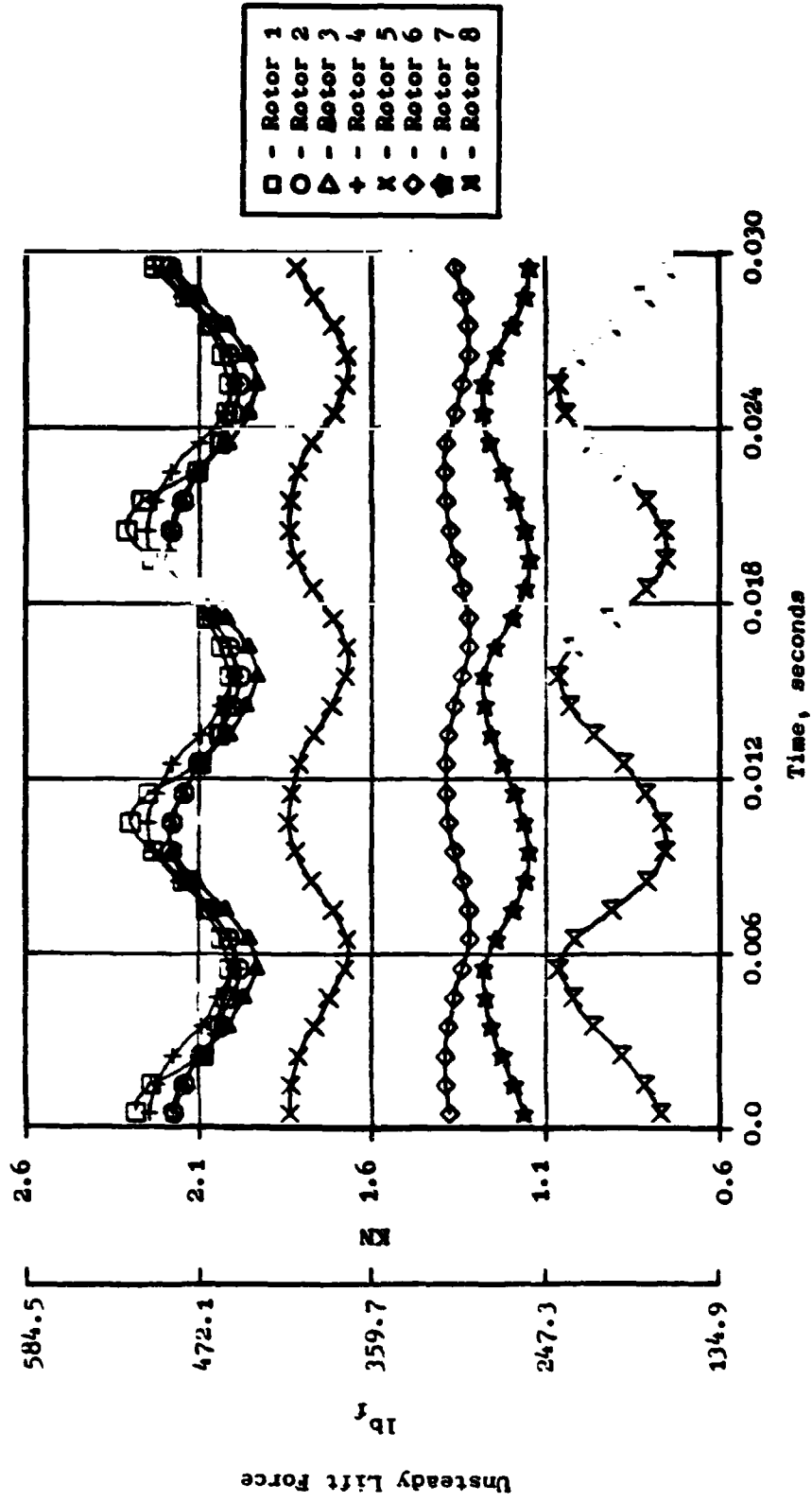
Figure 28. Unsteady Blade Lift Force as a Function of Time at 100Hz.

68
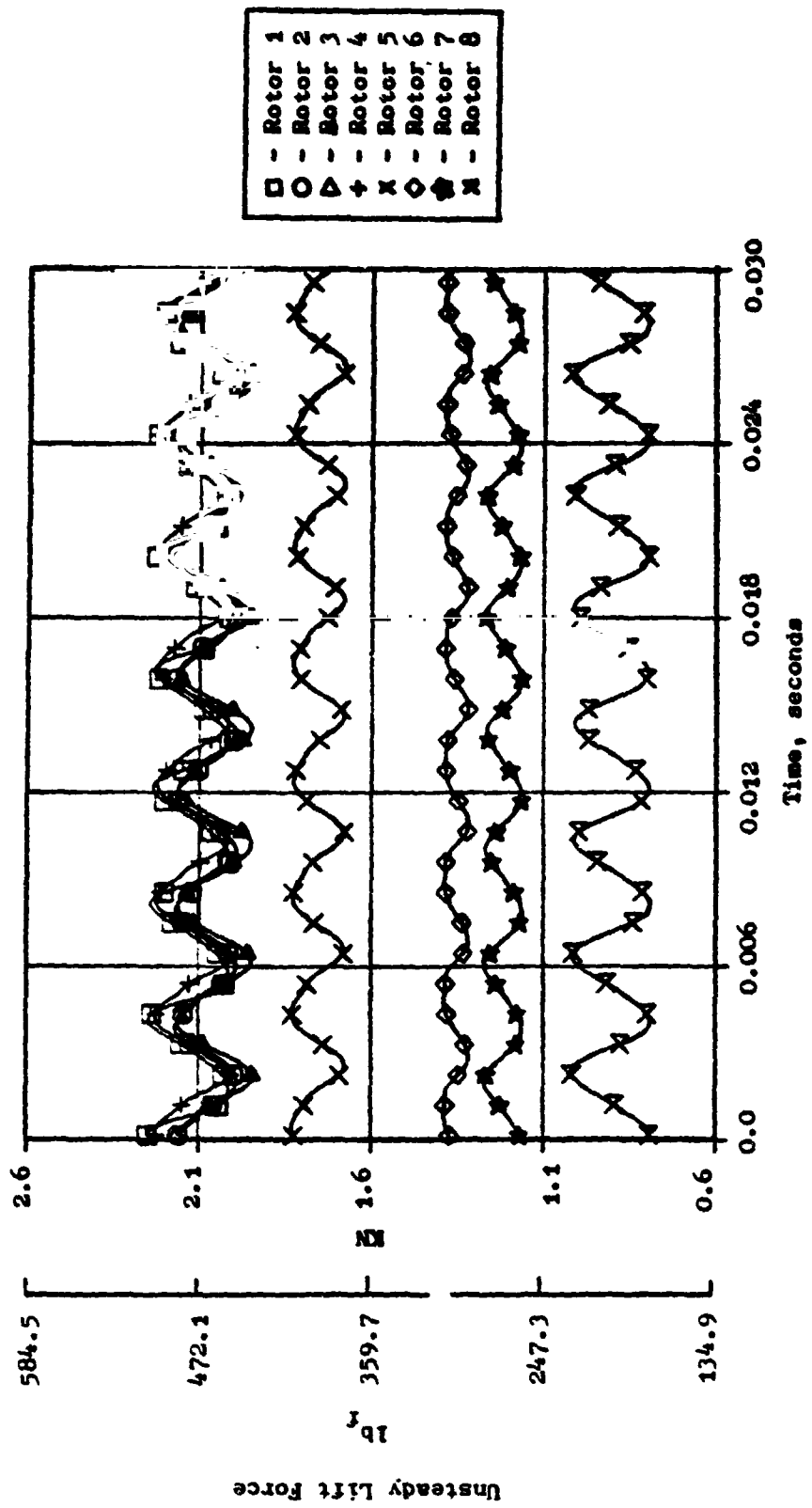
Figure 29.   Unsteady Blade Lift Force as a Function of Time at 250Hz.

69
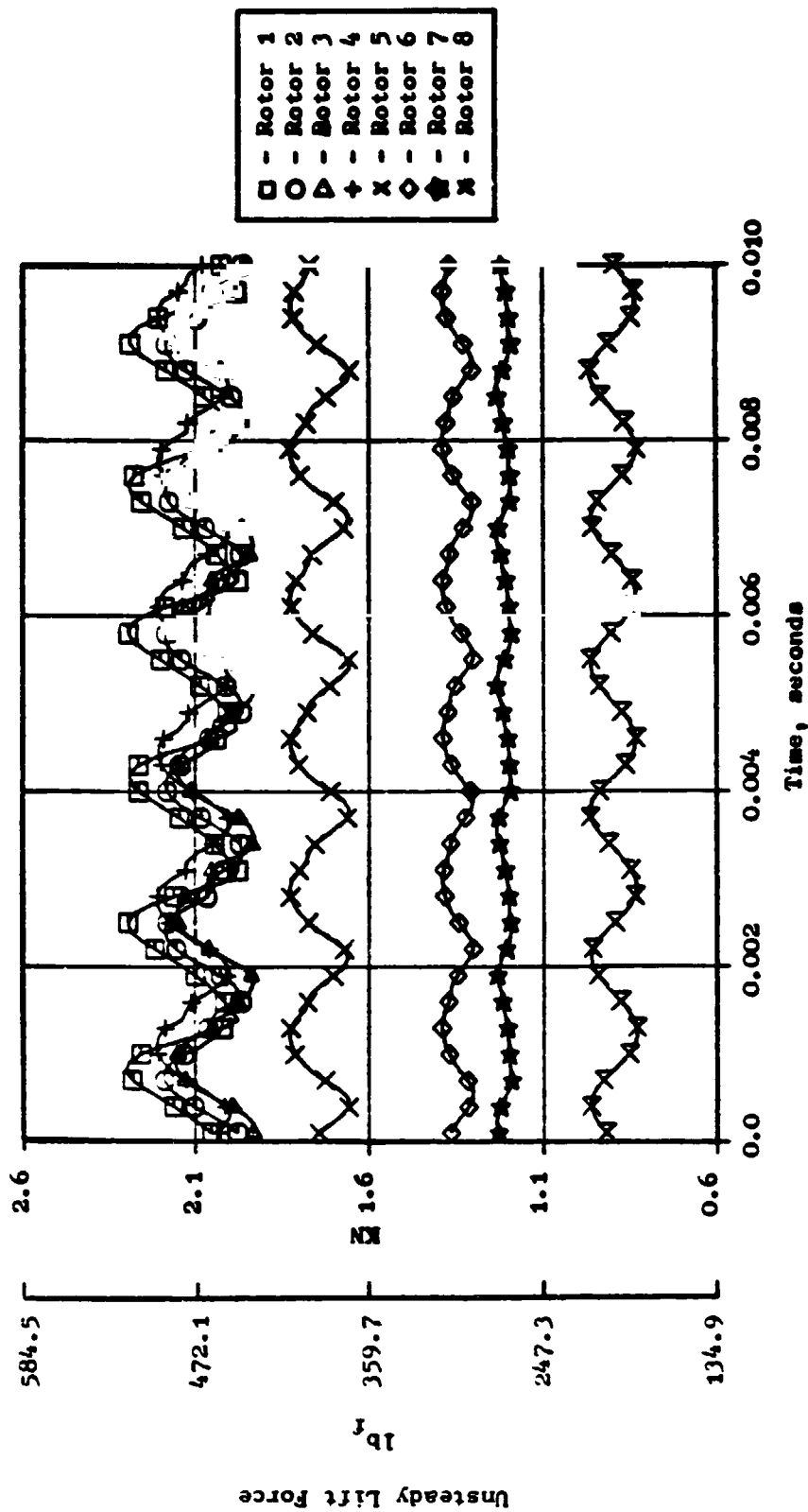
Figure 30. Unsteady Blade Lift Force as a Function of Time at 600Hz.

70

The resonance behavior of the duct betw ˙ ːr the P^3G and the first rotor is shown in Figure 31. In this figure, the amplitude of the IGV total-pressure oscillation is plotted as a function of the P^3G frequency. The total-pressure loss and the amplitude of the P^3G area fluctuation are   d constant. Examination of this figure reveals that while the same amplitude perturbations are introduced at the P^3G, the maximum amplitude of the total-pressure oscillation occurs at about 230 Hz. This frequency is commensurate wi⁺h the resonance frequency computed according to the formula for a closed-closed organ pipe. It should be noted that a rotor generate₃ a substantial change in acoustic impedence and thus, can be treated as a closed end in an acoustic analysis. The P^3G plane is choked at all times. Therefore, the duct between the P^3G and the first rotor can be treated essentially as a closed-closed system.

After the completion of the time-dependent analysis, the model was throttled to the point of instability for the purpose of estimating the stability limit of the compressor under planar inlet distortions. This study is described in the following subsection.

4.1.4 Surge Line Estimation

The stability limits of t˙ ₑ "Mehalic" configuration of the J85 compressor were obtained by throttling the model to instability (surge). The surge line estimation stud, was conducted at 100% corrected speed for five different frequencies, i.e., 100, 150, 200, 250, and 300 Hz.

The instability point of the model was determined through observations of the migration of the mean operating point. This migration charted on the steady-state compressor map was normally well behaved until the point of model instability was encountered. At the instabil' point, however, the average operating point departed abruptly from the path it followed and wandered erratically until the solution failed. Once the model reached the system stability limit, this erratic behavior of the mean operating point was observed even if the throttling was terminated. Therefore, the instability point of the model was determined as the point ɛt which the average operating point abruptly departed from its path even in the absence of throttling.

After the point of instability was defined, the system model was throttled to instability to investigate the effect of the P^3G frequency. First, the model was brought to steady operation through settling and ramping after it entered computation at $W_c = 19.79$ Kg/sec (43.5 lb_m/sec). The amplitude of the P^3G area oscillation was 10% peak-to-peak for all frequencies. The total-pressure loss across the P^3G was set at 45% of the inlet total pressure. The loss is commensurate with the actual total-pressure loss across the P^3G determined experimentally by NASA. After the model was allowed to
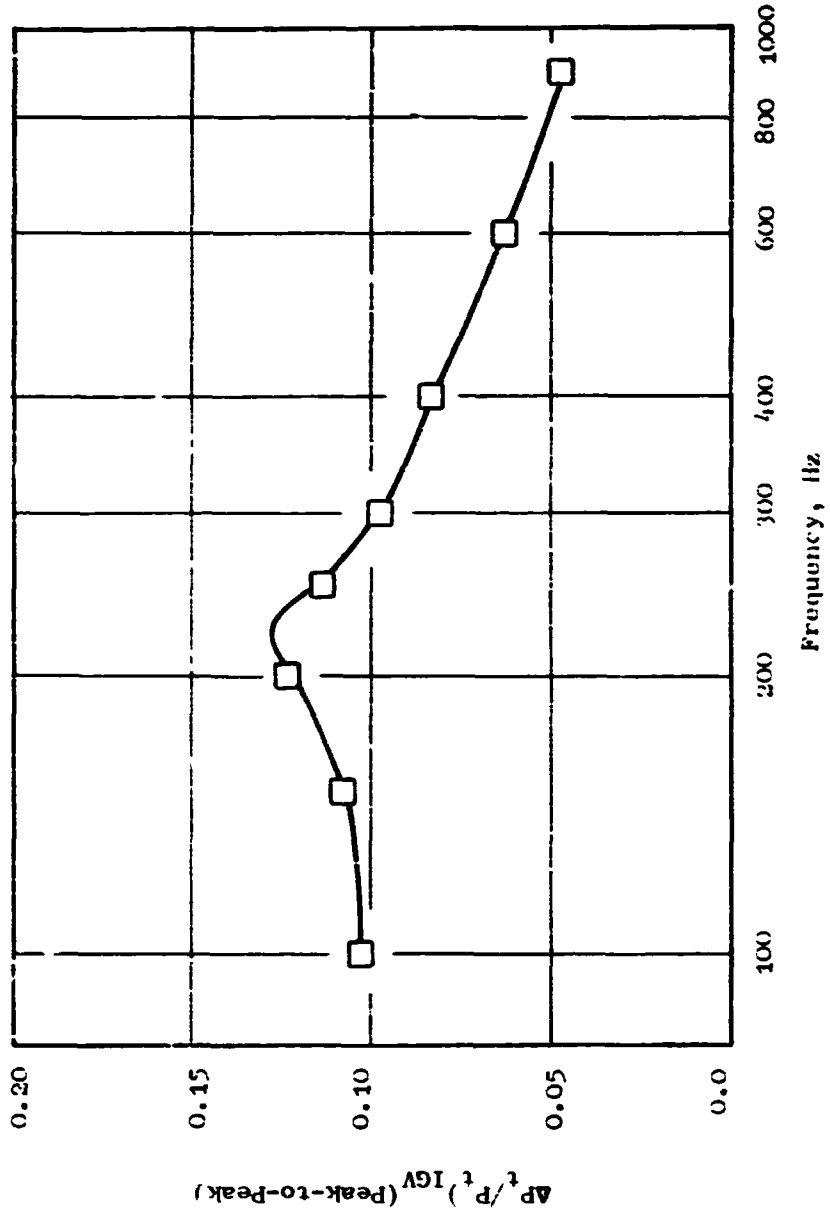
Figure 31. Amplitude of IGV Total-Pressure Oscillation as a Function of Frequency.

72

run for approximately 10 to 20 cycles of the planar wave, the model was
throttled for a period of 2 cycles. Then, the model was run for 4 cycles and
observed for occurrence of instability. If the model was stable, it was
throttled again for 2 cycles and then, observed for 4 cycles. This process
was repeated until the point of model instability was observed. The throttling
was conducted at a rate slow enough to assure a quasi steady-state throttling
process; the exit flow function was reduced at the rate of 0.00005 $(\sqrt{°R}$ -ft)
or less.

The results of the stability analyses are presented graphically in
Figures 32 through 36. These figures show the instability point, as well as
the locii of the mean operating point for ramping and throttling. Examination
of these figures reveal that the locus of the average operating point deviates
further from the steady-state speed line at P^3G frequencies that are close to
the resonance frequency of the P^3G-to-first compressor rotor system. It is
believed that the larger deviation is due to the large amplitude of the planar
wave induced by the resonance of the duct (see Figure 31).

The loss in the surge pressure ratio is also greater at these frequen-
cies. This is illustrated clearly in Figures 37 and 38. These figures present
the distortion sensitivity as a function of the P^3G frequency and the nor-
malized frequency, f^*, defined as

$$f^* = \frac{\text{frequency of } P^3G}{\text{resonance frequency of } P^3G\text{-to-first rotor system}}$$

The distortion sensitivity is defined by the following relationship

$$DS = \Delta PRS/ \left. \Delta P_t/2\bar{P}_t\right)_{IGV}$$

where ΔPRS and $\bar{P}_t$ represent the loss of surge pressure ratio and the
average total pressure, respectively. Figures 37 and 38 show that the distor-
tion sensitivity is maximum at approximately $f_{P3G} = 230$ Hz or $f^* = 1$.

4.2   FREQUENCY RESPONSE ANALYSIS

The frequency response characteristics of the $J85-13/P^3G$ test
installation were investigated using the Digital Surge Prediction (DSP) pro-
gram described previously. The model geometry employed in this linearized
analysis was essentially the same as the one used in the time-dependent
analysis. However, the geometry was broken into two parts, i.e.,
bellmouth-to-P^3G and P^3G-to-combustor exit. The frequency response
analysis was performed separately for the two sections. Further, the
number of volumes were reduced to 28 and 31 for the sections ahead and aft

73
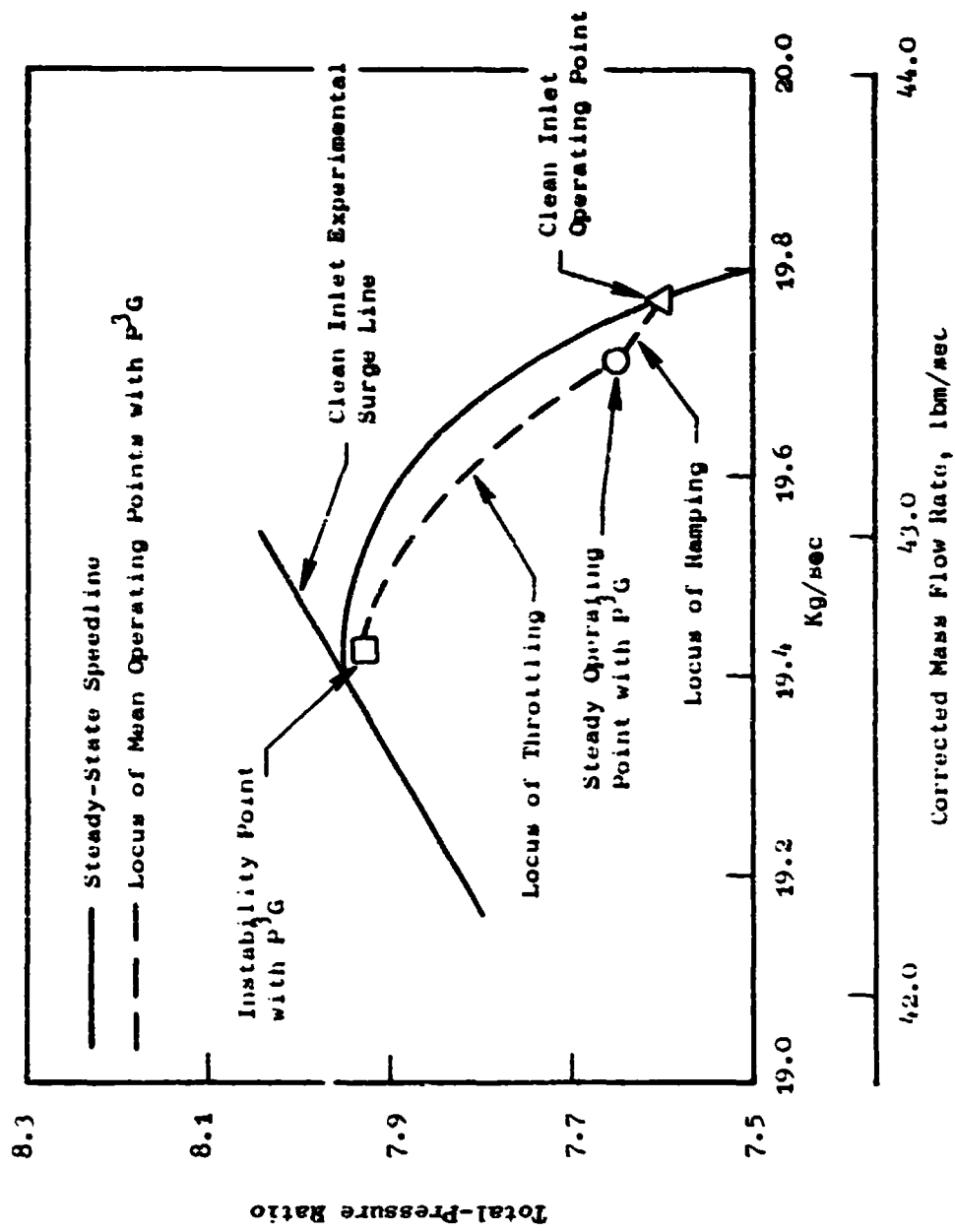
Figure 32. J85-13 Compressor Instability Point with Inlet Planar Wave Distortion, $f_{P^3G} = 100 Hz$, $\Delta P t/P t)_{IGV} = .10$.

74
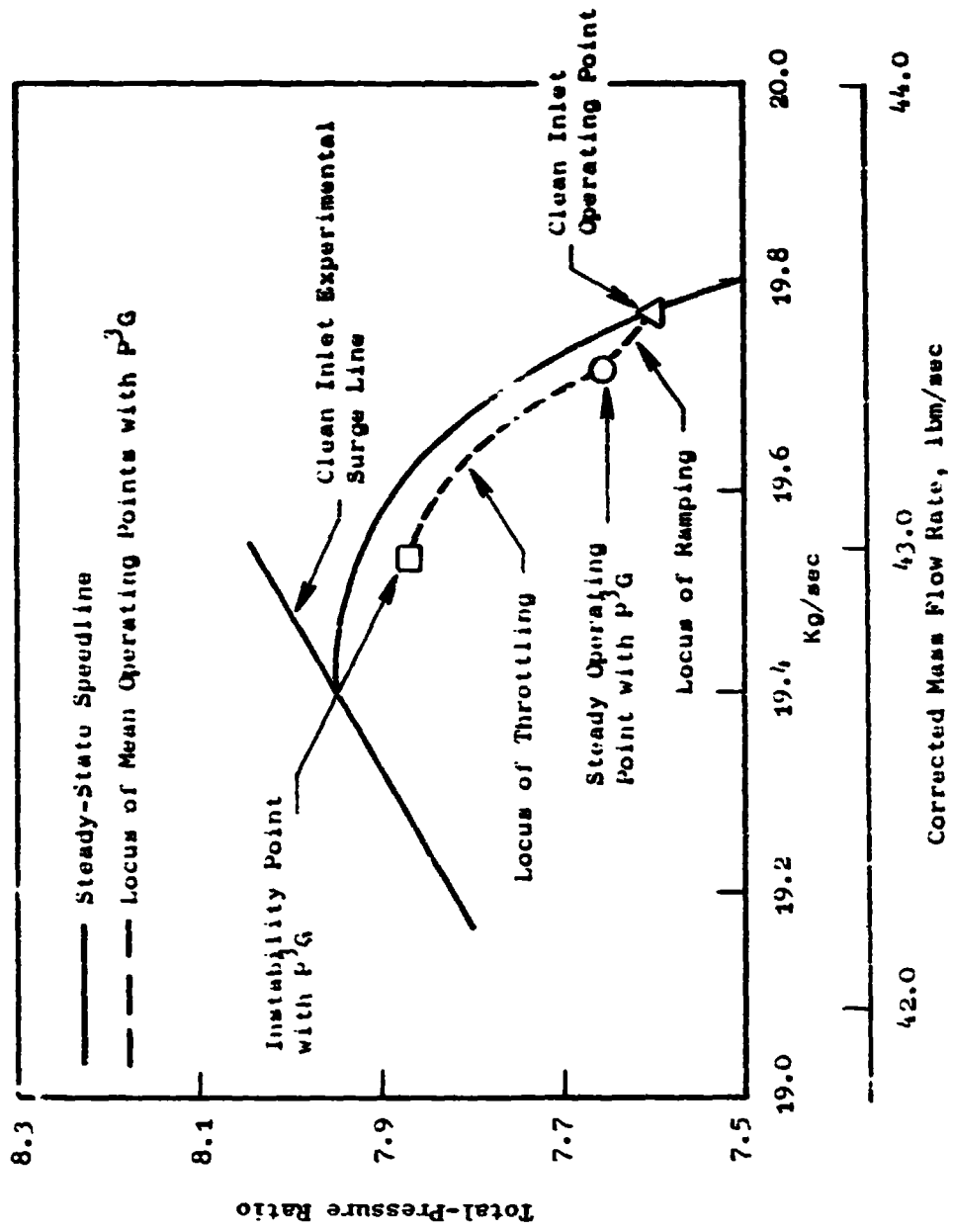
Figure 33. J85-13 Compressor Instability Point with Inlet Planar Wave Distortion, $f_p{}^3{}_G = 150Hz$, $\Delta Pt/Pt)_{IGV} = .108$.
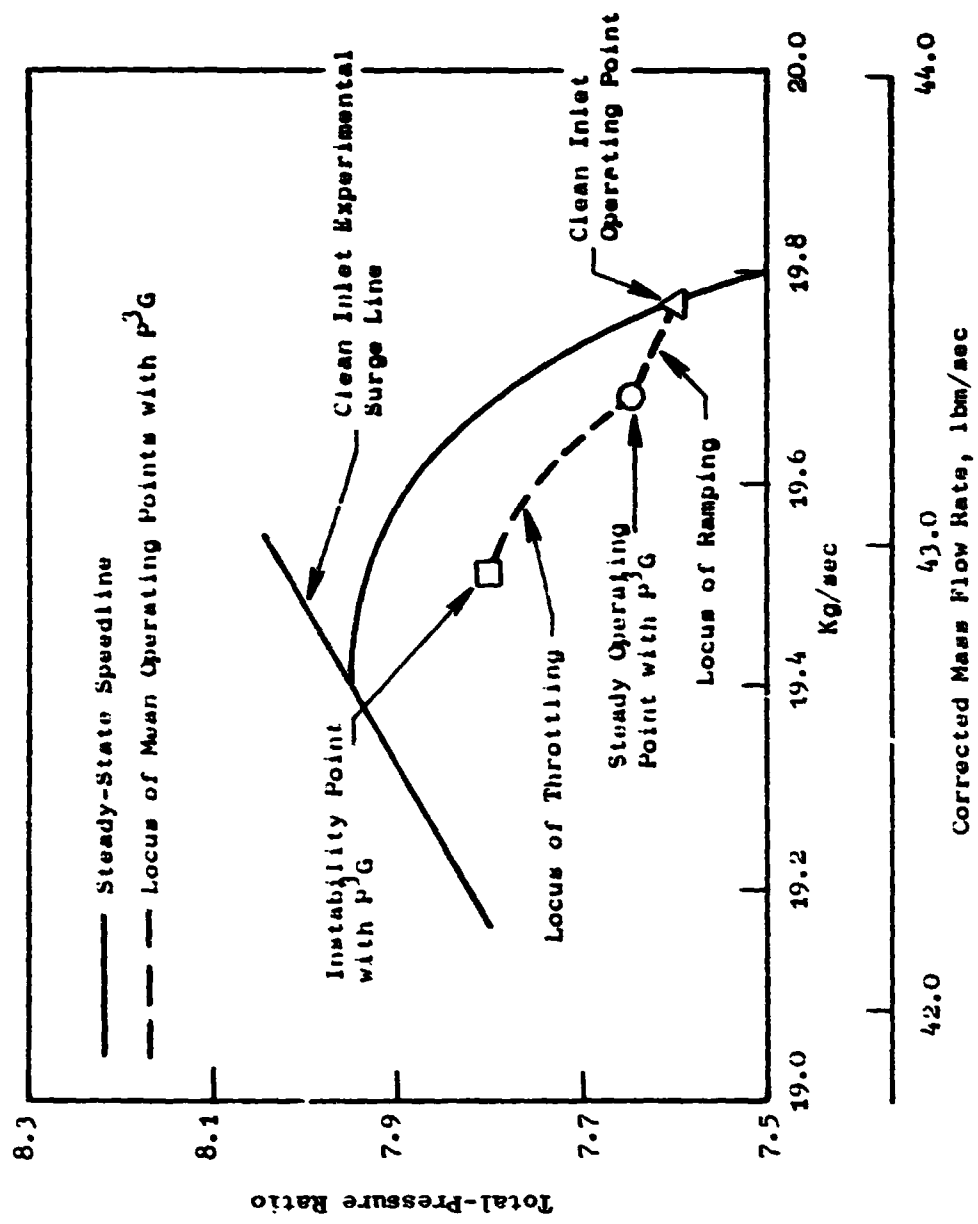
Figure 34. J85-13 Compressor Instability Point with Inlet Planar Wave Distortion, f_{P^3G} = 200Hz, $\Delta Pt/Pt)_{IGV}$ = .123.
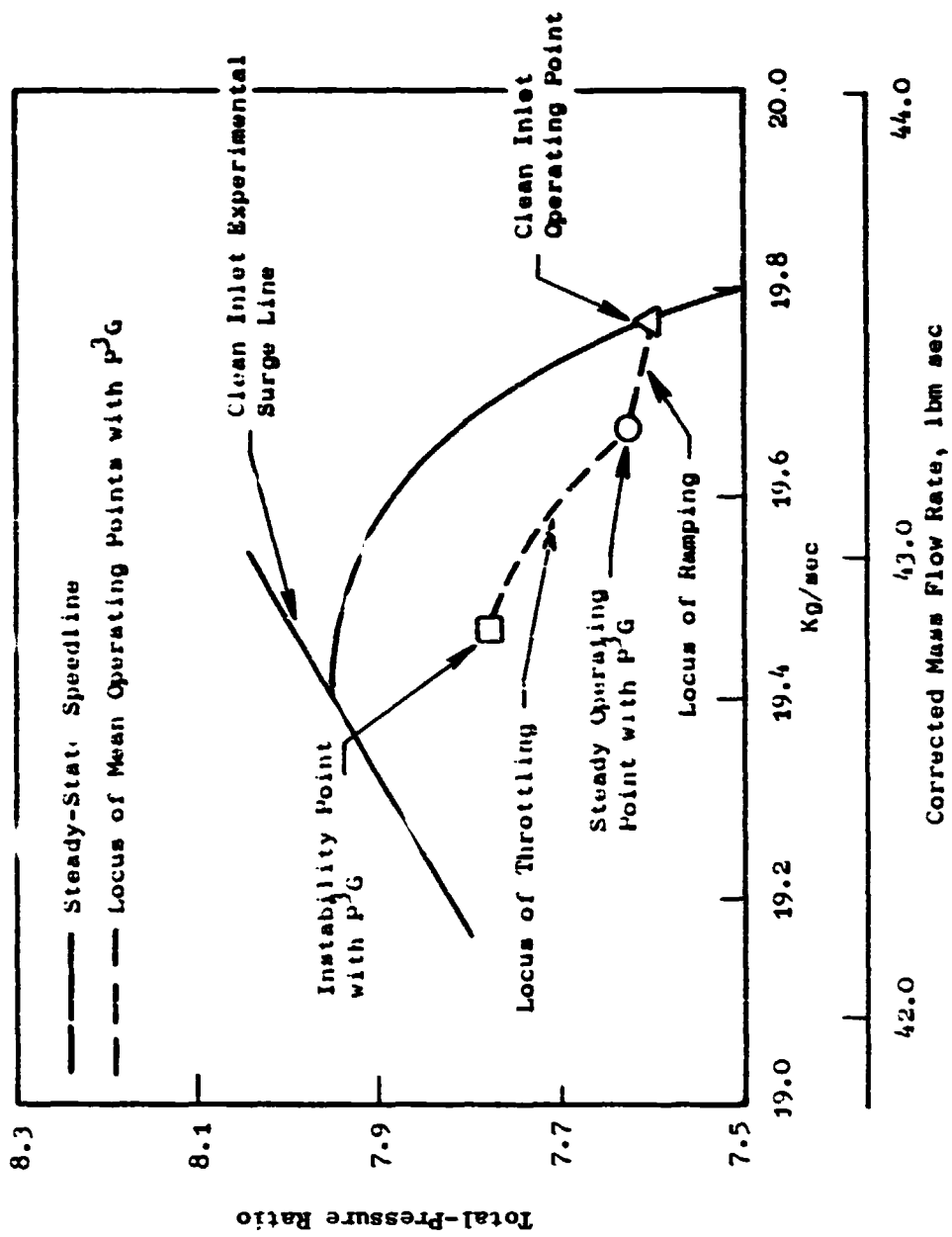
Figure 35. J85-13 Compressor Instability Point with Inlet Planar Wave Distortion, $f_p{}^3_G = 250$Hz, $\Delta Pt/Pt)_{IGV} = .115$.
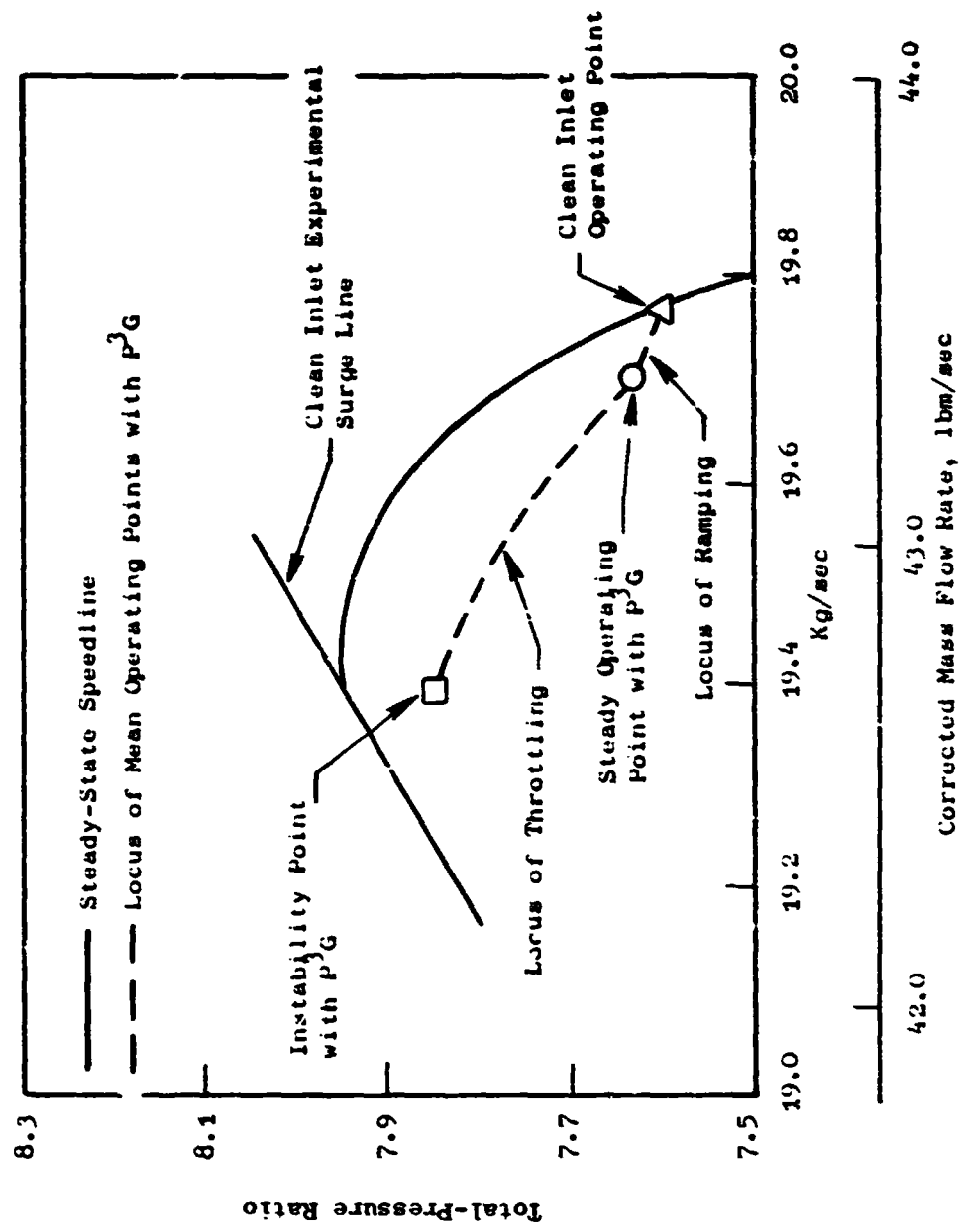
Figure 36. J85-13 Compressor Instability Point with Inlet Planar Wave Distortion, f_{P^3G} = 300Hz, $\Delta Pt/Pt)_{IGV}$ = .099.
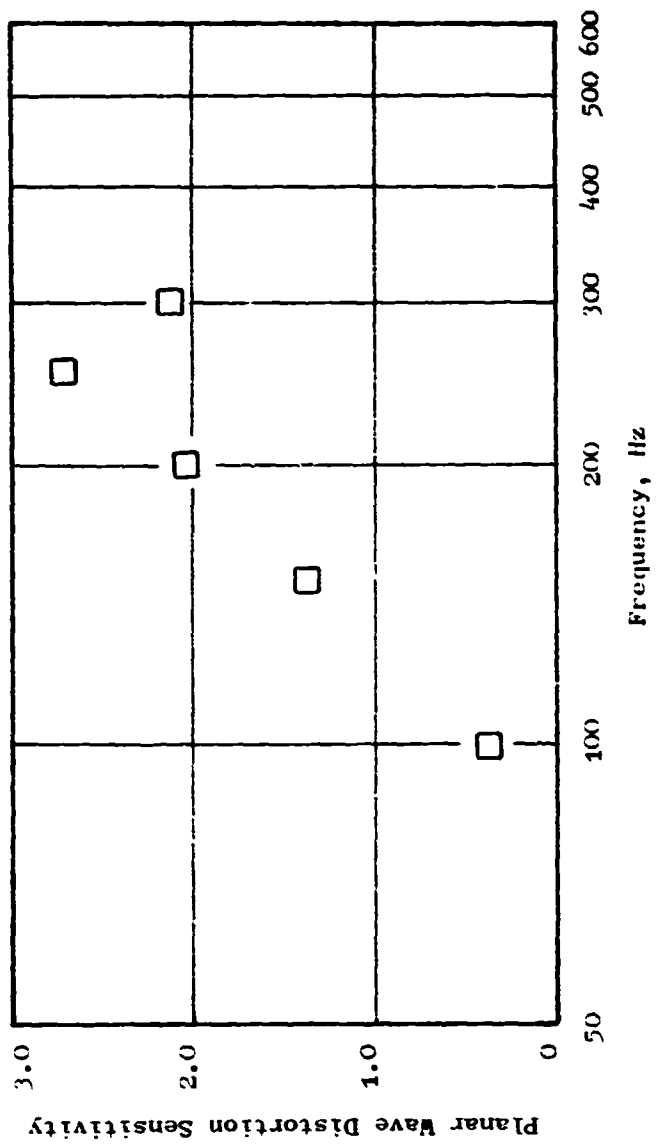
Figure 37. Planar Wave Distortion Sensitivity at 100% Speed.
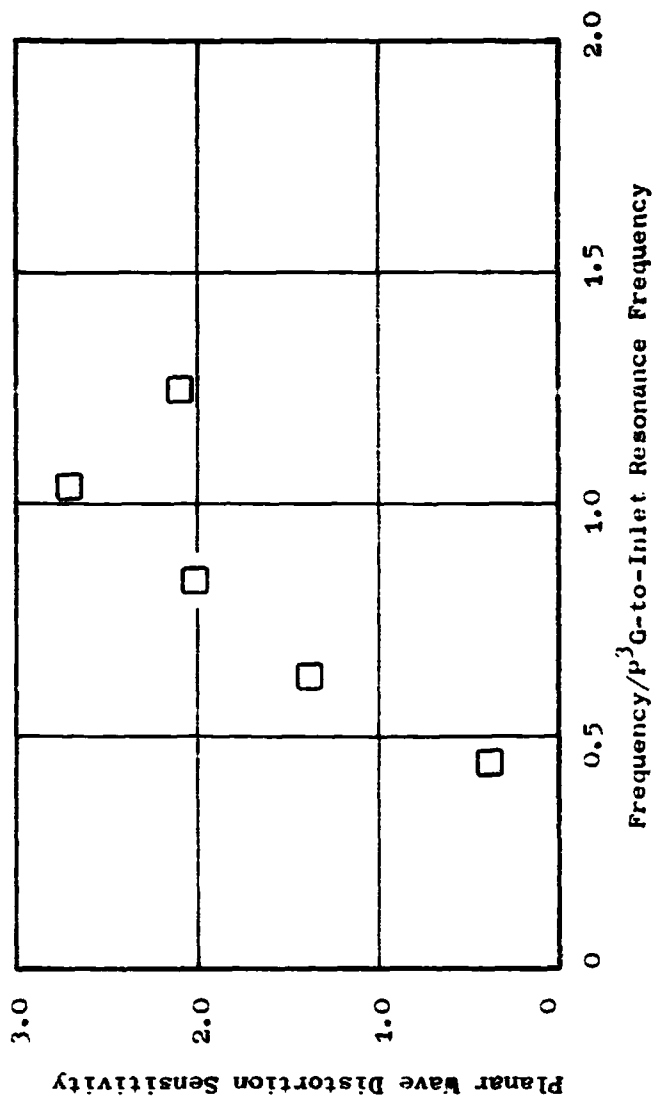
Figure 38. Planar Wave Distortion Sensitivity as a Function of Reduced Frequency.

of the P^3G, respectively (59 total); whereas 79 volumes were used to describe the entire system in the time-dependent analysis. These modifications to the geometry were necessary because of the limited memory capacity of the available computer and exponential overflow and underflow in evaluating the characteristic equation of a large size matrix.

For the section ahead of the P^3G, the analysis was conducted for the frequencies ranging from 10 to 600 Hz. The average length of the volumes describing this section was 4 inches. Therefore, 600 Hz was the maximum frequency at which the model can be expected to yield reasonably accurate response characteristics. The frequency range for the region aft of the P^3G was from 10 to 1000 Hz.

The boundary conditions for the bellmouth-to-P^3G system were: 1) Constant total pressure and total temperature at the bellmouth, and 2) Oscillating flow function at the P^3G. In an actual engine test, the entire test setup or the bellmouth is placed in a large plenum. Usually, the total pressure and total temperature of the plenum are not affected by the operation of the engine. Therefore, the constant total-property condition was employed as the inlet boundary conditions. The P^3G is considered as a device that primarily oscillates the mass flow rate. However, the DSP program does not allow fluctuating the exit flow. Thus, an approximation of the actual boundary condition, i.e. oscillating flow function, was introduced at the exit. The frequency analysis based upon this approximate exit boundary condition may yield amplitudes and phase angles which differ from the actual values, whereas, it should give correct resonance frequency and locations of nodal points. Consequently, the results of the frequency analysis for the section ahead of the P^3G should be used only in studying the frequency response trend.

The boundary conditions for the P^3G-to-combustor exit system were: 1) Oscillating flow at the P^3G, and 2) Constant flow function at the combustor exit. As stated previously, the P^3G oscillates the mass flow rate. Therefore, oscillating flow was introduced as the inlet boundary condition. During the actual operation of a gas turbine engine, the turbine diaphragm is choked due to high pressure and high temperature of the combustor gas. This choked condition was simulated by assigning the constant flow function to the combustor exit plane. These two boundary conditions correctly describe the actual physical conditions at the respective planes. Therefore, the resultant frequency analysis for the section aft of the P^3G will be exact within the accuracy of computation.

Prior to performing the analysis at various frequencies, the frequency response characteristics for the section aft of the P^3G at 100 Hz were compared with those obtained from the time-dependent analysis to verify the

81

validity of the DSP program. The time-dependent analysis was performed with less than 0.5% IGV total-pressure variation about the mean value to approximate the small perturbation condition of the linearized analysis. The comparison shows that the static pressure response in the duct between the P^3G and the IGV of the compressor computed by the two different methods agrees well in amplitude, Figure 39, as well as in phase angle, Figure 40. The amplitudes calculated by the DSP program differ from those obtained by the time-dependent analysis by less than 10% at all locations. The phase angles show a closer agreement. Therefore, it is concluded that the linearized analysis technique can be employed successfully in evaluating the resonance frequency, nodal points, etc. of a compression system such as the J85-13/P^3G.

A similar comparison and the resultant excellent agreement between the linearized analysis and the time-dependent analysis in evaluating the frequency response characteristics of the J85-13 engine are presented in Reference 4. Therefore, they are not discussed here.

Subsequently, the frequency response analysis for the two sections were performed at the frequencies stated previously. Some of the results are summarized in Figures 41 through 48. The remaining results are presented in Appendix D. The results show that the dominant resonance frequency of the P^3G-to-combustor exit system is approximately 230 Hz, Figure 41. This value is equivalent to the resonance frequency of the duct between the P^3G and the first rotor of the compressor evaluated according to the closed-closed formula for organ pipes. Figure 42 shows that the bellmouth-to-P^3G system has pressure response peaks at about 31, 90, 150, 210, 250, and 280 Hz. Note that 31 Hz is the fundamental resonance frequency of the bellmouth-to-P^3G system and 90, 150, 210, and 280 Hz are approximately equal to the odd harmonics of the open-closed system. It is believed that 250 Hz is associated with another open-closed system within the bellmouth-to-P^3G section. This subsystem is defined by the geometry between the second strut and the P^3G, see Figures 1 and 10.

Figures 43 through 48 present the results of the nodal analysis for the two sections of the J85-13/P^3G test installation at different frequencies.

4.3 VERIFICATION STUDY OF THE EXPLICIT ANALYTICAL SURGE CRITERIA

The analytical surge criteria derived in Subsection 3.5 were tested with the "Moss" and "Mehalic" configurations of the J85 engine. The criteria yielded instability points slightly beyond the experimental surge line for both engines at 100% speed. However, these criteria were ineffective at low speeds for both configurations of the engine. It is believed that the

82
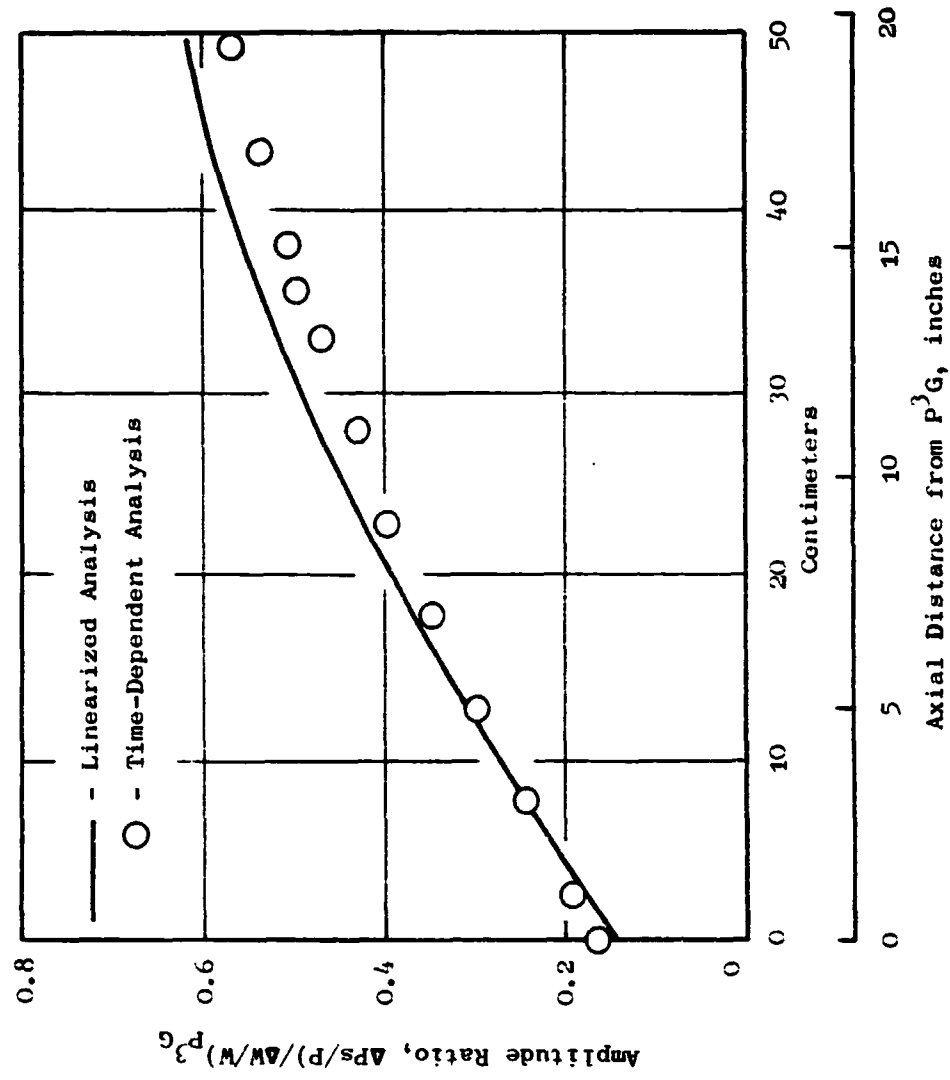
Figure 39. Comparison of Amplitudes Obtained by Two Different Methods.

83
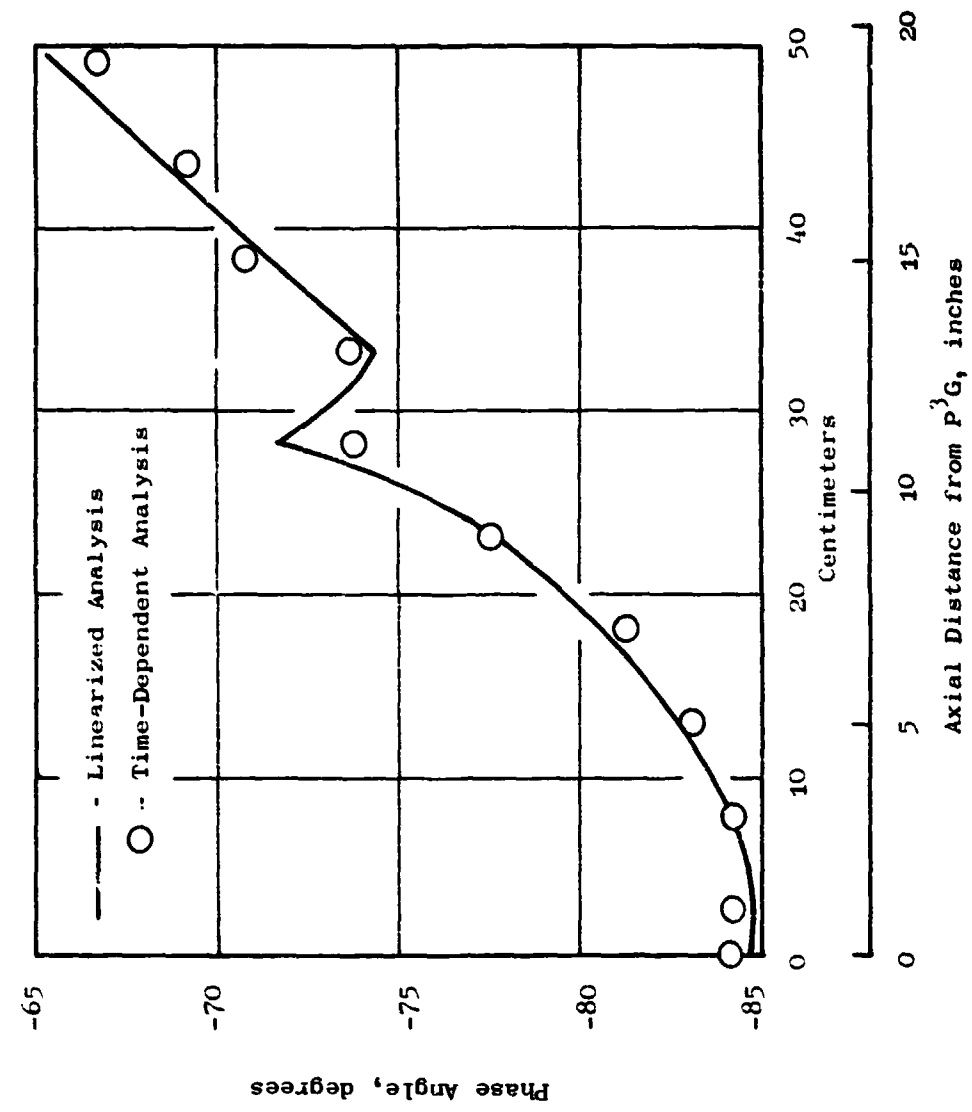
Figure 40. Comparison of Phase Angles Obtained by Two Different Methods.

84
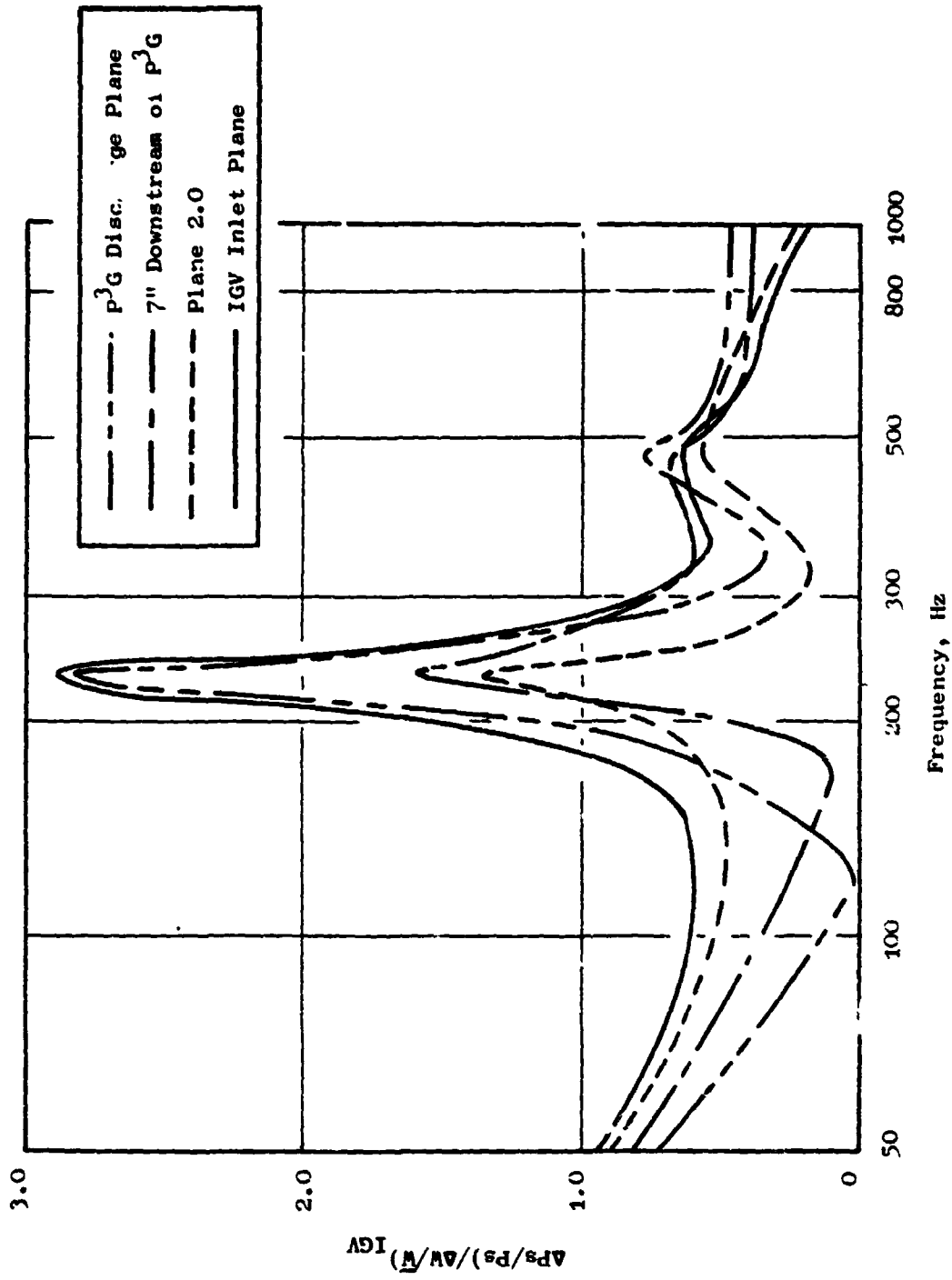
Figure 41. Static Pressure Frequency Response to P^3G Flow Oscillation, P^3G-to-IGV.
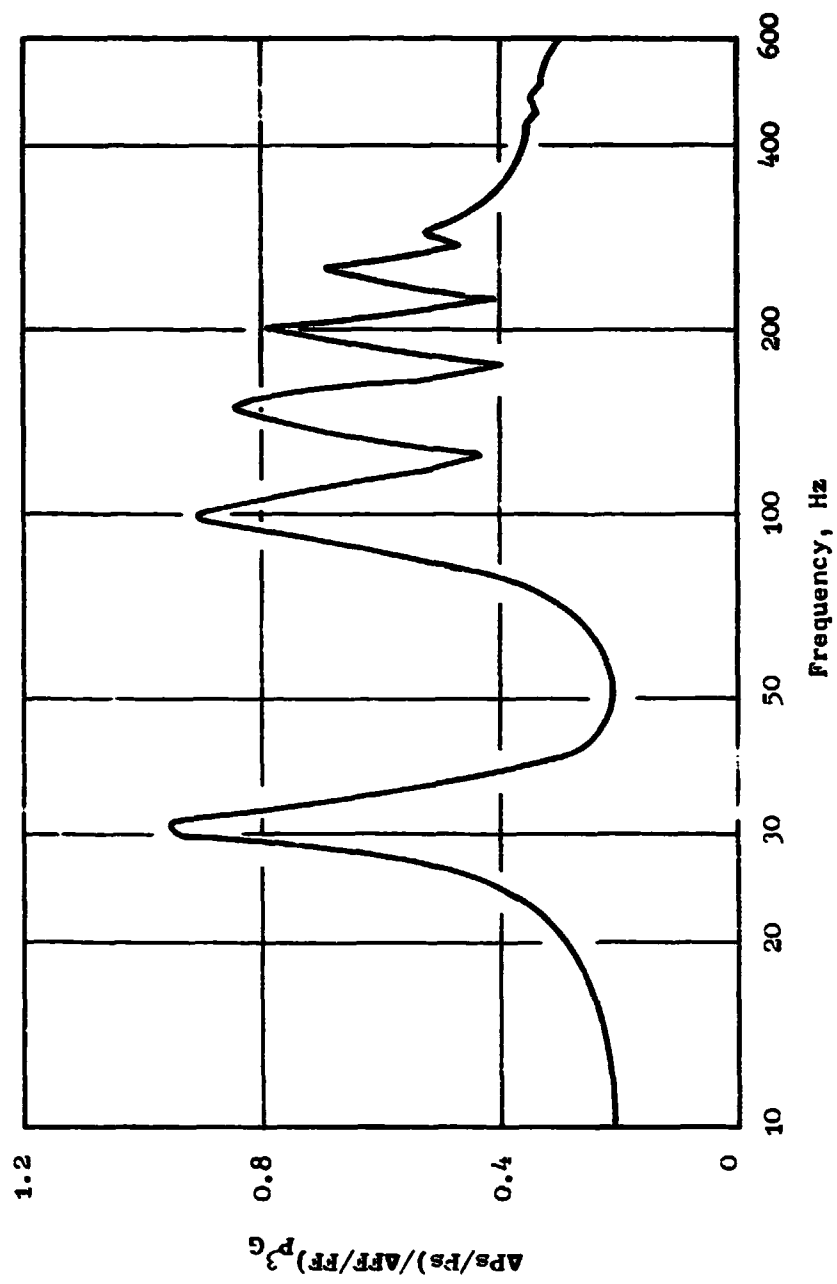
Figure 42. Static Pressure Frequency Response to P^3G Flow Function Oscillation, Bellmouth-to-P^3G.
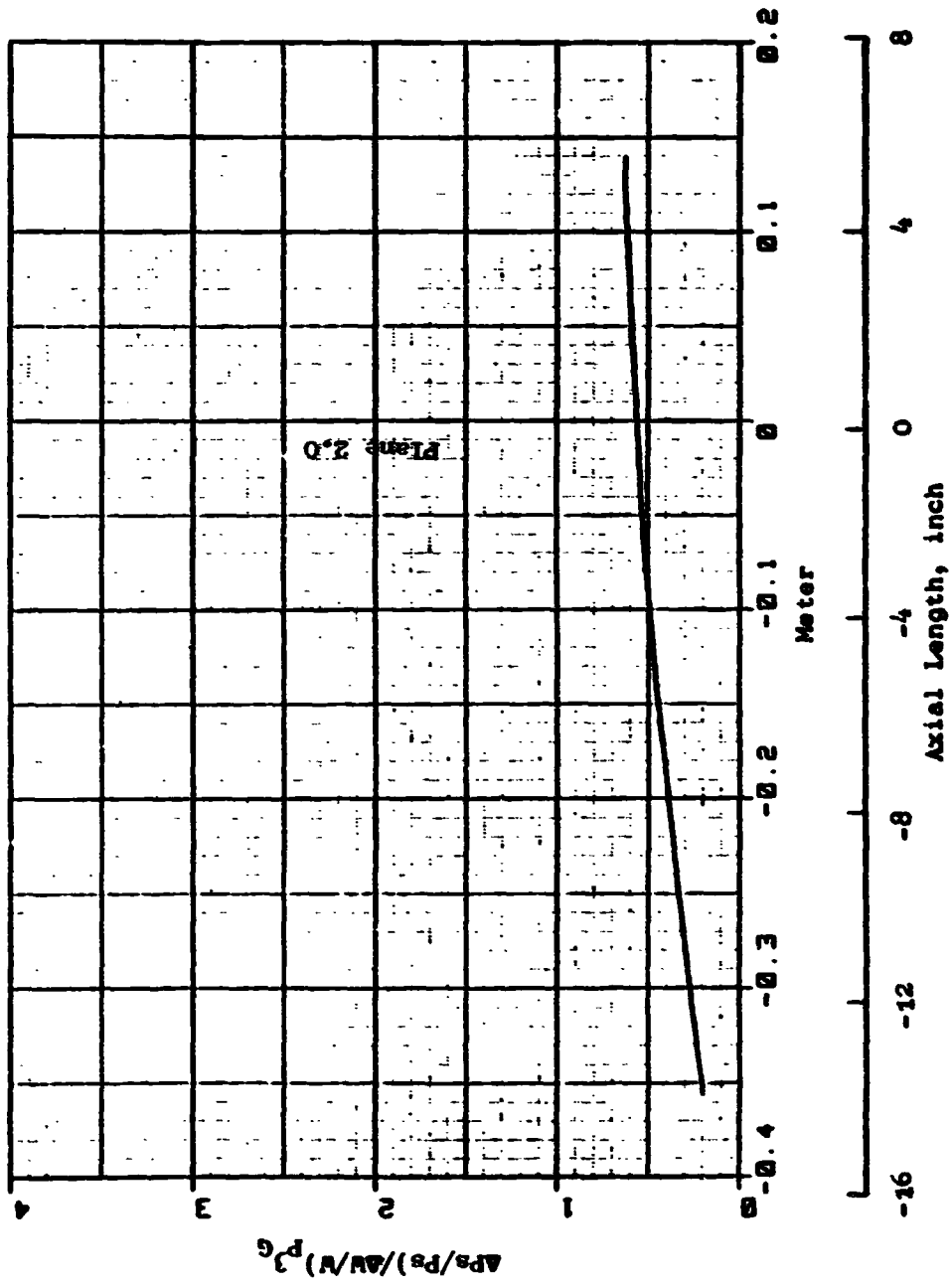
Figure 43. Result of Nodal Analysis at f_{p^3G} = 100Hz, P^3G-to-IGV.
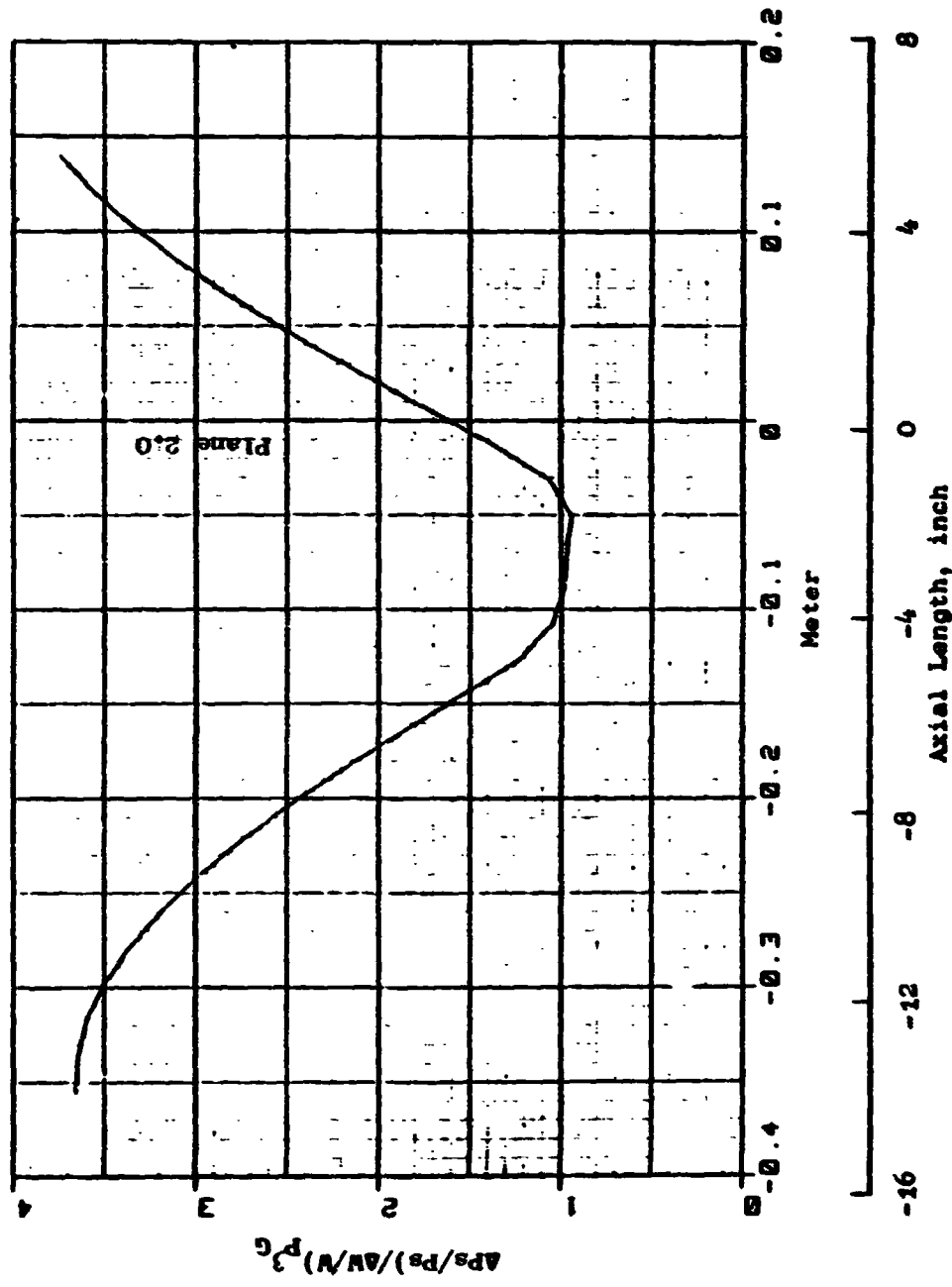
Figure 44. Result of Nodal Analysis at $f_{p^3_G} = 250Hz$, p^3G-to-IGV.
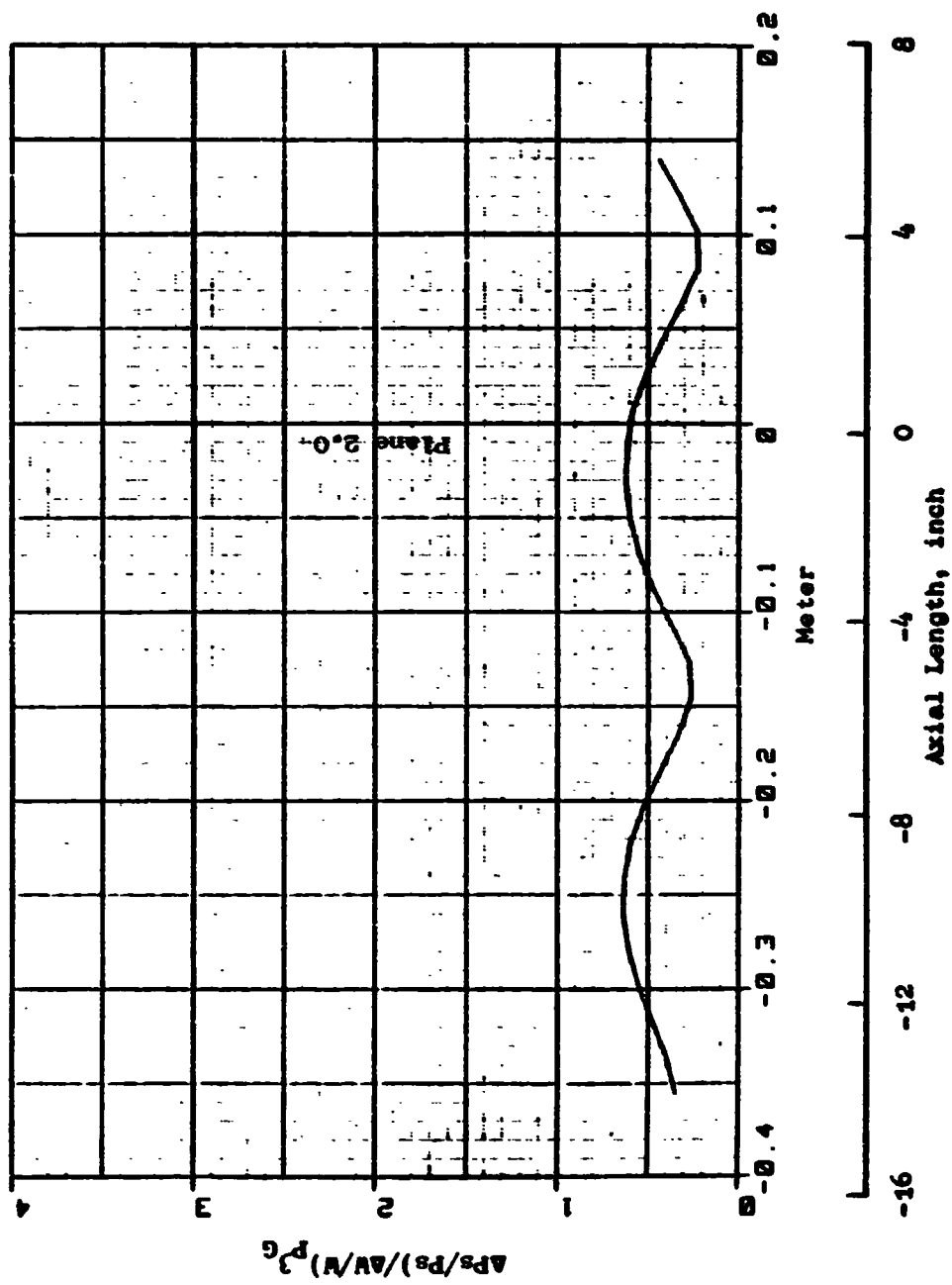
Figure 45. Result of Nodal Analysis at f_{P^3G} = 600Hz, P^3G-to-IGV.
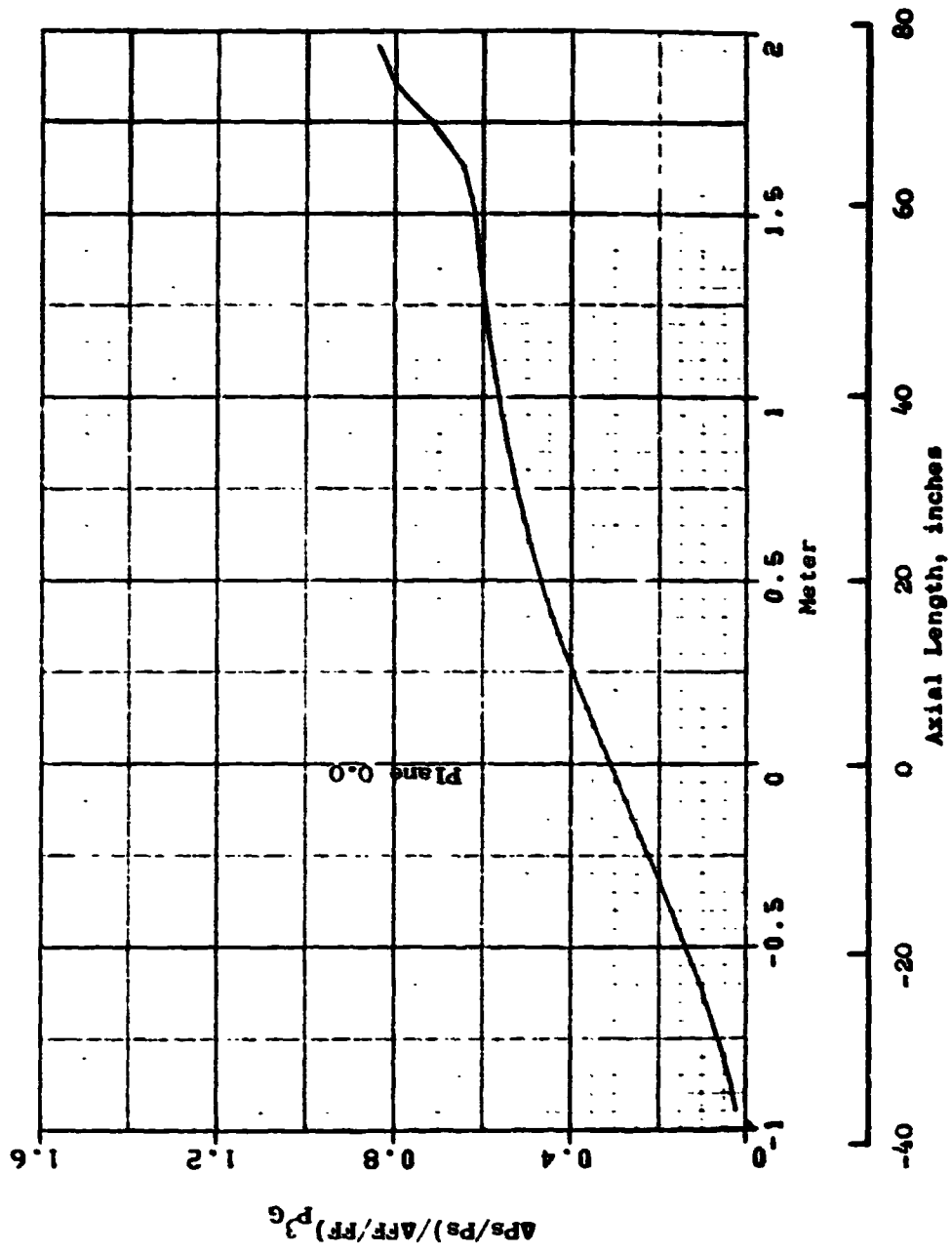
Figure 46. Result of Nodal Analysis at $f_{P^3_G} = 30Hz$, Bellmouth-to-P^3G.
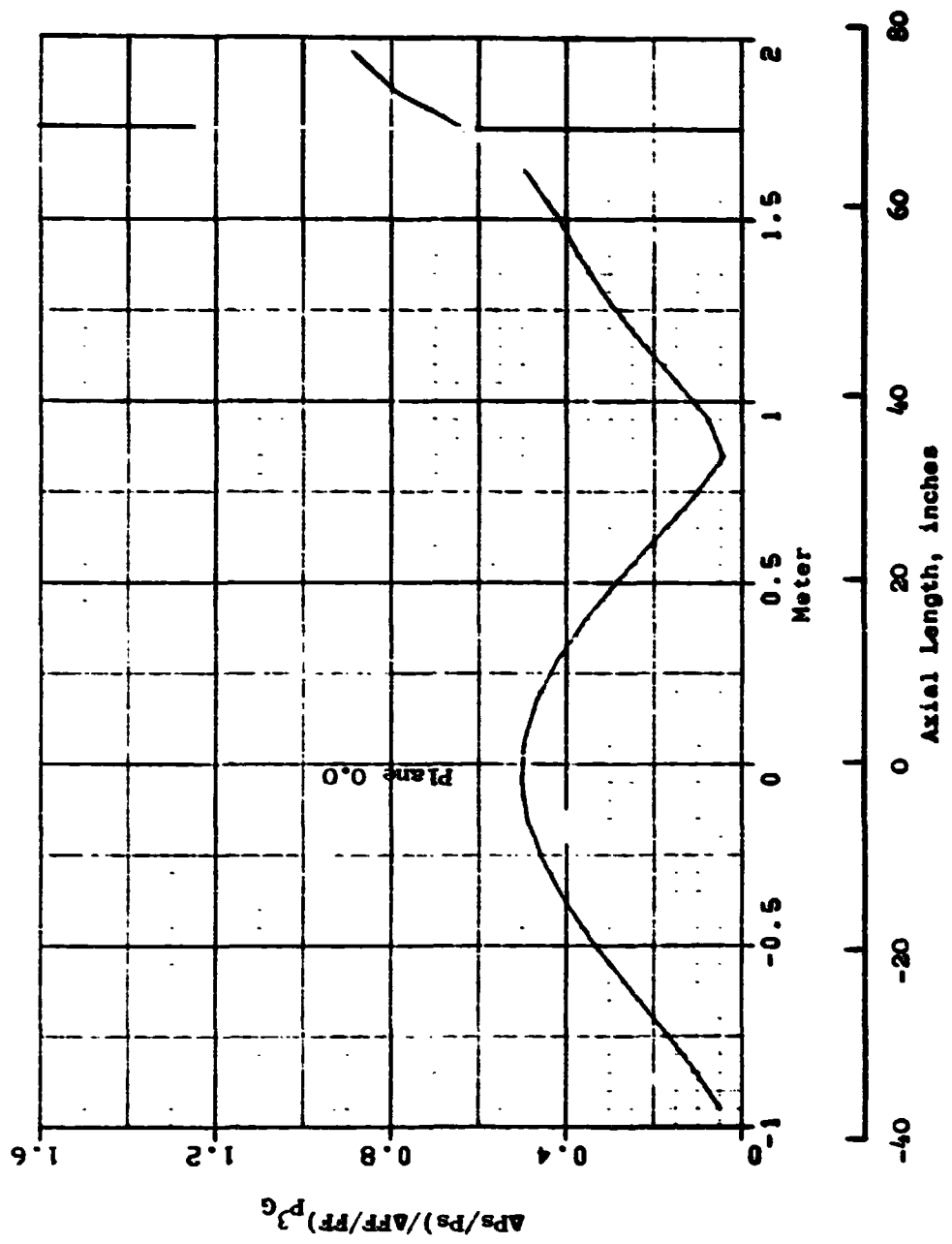
Figure 47. Result of Nodal Analysis at $f_{P_3^'G} = 100$Hz, Bellmouth-to-$P_3^'$G.

91
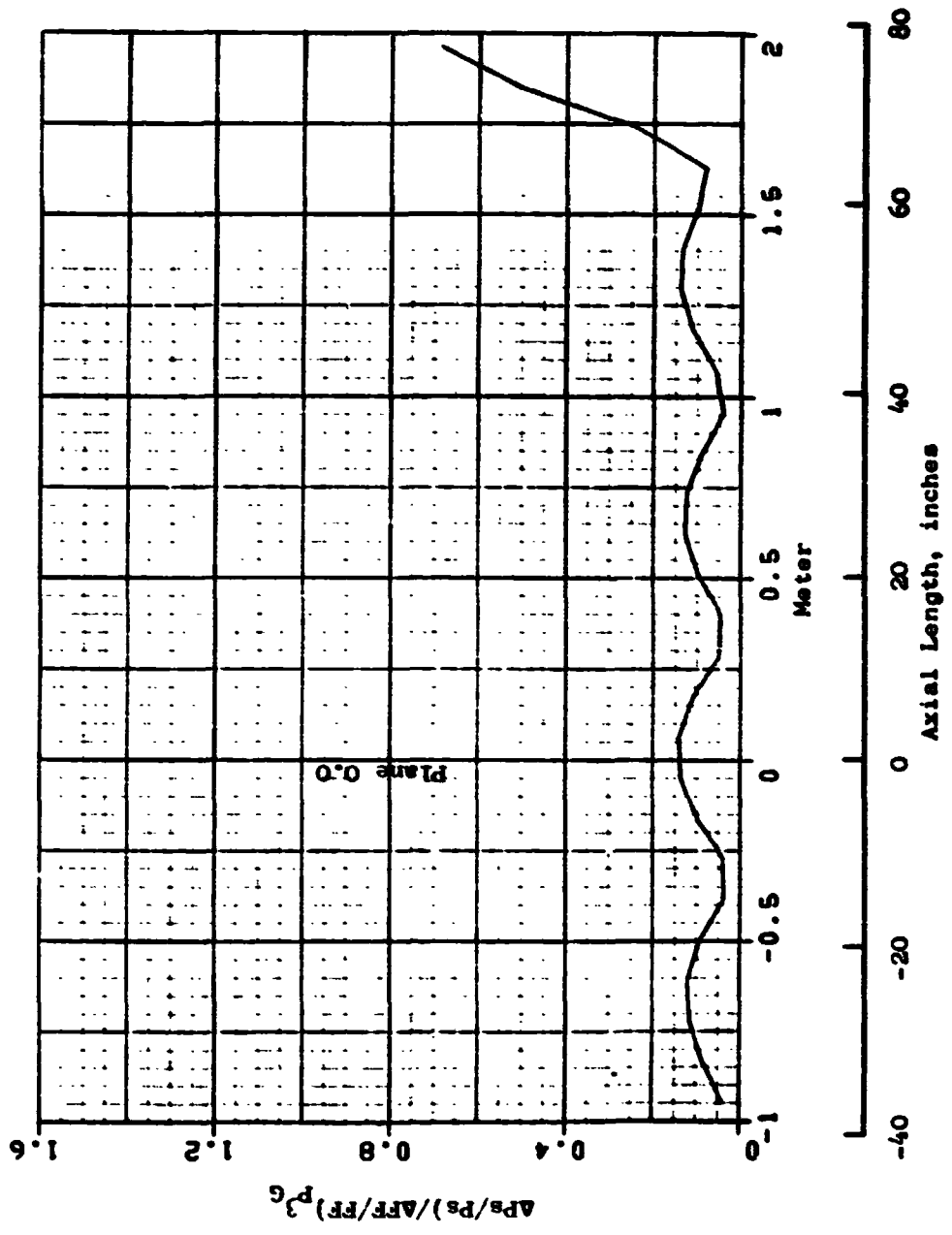
Figure 48. Result of Nodal Analysis at f_{p^3G} = 250Hz, Bellmouth-to-p^3G.

92

ineffectiveness of the criteria at low speeds is mostly due to the inadequate boundary condition employed at the rotor exit. It was assumed that the flow function at each rotor exit is constant. This assumption is adequate at 100% spe⅃ since the corrected flow rate does not change significantly along the speed line; thus, the relative Mach number of flow at the exit of each rotor is almost constant. However, this boundary condition is inappropriate at low speeds since the corrected flow rate and consequently, the relative Mach number changes significantly as the operating point migrates along a speed line.

Figure 49 presents the instability point of the "Moss" engine at 100% speed as computed by the explicit analytical stability criteria along with the stability limits determined by other methods. Figure 50 is a similar plot for the "Mehalic" engine. The occurrence of the instability was indicated by the second inequality, Equation 76, of the criteria; the first criterion, Equation 75, was satisfied even when the second criterion indicated an instability. The second criterion contains the slopes of the blade characteristics, ω', δ and β_c, see Appendix A. It is believed that these slopes play an important role in the stability of the compressor and thus, the instability was indicated more readily by the second inequality. For both engines, the instability occurred at the first rotor only.

A critique of the explicit analytical stability criteria is presented through a discussion of the three major assumptions employed in their derivation. These assumptions are:

1) The flow is homentropic.

2) At each rotor exit, the flow function is constant, and

3) The stability of the entire compressor can be determined by examining the stability of individual rotors.

The first assumption was introduced to simplify the derivation and thus, the resultant criteria. This condition allows one to write Equation 69, Subsection 3.5, as a 2 x 2 matrix instead of a 3 x 3 matrix since the energy equation vanishes. Also, the characteristic equation, Equation 74, is reduced to a quadratic equation from a cubic equation. Consequently, derivation of the criteria becomes simpler. It was assumed that the variation of the entropy has an insignificant influence on the compressor instability. However, it is clear that the exclusion of the entropy as a parameter does not allow the criteria to detect any instabilities that may be indicated by the violation of the second law of the thermodynamics.

Introduction of the second assumption as a boundary condition was discussed before. It was stated that this assumption is quite valid at high
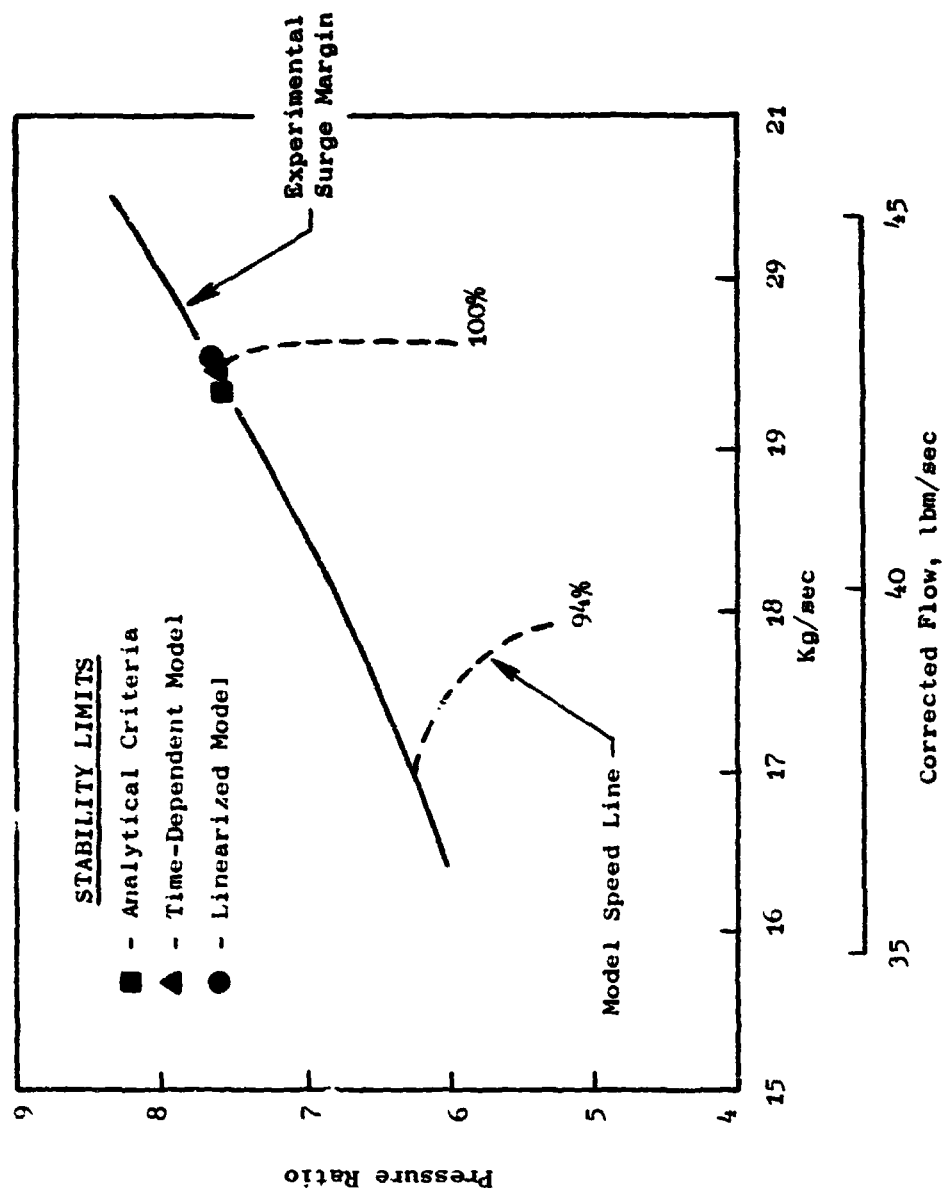
Figure 49. Stability Limits of J85-13 "Moss" Engine Computed by Different Methods.
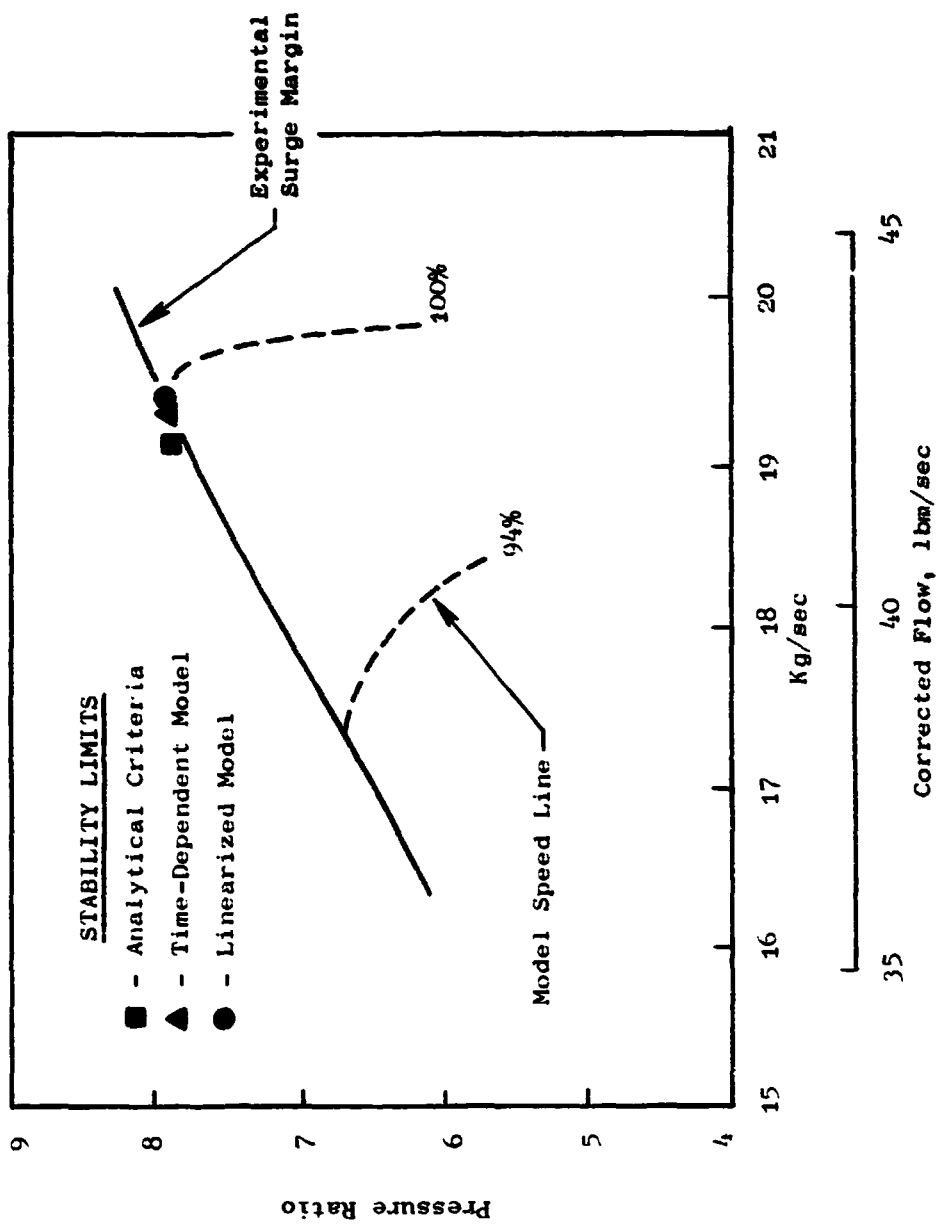
Figure 50. Stability Limits of J85-13 "Mehalic" Engine Computed by Different Methods.

speed; however, it is not nearly so valid at low speed. The inadequacy of this boundary condition at low speeds is demonstrated clearly by the fact that no instability point was predicted by the criteria at these speeds.

The third assumption was introduced also to simplify the explicit criteria. If the criteria are applied to the entire compressor, the characteristic equation of a large size matrix should be evaluated and consequently, derivation of explicit stability criteria will be extremely difficult, if not impossible. The stability criteria for each rotor volume, however, cannot account for the interaction of the instability of other rotor volumes with that of the rotor volume under consideration.

The feasibility of employing explicit analytical stability criteria to predict the instability was demonstrated. This was accomplished by obtaining the instability points of two different configurations of the J85 engine at 100% speed that agree well with the experimentally determined stability limits. However, it is believed that a further investigation, and ensuing improvements, of the analytical stability criteria is necessary to obtain more reliable stability predictions at all operating conditions of a compressor. This investigation should include: 1) Introduction of the energy equation in the form of entropy change into the derivation of the criteria to account for the possible violation of the second law of the thermodynamics at the instability limits, and 2) Development of boundary conditions or other techniques that allow for a stronger interaction of compressor stages in evaluating stability. In addition, it is desirable to explore the possibility of obtaining stability criteria through a completely new approach such as a parametric study that relates the occurrence of instability to the geometric and aerodynamic parameters of a compressor.

5.0 CONCLUSIONS AND RECOMMENDATIONS

The main objective of this program was to develop a computer simulation program that is capable of modelling the operation of the J85-13 Planar Pressure Pulse Generator test installation. This task was accomplished successfully by modifying an existing computer program that was developed to simulate a test installation, called the F101 Fan/P^3G, similar to the J85-13/P^3G. This conclusion is supported by the following specific a.complishments:

1) An expression for the unsteady-lift force was developed and added to the existing program to improve the modelling of the unsteady aerodynamic behavior of compressor blades,

2) The modified program was validated through a comparison of the simulation results with the experimental data obtained during the F101 Fan/P^3G test,

3) The simulation program was utilized successfully in modelling operating point excursions of the J85-13 engine about a stationary mean operating point. The model was stable over a wide range of P^3G frequencies and amplitudes, and

4) The J85-13 engine was then throttled to the stability limits and the planar wave distortion sensitivity of the engine was determined at various P^3G frequencies. The instability points were identified by a consistent pattern of the model behavior, i.e., a rapid departure of the mean operating point from a well-behaved path.

As supported by the items listed in the preceding paragraph, the J85-13/P^3G simulation program was developed successfully and its validity was verified. However, due to lack of proper interstage and over-the-rotor test data, the validation of using the unsteady-lift force for the description of the unsteady aerodynamic behavior of compressor blades was indirect, i.e., through a comparison of the analytical and experimental pressure waveforms in the ducts ahead and aft of the F101 fan. Therefore, it is recommended that these types of test data be taken during the future J85-13/P^3G test and be utilized for the direct validation of the simulation technique. Such experimental data will be useful also in refining the expression for the unsteady-blade-lift force as well as in evaluating the constants contained in the expression.

The frequency response characteristics of the J85-13/P^3G test apparatus were determined in support of selecting instrumentation locations.

97

The fundamental resonance frequencies of two subsystems of the test instal-
lation, i. e., bellmouth-to-P^3G and P^3G-to-combustor exit, were identified.
The nodal analyses of the two subsystems were performed as well.

In addition, the feasibility of employing a set of explicit analytical
criteria in evaluating the stability of an axial compressor was investigated.
These criteria successfully yielded the instability points for two different
configurations, "Moss" and "Mehalic", of the J85-13 compressor at 100%
speed. However, they were ineffective at lower speeds. It is believed that
this was mainly due to the boundary conditions whose validity was weakened
at lower speeds. The following items are recommended to improve the
explicit analytical stability criteria.

1) Development of new boundary conditions that describe the actual
aerodynamics more accurately at low speeds,

2) Development of a new technique that permits a proper coupling of
stages in determining the instability,

3) Addition of entropy as a parameter to account for the possible
violation of the second law of thermodynamics of instability
points, and

4) Feasibility study of alternative approaches for the derivation of the
stability criteria. One of such approaches is a parametric study
that relates the occurrence of instability to the geometric and
aerodynamic characteristics of a compressor. This approach may
yield an independent set of criteria as well as serve as a means of
enhancing and simplifying the existing criteria.

98

APPENDIX A

Derivation of Explicit Analytical Surge Criteria

In this appendix, the relationships used in the explicit analytical criteria (see Sub-section 3.4) are derived.

The governing equations for the homentropic flow of a compressible fluid through a compression system are given in volume-averaged form as,

$$\frac{\partial \bar{\rho}}{\partial t} = f_1 = \frac{1}{V}\left[W_1 - W_2 \right] \qquad \text{(A-1)}$$

$$\frac{\partial \bar{W}}{\partial t} = f_2 = \frac{g_c}{L}\left[\frac{W_1^2}{g_c \rho_1 A_1} - \frac{W_2^2}{g_c \rho_2 A_2} + P_1 A_1 - P_M(A_1 - A_2) + F_z \right]$$

$$= \frac{g_c}{L}\left[\frac{W_1^2}{g_c \rho_1 A_1} - \frac{W_2^2}{g_c \rho_2 A_2} + A_e (P_1 - P_2) + F_z \right] \qquad \text{(A-2)}$$

where

$$P_M = \frac{1}{3}P_1 + \frac{2}{3}P_2 \qquad \text{(A-3)}$$

$$A_e = \frac{2}{3}A_1 + \frac{1}{3}A_2 \qquad \text{(A-4)}$$

For this nonlinear system, the stability criteria are given as

$$(1)\ \frac{\partial f_1}{\partial \rho_1} + \frac{\partial f_2}{\partial W_2} \ < \ 0 \qquad \text{(A-5)}$$

$$(2)\ \frac{\partial f_1}{\partial \rho_1} \frac{\partial f_2}{\partial W_2} \ > \ \frac{\partial f_1}{\partial W_2} \frac{\partial f_2}{\partial \rho_1} \qquad \text{(A-6)}$$

where the partial derivatives are

$$\frac{\partial f_1}{\partial \rho_1} = \frac{1}{V}\frac{\partial W_1}{\partial \rho_1} \qquad \text{(A-7)}$$

$$\frac{\partial f_1}{\partial W_2} = - \frac{1}{V} \tag{A-8}$$

$$\frac{\partial f_2}{\partial \rho_1} = \frac{g_c}{L} \left[\frac{1}{g_c \rho_1 A_1^2} (2W_1 \rho_1 \frac{\partial W_1}{\partial \rho_1} - W_1^2) + A_e \frac{\partial P_1}{\partial \rho_1} + \frac{\partial F_z}{\partial \rho_1} \right] \tag{A-9}$$

$$\frac{\partial f_2}{\partial W_2} = \frac{g_c}{L} \left[\frac{-1}{g_c f_z A_2^2} (2W_2 \rho_2 - W_2^2 \frac{\partial \rho_2}{\partial W_2}) - A_e \frac{\partial P_2}{\partial W_2} + \frac{\partial F_z}{\partial W_2} \right] \tag{A-10}$$

The partial derivatives in the right-hand side of Equations A-7 through 10 are derived below.

Derivation of $\dfrac{\partial P_1}{\partial \rho_1}$

The relation between pressure and density for an isentropic process of a perfect gas is

$$P_1 = C \rho_1^\gamma \tag{A-11}$$

where C is a constant. Thus, the partial derivative, $\dfrac{\partial P_1}{\partial \rho_1}$ can be written as

$$\frac{\partial P_1}{\partial \rho_1} = C \gamma \rho_1^{\gamma-1} \tag{A-12}$$

$$= \gamma P_1 / \rho_1$$

Derivation of $\dfrac{\partial W_1}{\partial \rho_1}$

The mass flow rate, W_1, can be expressed in terms of density and velocity as

$$W_1 = \rho_1 A_1 C_{z1} \tag{A-13}$$

where A_1 is the area and C_{z1} is the axial velocity.
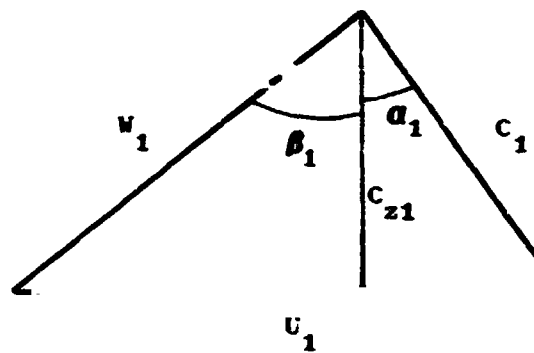
Figure A-1. Rotor Inlet Velocity Diagram.

Substitution of the relationship, $C_{z1} = C_1 \cos\alpha_1$, Figure A-1, into Equation A-13 gives

$$W_1 = \rho_1 A_1 C_1 \cos\alpha_1 \tag{A-14}$$

$\cos\alpha_1$ in Equation A-14 is independent of the density, ρ_1. Therefore, the partial derivative of W_1 with respect to ρ_1 becomes

$$\frac{\partial W_1}{\partial \rho_1} = \frac{W_1}{\rho_1} + W_1 \frac{\partial \ln C_1}{\partial \rho_1} \tag{A-15}$$

The absolute velocity, C_1 in Equation A-14 can be expressed as

$$C_1 = M_1 \sqrt{\gamma P_1 \cdot \rho_1} \tag{A-16}$$

and thus

$$\frac{\partial \ln C_1}{\partial \rho_1} = \frac{1}{2} \left[\frac{\partial \ln M_1^2}{\partial \rho_1} + \frac{\partial \ln P_1}{\partial \rho_1} - \frac{1}{\rho_1} \right] \tag{A-17}$$

For an isentropic flow, the density ratio is

$$\frac{\rho_{t1}}{\rho_1} = \left(1 + \frac{\gamma-1}{2} M_1^2\right)^{\frac{1}{\gamma-1}} \tag{A-18}$$

Thus, the derivative $\partial \ln M_1^2 / \partial \rho_1$ becomes

$$\frac{\partial \ln M_1^2}{\partial \rho_1} = -\frac{2}{\rho_1 M_1^2}\left(1 + \frac{\gamma-1}{2} M_1^2\right) \tag{A-19}$$

Substitution of Equation A-19 and the isentropic relation

$$\frac{\partial \ln P_1}{\partial \rho_1} = \frac{\gamma}{\rho_1} \tag{A-20}$$

into Equation A-17 yields

$$\frac{\partial \ln C_1}{\partial \rho_1} = -\frac{1}{\rho_1 M_1^2} \tag{A-21}$$

Subsequent introduction of this relationship into Equation A-15 gives

$$\frac{\partial W_1}{\partial \rho_1} = \frac{W_1}{\rho_1 M_1^2}(M_1^2 - 1) \tag{A-22}$$

Derivation of $\dfrac{\partial P_2}{\partial W_2}$

The boundary condition at the exit of a rotor volume is given as

$$\frac{W_2 \sqrt{T_2}}{P_2} = C \tag{A-23}$$

where C is a constant.

103

Substitution of the isentropic relations

$$P_2 = C \rho_2^\gamma \qquad (A-24)$$

$$T_2 = C \rho_2^{\gamma-1} \qquad (A-25)$$

into Equation A-23 and rearrangement yields

$$\rho_2 = C W_2^{\frac{2}{\gamma+1}} \qquad (A-26)$$

Therefore, the partial derivative becomes

$$\frac{\partial \rho_2}{\partial W_2} = \frac{2}{\gamma+1} \frac{\rho_2}{W_2} \qquad (A-27)$$

Derivation of $\dfrac{\partial P_2}{\partial W_2}$
_____

Equation A-26 can be rewritten, with the aid of the relation given by Equation A-24, as

$$P_2 = C W_2^{\frac{2\gamma}{\gamma+1}} \qquad (A-28)$$

Therefore, the partial derivation of P_2 with respect to W_2 is

$$\frac{\partial P_2}{\partial W_2} = \frac{2\gamma}{\gamma+1} \frac{P_2}{W_2} \qquad (A-29)$$

Derivation of $\dfrac{\partial F_z}{\partial W_2}$
_____

The blade force, F_z, can be expressed in terms of the tangential force, F_T, and axial component of the drag force, F_{Dz}, as

$$F_z = F_T \tan\beta_\infty - F_{Dz} \qquad (A-30)$$

104

where the corrected-lift-direction angle, β_{∞}, and the drag force, F_{Dz}, are not a function of the exit independent variable, W_2. Therefore, the partial differentiation of F_z with respect to W_2 yields

$$\frac{\partial F_z}{\partial W_2} = \frac{\partial F_T}{\partial W_2} \tan \beta_{\infty} \tag{A-31}$$

From Euler's Turbine Equation, the tangential force is obtained as

$$F_T = \frac{1}{g_c (r_1 + r_2)} \left[\frac{r_2 W_2^2}{\rho_2 A_2} \tan \alpha_2 - \frac{r_1 W_1^2}{\rho_1 A_1} \tan \alpha_1 \right] \tag{A-32}$$

where r_1 and r_2 are the pitch-line radii at the inlet and exit of a rotor, respectively.
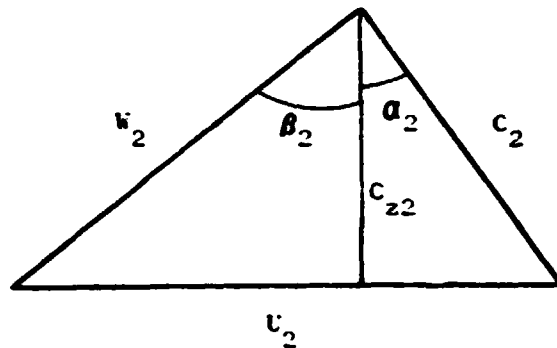
Figure A-2. Rotor Exit Velocity Diagram.

Introduction of the angular relationship, depicted in Figure A-2,

$$\tan \alpha_2 = \frac{U_2 \rho_2 A_2}{W_2} - \tan \beta_2 \tag{A-33}$$

enables one to rewrite Equation A-32 as

105

$$F_T = \frac{1}{g_c}\left[r_2 W_2 U_2 - \frac{W_2^2 r_2}{\rho_2 A_2}\tan\beta_2 - \frac{r_1 W_1^2}{\rho_1 A_1}\tan\alpha_1 \right] \qquad (A-34)$$

The third term in the right-hand side of Equation A-34 is independent of W_2. Further, the relative exit air angle, β_2, and the pitch-line blade speed, W_2, are also independent of W_2. Therefore, the partial derivative, $\partial F_T/\partial W_2$ becomes

$$\frac{\partial F_T}{\partial W_2} = \frac{2r_2}{g_c(r_1 + r_2)}\left[U_2 - \frac{2\gamma}{\gamma+1}\frac{W_2}{A_2\rho_2}\tan\beta_2 \right] \qquad (A-35)$$

Substitution of this relationship transforms Equation A-31 into

$$\frac{\partial F_z}{\partial W_2} = \frac{2r_2}{g_c(r_1 + r_2)}\left[U_2 - \frac{2\gamma}{\gamma+1}\frac{W_2}{A_2\rho_2}\tan\beta_2 \right] \qquad (A-36)$$

Derivation of $\dfrac{\partial F_z}{\partial\rho_1}$
_____

All the quantities in the right-hand side of Equation A-30 are a function of the density, ρ_1. Therefore,

$$\frac{\partial F_z}{\partial\rho_1} = \frac{\partial F_T}{\partial\rho_1}\tan\beta_\infty + F_T\frac{\partial\tan\beta_\infty}{\partial\rho_1} - \frac{\partial F_{Dz}}{\partial\rho_1} \qquad (A-37)$$

Derivation of the partial derivatives in Equation A-37 is lengthy and tedious. Therefore, only the results are presented here.

$$\frac{\partial F_T}{\partial\rho_1} = \frac{-2}{g_c(r_1 + r_2)A_1\rho_1 M_1^2}\left[\frac{A_1^2\rho_1 W_1^2}{A_2\rho_2 W_1}r_2 u_2 m_\delta\frac{1 + \tan^2\beta_1^*}{(1 + \tan\beta_1\tan\beta_1)^2} \right.$$

$$\left. \frac{1 + \tan^2\beta_2^*}{(1 - \tan\beta_2^*\tan\delta)^2} - \frac{W_1^2}{\rho_1}r_1(M_1^2 - 2)\tan\alpha_1 \right] \qquad (A-38)$$

106

$$\frac{\partial \tan\beta_{\infty}}{\partial \rho_1} = \frac{U_1 A_1}{W_1 M_1^2 \cos^2\beta_{\infty}} \left| \frac{1}{2} \cos^2\beta_1 + \frac{1 + \tan^2\beta_1^*}{(1 + \tan\beta_1^* \tan\beta_1)^2} \right.$$

$$\left. - \left[\frac{1}{2} m_\delta \cos^2\beta_2 \frac{1 + \tan^2\beta_2^*}{(1 - \tan\beta_2 \tan\delta)^2} + m_{\beta c} \cos^2\beta_c \right] \right| \tag{A-39}$$

$$\frac{\partial F_{Dz}}{\partial \rho_1} = \frac{\partial F_K}{\partial \rho_1} F_\beta + F_K \frac{\partial F_\beta}{\partial \rho_1} \tag{A-40}$$

$$\text{where } F_K = \frac{\gamma A_1}{2} \frac{\omega' P_1}{P_{t1}'} \left[M_1'^2 + \frac{M_1'^4}{4} + \frac{M_1'^6}{40} \right] \tag{A-41}$$

$$F_\beta = \cos^2\beta_1 + \sin\beta_1 \cos\beta_1 \tan\beta_\infty \tag{A-42}$$

$$\frac{\partial F_K}{\partial \rho_1} = F_K \left(\frac{\partial \ln\omega'}{\partial \rho_1} + \frac{\gamma}{\rho_1} + \frac{\partial \ln F_M}{\partial \rho_1} - \frac{\partial \ln P_{r1}}{\partial \rho_1} \right) \tag{A-43}$$

$$\frac{\partial \ln\omega'}{\partial \rho_1} = m_{\omega'} \left[\frac{U_1 A_1}{W_1 M_1^2} \frac{1 + \tan^2\beta_1^*}{(1 + \tan\beta_1^* \tan\beta_1)} \right] \tag{A-44}$$

$$\frac{\partial \ln F_M}{\partial \rho_1} = \frac{\left(1 + \frac{M_1'^2}{2} + \frac{3 M_1'^4}{40} \right)}{\left(1 + \frac{M_1'^2}{4} + \frac{M_1'^4}{40} \right)} \frac{\partial \ln M_1'^2}{\partial \rho_1} \tag{A-45}$$

$$\frac{\partial \ln M_1'^2}{\partial \rho_1} = \frac{1}{\rho_1 M_1^2} \left[(1 - \gamma) M_1^2 - 2 + \frac{2 A_1 U_1 \rho_1}{W_1} \cos^2\beta_1 \tan\beta_1 \right] \tag{A-46}$$

$$P_{r1} = (1 + \frac{\gamma - 1}{2} M_1'^2)^{\frac{\gamma}{\gamma - 1}} \tag{A-47}$$

107

$$\frac{\partial \ln P_{r1}}{\partial \rho_1} = \frac{\gamma}{2} \frac{M_1'^2}{(1 + \frac{\gamma-1}{2}M_1'^2)} \frac{\partial \ln M_1'^2}{\partial \rho_1} \qquad \text{(A-48)}$$

$$m_\omega' = \frac{d\omega'}{d\tan i} \qquad \text{(A-50)}$$

$$m_\delta = \frac{d\tan\delta}{d\tan i} \qquad \text{(A-51)}$$

$$m_{\beta_c} = \frac{d\tan\beta_c}{d\tan i} \qquad \text{(A-51)}$$

The slopes, m_ω', m_δ and m_{β_c}, of the blade characteristics are evaluated from the polynomial representatives of the loss coefficient, ω', the deviation angle, $\tan\delta$, and the lift-direction correction angle, $\tan\beta_c$. These polynomials as a function of $\tan i$ are discussed in Section 3.2.

APPENDIX B

Results of F101 Fan/P^3G Simulation
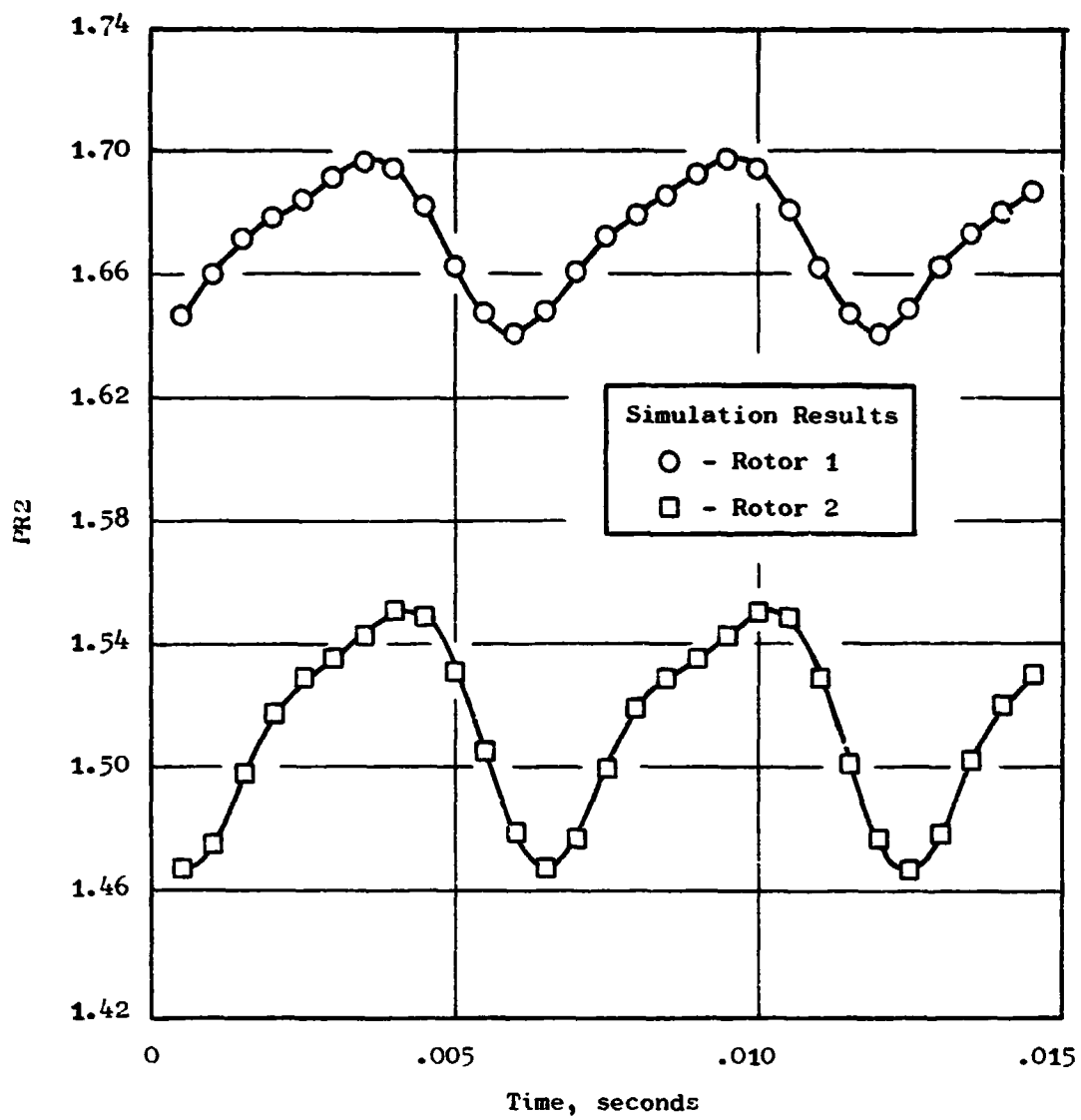
Figure B-1. F101-Fan Blade Row Total-Pressure Ratio as a Function of Time, 100% $N/\sqrt{\theta}$, f_{p^3G} = 42Hz.
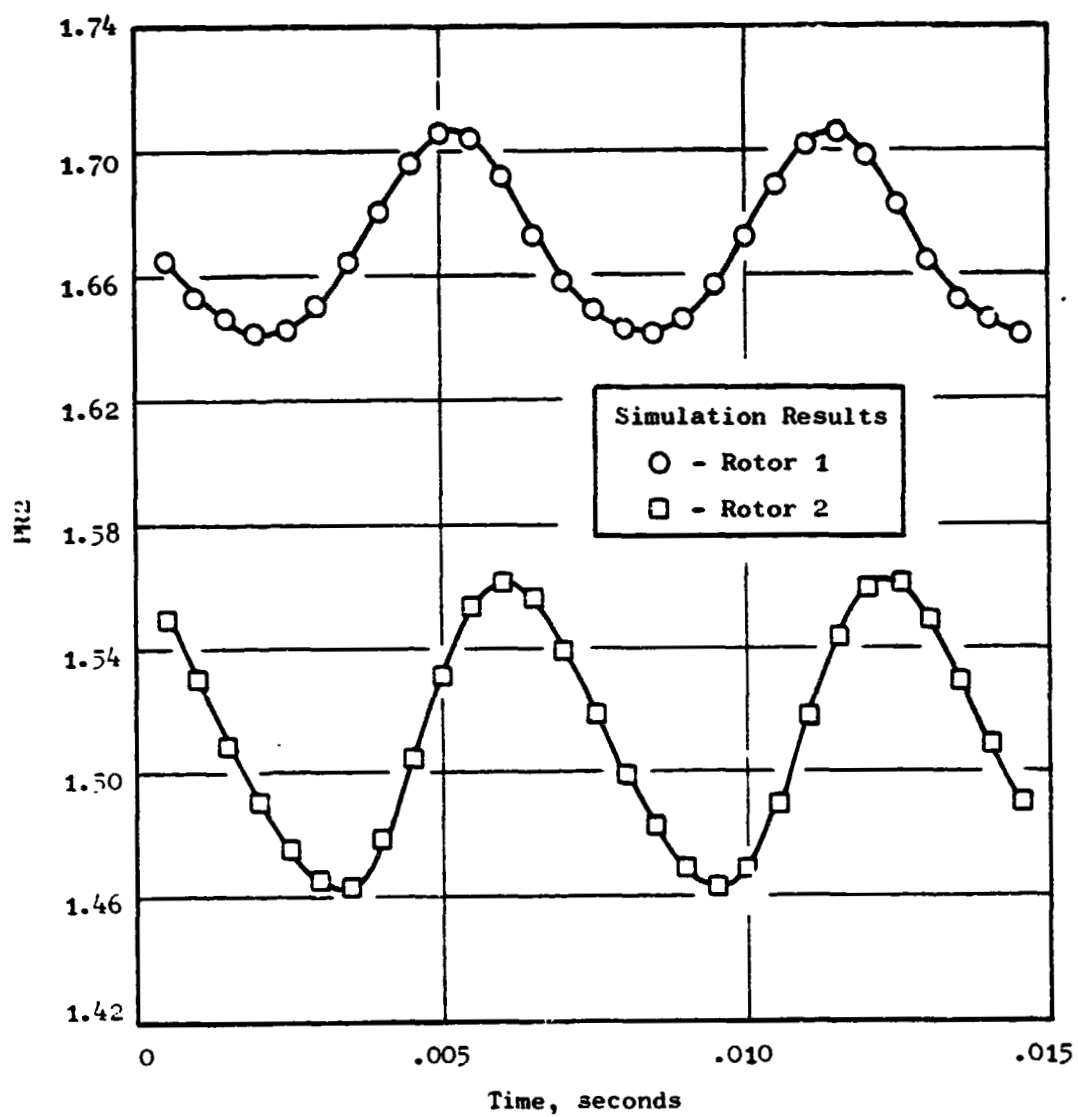
Figure B-2. F101-Fan Blade Row Total-Pressure Ratio as a Function of Time, 100% $N/\sqrt{\theta}$, $f_{P_G^3}$ = 80Hz.
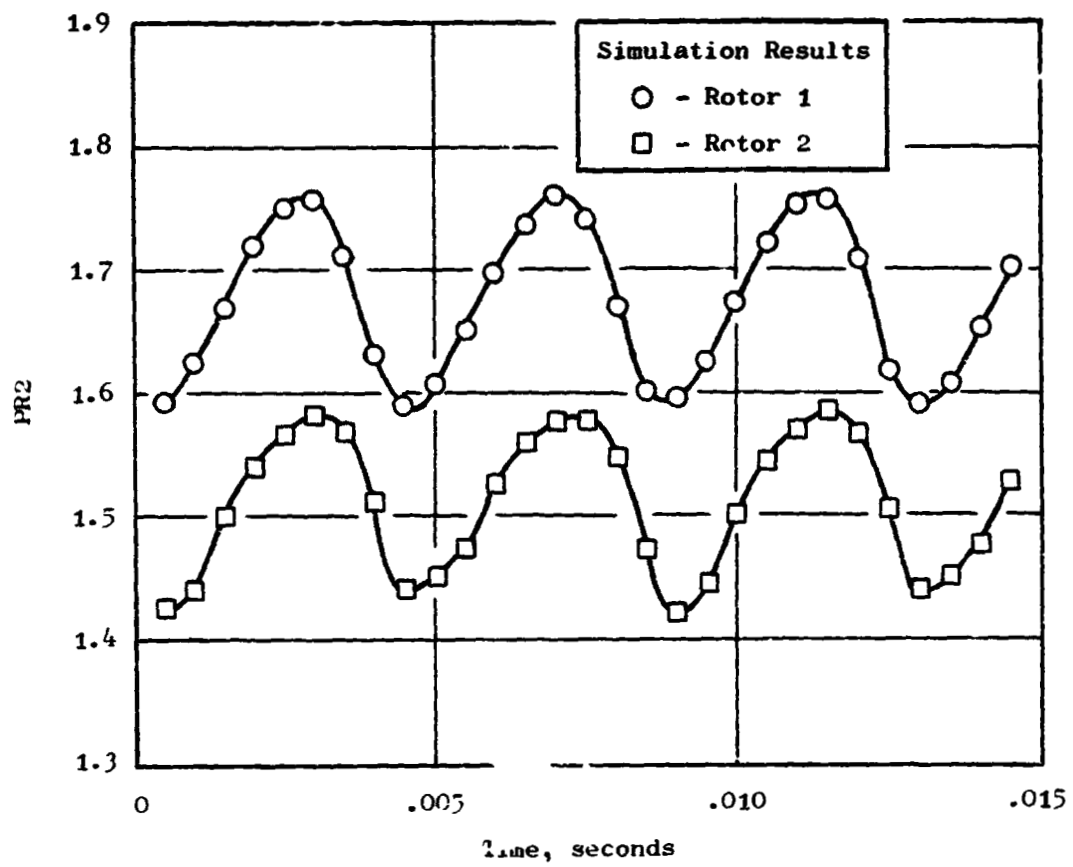
Figure B-3. F101-Fan Blade Row Total-Pressure Ratio as a Function of Time, 100% $N/\sqrt{\theta}$, f_{P3_G} = 118Hz.
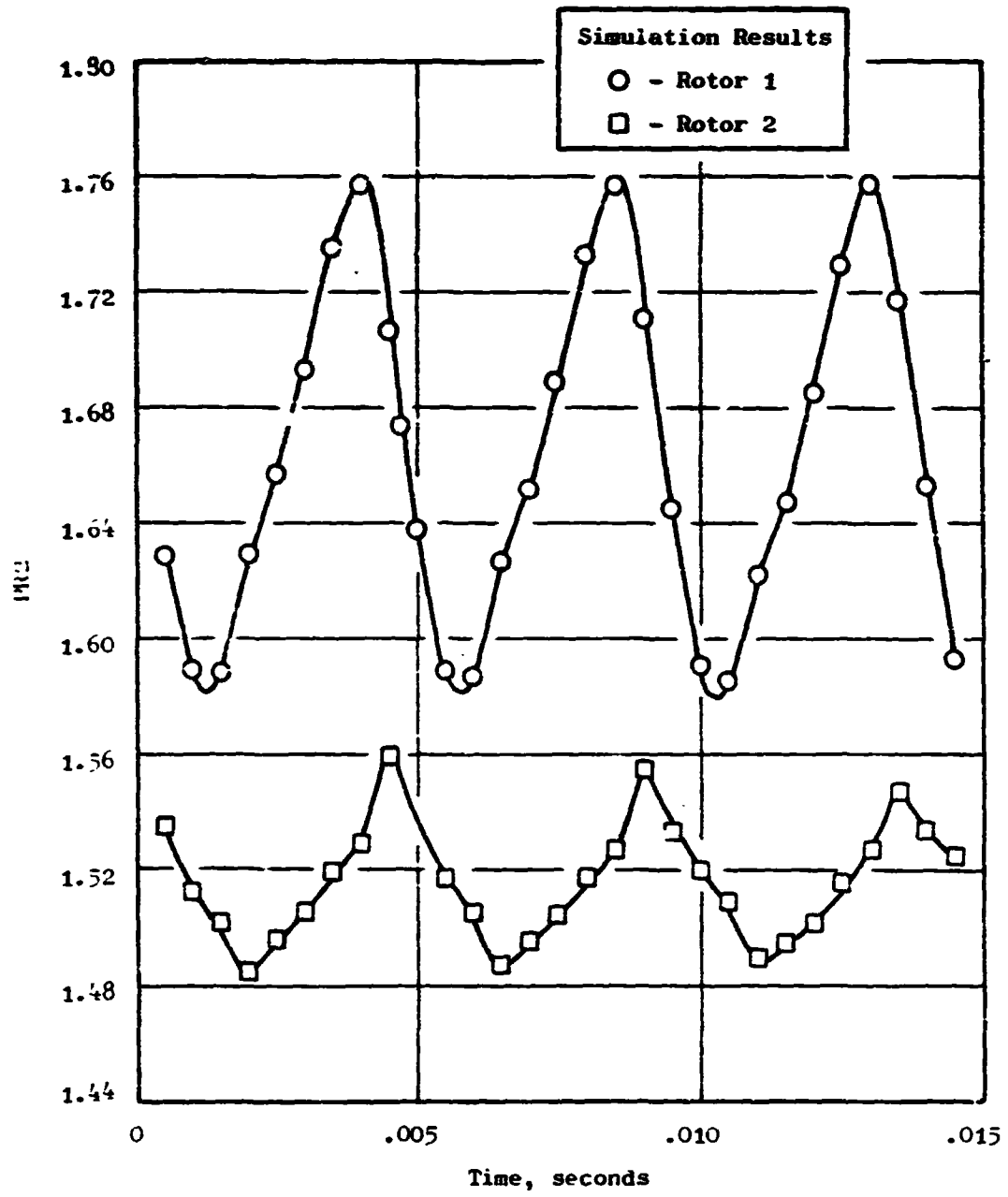
Figure B-4. F101-Fan Blade Row Total-Pressure Ratio as a Function of Time, 100% $N/\sqrt{\theta}$, f_{PG}^3 = 220Hz.

113
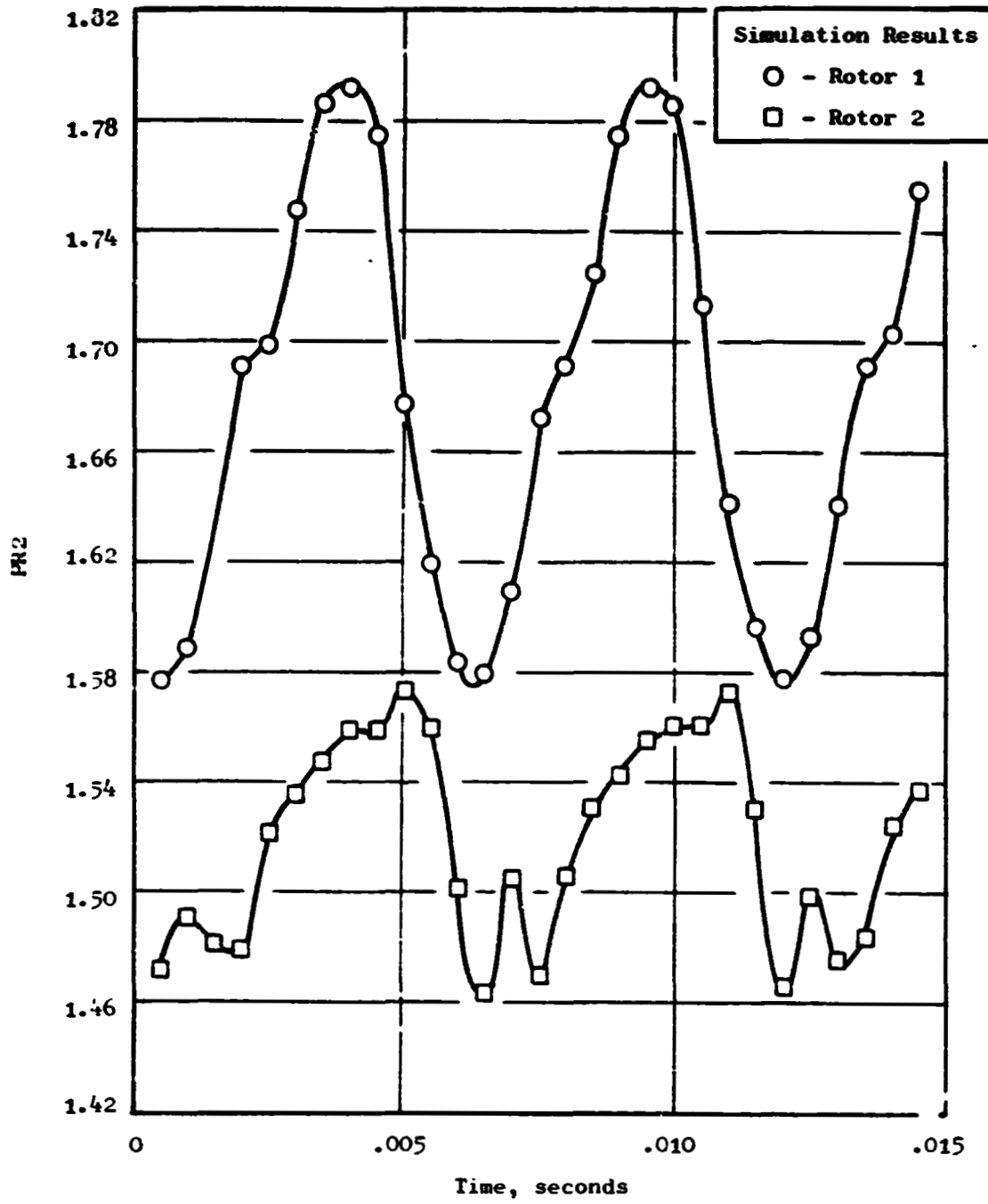
Figure B-5. F101-Fan Blade Row Total-Pressure Ratio as a Function of Time, 100% $N/\sqrt{\theta}$, $f_{P}{}^{3}{}_{G}$ = 350Hz.

114
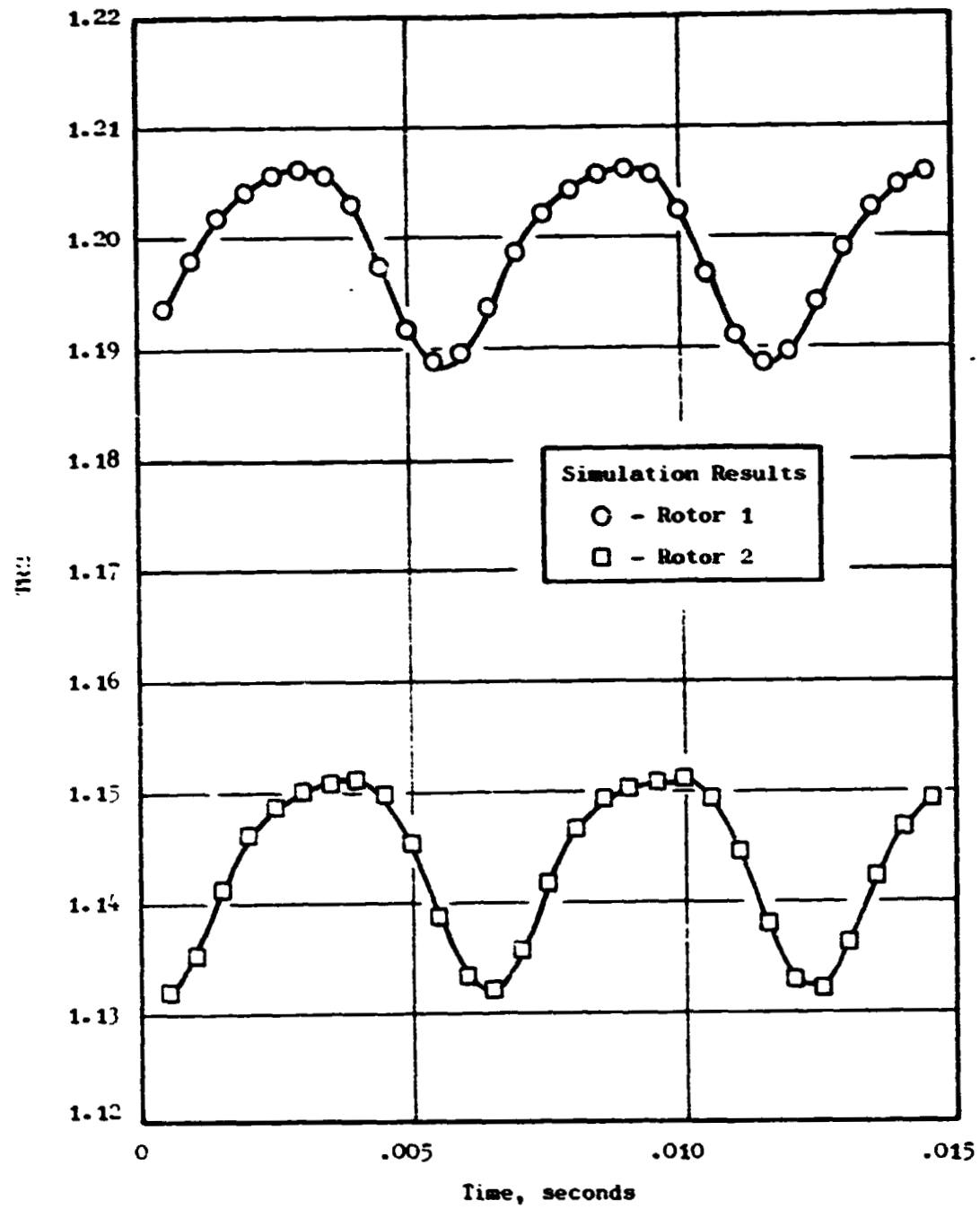
Figure B-6. F101-Fan Blade Row Total-Temperature Ratio as a Function of Time, 100% $N/\sqrt{\theta}$, f_{p3_G} = 42Hz.

115
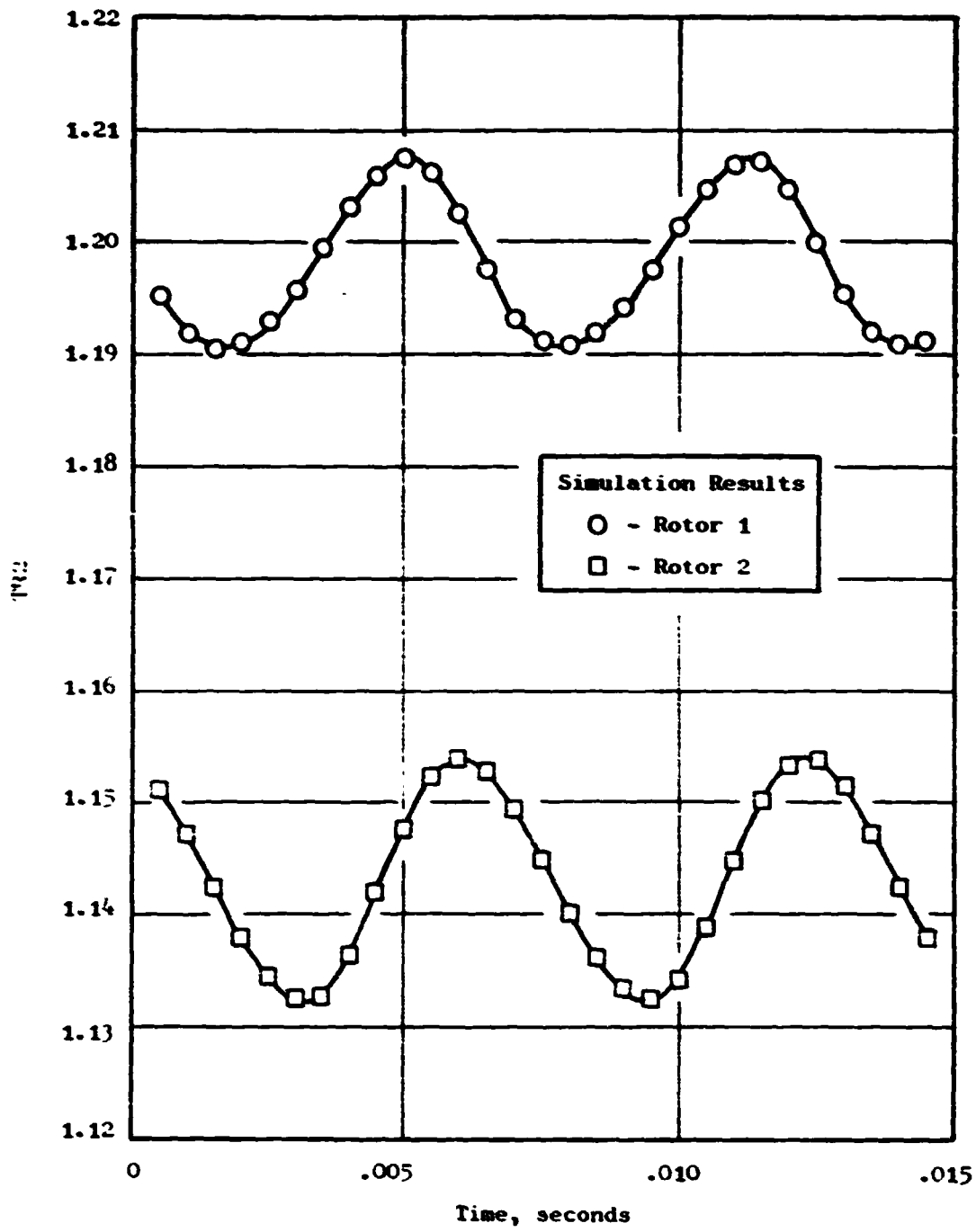
Figure B-7. F101-Fan Blade Row Total-Temperature Ratio as a Function of Time, 100% $N/\sqrt{\theta}$, $f_{p_3{}_G}$ = 80Hz.
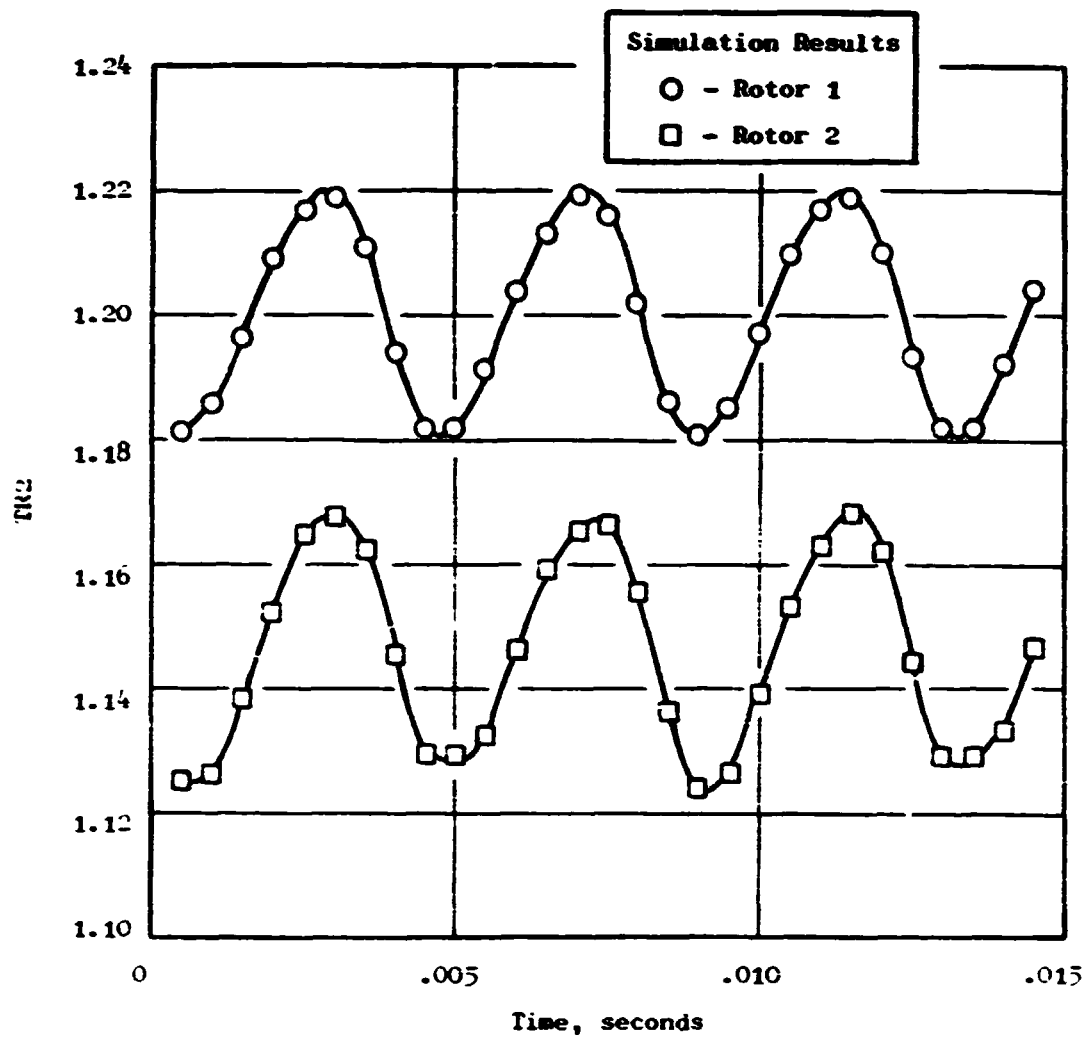
Figure B-8.   F101-Fan Blade Row Total-Temperature Ratio as a Function
of Time, 100% $N/\sqrt{\theta}$, $f_{p}j_{G}$ = 118Hz.
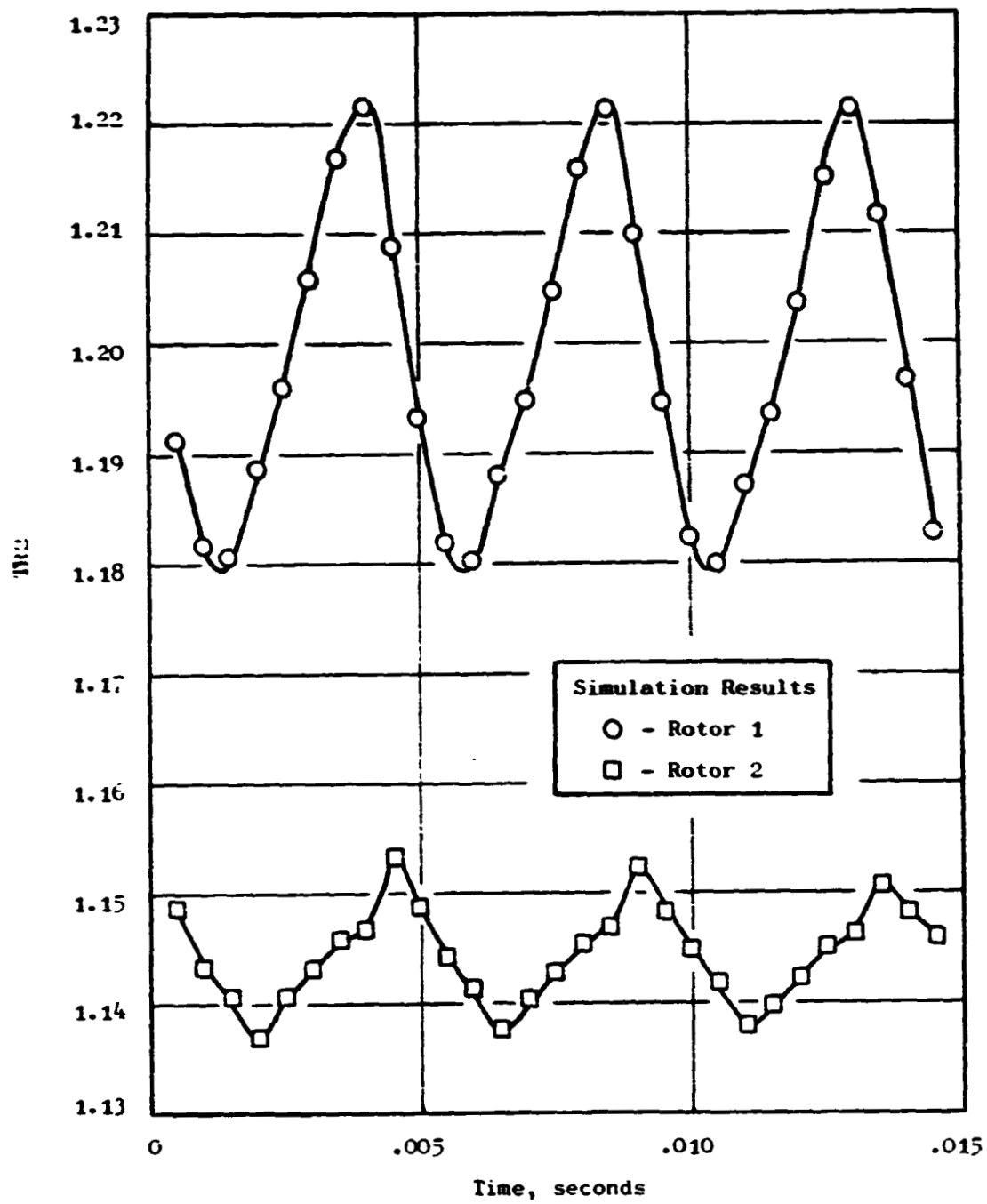
Figure B-9. F101-Fan Blade Row Total-Temperature Ratio as a Function of Time, 100% $N/\sqrt{\theta}$, f_{p^3G} = 220Hz.
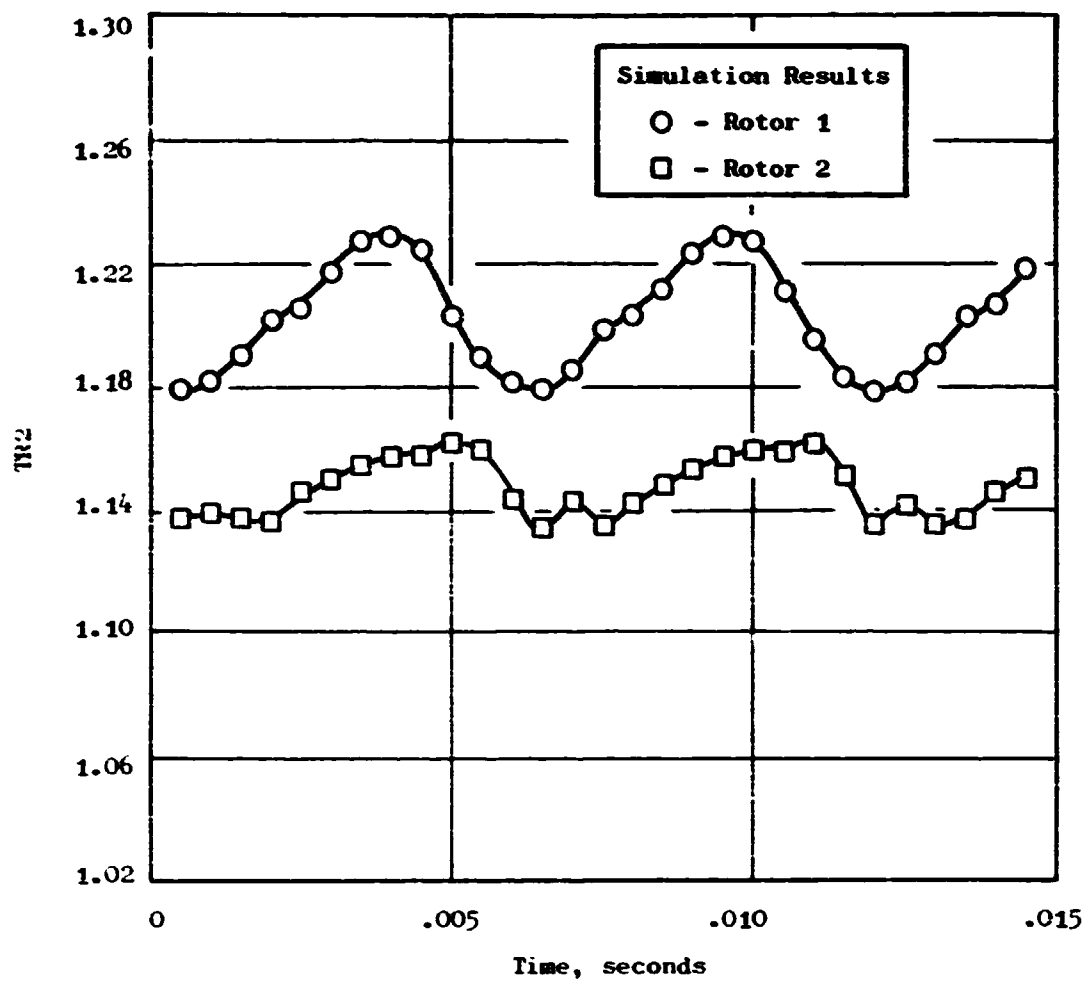
Figure B-10. F101-Fan Blade Row Total-Temperature Ratio as a Function of Time, 100% $N/\sqrt{\theta}$, f_{P3G} = 350Hz.

APPENDIX C

Results of J85-13/P^{3}G Simulation

120
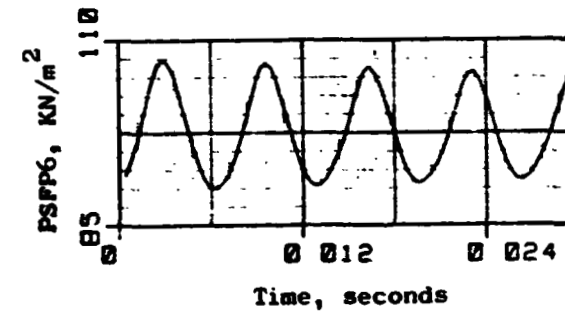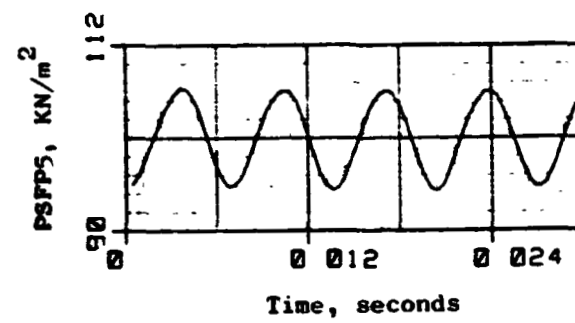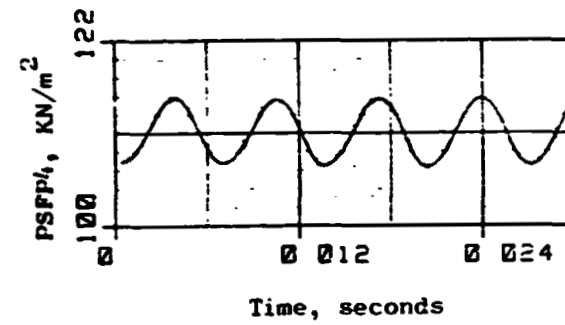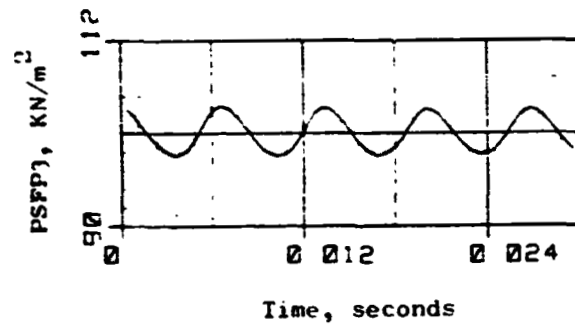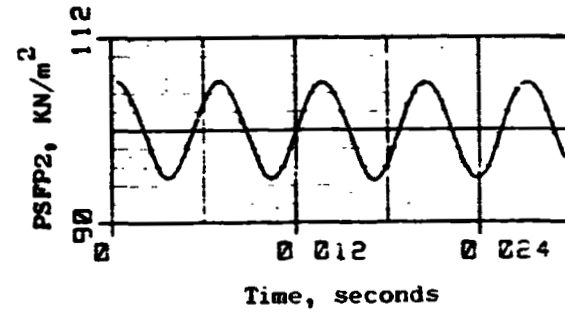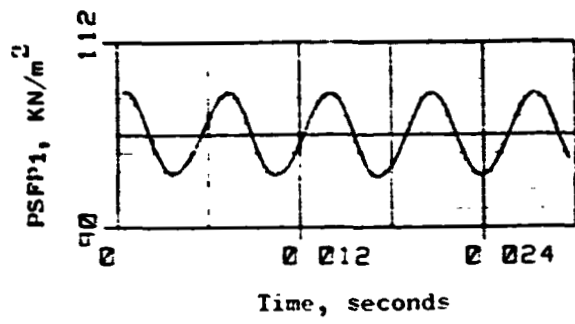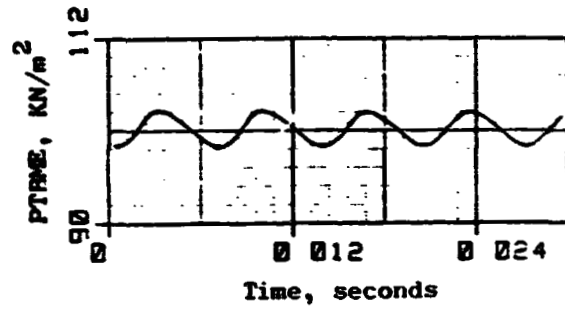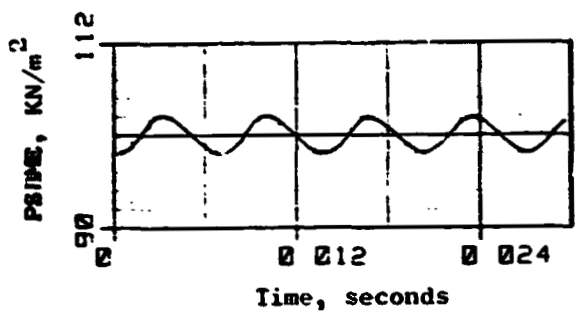
Figure C-1. J85-13/P^{3}G Simulation Results, f_{P^3G} = 150Hz.
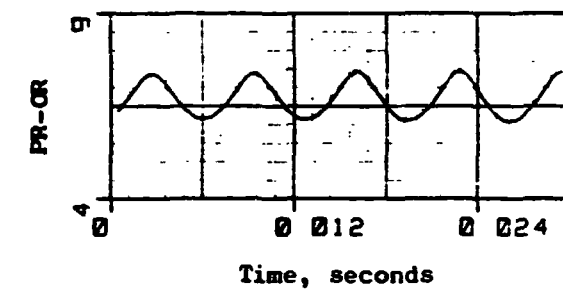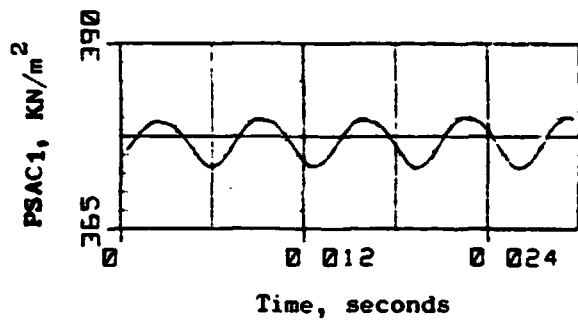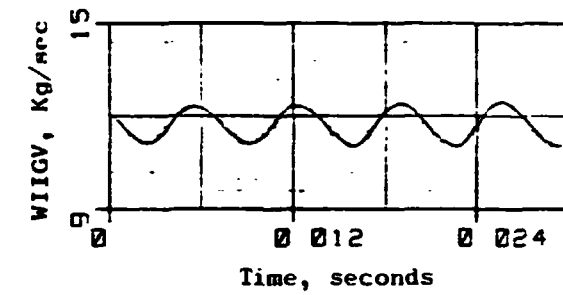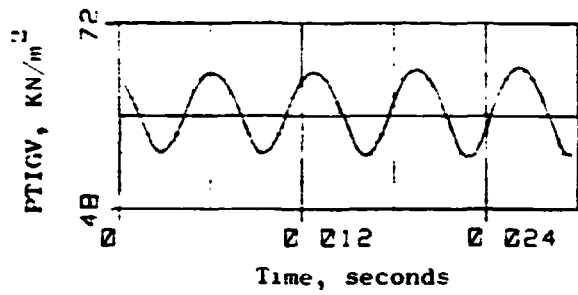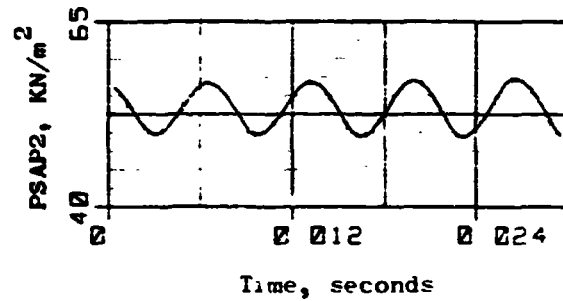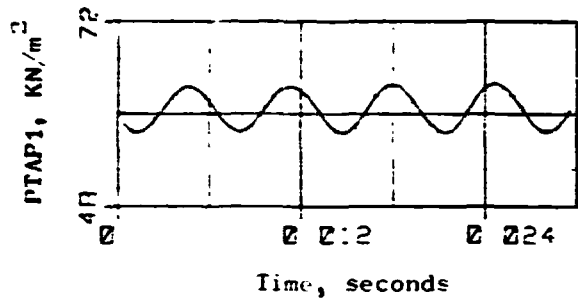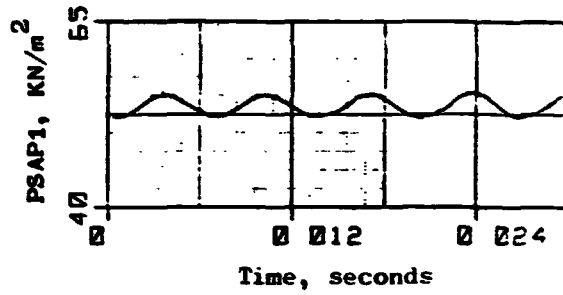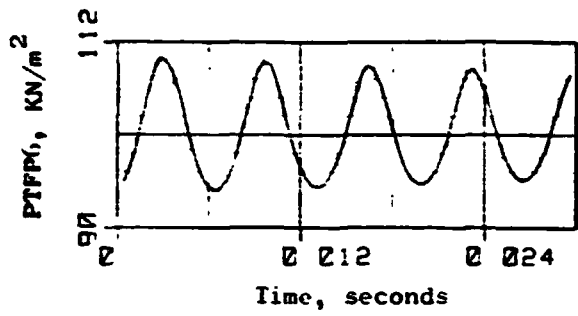
Figure C-2. J85-13/P³G Simulation Results, f_{P^3G} = 150Hz (Concluded).

122
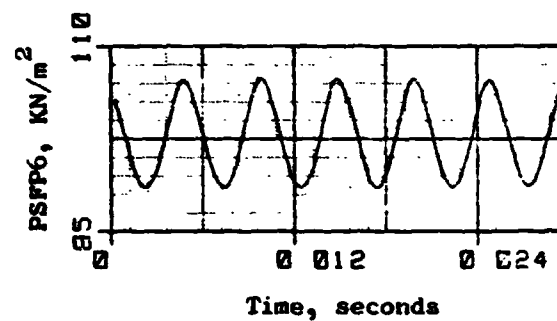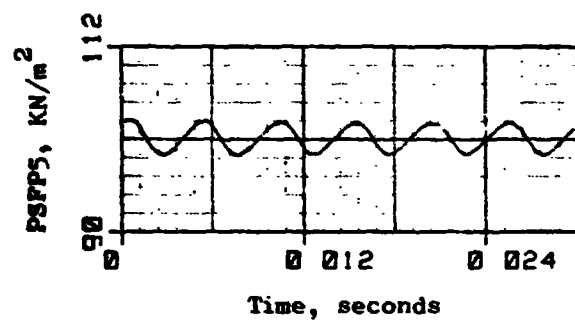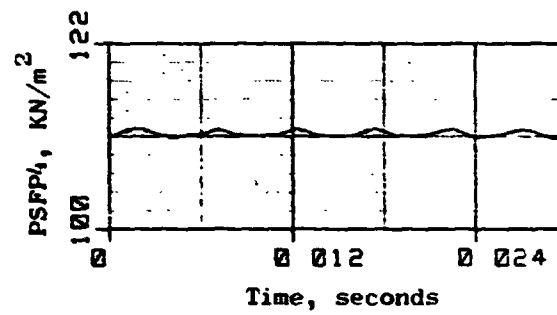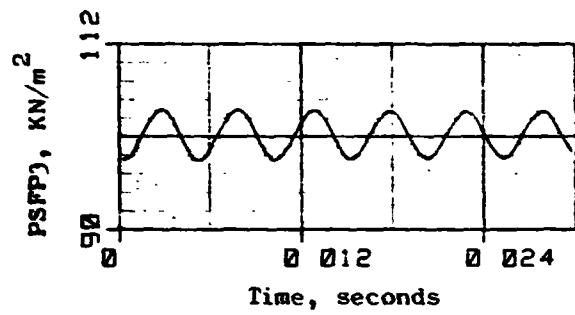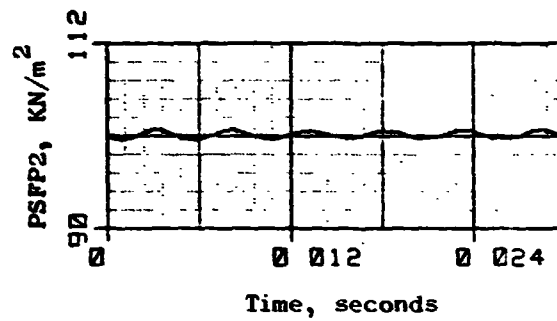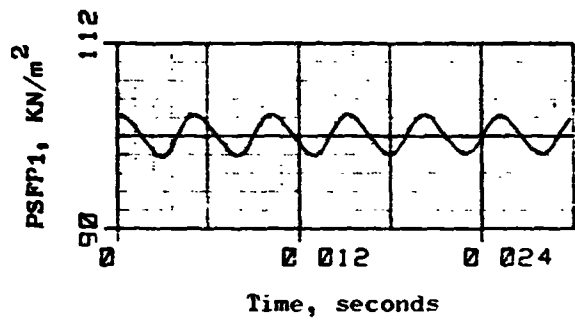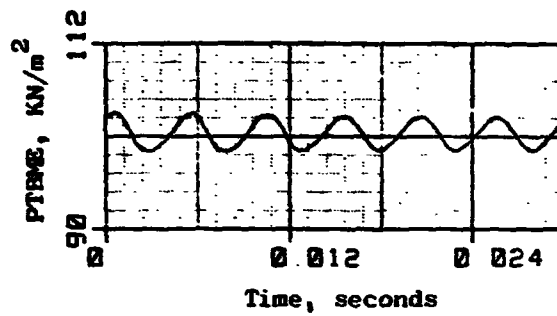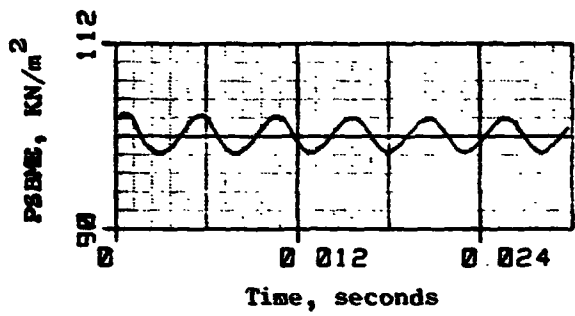
Figure C-3. J85-13/P³G Simulation Results, f_{P^3G} = 200Hz.   123
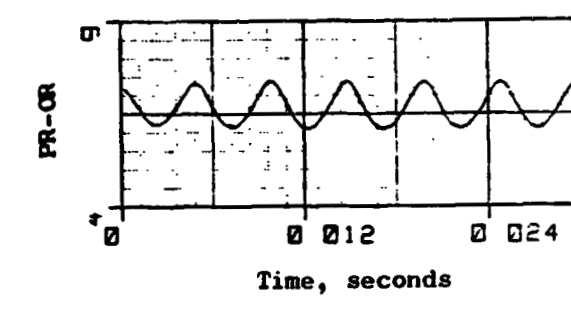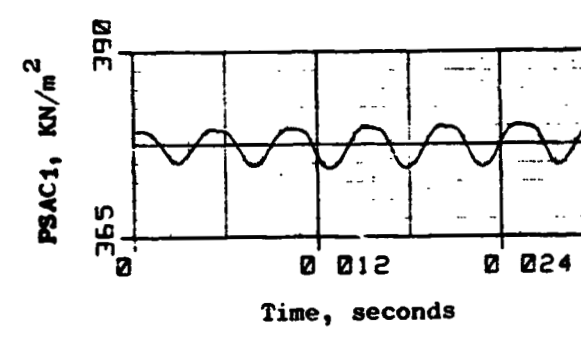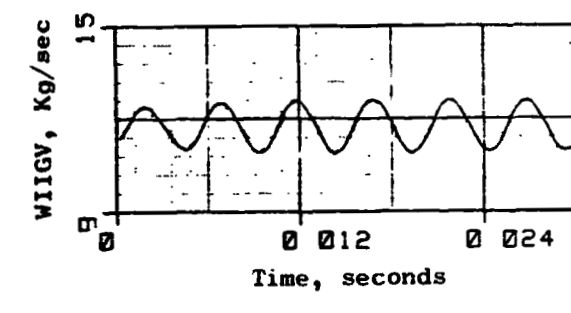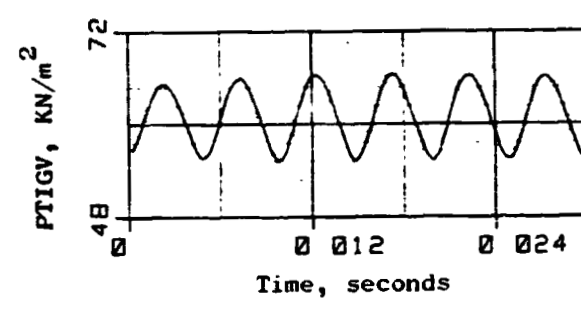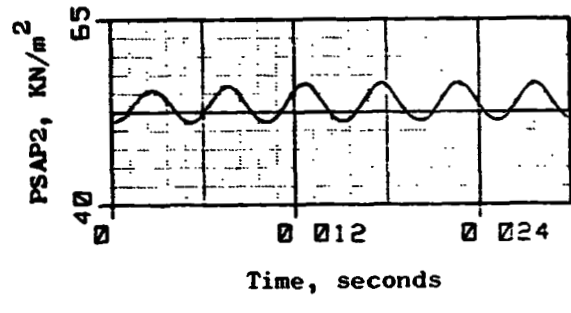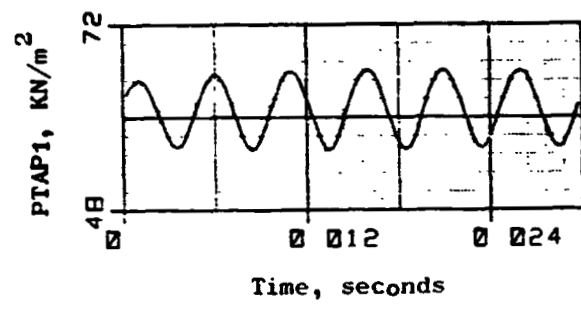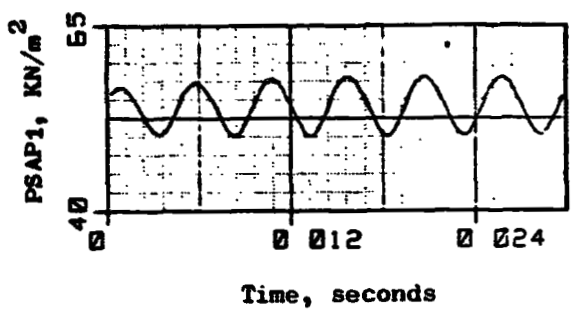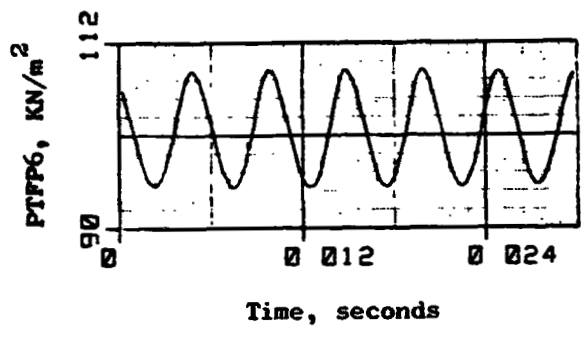
Figure C-4. J85-13/P³G Simulation Results, f_{P^3G} = 200Hz (Concluded).

124
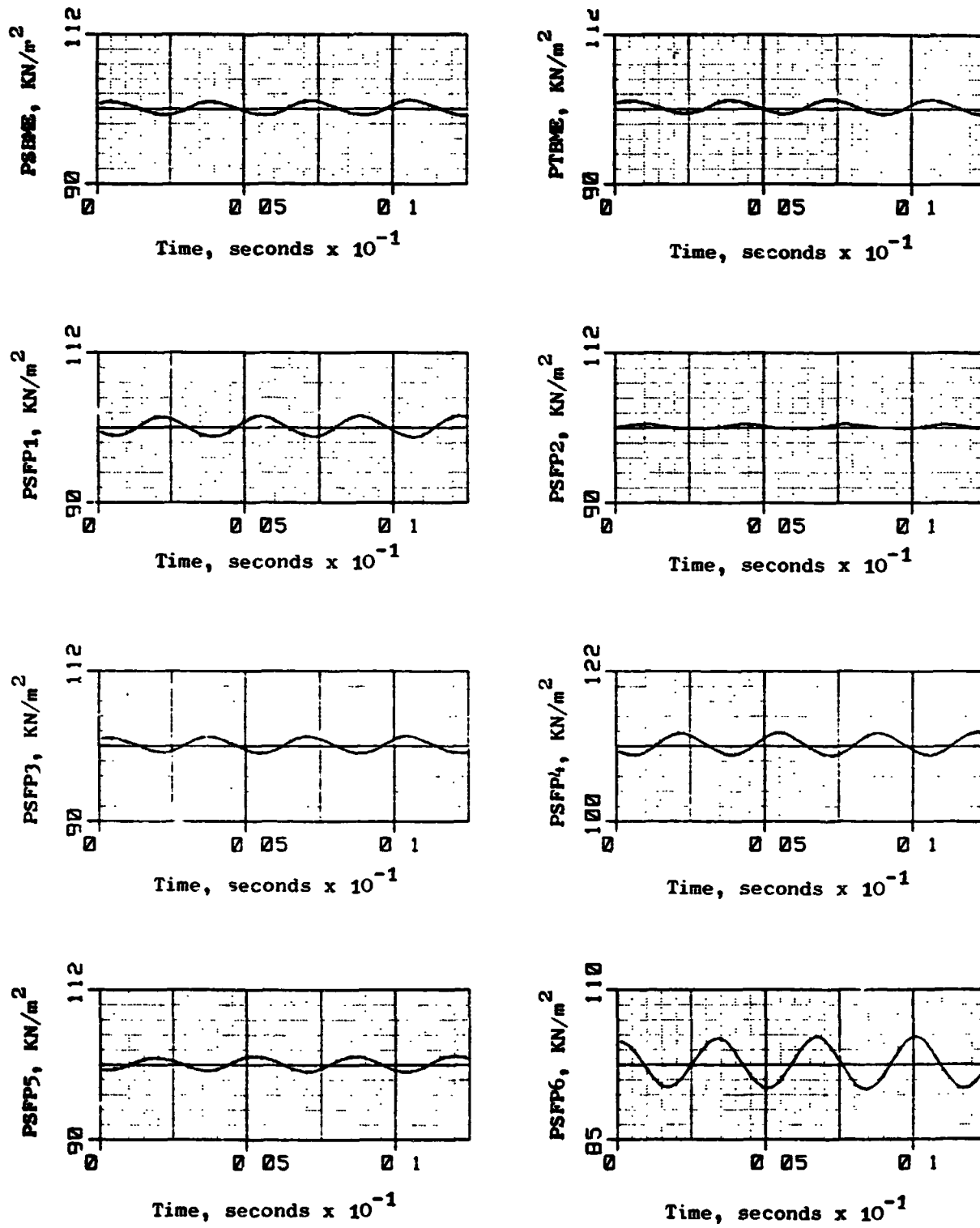
Figure C-5. J85-13/P³G Simulation Results, f_{P^3G} = 300Hz.
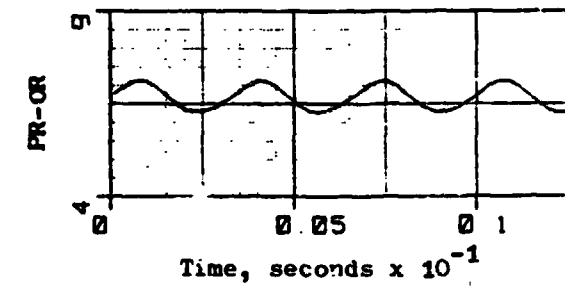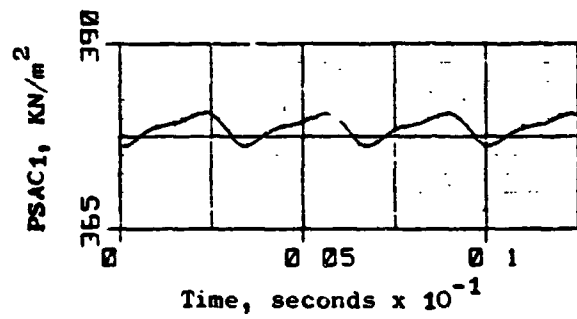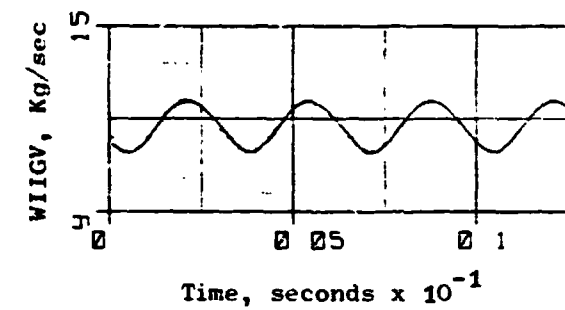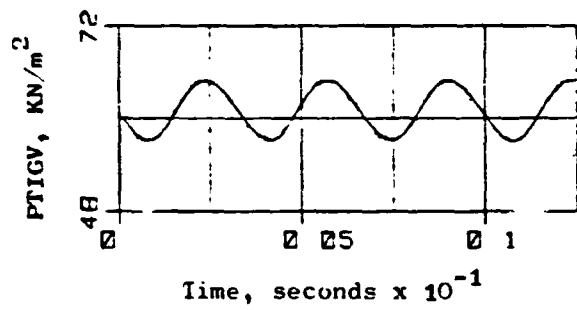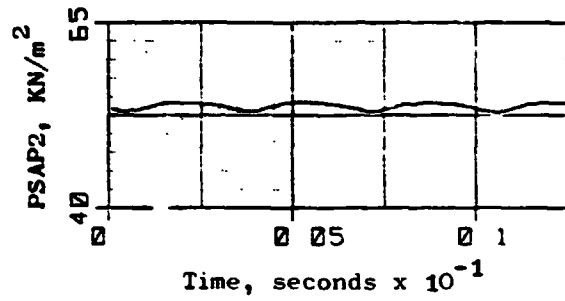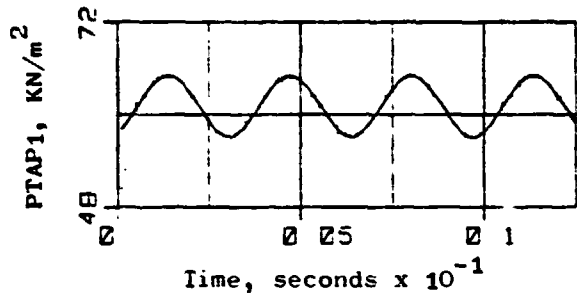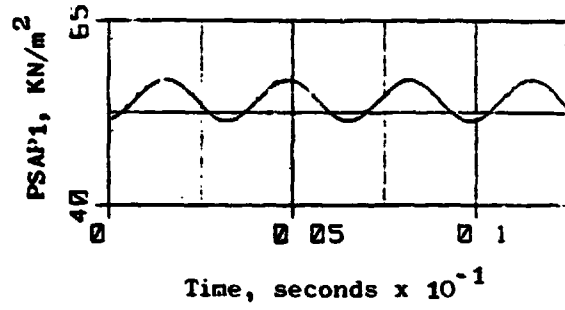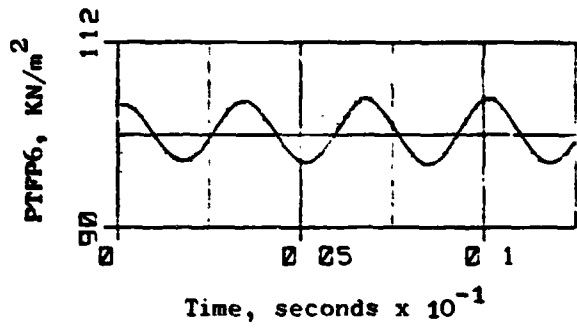
Figure C-6. J85-13/P^{3}G Simulation Results, f_{P^3G} = 300Hz (Concluded).
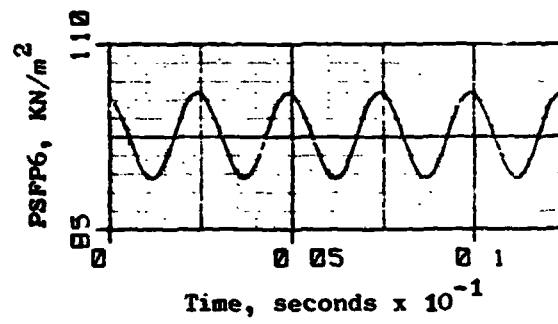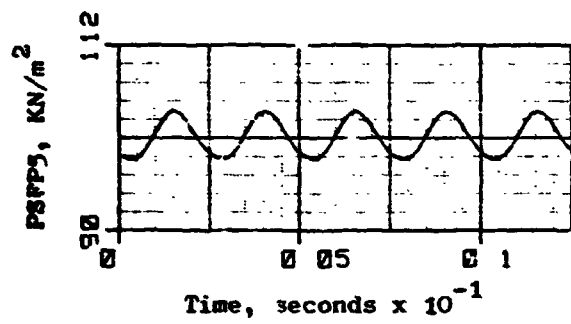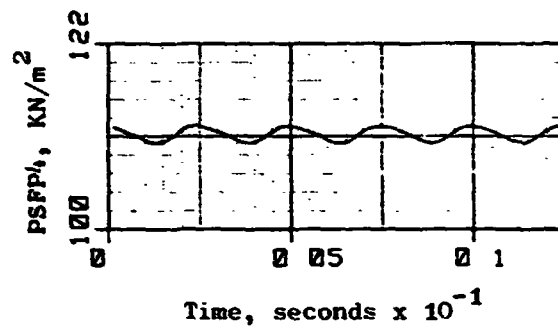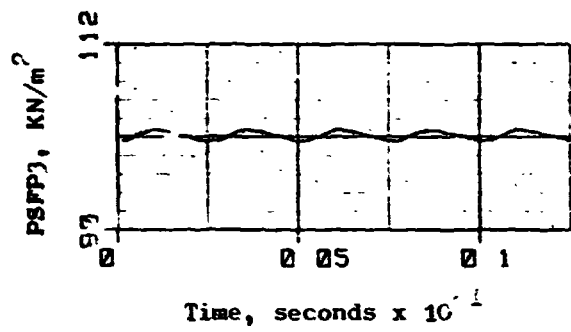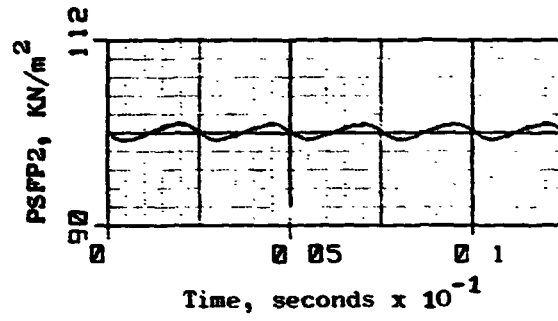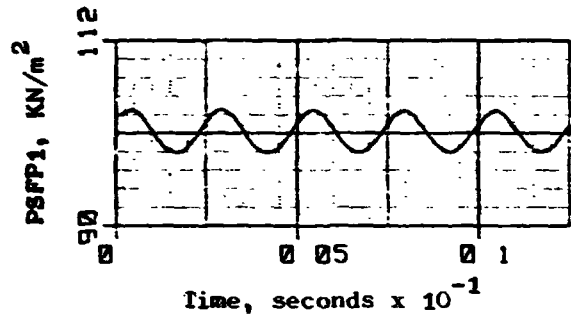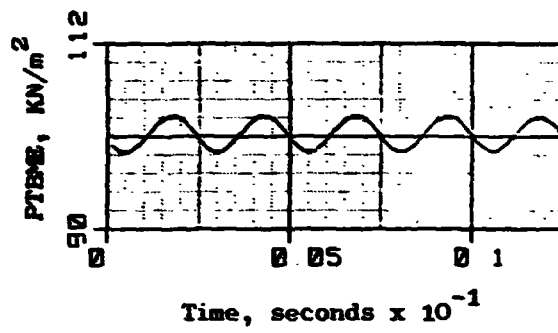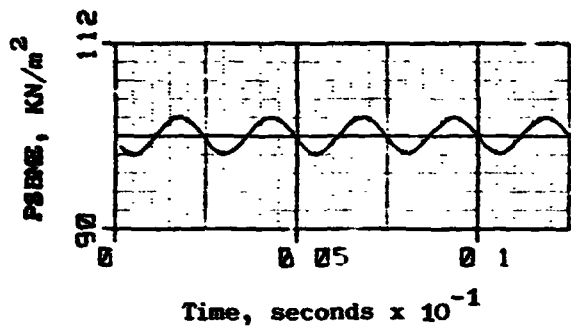
Figure C-7. J85-13/P³G Simulation Results, f_{P^3G} = 400Hz.

127
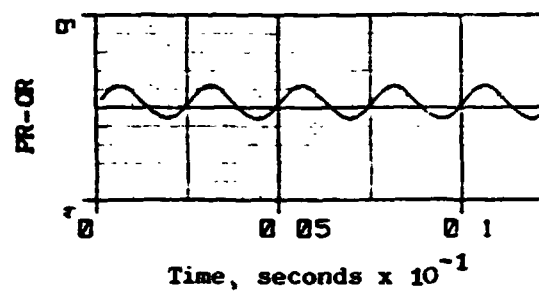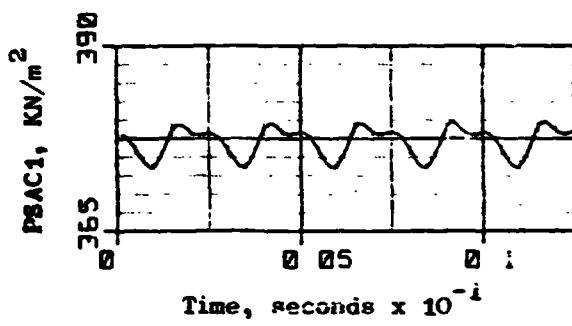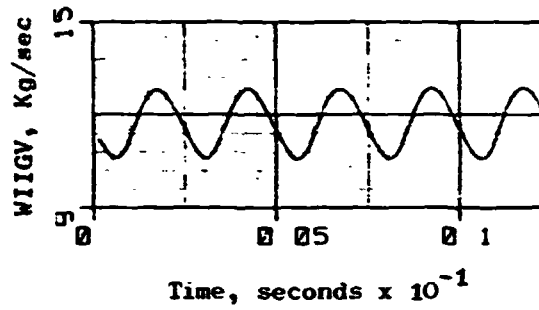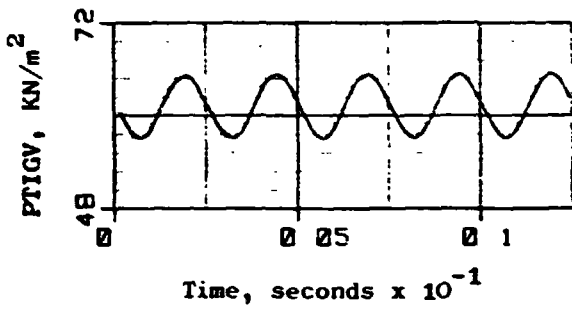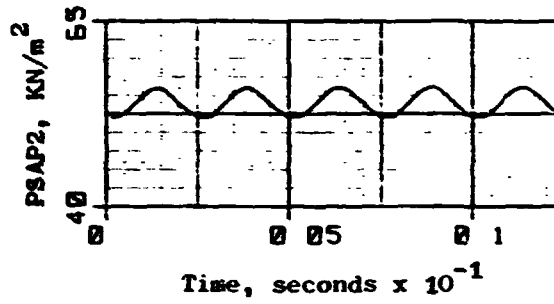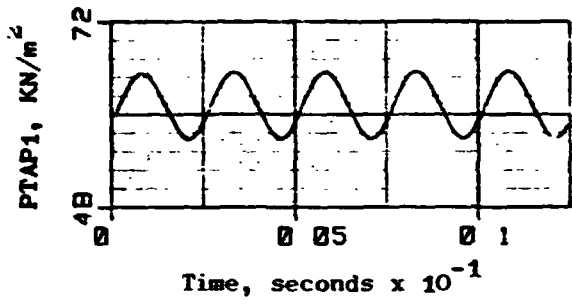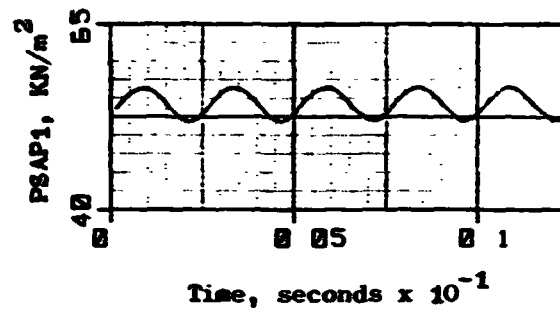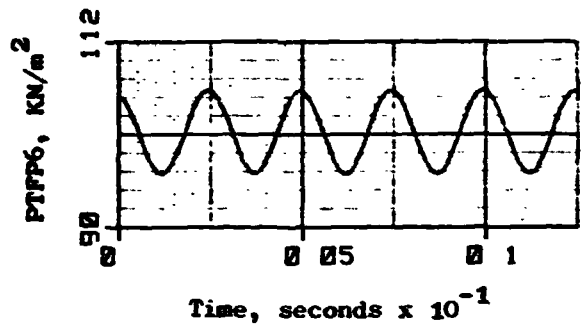
Figure C-8. J85-13/P^{3}G Simulation Results, f_{P^3G} = 4ᵤᵤHz (Concluded).

128
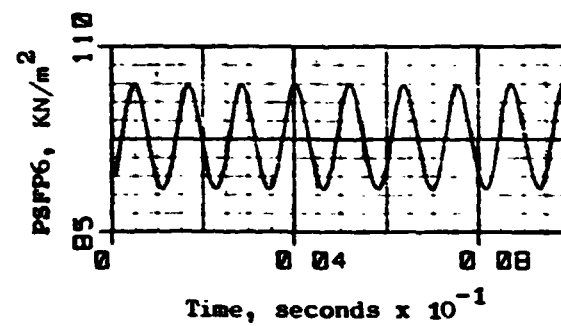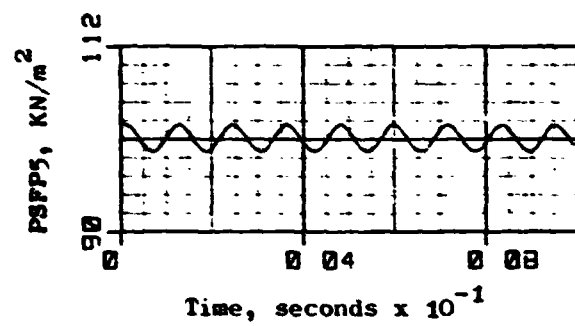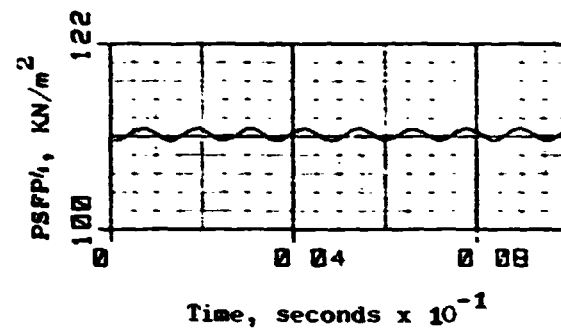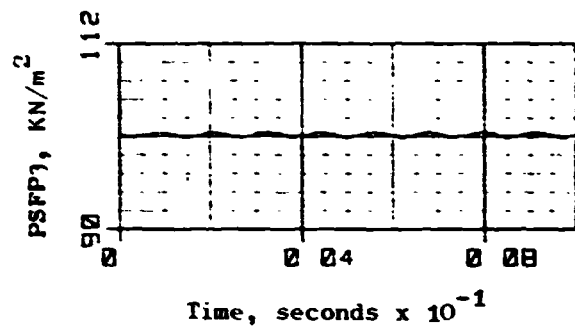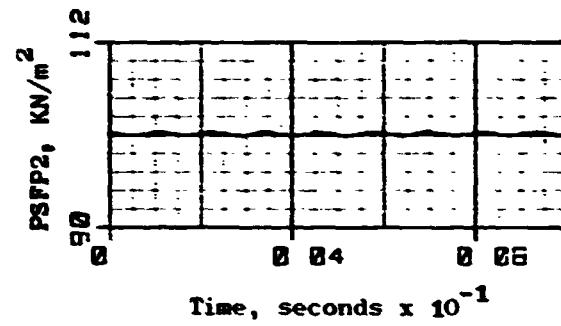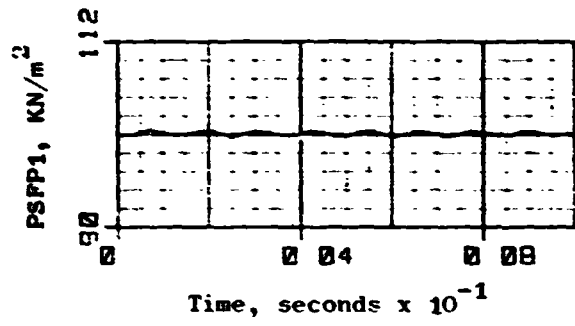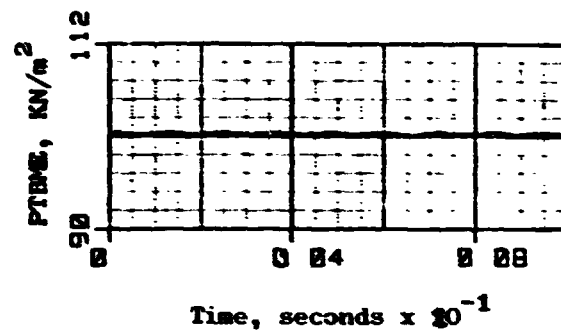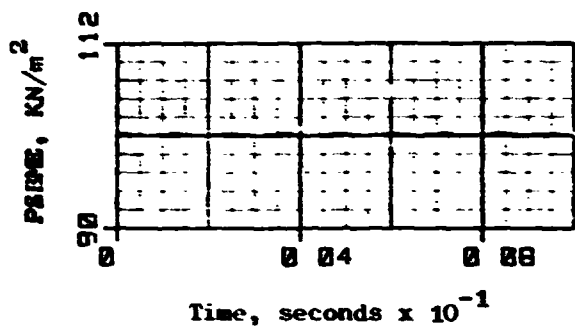
Figure C-9. J85-13/P^{3}G Simulation Results, f_{P^3G} = 850Hz.

129
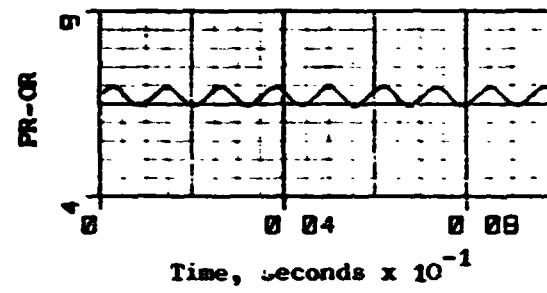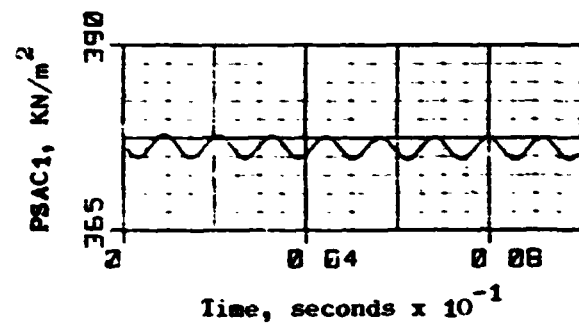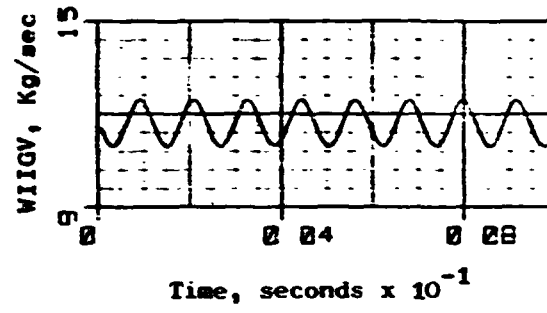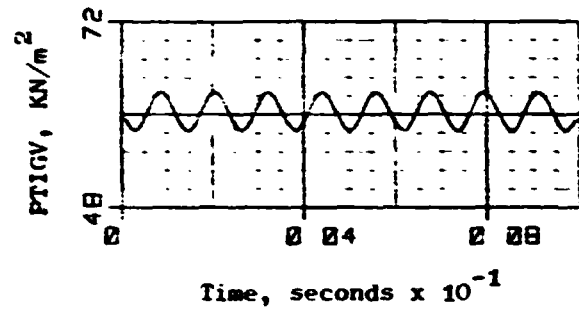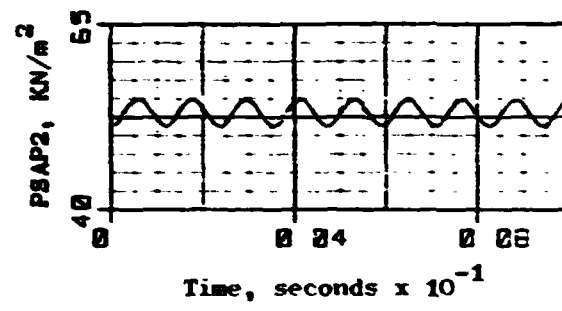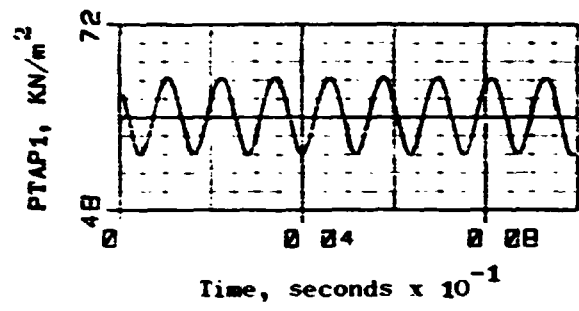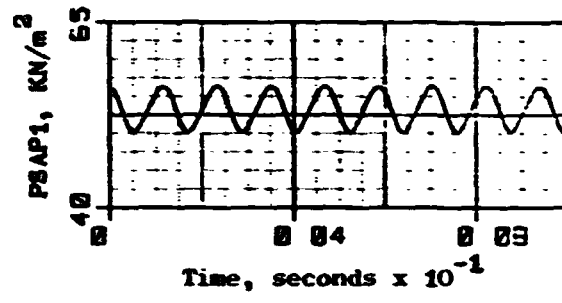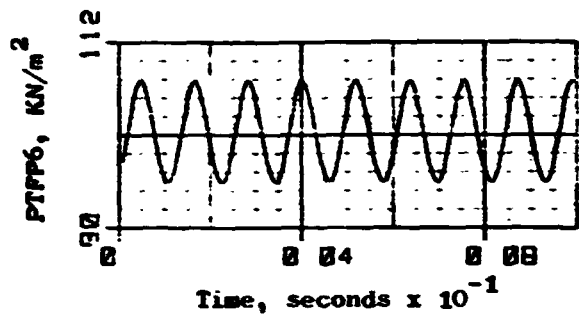
Figure C-10. J85-13/P^{3}G Simulation Results, f_{P^3G} = 850Hz (Concluded).

130
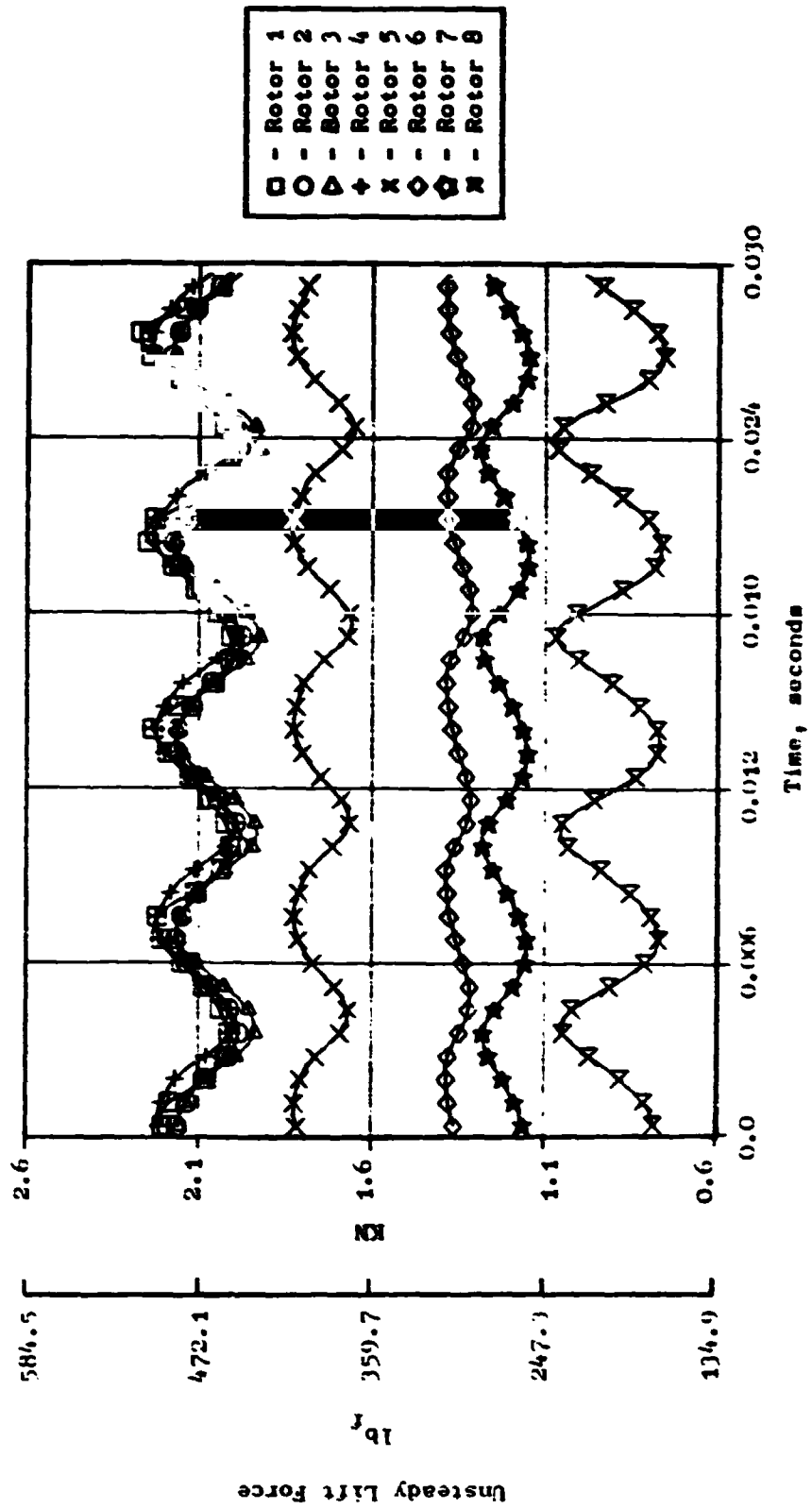
Figure C-11. Unsteady Blade Lift Force as a Function of Time at 150Hz.

131
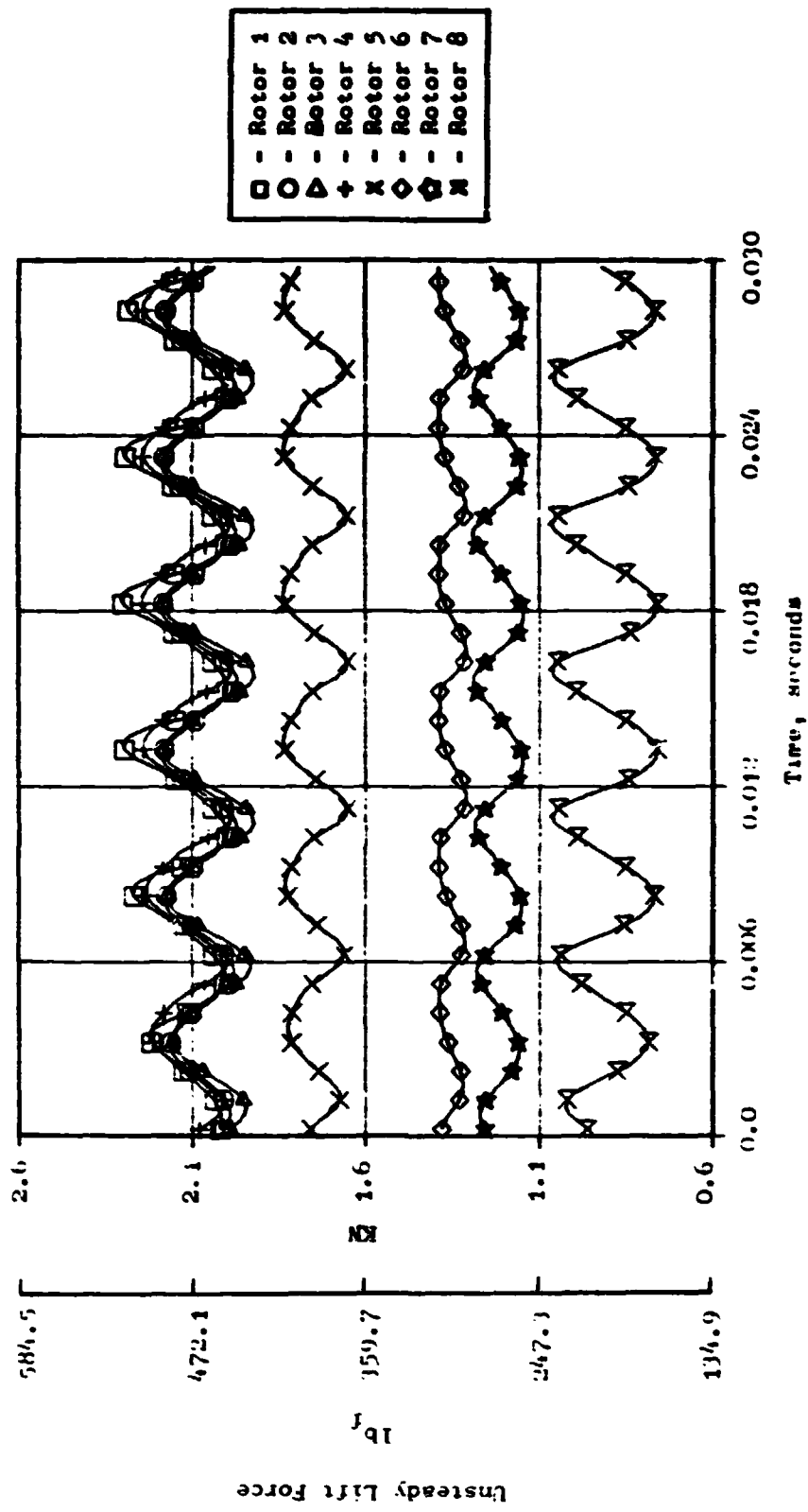
Figure (-12. Unsteady Blade Lift Force as a Function of Time at 200Hz.

Legend:
□ – Rotor 1
○ – Rotor 2
△ – Rotor 3
+ – Rotor 4
× – Rotor 5
◇ – Rotor 6
⊕ – Rotor 7
⊠ – Rotor 8
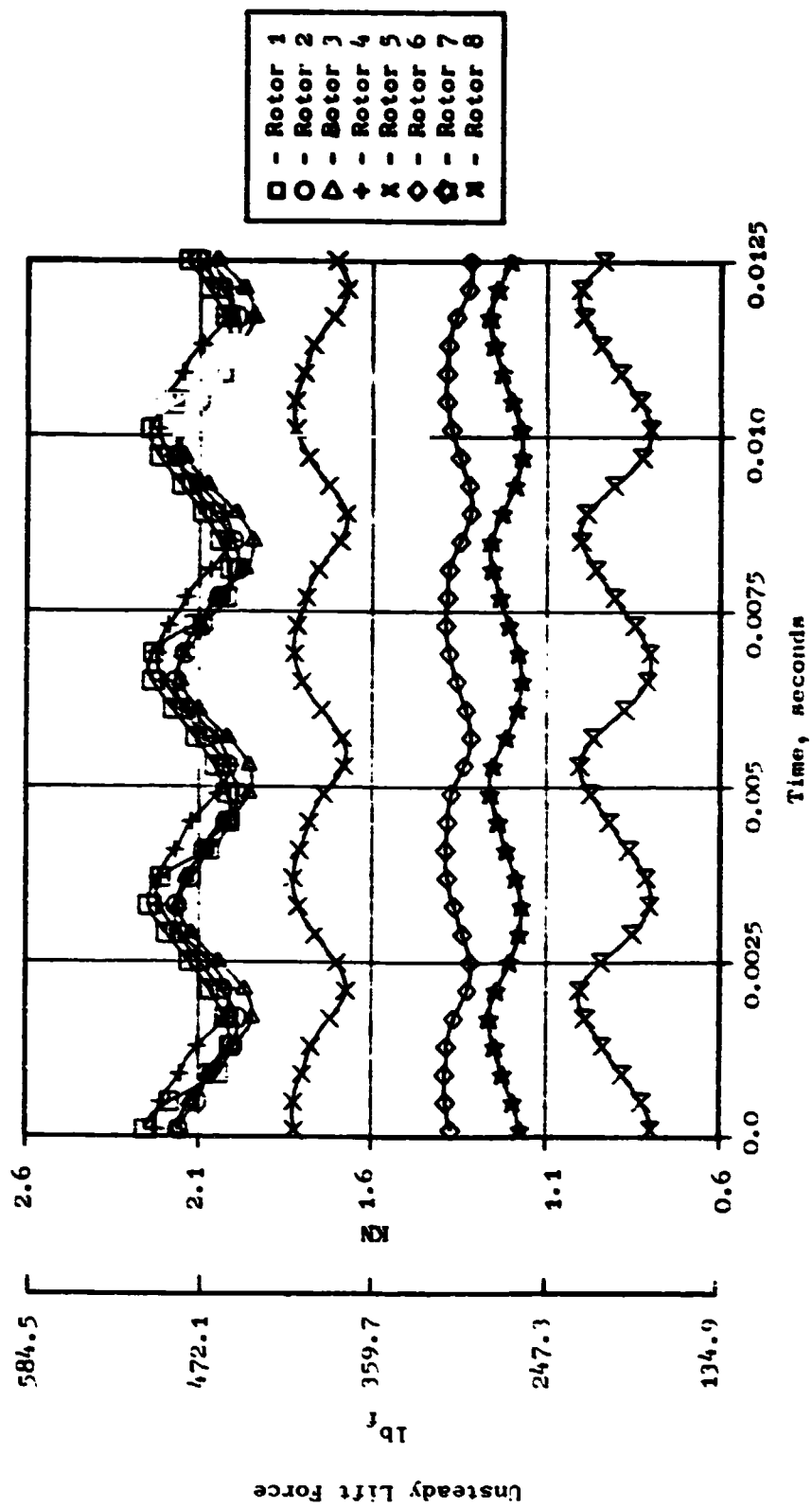
Figure C-13. Unsteady Blade Lift Force as a Function
of Time at 300Hz.

133

Figure C-14. Unsteady Blade Lift Force as a Function of Time at 400Hz.

Legend:
□ – Rotor 1
○ – Rotor 2
△ – Rotor 3
+ – Rotor 4
× – Rotor 5
◇ – Rotor 6
✿ – Rotor 7
✕ – Rotor 8

Time, seconds

KN

lb_f

Unsteady Lift Force

134
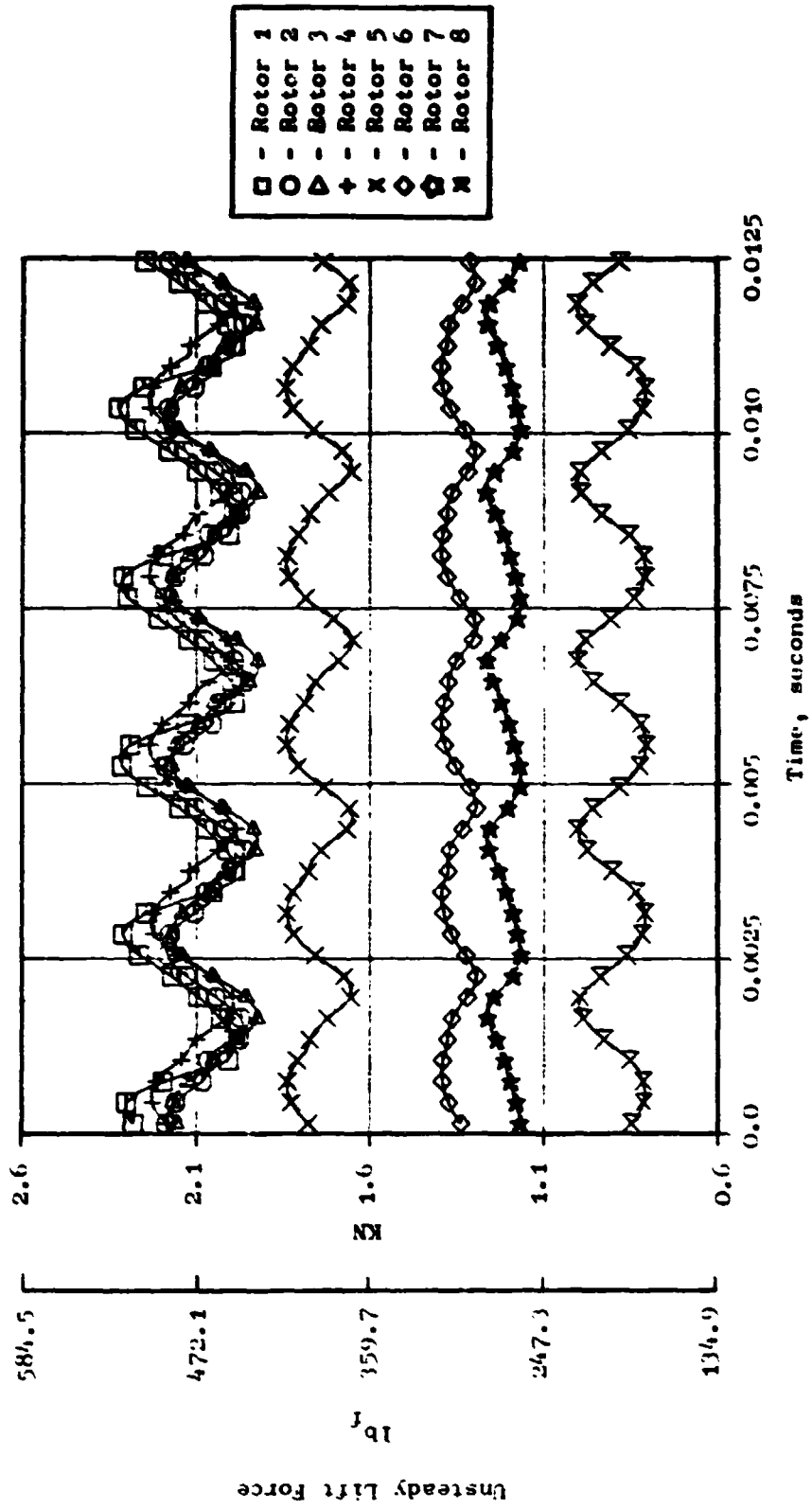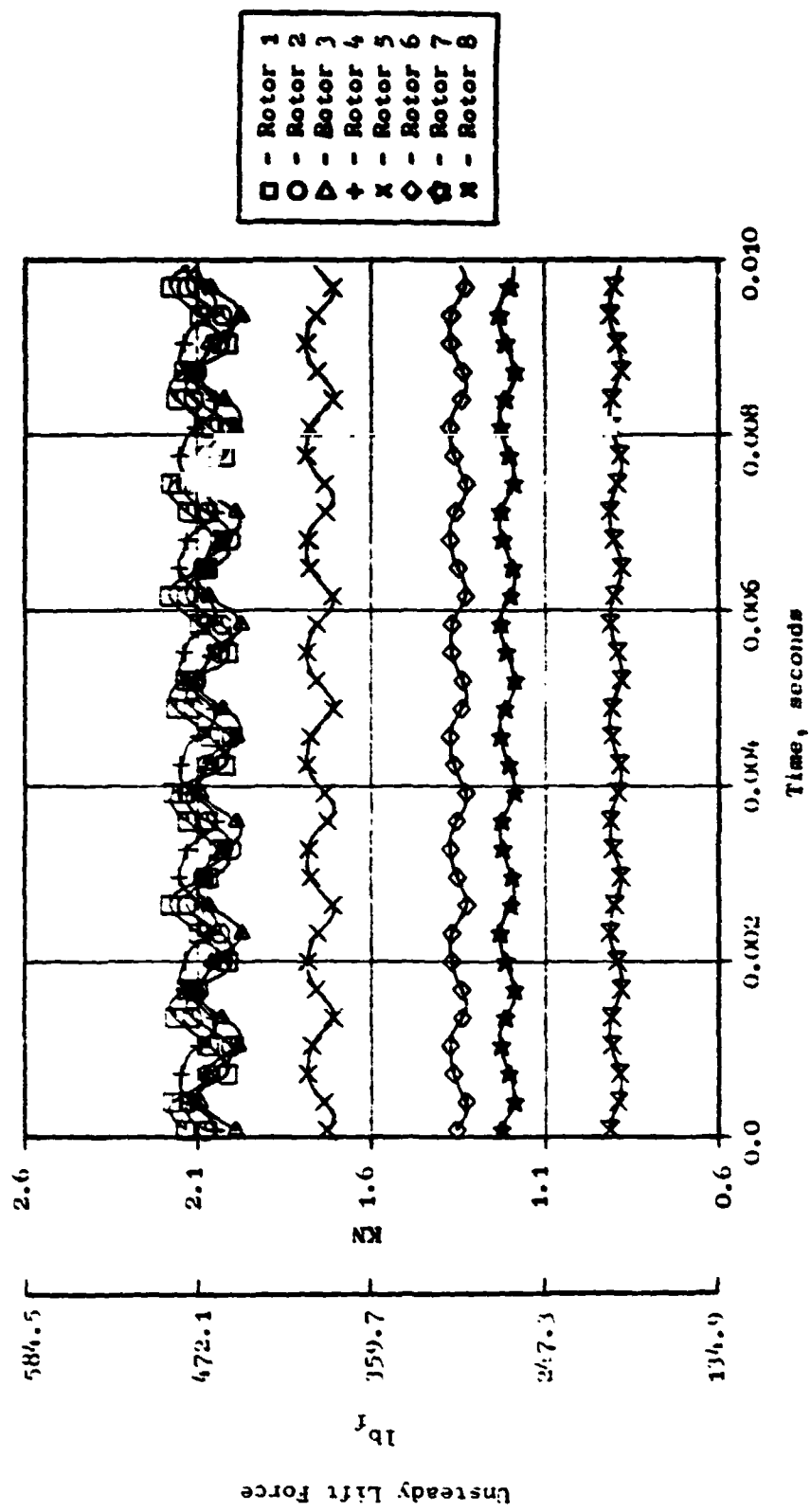
Figure C-15. Unsteady Blade Lift Force as a Function
of Time at 850Hz.

APPENDIX D

Results of J85-13/P^{3}G Frequency Response Analysis
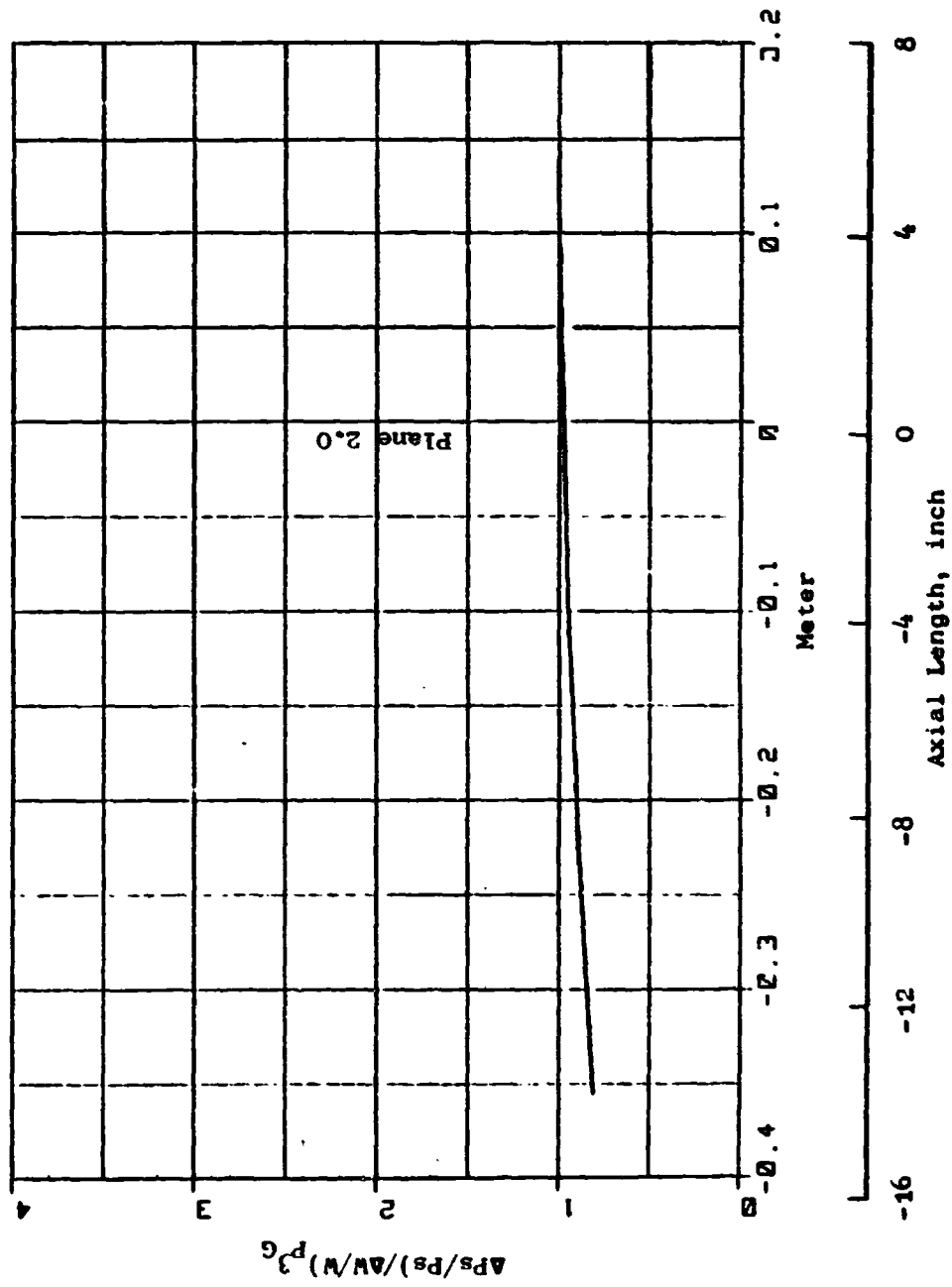
Figure D-1. Result of Nodal Analysis at $f_{P_G^3} = 50$Hz, P_G^3-to-IGV.

137
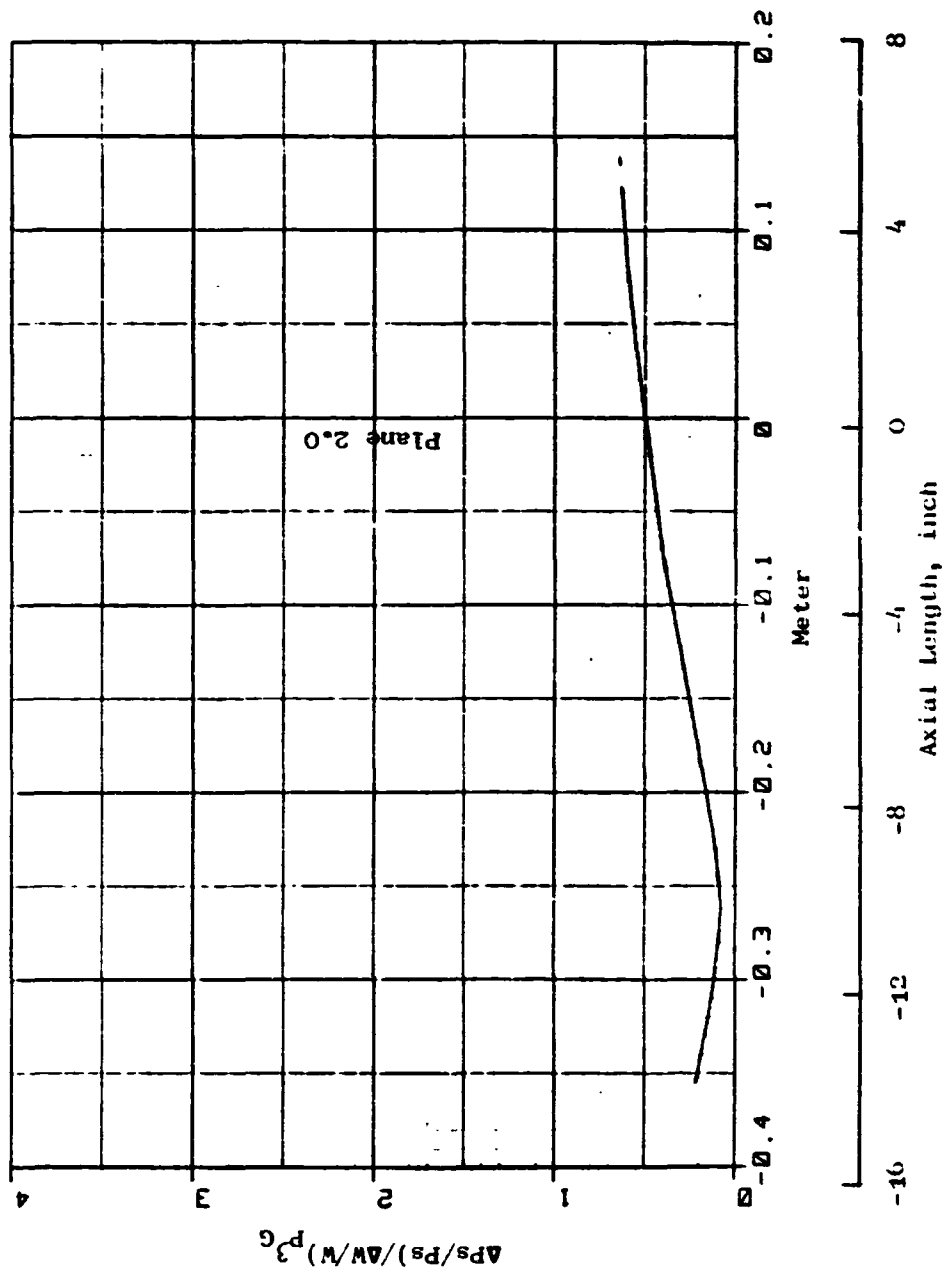
Figure D-2. Result of Nodal Analysis at $(P_p^3)_G = 150Hz$, P^3G-to-IGV.
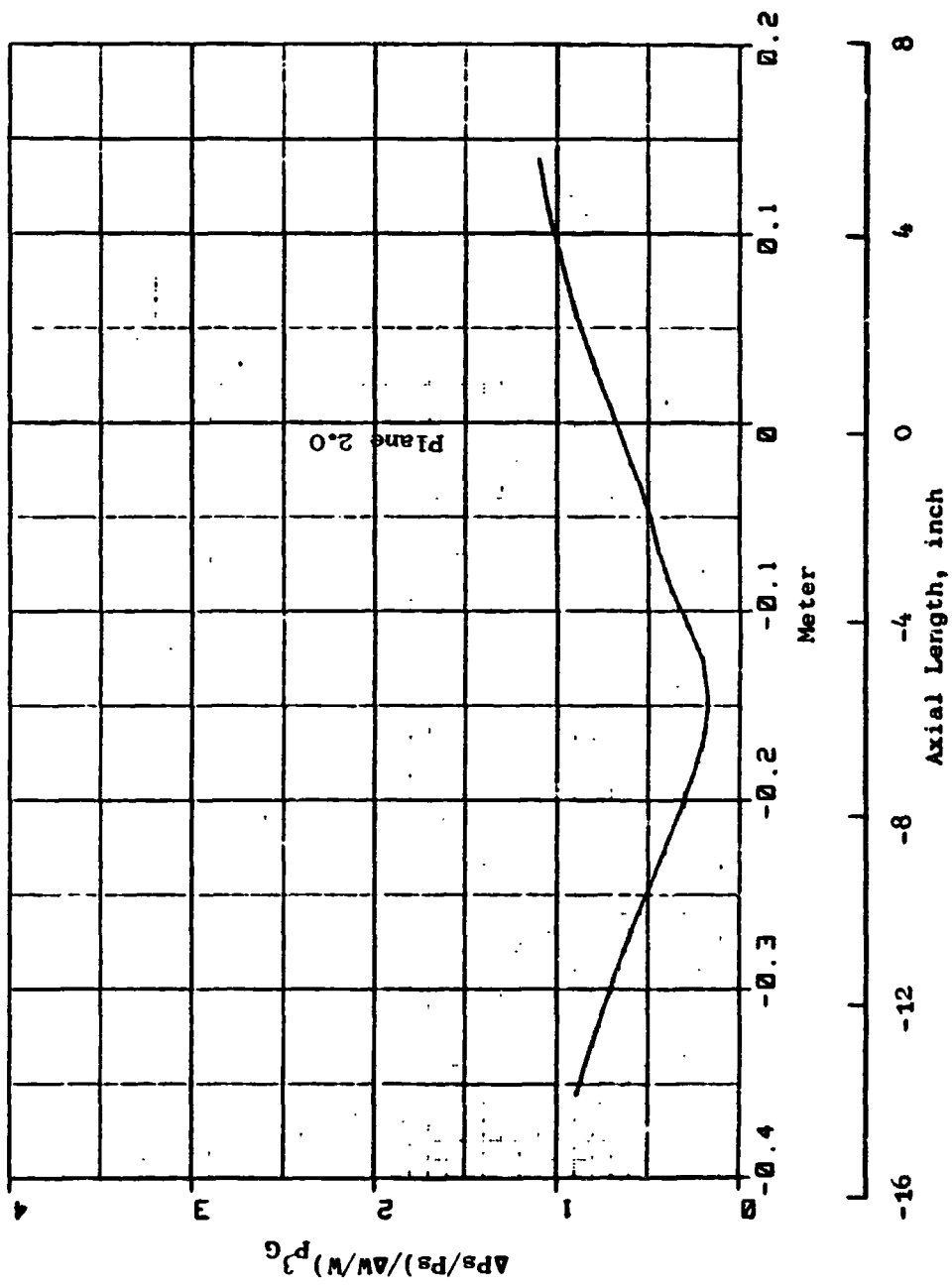
Figure D-3. Result of Nodal Analysis at $1_P3_G = 200Hz$, P^3G-to-IGV.
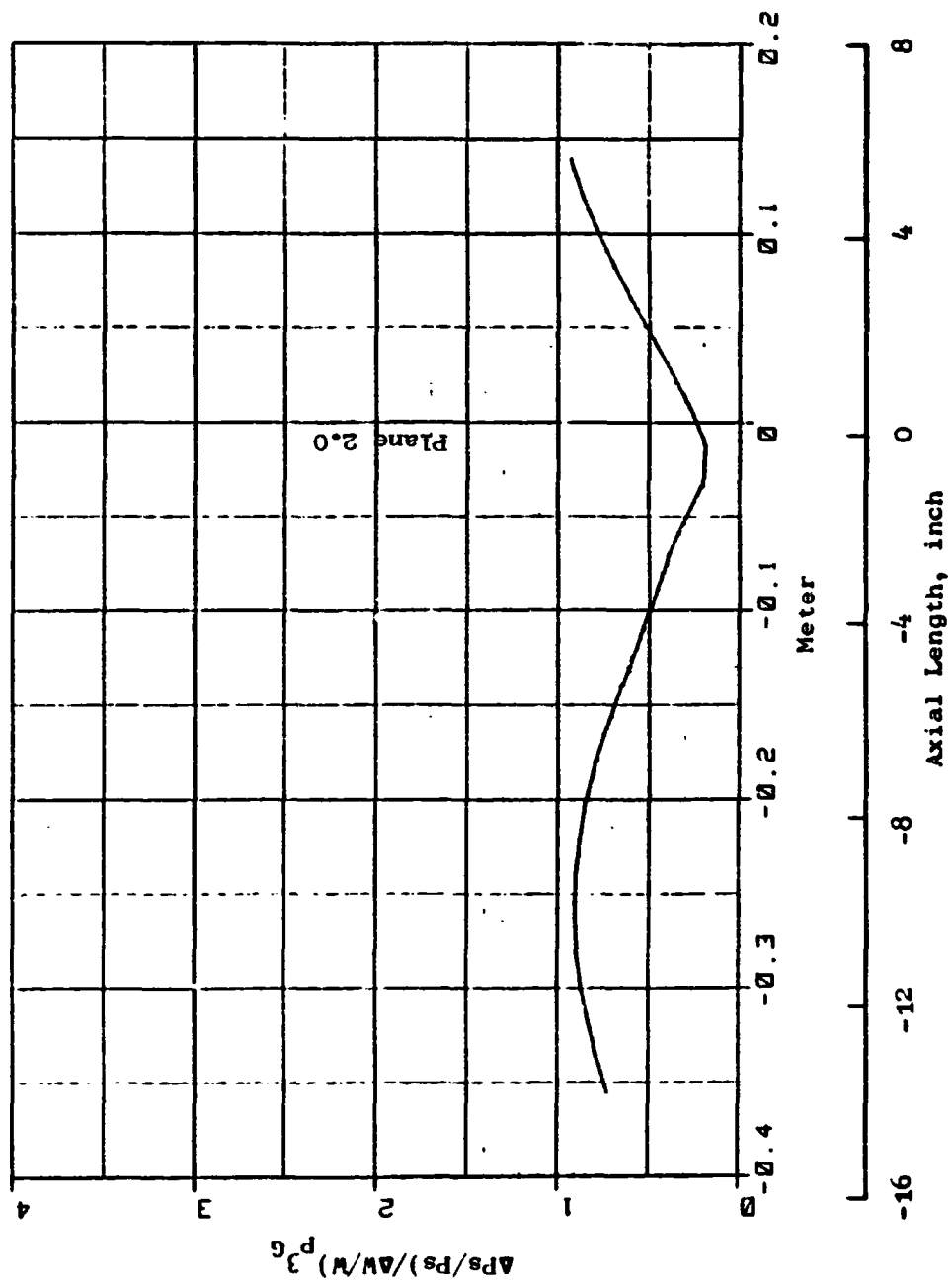
Figure D-7. Result of Nodal Analysis at $I_{P}{}^{3}{}_{G} = 300Hz$, $P^{3}G$-to-IGV.

140
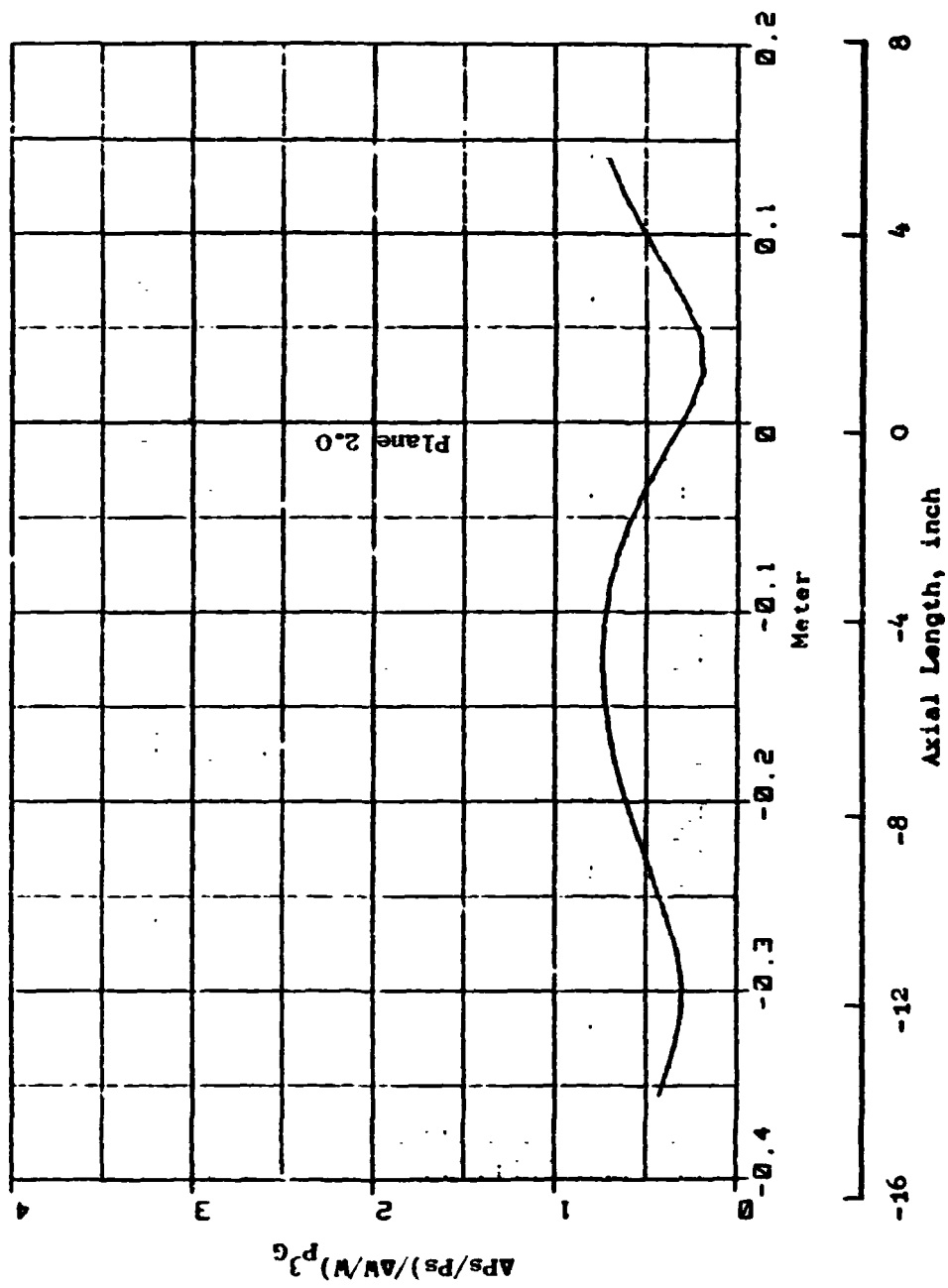
Figure D-5. Result of Nodal Analysis at $(P^3)_G = 400Hz$, P^3G-to-IGV.
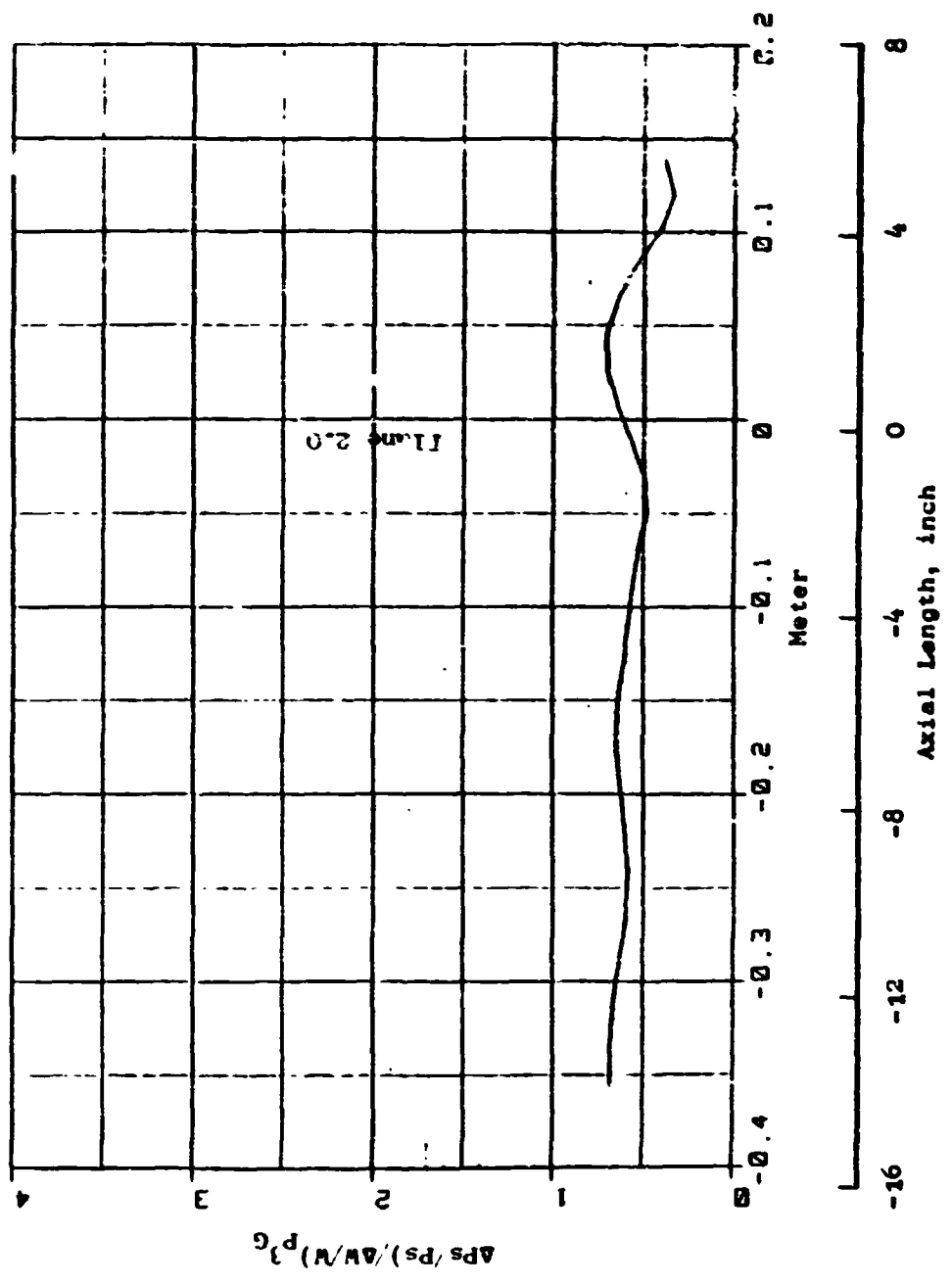
Figure D-6. Result of Nodal Analysis at $|p'_G| = 800Hz$, $P'G$-to-IGV.
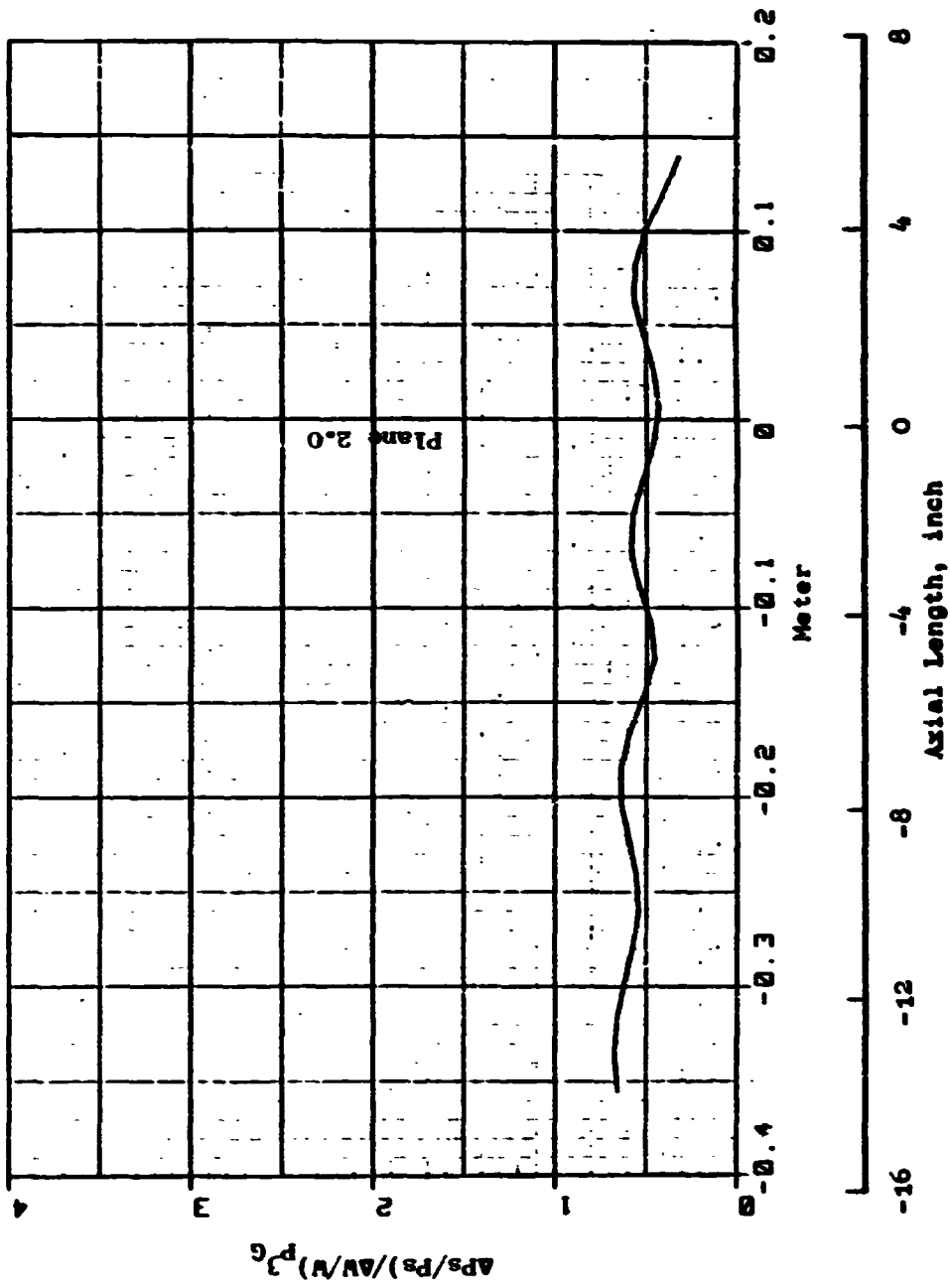
142

Figure D-7. Result of Nodal Analysis at $f_{p_G^3} = 1500$Hz, P^3G-to-IGV.

143
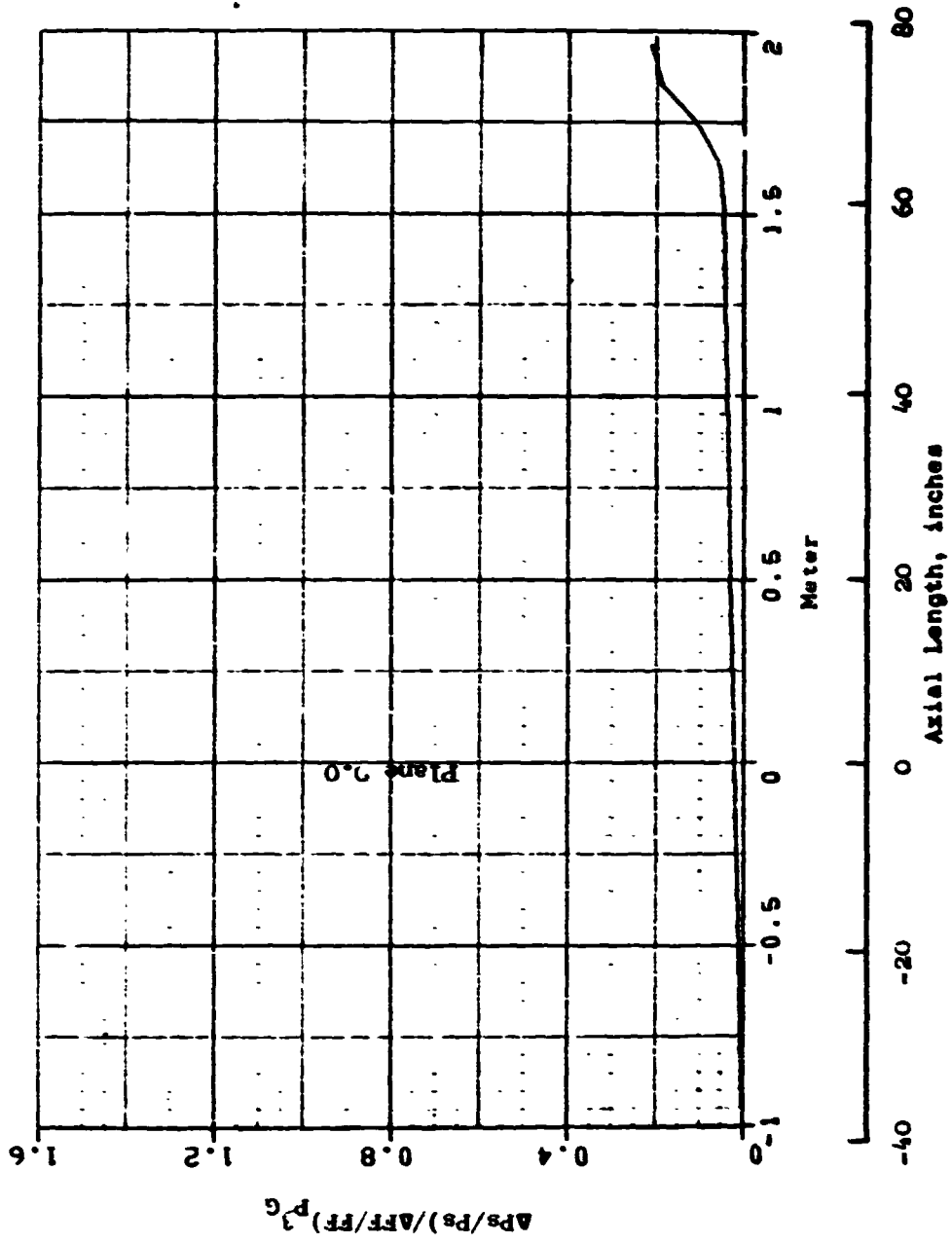
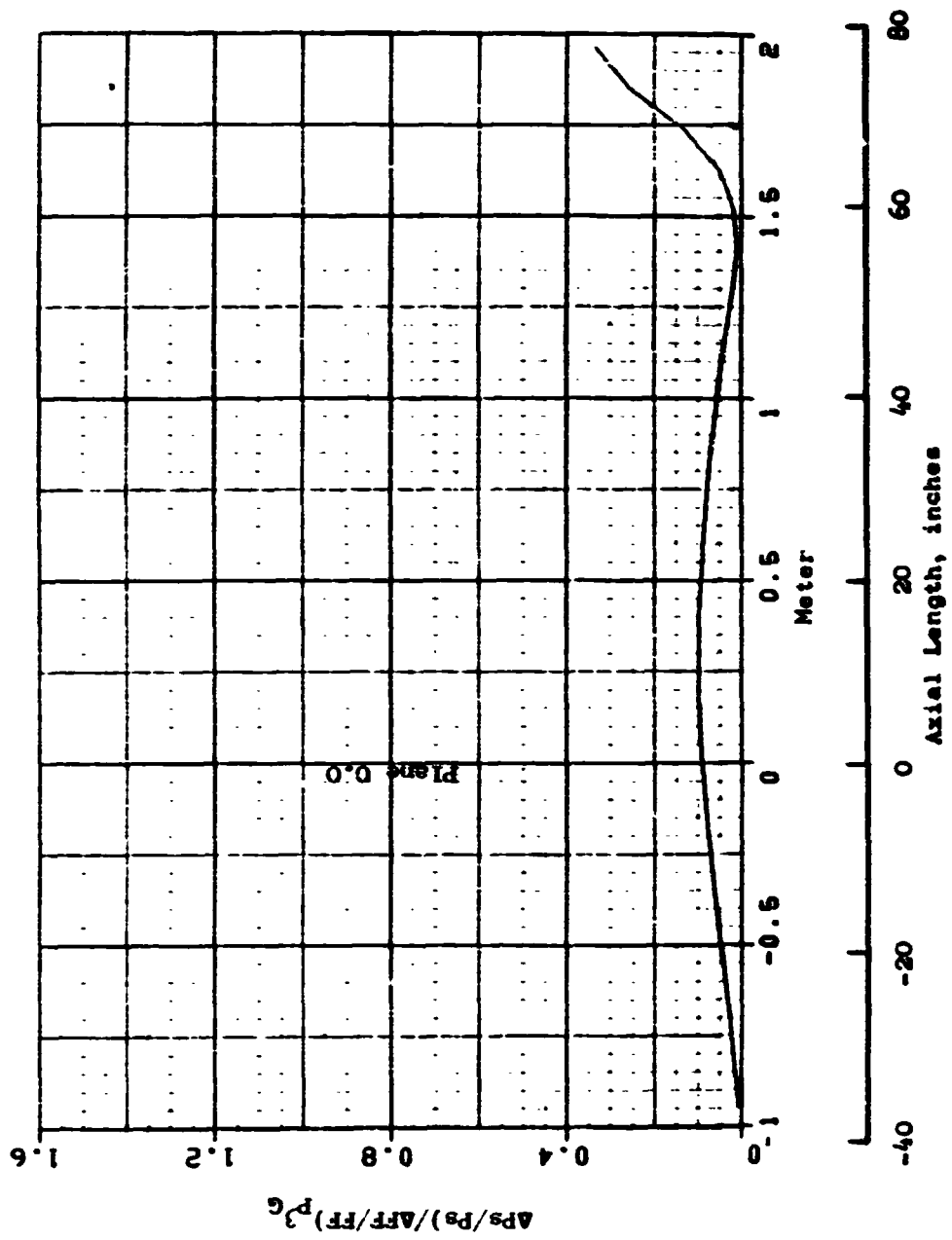Figure II-8. Result of Nodal Analysis at $F_p^3 G$, 10Hz, Bellmouth-to-IGV.

144

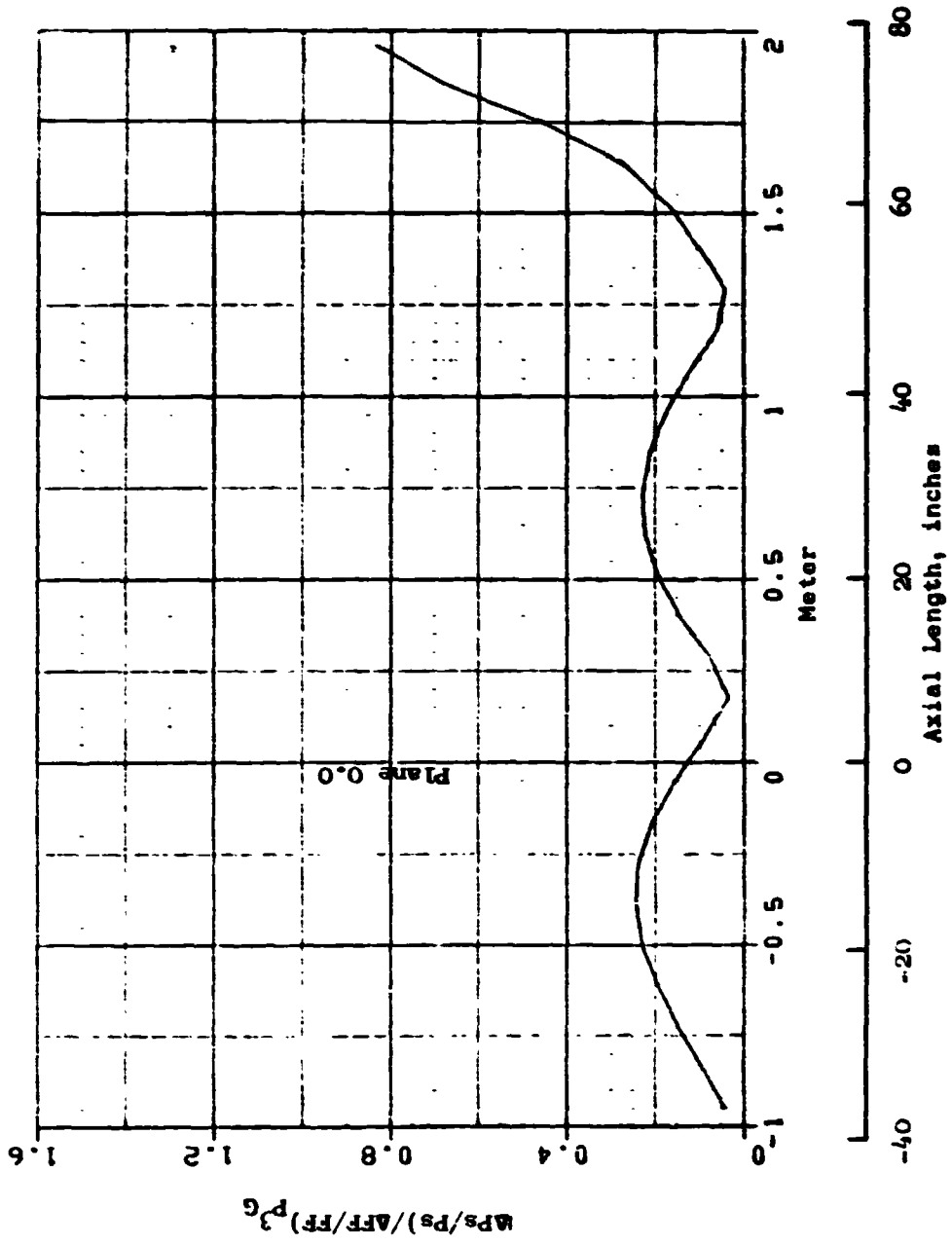Figure D-9. Result of Nodal Analysis at $F_1^1J_G = 75Hz$, Bellmouth-to-IGV.

Figure D-10. Result of Nodal Analysis at $f_p^3_G$ = 150Hz, Bellmouth-to-IGV.

Figure D-11. Result of Nodal Analysis at $f_p^3{}_G$ = 200Hz, Bellmouth-to-IGV.

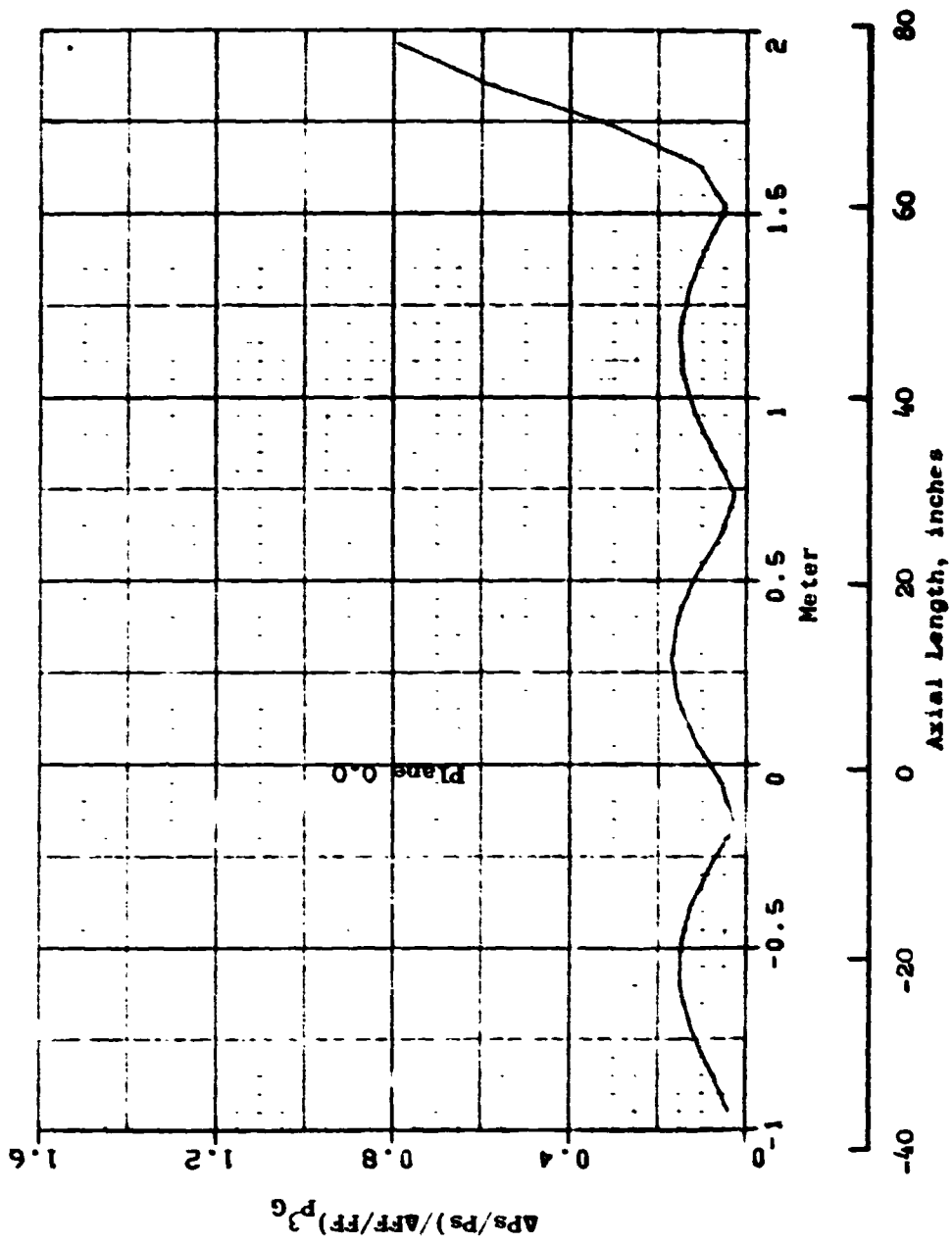Figure D-12. Result of Nodal Analysis at $1_{\text{r}} f_G = 300 \text{Hz}$, Bellmouth-to-IGV.

Figure D-13. Result of Nodal Analysis at $f_p^3{}_G = 400\text{Hz}$, Bellmouth-to-IGV.

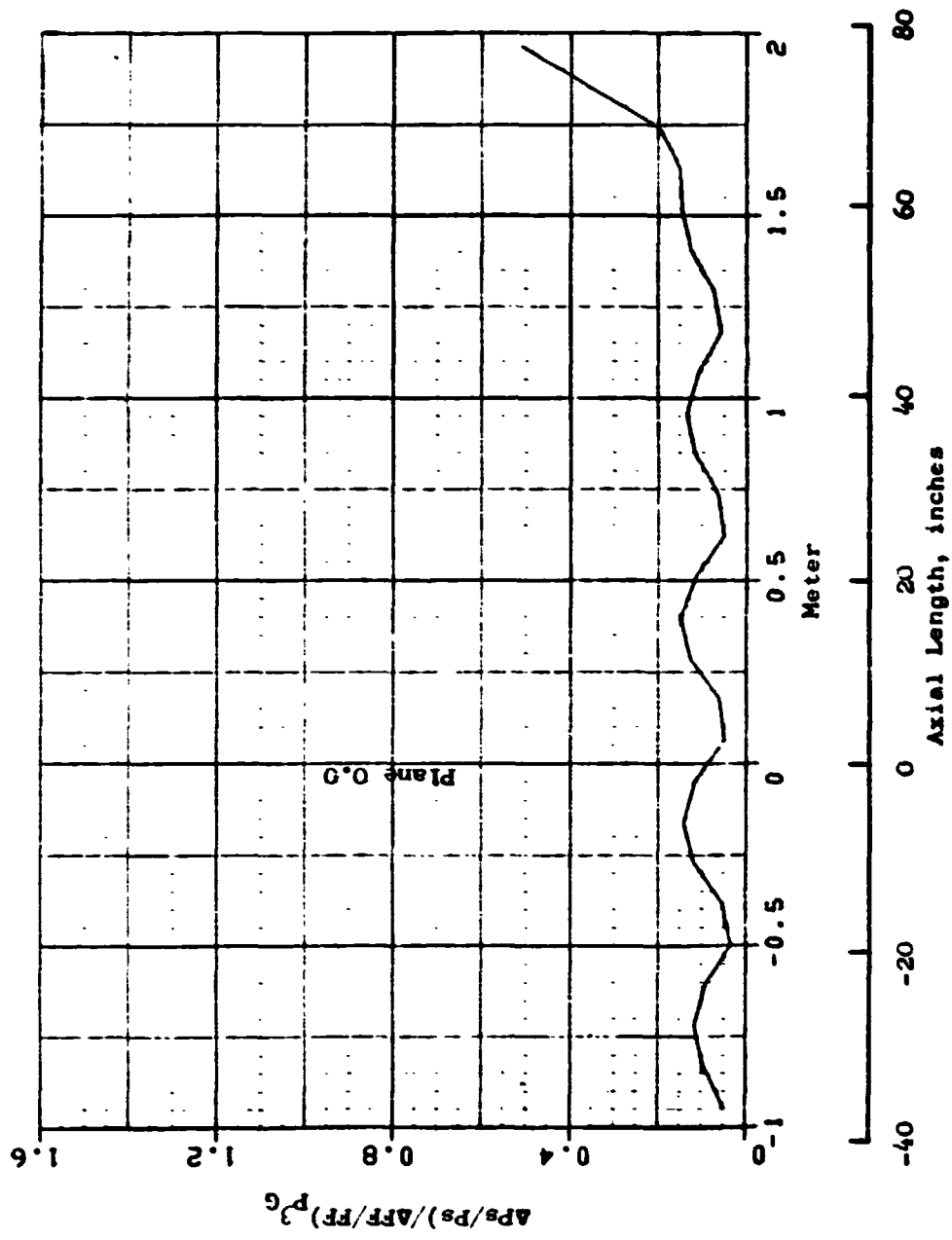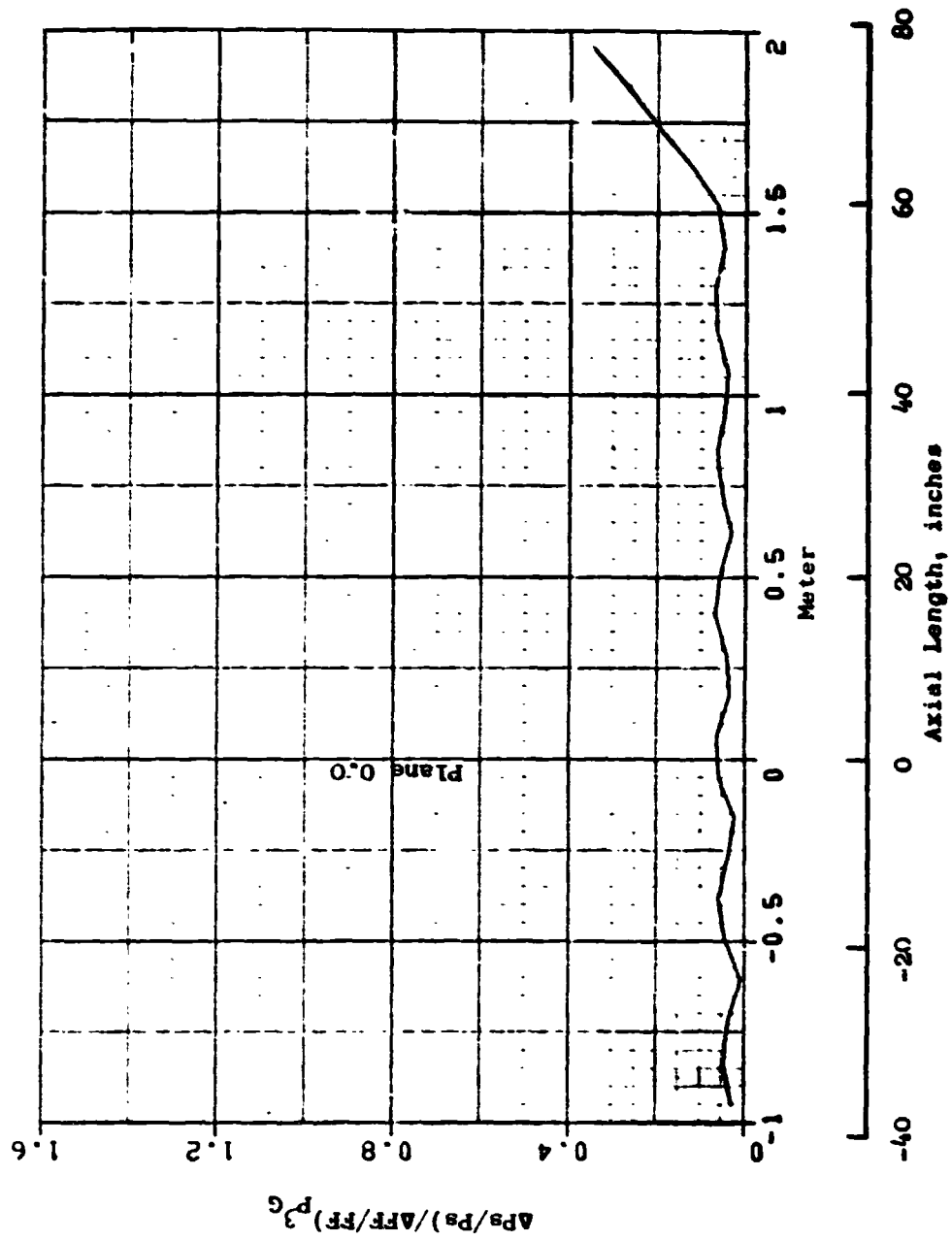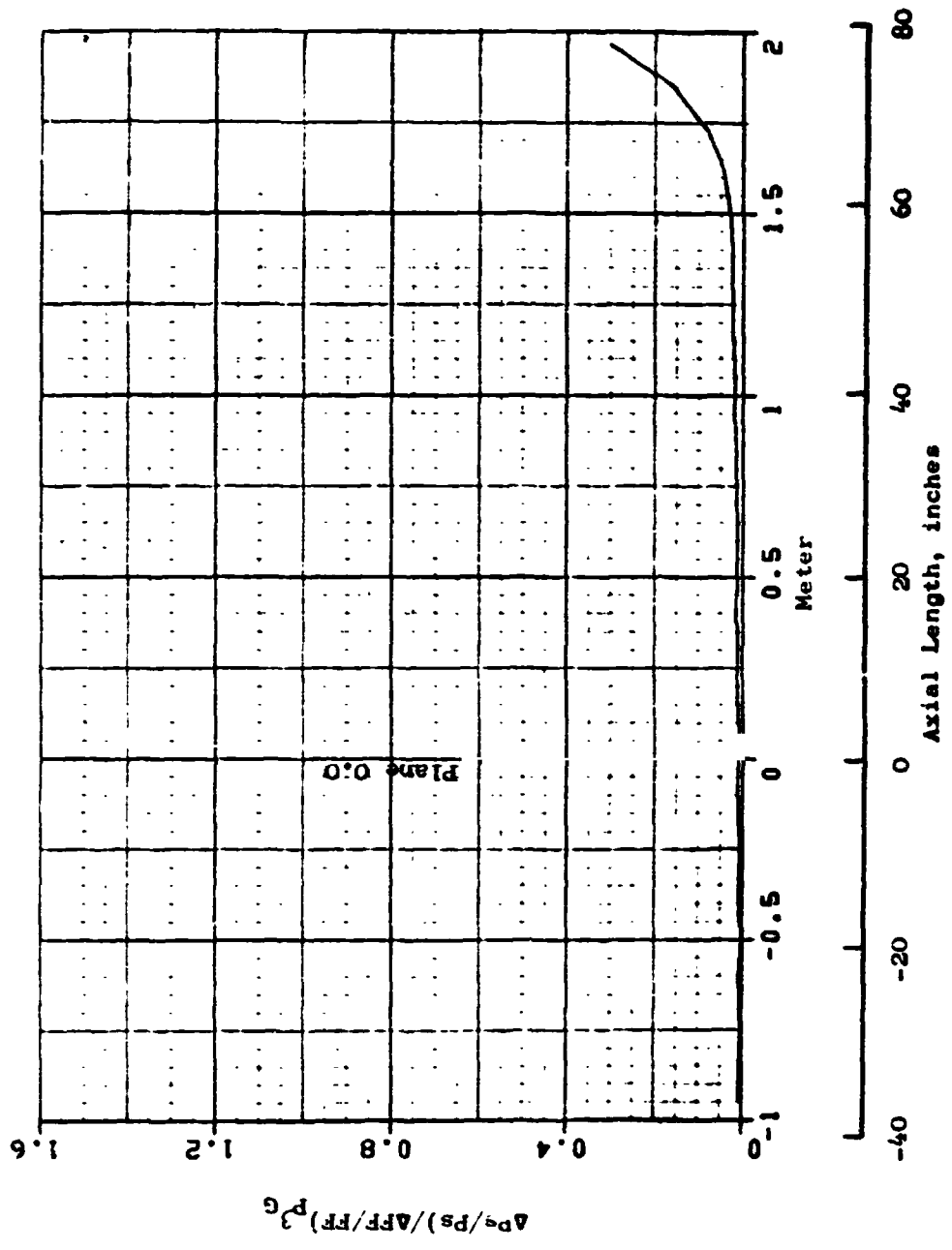Figure D-14. Result of Nodal Analysis at $f_\mu^3 G = 600 Hz$, Bellmouth-to-IGV.

150

REFERENCES

1. Reynolds, G. G., Vier, W. F., and Collins, T. P., "An Experimental Evaluation of Unsteady Flow Effects on an Axial Compressor - P^3G Generator Program", Air Force Aero Propulsion Laboratory Technical Report AFAPL-TR-73-43, July 1973.

2. Mehalic, C. M., and Lotting, R. A., "Steady State Inlet Temperature Distortion Effects on the Stall Limits of a J85-GE-13 Turbojet Engine," National Aeronautics and Space Administration Technical Memorandum TMX-2990, 1974.

3. Tesch, W. A., and Steenken, W. G., "Blade Row Dynamic Digital Compressor, Volume 1, J85 Clean Inlet Flow and Parallel Compressor Models," National Aeronautics and Space Administration Contract Report, CR-134979, 1976.

4. Tesch, W. A., Moszee, R. H., and Steenken, W. G., "Linearized Blade Row Compressor Component Model, Stability and Frequency Response Analysis of a J85-13 Compressor," National Aeronautics and Space Administration Contract Report, CR-135162, 1976.

5. Tesch, W. A., and Steenken, W. G., "Dynamic Blade Row Compression Component Model for Stability Studies," Journal of Aircraft, Volume 14, Number 8, PP. 827-829, August 1977.

6. Bisplinghoff, R. L., Ashley, H., and Halfman, R. L., "Aeroelasticity," Addison-Wesley, Cambridge, 1955.

7. Reynolds, G. G., and Steenken, W. G., "Dynamic Digital Blade Row Compression Component Stability Model, Model Validation and Analysis of Planar Pressure Pulse Generator and Two-Stage Fan Test Data," Air Force Aero Propulsion Laboratory Technical Report AFAPL-TR-76-76, August 1976.

8. Shepherd, D. G., "Elements of Fluid Mechanics," Harcourt, New York, 1965.